

Quantitative modeling of the magnetic  
field-dependent optical transmission of silica  
coated nickel nanorod colloids

Dissertation

zur Erlangung des Grades  
des Doktors der Naturwissenschaften  
der Naturwissenschaftlich-Technischen Fakultät  
der Universität des Saarlandes

von  
Florian Benjamin Krämer

Saarbrücken  
Dezember 2016

**Tag des Kolloquiums: 31.5.2017**

**Dekan: Univ.-Prof. Dr. Guido Kickelbick**

**Mitglieder des**

**Prüfungsausschusses: Univ.-Prof. Dr. Rolf Pelster**

**Univ.-Prof. Dr. Rainer Birringer**

**Univ.-Prof. Dr. Christian Wagner**

**Dr. Samuel Grandthyll**





### **Eidesstattliche Versicherung**

Hiermit versichere ich an Eides statt, dass ich die vorliegende Arbeit selbstständig und ohne Benutzung anderer als der angegebenen Hilfsmittel angefertigt habe. Die aus anderen Quellen oder indirekt übernommenen Daten und Konzepte sind unter Angabe der Quelle gekennzeichnet. Die Arbeit wurde bisher weder im In- noch im Ausland in gleicher oder ähnlicher Form in einem Verfahren zur Erlangung eines akademischen Grades vorgelegt.

Ort, Datum

Unterschrift

## Kurzzusammenfassung

Ziel dieser Arbeit ist es, siliziumdioxidumhüllte Nickelnanostäbe auf ihre Eignung als Sondenpartikel für die aktive Mikrorheologie und als Modellpartikel zur Untersuchung von Wechselwirkungen in weichen Matrizen zu untersuchen. Dazu werden Nickelnanostäbe mit Durchmessern von  $\sim 20$  nm und Längen von 150 – 1000 nm durch Abscheidung in Template aus nanoporösem Aluminiumoxid hergestellt und in eine wässrige kolloidale Suspension überführt. Durch Anwendung des Stöberprozesses werden die Stäbe mit einer 30 – 60 nm dicken Siliziumdioxidschicht umhüllt. Die Transmission linear polarisierten Lichts durch kolloidale Suspensionen dieser Partikel wird in statischen und oszillierenden magnetischen Feldern sowohl experimentell gemessen als auch theoretisch modelliert. Die Modellierung berücksichtigt dabei sowohl die magnetischen als auch die hydrodynamischen und optischen Eigenschaften der Partikel, wobei besondere Aufmerksamkeit der Bestimmung der optischen Querschnitte der Partikel zukommt. Basierend auf Größenabmessungen der Partikel, welche im Transmissionselektronenmikroskop bestimmt werden, wird das magnetfeldabhängige optische Transmissionssignal modelliert. Es zeigt sich eine sehr gute Übereinstimmung zwischen den gemessenen und den modellierten Signalen. Einflüsse des Partikels und Einflüsse der umgebenden Matrix auf Wechselwirkungen in weichen Matrizen können somit getrennt werden und die Partikel eignen sich als Sondenpartikel für die Mikrorheologie als auch als Modellpartikel.

## Abstract

The main objective of the present work is to test whether silica coated nickel nanorods can serve as probe particles for active microrheology and as model particles that can be used to investigate interactions in soft materials. For this purpose, nickel nanorods with diameters of  $\sim 20$  nm and lengths of 150 – 1000 nm are synthesized by deposition of nickel into nanoporous alumina templates and transferred into an aqueous colloidal suspension. By applying the Stöber process, the rods are coated with a silica shell of 30 – 60 nm thickness. The transmission of linear polarized light through the colloidal particle suspension in static and oscillating magnetic fields is experimentally measured and theoretically modeled. In the modeling, the magnetic, hydrodynamic, and optic properties of the particle are considered. Thereby, special attention is paid on the determination of the optical cross sections of the particles. Based on size parameters which are obtained by analyzing transmission electron micrographs, the magnetic field-dependent optical transmission is modeled. A very good agreement between the measured and modeled signal is found. Thus, contributions of the particle and contributions of the surrounding matrix to the results of microrheologic measurements can be separated and the particles are suitable as probe particles for microrheology and as model particles that can be used to investigate interactions in soft materials.

# Contents

<b>1</b>	<b>Introduction</b>	<b>1</b>
<b>2</b>	<b>Particle synthesis</b>	<b>7</b>
2.1	PVP coated Ni nanorods . . . . .	7
2.2	The Stöber process . . . . .	8
2.3	Silica coating of Ni nanorods . . . . .	11
<b>3</b>	<b>Experimental methods</b>	<b>13</b>
3.1	TEM . . . . .	13
3.2	Magnetic field-dependent optical transmission (MOT) . . . . .	13
3.2.1	Static MOT . . . . .	14
3.2.2	Oscillating MOT . . . . .	15
<b>4</b>	<b>Theory</b>	<b>19</b>
4.1	Magnetism of Ni nanorods . . . . .	19
4.1.1	Micromagnetic energy functional of ferromagnetic materials . . . . .	20
4.1.2	Single domain particles . . . . .	22
4.1.3	Shape anisotropy . . . . .	24
4.1.4	The Stoner-Wohlfarth model . . . . .	25
4.1.5	Pseudo-superparamagnetic behavior . . . . .	27
4.1.6	Orientation of the magnetic moment in OF-MOT measurements . . . . .	29
4.2	Hydrodynamic properties of Ni nanorods . . . . .	32
4.2.1	The rotational friction coefficient of a sphere . . . . .	33
4.2.2	The rotational friction coefficient of a spheroid . . . . .	36
4.2.3	The rotational friction coefficient of a cylinder . . . . .	37
4.2.4	Influence of deviations from the considered model . . . . .	41
4.3	Absorption and scattering of light . . . . .	44

4.3.1	Physical basis . . . . .	44
4.3.2	Field vectors and the Maxwell equations . . . . .	45
4.3.3	Extinction, scattering, and absorption . . . . .	46
4.3.4	General formulation of the problem . . . . .	47
4.3.5	Solving the scattering problem for spheres . . . . .	49
4.3.5.1	Mie theory . . . . .	49
4.3.5.2	Spheres small compared to the wave length . . . . .	55
4.3.5.3	Spheres in the electrostatic approximation . . . . .	56
4.3.6	Solving the scattering problem for spheroids . . . . .	59
4.3.6.1	The separation of variables method (SVM) . . . . .	59
4.3.6.2	Spheroids in the electrostatic approximation . . . . .	59
4.3.7	Solving the scattering problem for arbitrarily shaped particles by the finite element method (FEM) . . . . .	60
4.3.8	The Beer-Lambert law . . . . .	62
<b>5</b>	<b>Modeling</b>	<b>65</b>
5.1	DC-MOT . . . . .	65
5.2	OF-MOT . . . . .	68
5.2.1	Equation of rotational motion . . . . .	69
5.2.2	Characteristic frequency of nanorods . . . . .	70
5.2.3	Modeling of the DC-MOT and the OF-MOT response respecting distributions in the geometric parameters of the particles . . . . .	71
<b>6</b>	<b>Results I - Analysis of DC-MOT measurements of colloidal suspensions of PVP coated Ni nanorod</b>	<b>75</b>
6.1	Structural characterization . . . . .	75
6.2	Static magnetic field-dependent optical transmission . . . . .	78
6.3	Calculation of optical cross sections . . . . .	80
6.3.1	Spheroids in the electrostatic approximation (EA) . . . . .	80
6.3.2	Spheroids by the separation of variables method (SVM) . . . . .	82
6.3.3	Spheroids by the finite element method (FEM) . . . . .	83
6.3.4	Capped cylinders by FEM . . . . .	84
6.4	Analysis of DC-MOT measurements . . . . .	84
6.4.1	Model A: capped cylinders by FEM . . . . .	86
6.4.2	Model B: spheroids by EA . . . . .	87
6.5	Optical interaction of two particles . . . . .	91

## CONTENTS

---

<b>7 Results II - Quantitative modeling of DC- and OF-MOT signals of silica coated Ni nanorods colloids</b>	<b>97</b>
7.1 Structural characterization . . . . .	97
7.2 Static magnetic field-dependent optical transmission (DC-MOT) . . . . .	100
7.3 Dynamic magnetic field-dependent optical transmission (OF-MOT) . . . . .	106
7.4 Polydispersity . . . . .	108
7.5 Multi-core particles . . . . .	113
7.5.1 Modeling OF-MOT using polydisperse single core and linear multi-core particles . . . . .	117
7.5.2 Modeling DC-MOT using polydisperse single core and linear multi-core particles . . . . .	124
<b>8 Summary</b>	<b>129</b>
<b>9 Outlook</b>	<b>133</b>
<b>A Additional TEM micrographs of PVP coated Ni nanorods</b>	<b>137</b>
<b>B Additional TEM micrographs of silica coated Ni nanorods</b>	<b>141</b>
<b>C Vitality of human cells interacting with differently coated Ni nanorods</b>	<b>145</b>
<b>D Colloidal stability of silica encapsulated nanorods in aqueous dispersions</b>	<b>149</b>
<b>E Legal notice</b>	<b>157</b>
<b>F Publications</b>	<b>159</b>
F.1 Papers . . . . .	159
F.2 Conference contributions . . . . .	160



# Chapter 1

## Introduction

In 1827, Robert Brown observed irregular jerky motion of pollen on a water droplet and by that discovered what was later called the Brownian motion [1]. In 1905, Albert Einstein explained this motion as the result of the thermal movement of water molecules and related it to the viscosity of water [2]. This famous example illustrates the use of probe particles to study the viscoelasticity of liquid materials. The investigation of the deformation and flow properties of materials is called rheology. An additional consideration of how the dynamic behavior of materials change with length scale leads to the extended definition of microrheology [3]. The random motion of the pollen was observed in a passive manner as done in passive microrheology where the probe particles are moved by their inherent thermal energy. In typical microrheological experiments, the trajectory of a probe particle is measured as a function of time, e.g. by optical microscopy. A generalized Stokes-Einstein relation is then used to extract frequency-dependent rheological properties [4], like the storage and loss modulus.

Although several types of measurement can be used to study a variety of materials in passive microrheology [3], it is limited to systems where the thermally activated particle motion is comparatively high. In purely elastic soft materials or fluids of high viscosity, an active control of the particle motion is more appropriate.

One possibility for an active control of microscopic particles is to use optical tweezers where microscopic particles are moved into the focus of a laser beam [5]. Typically, the beam is mirrored into an optical microscope to focus it in the object plane. If the particle is transparent at the used wavelength, a momentum transfer caused by the refraction of light by the particle results in a force moving it into focus. A difference between the position of the laser beam and the position of the particle due to viscous drag or elastic

interactions of the particle with the matrix can be observed and its analysis allows to extract rheological properties of the medium. Brau et al. outlined the usage of optical tweezers to measure the microrheological behavior of several materials like glycerol, methyl cellulose solutions, actin matrices, and cellular membranes [6] and Wilson et al. performed passive and active (using optical tweezers) microrheological measurements of PMMA colloids [7].

Another method to perform active microrheology is to manipulate magnetic particles using external magnetic fields [8–11]. In most of these experiments spherical magnetic *beads* are used [12–14]. Using ferromagnetic particles additionally allows to exert torques using homogeneous external fields on the particles and thus to change the orientation of the particles. The comparison of the orientation of the particle’s magnetic moment and the orientation of the external field can be used to extract rheological quantities.

An anisotropic particle shape also allows to investigate rotation axis dependent interactions with the surrounding matrix as well as to observe their orientation optically, emphasizing their suitability as probe particles in active microrheology [15]. One example for the use of such anisotropic particles are Ni microrods ( $d \approx 200$  nm and  $l \approx 5 - 20$   $\mu\text{m}$ ) which were investigated as magneto-optical switches [16], probe particles in interfacial shear microrheology [17], and magnetic rotational spectroscopy [18, 19]. A direct observation of field-induced rotation by light microscopy is possible at the larger size of these rods which also implies a comparatively high weight limiting the temporal stability of suspension in liquids of low viscosity [16]. To reduce the effect of sedimentation, smaller particles have to be employed which unfortunately limits their observability using optical microscopy. However, the reduced depolarization factor along the rod axis leads to an increased electrical polarizability with a resulting optical extinction cross section that shows a strong dependence on the orientation of the particle relative to the polarization direction of the incident light which allows the detection of the orientation of ensembles of particles [20].

The electronic structure of Ni is responsible for its ferromagnetism and a moderate damping of its plasmon resonance. This results in collinear magnetic and optical anisotropies which can be used to produce magnetic field-dependent optical effects [20–22]. These effects may result in particular applications for homogeneous protein detection [23] and magnetic field-dependent optical switches [16, 20]. The optical transmission through Ni nanorod colloids in static external magnetic field (direct current magnetic

field-dependent optical transmission, DC-MOT) was already studied and the obtained magnetic moments per particle agreed with values measured by vibrating sample magnetometry (VSM) [20, 24, 25].

Dynamic magnetic field-dependent optical transmission measurements in rotating magnetic fields were used to observe a field and frequency dependent phase lag which is related to the rotational diffusion coefficient  $D_r$ . This method was used to measure the rotational diffusion coefficient of Polyvinylpyrrolidone (PVP) coated Ni nanorods [24, 25]. Although the results agreed with AC magnetization and dynamic light scattering, the absolute values were smaller by a factor of  $\sim 2$  than theoretically expected based on the size of the nanorods obtained by electron microscopy. Since the rotational diffusion coefficient is related to the rotational friction coefficient by  $\xi_r = k_B T / D_r$  [2], the experimental value of  $\xi_r$  is larger than the theoretically expected one. This may be explained by differences in the geometric dimensions of the particle measured in vacuum by transmission electron microscopy compared to the geometric dimension of the particle when dispersed in a liquid matrix. One reason for this discrepancy may be found in the organic PVP coating of the Ni nanorods. The thickness of this polymeric layer is unknown when dispersed in a liquid matrix like water. Furthermore, the rough surface of the Ni core itself leads to a particle-matrix-interface with an ill-defined shape and position, Fig. 1.1(a).

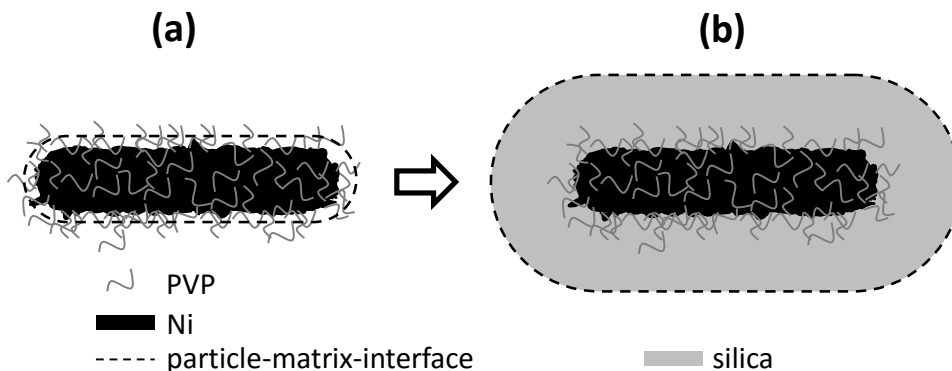


**Figure 1.1:** Illustration of the ill-defined particle-matrix-interface of a PVP coated nanorod (a) and the desired particle-matrix-interface of a nanorod with an additional silica coating.

This indeterminableness of crucial parameters, i.e. length and diameters of the particles, when dispersed in water hampers the calculation of an exact value for the rotational friction coefficient. To solve this problem, an additional inorganic layer might be used to

provide a well-defined particle-matrix-interface, Fig. 1.1(b). Due to its mechanical stability and its well investigated properties, silica is a promising candidate for this purpose and it was already used to coat nanoparticles such as silver and gold spheres [26, 27] or gold rods [28]. Furthermore, the the usage of a silica shell offers the possibility for various particle and surface functionalizations, e.g. fluorescence labeling [29] or hydrophobization [30]. The objective of this work is to synthesize silica encapsulated Ni nanorods and to investigate their hydrodynamic properties in terms of the rotational friction coefficient.

Nanorods are synthesized by a template method and encapsulated by silica using the Stöber process. The synthesized particles are dispersed in a medium with well-defined interaction mechanisms, i. e. a Newtonian fluid where the dynamic behavior in general and the rotational friction coefficient of the particle in particular is determined by the Navier-Stokes equations. The geometric dimensions of the particles can be measured by analyzing transmission electron micrographs and their rotational friction coefficient calculated based on theoretical models. To determine the rotational friction coefficient experimentally, one could use AC magnetization measurements, as already done for PVP coated Ni nanorods [24, 25]. To avoid hydrodynamic and dipolar particle-particle interactions, the particle concentration should be as low as possible. A method suitable to measure the rotational friction coefficient at low particle concentrations is the magnetic field-dependent optical transmission in oscillating magnetic fields (OF-MOT) which was already employed for the analysis of the gelation of gelatin aqueous solution [15]. In this method, the particles in suspension are forced to an oscillatory motion by an external magnetic field. As in static or rotating magnetic field MOT, the orientation of the particle ensemble is observed using the transmission of linearly polarized light. The time-dependent transmitted intensity depends on several particle properties, i. e. the magnetic moment, the rotational friction coefficient, and the orientation dependent optical cross section. All these properties are determined by the geometric dimensions of the particles implying the possibility to model the complete OF-MOT signal. A quantitative agreement of the modeled with the measured data is expected if the modeling of all parameters, including the rotational friction coefficient, is correct. Hence, the central idea of this work is the comparison between measured and modeled OF-MOT signal of colloidal suspensions of silica coated Ni nanorods in order to critically investigate whether or not their magnetic, optical, and particularly hydrodynamic properties are well-defined.

The most challenging part of the modeling is the determination of the orientation de-

---

pendent optical cross section of the particles. In previous studies, the electrostatic approximation (EA) was used to estimate these cross sections [20]. The usage of the EA was motivated by its major advantage of providing closed analytic expressions. However, the accuracy of the derived cross sections remains questionable because the assumption in the EA of a homogeneous electric field inside the nanorods is not justified for rod length  $L \approx \lambda$ . Furthermore, in order to apply the EA, the particle shape has to be approximated by prolate spheroids.

Thus, the cross sections should be calculated without these approximations using a more advanced method. To calculate the optical cross sections, it is necessary to solve the electromagnetic scattering problem which is a challenging task. G. Mie provided the first exact solution for spherical particles of arbitrary size [31]. Applying the separation of variables method (SVM) to spheroidal vector wave functions leads to a solution of the scattering problem for spheroids [32–34]. There are no exact solutions for arbitrarily shaped particles but semi-analytical methods are available, e. g. the T-matrix, and numerical methods as the finite difference time domain method (FDTD), the finite element method (FEM), and the discrete-dipole approximation (DDA). For more information concerning the different methods, reference is made to reviews by J. Parsons [35] and T. Wriedt [36]. The spectral properties of cylindrical particles have been investigated with a major focus on gold nanorods due to their distinct plasmon resonances [37–40] but size dependent optical cross sections for Ni nanorods could not be found in literature. In the present work, numerical values for the extinction cross sections of Ni nanorods with and without silica coating at a fixed wavelength for different particle lengths and diameters are derived using the finite element method (FEM).

In continuation of the studies performed in [20] and in order to increase the complexity of the modeling of the magnetic field-dependent optical transmission step by step, the first part of this work is focused on static field-dependent measurements of the optical transmission performed on suspensions of PVP coated Ni nanorods. These measurements can be analyzed to obtain basic characteristics of a nanorod colloid, such as average magnetic moment per particle, aspect ratio, and particle concentration. The determination of these quantities relies on an appropriate model for the nanorod optical extinction cross sections which were obtained using the electrostatic approximation in earlier studies [20]. In the present work, the improved cross section calculation by FEM and for reasons of comparison EA based cross sections will be used. One focus lies on the errors in the analysis of DC-MOT measurements associated with the approximation of electrostatic

homogeneous polarization and of the particle shape as spheroids with the objective to derive a more reliable analysis protocol.

In the next step, the established analysis of DC-MOT measurements is applied to colloidal suspensions of silica encapsulated Ni nanorods. This requires to expand the FEM based calculation of optical cross sections to a core-shell model corresponding to silica encapsulated Ni nanorods. In the last step, the rotational friction coefficient is included to model the dynamic OF-MOT signal. Finally, the modeled DC- and OF-MOT signals are compared to the corresponding measured signals.

The outline of the work is as follows: The synthesis of PVP and silica coated Ni nanorods is described in chapter 2. The used experimental methods, i. e. TEM, DC-MOT, and OF-MOT are presented in chapter 3. The theory to calculate the magnetic, hydrodynamic, and optical parameters of the particles is depicted in chapter 4. The resulting relations are used in chapter 5 to derive instructions to model the DC- and OF-MOT signal. Chapter 6 provides the results and discussion of DC-MOT measurements on colloidal suspensions of PVP coated Ni nanorods and the focus of chapter 7 lies on the results and the discussion concerning the comparison of modeled and measured magnetic field-dependent optical transmission of dispersions of silica coated Ni nanorods in static and oscillating magnetic fields. In chapter 8, the results are concluded and chapter 9 provides an outlook for further studies using silica encapsulated Ni nanorods. The appendices contain additional results and supplementary information.

# Chapter 2

## Particle synthesis

Ni nanorods were synthesized by a well-established [20, 24, 25, 41, 42] process which uses porous alumina layers as templates. The synthesis of colloidal suspensions of PVP coated Ni nanorods can be divided into four process steps. First, a double-stage anodic oxidation was carried out to obtain a porous alumina layer. Then the pore channels were filled with Ni by current-pulsed electrodeposition. The resulting rods were trapped in the alumina matrix, which was dissolved in the subsequent step. Finally, the obtained suspension was washed several times to obtain a stable colloidal suspension.

### 2.1 PVP coated Ni nanorods

In the following, the practical proceeding of the synthesis of Ni nanorod colloids is described. *The protocol was already published in [43], see appendix E.*

Porous alumina templates were synthesized by two-stage anodic oxidation [44]. The first anodization of Al foils was carried out by applying a constant voltage of 15 V for 24 h in 2M H<sub>2</sub>SO<sub>4</sub> at -6 °C using Pb foils as counter electrodes. The obtained alumina layer was dissolved in a solution of 0.12M H<sub>3</sub>PO<sub>4</sub> and 0.2M H<sub>2</sub>CrO<sub>4</sub> at 60 °C. A second anodization was performed at a constant voltage of 20 V under the same bath conditions as used in the first anodization. The cumulated areal charge density during the second anodization was limited to pre-defined values in the range of 2 – 9 C/cm<sup>2</sup> in order to obtain alumina layers of suitable thickness. The insulating barrier oxide thickness at the pore bottom was reduced by decreasing the applied voltage at the end of the second anodization process every 3 s in 1 V-steps until 5 V were reached [20]. After a 10 – 15 min etching step in 0.1M H<sub>3</sub>PO<sub>4</sub> at room temperature, which reduced structural inhomogeneities in the pore

channels and slightly increased their diameter, the pores were filled with Ni by pulsed electrodeposition in a Watts-bath (300 g/l NiSO<sub>4</sub> · 6H<sub>2</sub>O, 45 g/l NiCl<sub>2</sub> · 6H<sub>2</sub>O and 45 g/l H<sub>3</sub>BO<sub>3</sub>) at 35 °C, using Ni foils as counter electrodes [45–48]. A selected number #<sub>p</sub> of current pulses (50 mA/cm<sup>2</sup>), each consisting of a positive (duration t<sub>+</sub>) and a negative (t<sub>-</sub>) pulse separated by a break (t<sub>0</sub>), were applied to obtain rods of different length, Tab. 2.1. The rods were released by dissolving the alumina template layer in an aqueous NaOH solution (pH ≈ 11.5). The surfactant polyvinyl pyrrolidone (PVP) was added to prevent rod agglomeration by steric repulsion [49, 50]. Stable colloidal dispersions were obtained after repeated washing cycles consisting of centrifugation at 15557 rcf for 15 min and redispersion in double distilled water [24, 41]. Larger agglomerates were removed by sedimentation in a final slow centrifugation step at 200 rcf for 2 h.

The samples scn-1 – scn-3 of PVP coated Ni nanorods were encapsulated using an adapted Stöber process which will be described in the next section.

sample	pcn-1	pcn-2	pcn-3	pcn-4	scn-1	scn-2	scn-3
charge density [C/cm <sup>2</sup> ]	2	2	1.5	9	2	1.5	9
time in H <sub>3</sub> PO <sub>4</sub> [min]	10	10	10	15	10	10	10
# <sub>p</sub>	200	400	500	4000	300	500	4000
t <sub>+</sub> [ms]	16	4	4	4	4	4	4
t <sub>-</sub> [ms]	4	16	16	16	16	16	16
t <sub>0</sub> [ms]	200	200	200	400	200	200	200

**Table 2.1:** Parameter for the synthesis of Ni nanorods.

## 2.2 The Stöber process

The Stöber synthesis [51] which is a sol-gel process was adapted to coat the Ni nanorods with silica as first described in [52] which served as base for the following description. The reaction involves two steps: the formation of very small particles of a few nanometer followed by their aggregation to larger, but still microscopic, particles. Originally, Stöber and Fink developed the method to synthesize spherical silica colloids based on the hydrolysis of alkoxy silanes in a solution of ammonium hydroxide, water, and alcohol [51]. While the alcohol is used to homogenize the alkoxy silanes and the water, the ammonium hydroxide acts as a catalyst that accelerates the reaction by increasing the pH

## 2.2 The Stöber process

---

value [53]. The high pH value is important for a regular morphology of the particles [51]. The rates of nucleation and aggregation depend on the ratios of ammonium hydroxide, water, and alcohol. By choosing the appropriate amounts of precursors, it is possible to synthesize particles with a very narrow size distribution and diameters between 50 nm and 2  $\mu\text{m}$ .

In the following, an overview of the reactions occurring during the Stöber process will be given.

### Chemical reactions

The formation of the silica particles is divided into two phases, hydrolysis of alkoxy silanes leading to silicic acid molecules and condensation of these to form the final silica particles [54].

#### Hydrolysis

In the present work, tetraethyl orthosilicate (TEOS,  $\text{C}_8\text{H}_{20}\text{O}_4\text{Si}$ ) with the alkyl  $\text{R}=\text{C}_2\text{H}_5$  and the structure shown in Fig. 2.1 was used.

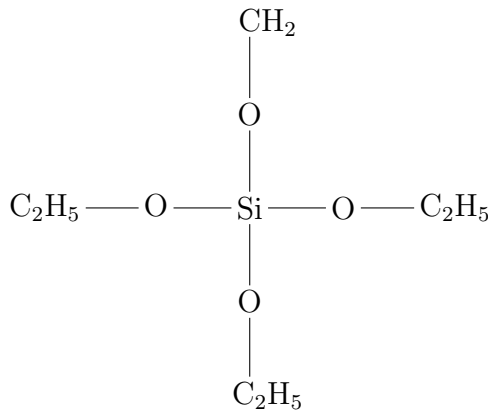
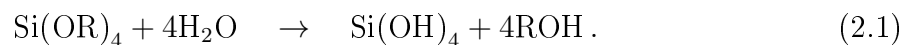


**Figure 2.1:** Structural formula of TEOS.

In the alkaline environment, the water dissociates and nucleophilic  $\text{OH}^-$  ions are present. These ions react with the alkoxy silane molecules and substitute its OR groups. Silicic acid and ethanol are generated by this hydrolysis



The hydrolysis is a nucleophilic substitution reaction. The alkoxy groups are not all replaced at the same time, but in several steps, Fig. 2.2. The substitution of the first

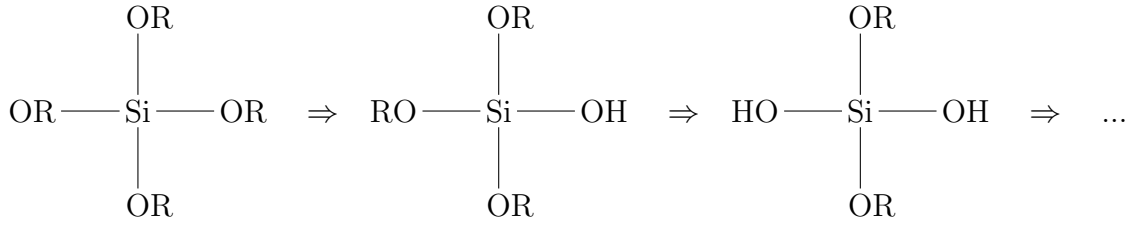
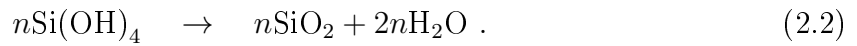


**Figure 2.2:** Substitution reaction during hydrolysis.

OR group is the crucial step because the electron density of the silicon atom is reduced and further OR groups are subsequently replaced [55].

### Condensation

In the condensation reaction, several silicic acid molecules react with each other under separation of water



This is an autocatalytic process because the formation of water occurring during the condensation accelerates the reaction. Crosslinking of the molecular precursors follows the reaction shown in Fig. 2.3.

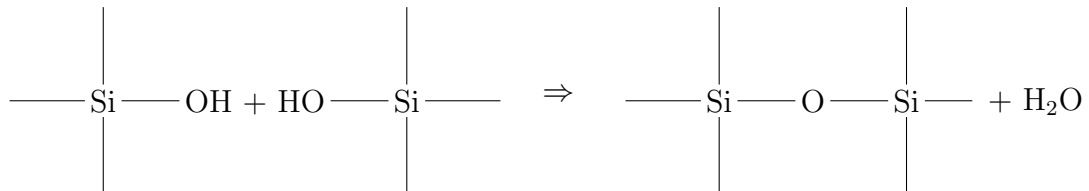


**Figure 2.3:** Formation of silica particles.

Since partially hydrolyzed alkoxy silanes can also react to build Si–O–Si bonds leading to silica and ethanol, not all OR groups need to be replaced by OH groups, Fig. 2.4.

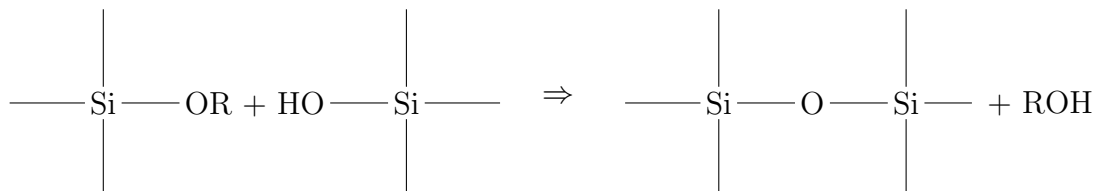


**Figure 2.4:** Side reaction during the Stöber process.

The Stöber process allows the synthesis of monodisperse silica particles. In an adapted form, the process can also be used to cover nanoparticles with a silica shell [26, 53, 56–

## 2.3 Silica coating of Ni nanorods

---

58]. The requirements to coat Ni nanorods with silica using an adapted Stöber process will be discussed in the next section.

## 2.3 Silica coating of Ni nanorods

Silica coating of nanoparticles requires a high chemical affinity of the surface of the particles to silica. Furthermore, to obtain single core particles, it is important that the primary particles are individually dispersed in the reaction mixture.

To prevent agglomeration during the preparation of the Ni nanorods, PVP was added to the NaOH solution in which the alumina template was dissolved. PVP adsorbes on the rod surface and provides steric repulsion to counteract short range Van-der-Waals forces as already mentioned in section 2.1. While the growth of silica on Ni oxides was already reported in literature, it was shown that the affinity of Ni to silica is low [59]. Although the nanorods are expected to be covered by a NiO surface oxide layer, it remains questionable if its thickness is sufficiently large to allow adsorption of silica on the rod surfaces. However, PVP facilitates the growth of silica on various surfaces [57] suggesting that silica coating is likely to grow on top of the PVP layer of the Ni nanorods.

The individual dispersion of the nanorods in the reaction mixture poses an additional challenge. In stable aqueous colloids, the long range dipolar attractive forces due to the permanent magnetic moment of the rods is counteracted by electrostatic repulsion of the positively charged rods. This repulsion is greatly reduced in solutions of high ionic strength or at high pH values like in the ammonium hydroxide solution used in the Stöber process. To reduce rod agglomeration during the Stöber process, the interparticle distance is increased by using very low particle concentrations resulting in a large volume of the reaction mixture. As particles have to be separated from the solvent after finishing the Stöber process by centrifugation, finding the optimal particle concentration is determined by the compromise between a low particle concentration and the viability of the separation process. In the present work, 15 samples of silica coated Ni nanorods of different lengths and diameters with different ratios and amounts of precursors were synthesized. Although the particle concentrations during the Stöber process were chosen very low, the fraction of singly dispersed silica coated Ni nanorods was not satisfying in most cases. Hence, most of the prepared samples were discarded due to insufficient sample quality.

The ratio of precursors has to be adjusted to obtain the desired thicknesses of the silica

shells. A recipe published by Hardikar [26] who coated silver spheres with silica served as the starting point and the amounts of chemicals were adjusted to obtain a complete and homogeneous silica layer.

## Practical procedure for the silica coating of the Ni nanorods

To synthesize silica encapsulated nanorods (scn), the colloidal dispersion of PVP coated nanorods was diluted in a mixture of 2-propanol,  $\text{NH}_3$  solution (25%) and water at  $40^\circ\text{C}$ . By adding tetraethoxysilane (TEOS, 99.9%), the Stöber process was initialized. Details of the synthesis are shown in Tab. 2.2. The resulting particles were separated by centrifugation at 15557 rcf for at least 10 min and subsequently redispersed in double distilled water. A strong magnetic gradient field that attracts the ferromagnetic core of the silica encapsulated Ni nanorods was used to separate them from non magnetic pure silica spheres which are a by-product of the Stöber process. The washing steps were repeated until a stable dispersion of silica encapsulated Ni nanorods was obtained. In the case of the samples scn-1 and scn-2, an additional centrifugation step at 200 g for 60 min or 95 min was carried out to remove large agglomerates.

sample	scn-1	scn-2	scn-3
$\text{NH}_3$ solution (25%) [ml]	6.8	5.3	5.2
$\text{H}_2\text{O}$ [ml]	28	8.9	2.7
TEOS [ $\mu\text{l}$ ]	160	50	12.5
added nanorods [ $10^{10}$ ]	7.1	23	2.5
reaction time [min]	60	35	120
intermixing	ms	us	us

**Table 2.2:** Amounts of reagents and Ni nanorods added to 100 ml 2-propanol to synthesize silica coated nanorods (scn). Mixing during the Stöber process was performed with a magnetic stirrer (ms) or ultra sonic bath (us). The differences in the ratios of the reagents between the different samples arise from the different particle sizes which will be shown later.

In the next chapter, the experimental methods used to investigate the colloidal dispersions of PVP and silica encapsulated Ni nanorods, respectively, will be presented.

# Chapter 3

## Experimental methods

Transmission electron microscopy (TEM) was used for structural characterization of the particles. Static as well as dynamical magnetic field-dependent optical transmission (MOT) measurements were used for characterization of the particle concentrations, diameters and their characteristic relaxation frequencies.

### 3.1 Transmission electron microscopy (TEM)

All micrographs used for the present work were generated using a JEOL JEM-2011 transmission electron microscope. A small volume of the rod suspension was dropped onto a carbon coated copper grid and dried in the ambient atmosphere. The rods were visualized in bright field TEM micrographs using electrons accelerated with 200 kV. Supported by the image analysis software *ImageJ* [60], geometric dimensions of hundreds of particles were extracted from the TEM images. For this purpose, lengths and diameters were measured manually and tabulated in a way that conserves the relation of length and diameter of each particle.

### 3.2 Magnetic field-dependent optical transmission (MOT)

*Modified versions of sections 3.2 and 3.2.1 were already published as a part of publication [43], see appendix E.*

For magneto-optical transmission measurements, a HeNe laser L is used which generates

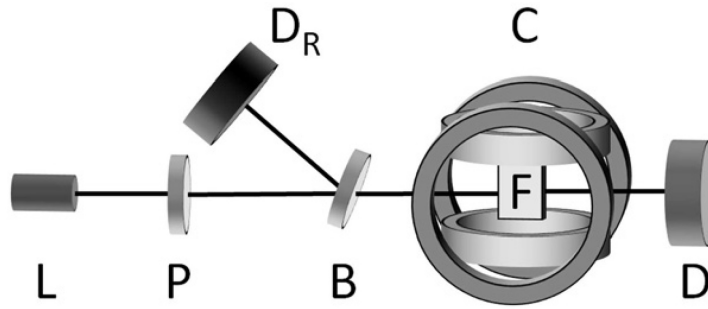


**Figure 3.1:** Experimental setup for magneto-optical transmission measurements of nanorod colloids [43].

linearly polarized light ( $\lambda = 632.8 \text{ nm}$ ) with a polarization direction defined by a half-wave plate P, Fig. 3.1. The laser beam propagates parallel to the  $z$ -direction. A beam splitter B directs about half of the light intensity to a reference detector  $D_R$ . The main beam passes a cuvette (High Precision Cell by Hellma Analytics, special optical glass) containing the colloidal suspension of the particles F (optical path length 1 cm). The cuvette is centered inside two sets of crossed Helmholtz coils C which generate magnetic fields up to  $H_{\text{ext}} = 150 \text{ Oe}$  parallel ( $x$ -direction) and perpendicular ( $y$ -direction) to the electric field vector of the incident light, respectively. The magnetic flux densities in both directions are detected by Hall probes. The temperature of the cuvette was kept at  $20^\circ \text{ C}$ . The transmitted intensity is measured by the sample detector D. Oscillations and drift in the laser intensity are compensated by computing the ratio of the two detector voltages,  $R = U_{D_R}/U_D$ , which is proportional to the transmittance  $T = I/I_0$ .

### 3.2.1 Static MOT

In static direct current magnetic field-dependent optical transmission (DC-MOT) measurements, the optical transmission of the particle suspension  $R$  is determined at different static magnetic fields  $H_{\text{ext}}$ . The measured voltage ratios are normalized to  $R_\times = R(H_{\text{ext}} = 0)$ , i.e.

$$R(H)/R_\times = T(H)/T_\times = I(H)/I_\times . \quad (3.1)$$

Another mode of operation for the presented MOT setup are measurements in oscillating magnetic fields (OF-MOT) that will be described in the following.

## 3.2 Magnetic field-dependent optical transmission (MOT)

---

### 3.2.2 Oscillating MOT

The setup used to perform oscillating magnetic field-dependent optical transmission (OF-MOT) measurements is basically identical to the one described above, Fig.3.1. Details of the technical implementation of the OF-MOT mode can be found in [15]. The amplitude and phase of the optical signal with respect to the magnetic field are measured as a function of the frequency using the Lock-In algorithm. While the maximum angular frequency supported by the setup is 30000 rad/s, the minimum frequency is limited by increasing measurement times but not technically.

In the following, a magneto-optical response function will be defined and it will be shown how it is obtained from the measured amplitude and phase lag.

The nanorods are exposed to a homogeneous magnetic field with a constant magnitude  $H_0$  oscillating about the  $y$ -axis, Fig.3.2:

$$\begin{aligned} H_y &= H_0 \cos(\beta(t)), \\ H_x &= H_0 \sin(\beta(t)) \end{aligned} \quad (3.2)$$

with

$$\beta(t) = \beta_0 \exp(i\omega t). \quad (3.3)$$

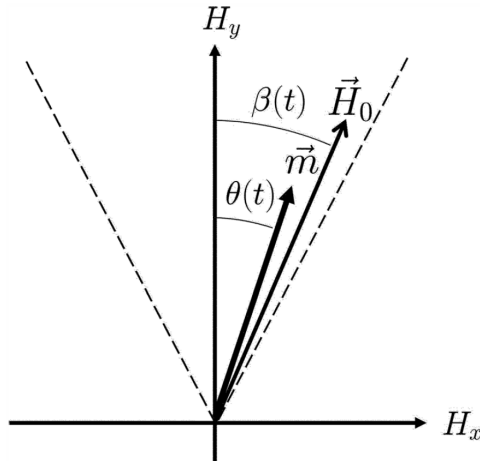


**Figure 3.2:** Oscillating magnetic field  $\vec{H}$  in the  $xy$ -plane around the  $y$ -axis within an angular range of  $\pm\beta_0$  (dashed lines).  $\theta(t)$  describes the oscillation of the nanorod axis which is assumed to be identical to the direction of the magnetic moment  $\vec{m}$  [15].

Due to this magnetic field, the particles are forced to an oscillation which can be described

by

$$\theta(t) = \theta_0 \exp(i(\omega t + \varphi)) = \hat{\theta}_0 \exp(i\omega t). \quad (3.4)$$

Using Eq. (3.3) and Eq. (3.4), the magneto-optical response function

$$\hat{X}(\omega) = \hat{\theta}_0(\omega)/\beta_0 \quad (3.5)$$

is defined. Due to the viscous drag of the particles, their orientation is phase shifted as compared to the oscillating external magnetic field. This results in an in-phase and an out-of-phase component. The response function can be described by a complex function

$$\hat{X}(\omega) = X'(\omega) + iX''(\omega) \quad (3.6)$$

with the real part

$$X'_\omega = A_\omega \cos(\phi_\omega) \quad (3.7)$$

and the imaginary part

$$X''_\omega = A_\omega \sin(\phi_\omega) \quad (3.8)$$

where  $A_\omega$  is the amplitude and  $\phi_\omega$  the phase shift measured at a given applied angular frequency  $\omega$ .

The most obvious approach to measure the oscillatory motion of the nanorods is to measure the transmitted intensity of the light polarized in  $y$ -direction. As will be shown later, the intensity  $I$  is proportional to  $\exp(-Ns(C_{\text{ext,L}} \cos(\Theta)^2 + C_{\text{ext,T1}} \sin(\Theta)^2))$ , where  $N$  is the particle concentration,  $s$  is the optical pathlength,  $C_{\text{ext,L}}$  and  $C_{\text{ext,T1}}$  are constants related to the optical properties of the particle, and  $\Theta$  is the angle between the particle axis and the polarization direction of light. At this point, the dependence of the intensity on the angle  $\Theta$  is crucial. Choosing  $\Theta = \theta$  implies a rod oscillation between  $\Theta = -12^\circ$  and  $\Theta = 12^\circ$  (mean angle  $0^\circ$ ), where the change in intensity is minimal and hence the resolution of measurements is poor. A significantly increased resolution is reached when the polarization direction of the incident light is tilted by an angle of  $45^\circ$  with respect to the  $y$ -direction, Fig.3.3.

The optical transmission in oscillating magnetic fields is determined by the magnetic, hydrodynamic, and optical properties of the nanorods. In order to model the whole DC and OF-MOT signal, theoretical models for these physical properties of Ni nanorods will be presented in the following chapter.

### 3.2 Magnetic field-dependent optical transmission (MOT)

---

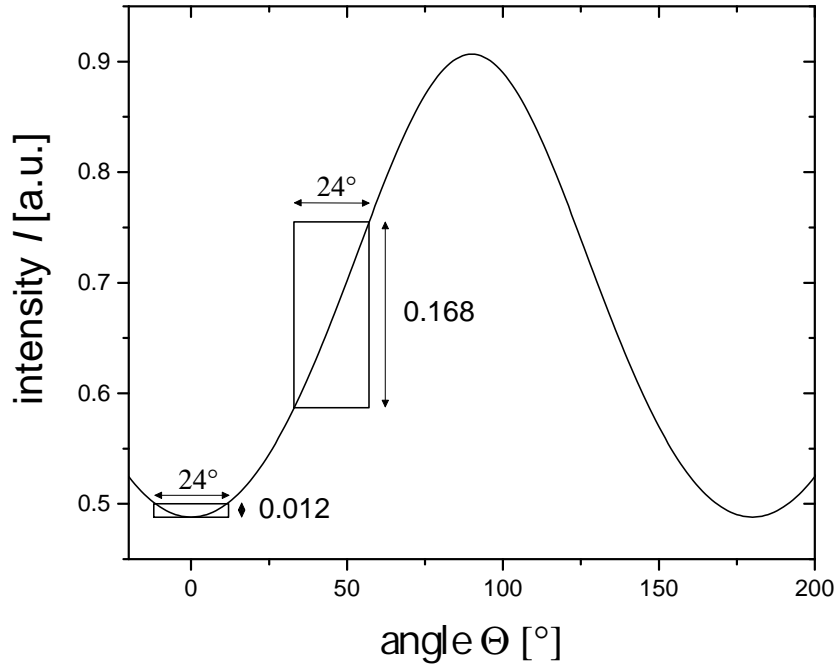


**Figure 3.3:** Calculated transmitted intensity of a typical colloid with parallel alignment of the nanorods as a function of the angle  $\Theta$  between the rod axis and the polarization direction of light (the shown intensity was calculated for an aqueous colloidal dispersion of silica encapsulated Ni nanorods with a core diameter of  $d_c = 20$  nm, a core length of  $l_c = 200$  nm, a shell thickness of  $D_{sh} = 50$  nm, a particle concentration of  $N = 10^{15} \text{ m}^{-3}$ , and an optical path length of  $s = 0.1$  m; all these quantities will be defined and discussed in detail in later chapters). The highest resolution is reached when the mean position of the oscillating rod encloses an average angle of  $45^\circ$  with the polarization direction so that the intensity variation upon oscillation within  $\pm\beta_0 = 12^\circ$  is maximized.



# Chapter 4

## Theory

This chapter provides the theoretical framework to describe the magnetic field-dependent optical transmission of PVP and silica coated Ni nanorods. First, their magnetic properties will be described and it will be shown that Ni nanorods of size used in this work are ferromagnetic single domain particles with a preferential alignment of the magnetic moment parallel to the long rod axis (section 4.1).

While the mean orientation of the particles in static magnetic field-dependent optical transmission (DC-MOT) measurements is determined by the ratio of thermal and magnetic energy, their time-dependent orientation in dynamical oscillating magnetic field-dependent optical transmission (OF-MOT) measurements also depends on their hydrodynamic properties. In this context, the rotational friction coefficient is the determining quantity. Its calculation will be described in section 4.2.3.

For both measurement modes, static and dynamic, the detection of the particle orientation is realized by the measurement of the transmission of linearly polarized light when passing the particle suspension. Hence, the quantities describing the interaction of the corresponding electromagnetic wave with the anisotropic particles, i.e. the orientation dependent optical cross sections, are introduced in section 4.3.

### 4.1 Magnetism of Ni nanorods

In the following treatment of the magnetism of the nanorods, the influence of the particle shell (consisting of silica or PVP) will be neglected and all considerations refer to the Ni core. Due to the exchange interaction between magnetic spins, ferromagnetic materials show a spontaneous or saturation magnetization  $M_s$  even in the absence of an external magnetic field. The alignment of the spins is in competition with their thermal energy,

causing the magnetization to decrease with increasing temperature and to vanish upon reaching the Curie temperature  $T_C$ . The present work treats nanorods made of Ni ( $T_C = 628$  K, [61]), which is a typical example for a material with ferromagnetism stemming from 3d electrons. The different terms of the micromagnetic energy functional of a ferromagnetic material that is minimized for the realized magnetic state will be described in the following.

### 4.1.1 Micromagnetic energy functional of ferromagnetic materials

Neglecting magnetostriction, surface and shape anisotropies, any ferromagnetic material adopts the magnetization  $\vec{M}(\vec{r})$  that minimizes the total magnetic energy

$$E_{\text{mag, tot}} = E_{\text{ex}} + E_{\text{a}} + E_{\text{Z}} + E_{\text{d}}. \quad (4.1)$$

which is the sum of the exchange energy  $E_{\text{ex}}$ , the anisotropy energy  $E_{\text{a}}$ , the Zeeman energy  $E_{\text{Z}}$ , and the demagnetization energy  $E_{\text{d}}$  [62]. These energy contributions will be explained in the following:

- In order to describe the exchange energy  $E_{\text{ex}}$ , the Hamilton operator

$$H = -2J \sum_{\langle ij \rangle} \vec{S}_i \vec{S}_j \quad (4.2)$$

is introduced. It represents the interaction of localized Spins in adjacent atoms where  $J$  is the interatomic exchange constant between the spins  $\vec{S}_i$  and  $\vec{S}_j$  at the lattice places  $i$  and  $j$ . Although Ni, as a 3d-ferromagnetic material, has no localized spins, the formalism can be transferred and in the continuum picture the exchange energy can be described by [63, section 7.1.1]<sup>1</sup>, [64, section 4.2.7]:

$$E_{\text{ex}} = \int A \left( \nabla \frac{\vec{M}}{M_s} \right)^2 dV. \quad (4.3)$$

$E_{\text{ex}}$  depends on the saturation magnetization  $M_s$  and the exchange constant  $A$  which is positive for all ferromagnetic materials. This causes the exchange energy to be minimized when the spins are aligned parallel to each other.

---

<sup>1</sup>This notation means that the citation points to section 7.1.1 in reference [63].

## 4.1 Magnetism of Ni nanorods

---

- The anisotropy energy  $E_a$  which for cubic systems with anisotropy constant  $K_1$  is given as

$$E_a = \frac{K_1}{M_s^4} (M_x^2 M_y^2 + M_y^2 M_z^2 + M_z^2 M_x^2) V. \quad (4.4)$$

The magnetocrystalline anisotropy originates from crystal field and spin-orbit interaction, resulting in a preferred alignment of the magnetic moment along specific crystallographic orientations [64, section 6.7.2], [63, section 5.5] which are called easy axes.

- The Zeeman energy [63, section 2.5]

$$E_Z = - \int \mu_0 \vec{M} \vec{H} dV \quad (4.5)$$

describes the interaction of the magnetization with an external magnetic field and is minimal for a parallel alignment.

- The demagnetizing energy [63, section 2.5.1], [64, section 6.7.4]

$$E_d = -\frac{1}{2} \int \mu_0 \vec{H}_d \vec{M} dV \quad (4.6)$$

has its origin in the demagnetizing field  $\vec{H}_d$ , which results from the magnetized sample itself. The magnetization of a homogeneously magnetized ferromagnetic material diverges on its surface. The relation  $\nabla \vec{M} = -\nabla \vec{H}$  [64] (appendix B) indicates an external stray field and a demagnetizing field opposite to the magnetization inside the particle. To minimize the demagnetization field, the magnetization splits into domains of different magnetic orientation, Fig. 4.1. Hence, macroscopic ferromagnetic samples do not necessarily exhibit a resulting macroscopic magnetization. However, for very small particles, a single domain state might be energetically preferred.

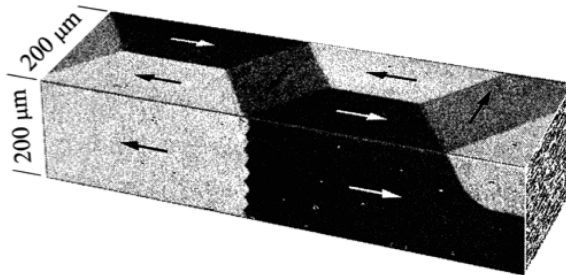


**Figure 4.1:** Illustration of a ferromagnetic sample whose magnetization splits into differently oriented domains [65]. Within each domain, the magnitude of the magnetization corresponds to the saturation magnetization whereas the orientations are different.

### 4.1.2 Single domain particles

Due to the exchange energy, the change of orientation of the microscopic magnetic moments between adjacent domains occurs by gradual rotation along several magnetic moments. The corresponding spatial region is called Bloch wall and its thickness

$$\delta_0 = \sqrt{\frac{A}{K_1}} \quad (4.7)$$

is determined by the magnetocrystalline anisotropy constant  $K_1$  and the exchange constant  $A$ . The excess energy per unit area  $\sigma_B$  which is necessary to form a Bloch wall results from the minimization of the energy contributions  $E_{\text{ex}} + E_a$  [61, 3.2.2.2]:

$$\sigma_B = 4\sqrt{AK_1}. \quad (4.8)$$

The total magnetic energy of a ferromagnetic sphere in single (a) and two (b) domain configuration is shown in Fig. 4.2 (a) and (b) and can be calculated to [42]

$$\begin{aligned} E_{\text{tot,a}} &= E_{\text{d,a}} = \frac{2}{9}\mu_0 M_s^2 \pi r^3, \\ E_{\text{tot,b}} &= E_{\text{d,b}} + \sigma_B \pi r^2 = \frac{1}{9}\mu_0 M_s^2 \pi r^3 + 4\sqrt{AK_1} \pi r^2. \end{aligned} \quad (4.9)$$

Fig. 4.3 shows  $E_{\text{tot,a}}$  and  $E_{\text{tot,b}}$  as functions of the diameter of the sphere. Below the critical diameter  $r_{\text{c, sphere}}$ , the single domain state is energetically preferred. Using Eqs. (4.9) and the condition  $E_{\text{tot,a}} = E_{\text{tot,b}}$  it follows that

$$r_{\text{c, sphere}} = 36 \frac{\sqrt{AK_1}}{\mu_0 M_s^2} \quad (4.10)$$

and a value of  $r_{\text{c, sphere}} = 15.7 \text{ nm}$  is found for Ni [42].

For non-spheroidal particles, the critical size for single-domain states can be retrieved

## 4.1 Magnetism of Ni nanorods

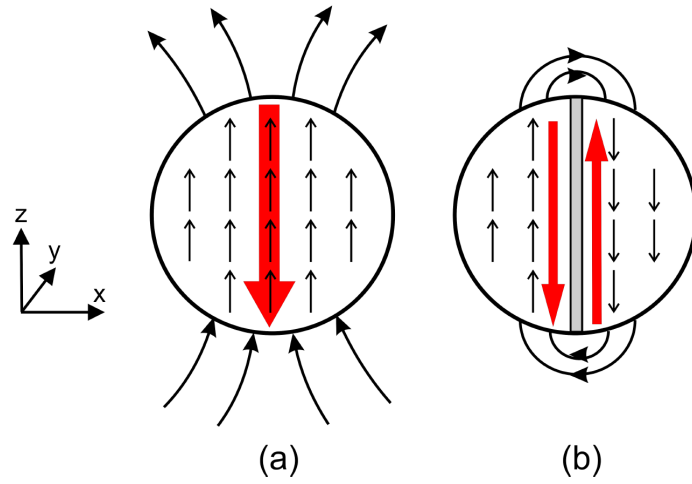


**Figure 4.2:** Two configurations of the magnetization of a ferromagnetic sphere with a preferred direction parallel to the  $z$ -axis [42]. The red arrows indicate the demagnetizing field  $H_d$ . The shown states are (a) the single domain state with maximum demagnetizing energy and (b) a state where splitting into two domains of different direction reduces the demagnetization energy but results in an additional energy contribution to insert the Bloch wall.

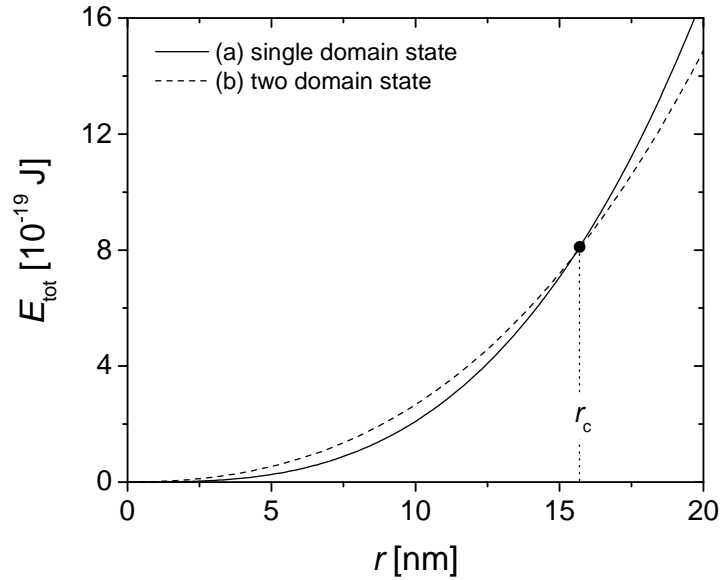


**Figure 4.3:** Total magnetic energy of a Ni sphere for the two magnetization configurations shown in Fig. 4.2 as functions of radius [42].

from micromagnetic computer simulations. For cylinders with aspect ratios  $> 1$ , Ross et al. [66] determined the critical diameter below which a single domain state is preferred and found a critical diameter of  $\sim 42$  nm for Ni. The direction of magnetization is determined by the dominant anisotropy, which in the case of Ni nanorods is the shape anisotropy.

### 4.1.3 Shape anisotropy

As already mentioned, the magnetization  $\vec{M}$  is discontinuous at the surface of a particle. For a homogeneously magnetized sample, this discontinuity implies the demagnetizing field

$$\vec{H}_d = \mathbf{N}_d \vec{M} \quad (4.11)$$

where  $\mathbf{N}_d$  is the demagnetization tensor which depends on the particle shape. After a transformation to principal axes,  $\mathbf{N}_d$  can be expressed by a diagonal matrix with entries  $N_1, N_2, N_3$  and  $N_1 + N_2 + N_3 = 1$ . Unfortunately, there is no simple method to determine  $N_i$  for arbitrarily shaped particles like cylinders. An axisymmetric shape with known demagnetizing factors is the prolate spheroid where  $N_{||} = N_1$  and  $N_{\perp} = N_2 = N_3$  are the demagnetizing factors parallel and perpendicular to the major axis. The respective demagnetizing energy is given by [67]

$$\begin{aligned} E_d &= \frac{1}{2} \mu_0 M_s^2 V (N_{\perp} \sin^2 \vartheta + N_{||} \cos^2 \vartheta) \\ &= \frac{1}{4} \mu_0 M_s^2 V (1 - 3N_{||}) \sin^2 \vartheta + \frac{1}{2} \mu_0 M_s^2 V N_{||} \end{aligned} \quad (4.12)$$

where  $\vartheta$  is the angle between the long axis of the spheroid and the direction of the magnetic moment. The second summand which is independent of  $\vartheta$  represents a physically irrelevant shift of the zero point of energy and will be neglected.

By defining the shape anisotropy constant for spheroids

$$K_s = \frac{1}{4} \mu_0 M_s^2 (1 - 3N_{||}), \quad (4.13)$$

the shape anisotropy energy is given by

$$E_s = K_s V \sin^2 \vartheta. \quad (4.14)$$

Thus, the shape anisotropy energy is minimized for  $\vartheta = 0$ . A parallel alignment of the magnetic moment with the long axis is preferred if the shape anisotropy is the dominant

## 4.1 Magnetism of Ni nanorods

---

contribution to the total anisotropy. This is the case for Ni cylinders with aspect ratios  $> 1.1$  as the shape anisotropy constant is larger than the crystal anisotropy constant [42].

To determine the magnetization of a homogeneously magnetized spheroid as a function of direction and magnitude of an external magnetic field, E.C. Stoner and E.P. Wohlfarth [68] have developed a simple vector model that will be presented in the following.

### 4.1.4 The Stoner-Wohlfarth model

The Stoner-Wohlfarth model is used to describe the behavior of the magnetization of a homogeneously magnetized prolate spheroid. In this model, it is assumed that all magnetic moments inside the particle are parallel to each other and thus the magnitude of the magnetization vector  $\vec{M}$  is constant and adopts the value of the saturation magnetization  $|\vec{M}| = M_s$ . The orientation of  $\vec{M}$  results from the competition between the shape anisotropy energy and the Zeeman energy.

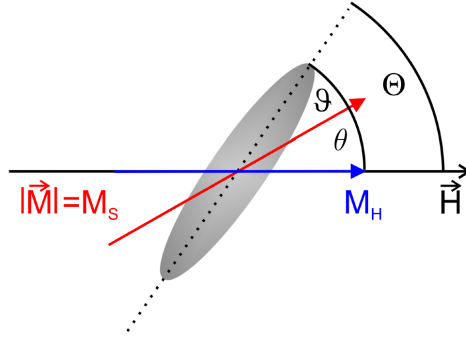


**Figure 4.4:** Schematic illustration of a Stoner-Wohlfarth particle and definition of angles used in the Stoner-Wohlfarth model [42].

Hence the total magnetic energy is

$$E_{\text{tot}} = E_s + E_Z. \quad (4.15)$$

Using the angles defined in Fig. 4.4, Eq. (4.15), it can be transformed to

$$\begin{aligned} E_{\text{tot}} &= K_s V \sin^2(\vartheta) - \mu_0 H V M_s \cos(\theta) \\ &= (K_s \sin^2(\Theta - \theta) - \mu_0 H M_s \cos(\theta)) V. \end{aligned} \quad (4.16)$$

Introducing the normalized quantities

$$\begin{aligned}\epsilon &= \frac{E_{\text{tot}}}{2K_s V}, \\ h &= \frac{H}{H_k} \text{ with } H_k = \frac{2K_s}{\mu_0 M_s}\end{aligned}\tag{4.17}$$

leads to the reduced energy density

$$\epsilon = \frac{1}{2} \sin^2(\Theta - \theta) - h \cos(\theta).\tag{4.18}$$

In a homogeneous magnetic field  $\vec{H}$ , the magnetization vector  $\vec{M}$  adopts the orientation that minimizes the reduced energy density  $\epsilon$  which is determined by

$$\begin{aligned}\frac{d\epsilon}{d\theta} &= -\cos(\Theta - \theta) \sin(\Theta - \theta) + h \sin(\theta) \stackrel{!}{=} 0 & \text{(I)}, \\ \frac{d^2\epsilon}{d\theta^2} &= -\sin^2(\Theta - \theta) + \cos^2(\Theta - \theta) + h \cos(\theta) \stackrel{!}{>} 0 & \text{(II)}.\end{aligned}\tag{4.19}$$

For a given particle orientation  $\Theta = \text{const}$ , the orientation of the magnetization vector  $\cos(\theta(h)) = M_H(H)/M_s$  can be determined and the following results are obtained:

- $\Theta = 90^\circ$  (particle parallel to the external field): The solutions of Eq. (4.19 (I)) are  $\theta = 0$ ,  $\theta = \pi$ , and  $\cos(\theta) = h$ . Local minima can be found for the conditions

$$\begin{aligned}\theta_1 = 0 & \quad \wedge \quad h > 1, \\ \theta_2 = \pi & \quad \wedge \quad h < -1, \\ \cos(\theta) = h & \quad \wedge \quad |h| < 1.\end{aligned}\tag{4.20}$$

The corresponding plot is shown in Fig. 4.5.

- $\Theta = 0^\circ$  (particle perpendicular to the external field): The solution of Eq. (4.19 (I)) are  $\theta = 0$ ,  $\theta = \pi$ , and  $\cos(\theta) = -h$ , but local minima can only be found for the conditions

$$\begin{aligned}\theta_1 = 0 & \quad \wedge \quad h > -1, \\ \theta_2 = \pi & \quad \wedge \quad h < 1.\end{aligned}\tag{4.21}$$

For  $\cos(\theta) = -h$  a local maximum is found. The obtained magnetization curve consists of two branches, the upper ( $-1 < h < \infty$ ) and lower ( $-\infty < h < 1$ ) one, Fig. 4.5.

## 4.1 Magnetism of Ni nanorods

---

- For arbitrary orientations ( $0^\circ < \theta < 90^\circ$ ), the magnetization curves can be determined using numerical methods. For each of these cases the solution has an upper and a lower branch, each showing a continuous behavior until a critical field value is reached, Fig. 4.5. The change of magnetization inside each branch is realized by a reversible rotation of the magnetic moments. Exceeding the critical field results in an irreversible jump of the magnetization from one branch to the other.

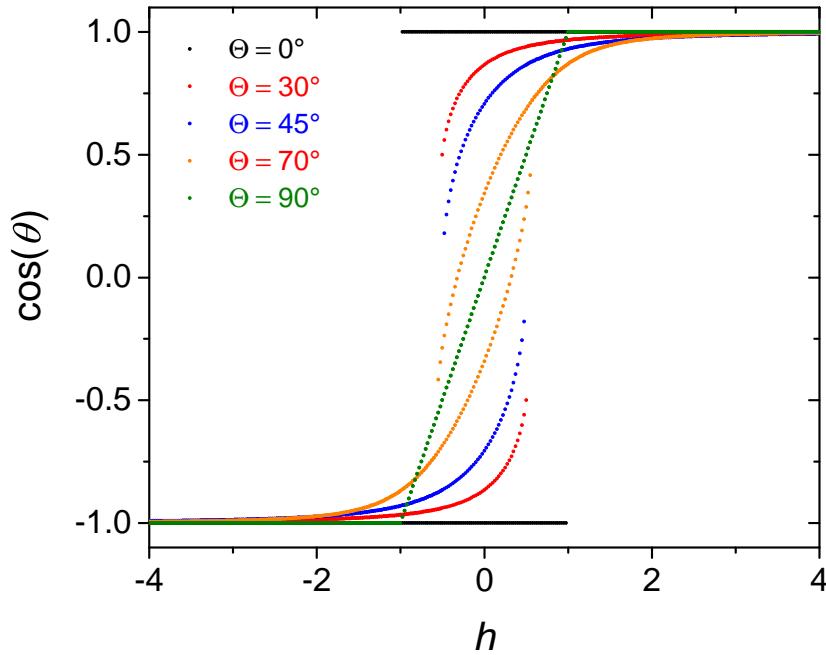


**Figure 4.5:** Magnetization curves of a Stoner-Wohlfarth particle as a function of the normalized external field  $h$  for different orientations  $\Theta$  [42].

In contrast to the particles in the Stoner-Wohlfarth model, the particles used in this work were not spatially fixed, but free to rotate in a purely viscous matrix. Although Ni nanorods are not inherently superparamagnetic, the magnetization of their colloidal dispersions can be described using the same formalism as used for superparamagnetic particles.

### 4.1.5 Pseudo-superparamagnetic behavior

The energetic considerations in section 4.1.4 describe a time independent orientation of the magnetic moment and did not consider any thermal energy contribution. The single domain state with constant magnetization direction is only obtained if the anisotropy

energy is larger than the thermal energy. If this condition is violated, thermally activated reorientations of the magnetic moments in absence of an external magnetic field result in a change of the direction of the magnetization which causes the time averaged magnetization of the particles to vanish. Applying an external field results in a preferential alignment and positive net magnetization in field direction despite continuous reorientations of the magnetization of the superparamagnetic particle. The orientation of the magnetization in field direction happens on a characteristic time scale whose corresponding constant is called the Néel relaxation time [69].

The magnetization behavior of superparamagnetic particles can be described using the Langevin function [70]

$$M(H) = M_s L(\zeta),$$

$$L(\zeta) = \coth(\zeta) - \frac{1}{\zeta}, \zeta = \frac{m\mu_0 H}{k_B T} \quad (4.22)$$

which is shown in Fig. 4.6.

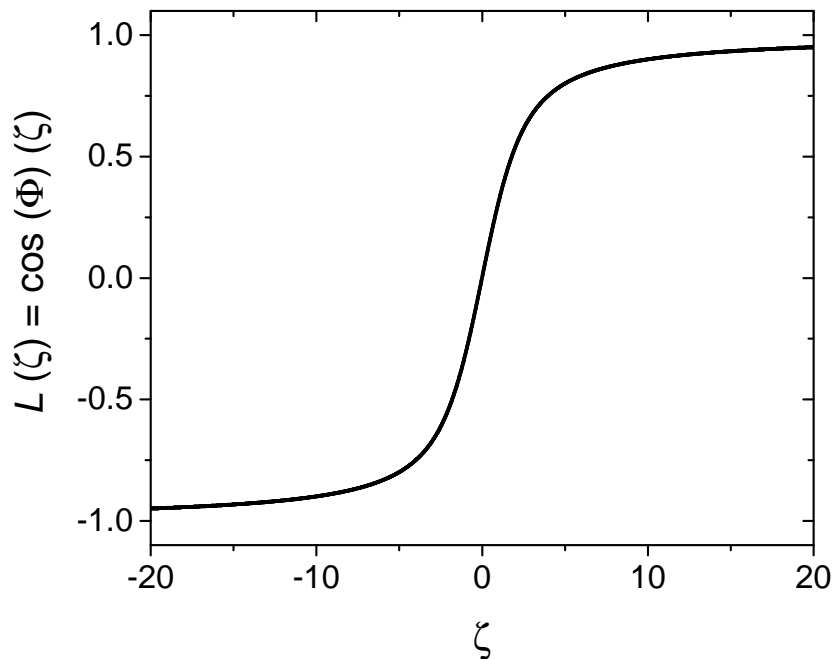


**Figure 4.6:** Langevin function  $L$  as a function of the ratio of magnetic and thermal energy  $\zeta$ .

Using a typical shape anisotropy constant of Ni nanorods  $K_s = 50 \text{ kJm}^{-3}$  [71, 72], the ratio of thermal energy and magnetic shape anisotropy energy of the smallest Ni nanorods

## 4.1 Magnetism of Ni nanorods

---

used in this work can be estimated to

$$\frac{K_s V}{k_B T} > 327. \quad (4.23)$$

The corresponding Néel relaxation time

$$\tau_N = \tau_0 \exp\left(\frac{K_s V}{k_B T}\right) \quad (4.24)$$

where the constant  $\tau_0$  assumes values of about  $10^{-9}$  s [73], can be calculated to  $\tau_N \approx 10^{133}$  s. Thus, all Ni nanorods used in this work are ferromagnetic and do not exhibit superparamagnetic behavior.

But if the particles are dispersed in a liquid matrix, a relaxation process occurs by rotation of the whole particle in field direction while the orientation of the moment relative to the particle is fixed. This process is called Brownian relaxation [74] and the time that an ensemble of rods needs to return to a uniform orientation distribution, after an external field has been removed, is called the corresponding relaxation time.

Thus, Ni nanorods dispersed in a colloidal dispersion show a magnetization behavior that can be described by Eq. (4.22), although they are uniaxial quasistatic ferromagnetic single domain particles.

The considerations describe the static magnetization behavior, but in experiments involving a dynamic external fields, the rotational friction of the particles which hampers an instantaneous rotation in field direction has a significant influence on the measured instantaneous magnetization.

In section 3.2.2, the nanorod axis was assumed to be identical to the direction of the magnetic moment in OF-MOT experiments. However, in this setup the particles are exposed to an oscillating magnetic field which is in general not parallel to the particle axis and thus the magnetic moment is expected to rotate out of the the rod axis by an angle which depends on the shape anisotropy constant  $K_s$ . In order to judge whether the approximation of a parallel alignment of the particle axis and the magnetic moment is justified, this angle will be estimated.

### 4.1.6 Orientation of the magnetic moment in OF-MOT measurements

In OF-MOT experiments, the distinct shape anisotropy of Ni cylinders is exploited to induce particle rotations by external magnetic fields. To exert a torque on the particle,

the magnetic moment has to rotate out of the rod axis by an angle  $\vartheta$ , Fig. 4.7. However, in the derivation of the equation of motion of the nanorod in section 3.2.2, a parallel alignment of the particle axis and the magnetic moment was assumed. In the following, an upper bound  $\vartheta_{\max}$  will be estimated to decide whether it is necessary to pay attention to complex reorientations of the magnetic moment.

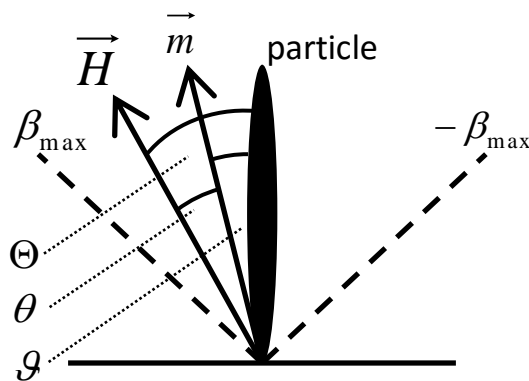


**Figure 4.7:** Definition of angles between the particle axis, its magnetic moment  $\vec{m}$ , and the external magnetic field  $\vec{H}$ .

If the phase shift between the oscillating applied magnetic field and the oscillation of the measured intensity approaches  $90^\circ$ , the amplitude of the rod oscillation vanishes while the external field oscillates between  $\beta_{\max}$  and  $-\beta_{\max}$ . Thus, the maximum value of  $\Theta$  is  $\beta_{\max}$  which was  $12^\circ$  in the experiments performed in this work. The Stoner-Wohlfarth model enables the calculation of the angle  $\theta$  between the magnetic moment of the rod and the external field and thus the angle  $\vartheta = \Theta - \theta$  between the magnetic moment and the rod axis. For this purpose, Eq. (4.18) can be used to calculate the reduced energy density  $\epsilon$  as a function of  $\theta$ . In absence of an external magnetic field ( $h = 0$ ), the minimum of  $\epsilon$  would be found for  $\theta = \Theta = 12^\circ$ , Fig. 4.8, indicating parallel alignment of magnetic moment and particle axis. For an external field as used in OF-MOT experiments ( $H = 60$  Oe), a typical shape anisotropy constant of Ni nanorods ( $K_s = 50$  kJ/m $^{-3}$ ), and the value  $M_s = 488 \cdot 10^3$  Am $^{-1}$  for the saturation magnetization of Ni [63], the normalized external field can be calculated to  $h = 0.03$  and the minimum of  $\epsilon$  shifts to  $\theta = 11.7^\circ$  indicating  $\vartheta = 0.3^\circ$ . Hence, the maximum deflection of the magnetic moment is 2.5% of the oscillation amplitude  $\beta_0$  so that it can safely be assumed that the magnetic moment and the axis of the particle in OF-MOT measurements are in parallel alignment.

Another crucial aspect determining the time dependent behavior of a nanorod in oscillating magnetic fields is its rotational friction due to the viscous drag which will be treated in the following.

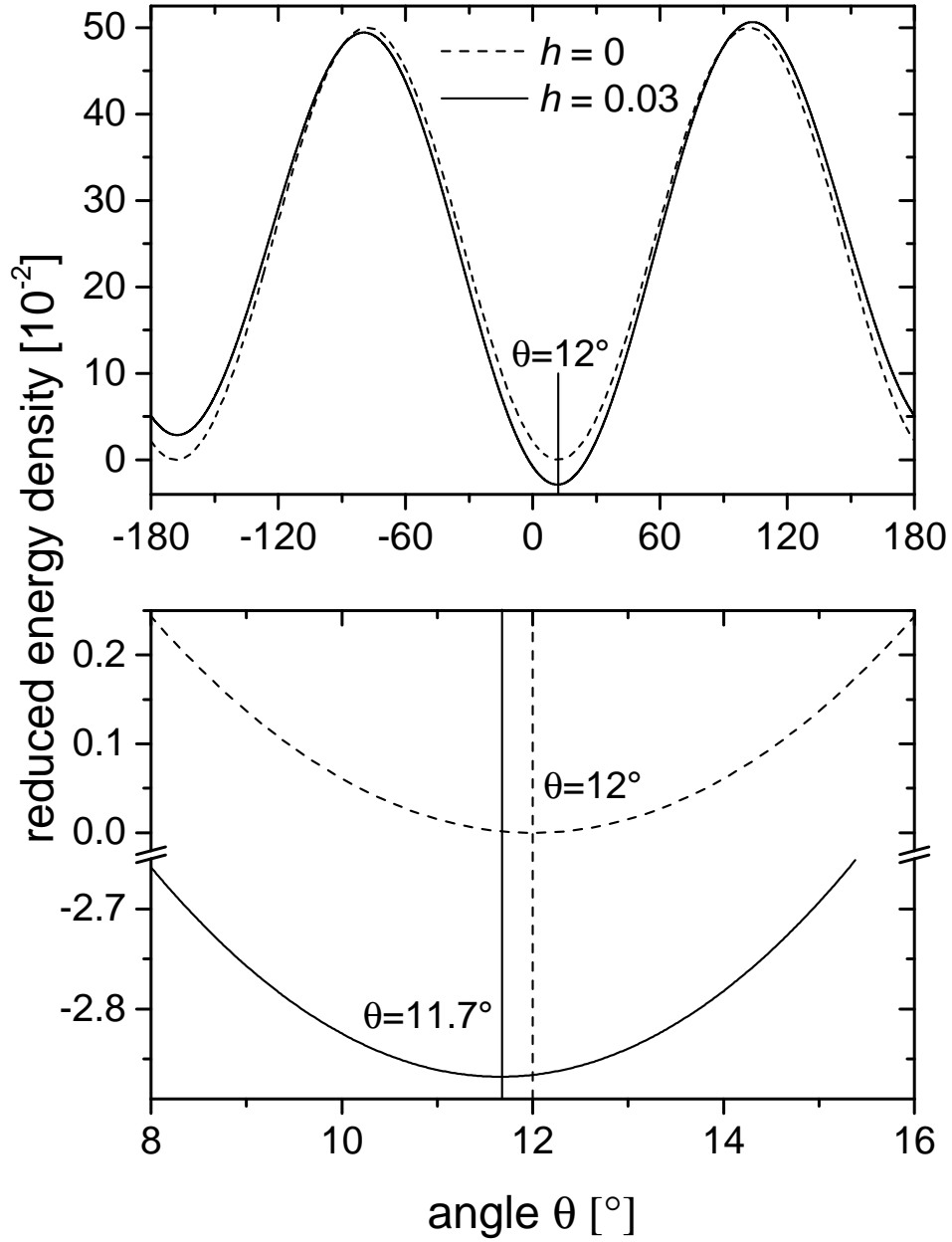


**Figure 4.8:** Reduced energy density  $\epsilon$  as defined in the SWM, Eq. (4.18), as a function of the angle  $\Phi$  between the magnetic moment and the external magnetic field. The lines represent the curve in absence of an external magnetic field ( $h = 0$ ) and for the configuration in OF-MOT measurements ( $h = 0.03$ ). The lower graph shows a magnification around  $\theta = 12^\circ$ . Negative energy densities occur because the constant term in Eq. (4.12) was neglected.

## 4.2 Hydrodynamic properties of Ni nanorods

A constant torque  $T$  exerted on a particle which is surrounded by a viscous matrix results in a continuous rotation with the angular frequency  $\omega$  that is determined by the friction due to the medium. The ratio

$$\frac{T}{\omega} = \xi_r \quad (4.25)$$

is called the rotational friction coefficient and is the physical quantity that determines the oscillatory rotational motion of the nanorods. It depends on the density  $\rho$ , on the viscosity  $\eta$  of the surrounding medium, on the particle volume and shape, and the direction of the rotation axis.

To determine the motion of a particle in a fluid, it is necessary to solve the fundamental equations describing the motion of a viscous fluid, the so called Navier-Stokes equations, which were published for incompressible fluids by Navier in 1827 and for compressible fluids by Poisson in 1831. Further deviations of these equations were given by De Saint-Venant in 1843 and by Stokes in 1845.

The following representation until chapter 4.2.1 follows the description in the textbook *Theoretische Hydromechanik* by N.J. Kotchin et al. [75].

In the case of an incompressible fluid, the Navier-Stokes equation is

$$\frac{d}{dt}\vec{v} = \vec{F} + \frac{\eta}{\rho} \Delta \vec{v} - \frac{1}{\rho} \nabla p \quad (4.26)$$

where  $\vec{v}$  is the velocity,  $\vec{F}$  the body force density,  $\eta$  the dynamic viscosity,  $\rho$  the density, and  $p$  the pressure acting on a small volume of the fluid. Together with the equation of continuity

$$\nabla \vec{v} = 0, \quad (4.27)$$

the motion of a fluid is completely determined.

The Eqs. (4.26) and (4.27) are very complex partial differential equations that cannot be solved exactly in most cases. One case which can be solved analytically is the case of a sphere rotating with constant angular frequency in a purely viscous incompressible fluid which will be presented in the following.

### 4.2.1 The rotational friction coefficient of a sphere

The first one who solved the problem of a sphere with radius  $a$  rotating with a small constant angular frequency  $\omega$  in a purely viscous incompressible fluid was Gustav Kirchhoff in his lectures on mechanics in 1897 [76]. In the present work, the presentation of the solution of this problem follows the description of the textbook *Theoretische Hydromechanik* by N.J. Kotchin et al. (1955) [75, chapter II §22].

To solve this spherically symmetric problem, spherical coordinates will be introduced. The spherical coordinates of a point in the three dimensional space are the radius  $r$ , the inclination  $\theta$  and the azimuth  $\varphi$ , Fig. 4.9.

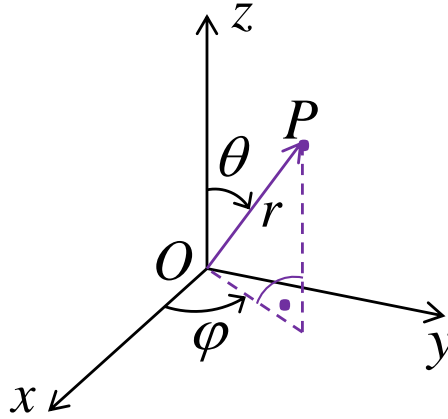


**Figure 4.9:** Definition of angles in spherical coordinates.

They are related to the cartesian coordinates  $x$ ,  $y$ , and  $z$  by the relations

$$\begin{aligned}x &= r \cdot \sin \theta \cdot \cos \varphi, \\y &= r \cdot \sin \theta \cdot \sin \varphi, \\z &= r \cdot \cos \theta.\end{aligned}\tag{4.28}$$

To solve the problem of a sphere rotating in a fluid, it is useful to transform the equations of motion of the fluids, Eqs. (4.26), to a general Lamb form and write it component-by-

component in spherical coordinates [75, chapter II §5]:

$$\begin{aligned}
 & \frac{\partial v_r}{\partial t} + v_r \frac{\partial v_r}{\partial r} + \frac{v_\theta}{r} \frac{\partial v_r}{\partial \theta} + \frac{v_\varphi}{r \sin \theta} \frac{\partial v_r}{\partial \varphi} - \frac{v_\theta^2 + v_\varphi^2}{r} \\
 &= F_r - \frac{1}{\rho} \frac{\partial p}{\partial r} + \frac{\eta}{\rho} \left( \frac{\partial^2 v_r}{\partial r^2} + \frac{1}{r^2} \frac{\partial^2 v_r}{\partial \theta^2} + \frac{1}{r^2 \sin^2 \theta} \frac{\partial^2 v_r}{\partial \varphi^2} + \frac{2}{r} \frac{\partial v_r}{\partial r} \right. \\
 & \quad \left. + \frac{\cot \theta}{r^2} \frac{\partial v_r}{\partial \theta} - \frac{2}{r^2} \frac{\partial v_\theta}{\partial \theta} - \frac{2}{r^2 \sin \theta} \frac{\partial v_\varphi}{\partial \varphi} - \frac{2v_r}{r^2} - \frac{2 \cot \theta}{r^2} v_\theta \right), \tag{4.29}
 \end{aligned}$$

$$\begin{aligned}
 & \frac{\partial v_\theta}{\partial t} + v_r \frac{\partial v_\theta}{\partial r} + \frac{v_\theta}{r} \frac{\partial v_\theta}{\partial \theta} + \frac{v_\varphi}{r \sin \theta} \frac{\partial v_\theta}{\partial \varphi} + \frac{v_r v_\theta}{r} - \frac{v_\varphi^2 \cot \theta}{r} \\
 &= F_\theta - \frac{1}{\rho r} \frac{\partial p}{\partial \theta} + \frac{\eta}{\rho} \left( \frac{\partial^2 v_\theta}{\partial r^2} + \frac{1}{r^2} \frac{\partial^2 v_\theta}{\partial \theta^2} + \frac{1}{r^2 \sin^2 \theta} \frac{\partial^2 v_\theta}{\partial \varphi^2} + \frac{2}{r} \frac{\partial v_\theta}{\partial r} \right. \\
 & \quad \left. + \frac{\cot \theta}{r^2} \frac{\partial v_\theta}{\partial \theta} - \frac{2 \cos \theta}{r^2 \sin^2 \theta} \frac{\partial v_\varphi}{\partial \varphi} + \frac{2}{r^2} \frac{\partial v_r}{\partial \theta} - \frac{v_\theta}{r^2 \sin^2 \theta} \right), \tag{4.30}
 \end{aligned}$$

$$\begin{aligned}
 & \frac{\partial v_\varphi}{\partial t} + v_r \frac{\partial v_\varphi}{\partial r} + \frac{v_\theta}{r} \frac{\partial v_\varphi}{\partial \theta} + \frac{v_\varphi}{r \sin \theta} \frac{\partial v_\varphi}{\partial \varphi} + \frac{v_r v_\varphi}{r} + \frac{v_\theta v_\varphi \cot \theta}{r} \\
 &= F_\varphi - \frac{1}{\rho r \sin \theta} \frac{\partial p}{\partial \varphi} + \frac{\eta}{\rho} \left( \frac{\partial^2 v_\varphi}{\partial r^2} + \frac{1}{r^2} \frac{\partial^2 v_\varphi}{\partial \theta^2} + \frac{1}{r^2 \sin^2 \theta} \frac{\partial^2 v_\varphi}{\partial \varphi^2} + \frac{2}{r} \frac{\partial v_\varphi}{\partial r} \right. \\
 & \quad \left. + \frac{\cot \theta}{r^2} \frac{\partial v_\varphi}{\partial \theta} + \frac{2}{r^2 \sin \theta} \frac{\partial v_r}{\partial \varphi} + \frac{2 \cos \theta}{r^2 \sin^2 \theta} \frac{\partial v_\theta}{\partial \varphi} - \frac{v_\varphi}{r^2 \sin^2 \theta} \right). \tag{4.31}
 \end{aligned}$$

Furthermore, the equation of continuity, Eq. (4.27), in spherical coordinates is:

$$\frac{\partial v_r}{\partial r} + \frac{1}{r} \frac{\partial v_\theta}{\partial \theta} + \frac{1}{r \sin \theta} \frac{\partial v_\varphi}{\partial \varphi} + \frac{2v_r}{r} + \frac{v_\theta \cot \theta}{r} = 0. \tag{4.32}$$

In this case, the linear velocity  $\omega a$  of the points of the equator of the sphere can be assumed as characteristic velocity. Thus the Reynolds number  $R$  which is defined as the ratio of inertial forces to viscous forces can be calculated to  $R = \frac{\rho \omega a \cdot a}{\eta}$ . Since  $\omega$  is assumed to be small and thus  $R$  is small, the left side of Eqs. (4.29), and (4.30), (4.31) can be set equal to zero [75]. Furthermore, the body force density will be neglected. The resulting equations can be solved using the ansatz

$$\begin{aligned}
 v_r &= 0 \\
 v_\theta &= 0 \\
 p &= \text{const} \\
 v_\varphi &= v(r, \theta)
 \end{aligned} \tag{4.33}$$

## 4.2 Hydrodynamic properties of Ni nanorods

---

where  $v(r, \theta)$  must be a solution to the equation

$$\frac{\partial^2 v}{\partial r^2} + \frac{1}{r^2} \frac{\partial^2 v}{\partial \theta^2} + \frac{2}{r} \frac{\partial v}{\partial r} + \frac{\cot \theta}{r^2} \frac{\partial v}{\partial \theta} - \frac{v}{r^2 \sin^2 \theta} = 0. \quad (4.34)$$

The fluid particles that are in contact with the sphere are assumed to have the same linear velocity as the surface of the sphere  $\omega a \sin \theta$ . This boundary condition is called no-slip (or stick) boundary condition and is characterized by the equation

$$v(a, \theta) = \omega a \sin \theta. \quad (4.35)$$

Regarding this boundary condition, it is obvious to use the ansatz

$$v(r, \theta) = A(r) \sin \theta \quad (4.36)$$

to solve Eq. (4.34) resulting in an ordinary differential equation, i. e. a Cauchy-Euler equation,

$$\frac{d^2 A}{dr^2} + \frac{2}{r} \frac{dA}{dr} - \frac{2A}{r^2} = 0 \quad (4.37)$$

which can be solved by integration:

$$A(r) = C_1 r + \frac{C_2}{r^2}. \quad (4.38)$$

The constants  $C_1$  and  $C_2$  are determined by the boundary conditions. For an unlimited fluid,  $C_1 = 0$  has to be assumed to ensure a vanishing velocity of the fluid at infinity. Hence,

$$v(r, \theta) = C \frac{\sin \theta}{r^2} \quad (4.39)$$

where  $C$  can be determined using the boundary condition represented by Eq. (4.35) to  $C = \omega a^3$ . Thus, the finally obtained relation for the velocity of the fluid is

$$v(r, \theta) = \frac{\omega a^3 \sin \theta}{r^2}. \quad (4.40)$$

For a constant rotation of the sphere, a torque has to be applied to it. To determine this torque, the stress on every infinitely small area between two circles of latitude has to be known. A useful relation for this problem can be found in [75, chapter II §5]:

$$p_{r,\varphi} = \eta \left( \frac{\partial v}{\partial r} - \frac{v}{r} \right) \Big|_{r=a} = -3 \eta \omega \sin \theta. \quad (4.41)$$

Since the area of the considered zones is  $2\pi a \sin \theta a d\theta$  and the length of the lever arms is  $a \sin \theta$ , the torque can be expressed by

$$\begin{aligned} T &= \int_0^\pi 3\eta\omega \sin \theta \cdot a \sin \theta \cdot 2\pi a^2 \sin \theta d\theta \\ &= 6\pi\eta\omega a^3 \int_0^\pi \sin^3 \theta d\theta \\ &= 8\pi\eta a^3 \omega. \end{aligned} \tag{4.42}$$

Thus, the rotational friction coefficient of a slowly rotating sphere of radius  $a$  inside an incompressible fluid with viscosity  $\eta$  is  $\xi_r = T/\omega = 8\pi\eta a^3$ . After solving the problem for the simplest geometry, i.e. a sphere, the problem for the simplest anisotropic shape, i.e. spheroids, will be treated in the following.

### 4.2.2 The rotational friction coefficient of a spheroid

The first one who treated the rotational friction of a spheroid was D. Edwards (1893) [77] whose work seems to be widely unknown, later Perrin worked on this topic [78]. Both works were mentioned by R. Gans (1928) [79]. Unfortunately, several of the final results derived by Perrin are incorrect resulting in some confusion in literature and corrections to Perrin's results were reported in [80]. The results of this work will be presented in the following.

For spheroids with semi-axes  $a$  and  $b = c$ , the rotational friction coefficients are complex functions of their outer dimensions. There are two independent rotational friction coefficients. One describes the rotation around the long semi-axis  $a$

$$\xi_{r,a} = \frac{4(1 - (c/a)^2)}{3(2 - (c/a)^2 a S)} \xi_{r,\text{sphere}}, \tag{4.43}$$

while the other one describes the rotation around the short semi-axes  $b$  and  $c$

$$\xi_{r,b} = \frac{4(1 - (c/a)^4)}{3(c/a)^2(aS(2 - (c/a)^2) - 2)} \xi_{r,\text{sphere}} \tag{4.44}$$

where  $\xi_{r,\text{sphere}} = 8\pi a c^2 \eta$  is the rotational friction coefficient of a sphere of equivalent volume. The parameter  $S$  defined by Perrin can be calculated by:

$$\begin{aligned} S &= S_0(1 - (c/a)^2)^{-1/2} \ln \{ [1 + (1 - (c/a)^2)^{1/2}] / p \} \quad (\text{prolate spheroid, } a/c > 1), \\ S &= S_0(1 - (c/a)^2)^{-1/2} \arctan [ ((c/a)^2 - 1)^{1/2} ] \quad (\text{oblate spheroid, } a/c < 1) \end{aligned} \tag{4.45}$$

## 4.2 Hydrodynamic properties of Ni nanorods

---

where  $S_0 = 2/a$ . The spheroid is the simplest anisotropic axial symmetric geometry that could be used to describe the particles used in this work. A better description of the shape is a cylinder whose rotational friction coefficient will be calculated in the following.

### 4.2.3 The rotational friction coefficient of a cylinder

Due to the complicated process of solving the partial differential equations in compliance with the boundary conditions, a simple estimation of the rotational friction coefficient of a rod rotating around its short axis following [81, section 8.2.2] is presented.

In the *shish-kebab* model, the rod of length  $L$  is approximated by  $N = L/a$  beads with diameter  $a$  which are numbered from  $-N/2$  to  $N/2$ , Fig.4.10. For a rod rotating with

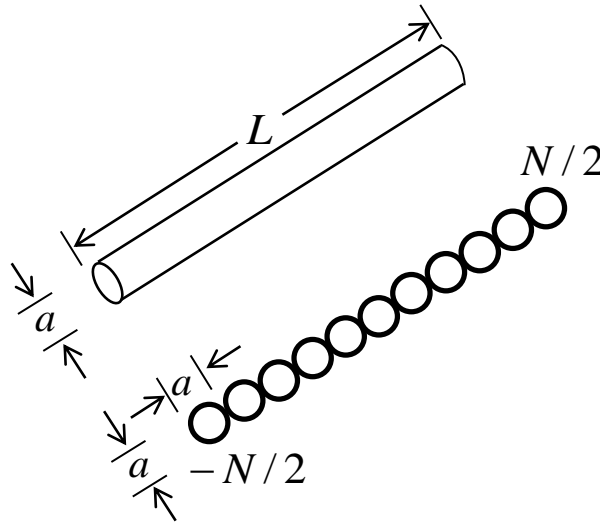


**Figure 4.10:** Rodlike particle and shish-kebab model which consists of  $N = L/a$  beads of diameter  $a$  placed along a straight line [81].

angular velocity  $\vec{\omega}$ , the bead  $n$  which has the distance  $nb$  to the center moves with the velocity  $\vec{v}_n = \vec{\omega} \times na\vec{u}$  where  $\vec{u}$  is the unit vector parallel to the long rod axis. The frictional force acting on the segment  $n$  is  $-\xi_t \vec{v}_n$  where  $\xi_t$  is the translational friction coefficient of the bead. The problem of calculating  $\xi_t$  for a sphere at small Reynolds numbers was first solved by Sir George Gabriel Stokes in 1850 [82] who found  $\xi_t = 3\pi\eta a$ . Further derivations can be found in [75, 83]. Using Stokes' expression for  $\xi_t$ , the total

torque is

$$\begin{aligned}
 \vec{T}_{\text{friction}} &= - \sum_{n=-N/2}^{N/2} na\vec{u} \times \xi_t \vec{v}_n \\
 &= - \sum_{n=-N/2}^{N/2} na\vec{u} \times (\xi_t \vec{\omega} \times na\vec{u}) \\
 &= -\xi_t \sum_{n=-N/2}^{N/2} n^2 a^2 \vec{\omega} \\
 &\approx -(3\pi\eta a) a^2 \frac{2}{3} \left(\frac{N}{2}\right)^3 \vec{\omega} \\
 &= -\eta \frac{\pi L^3}{4} \vec{\omega} .
 \end{aligned} \tag{4.46}$$

Following Eq. (4.25), the rotational friction coefficient is

$$\xi_r = \frac{\pi\eta L^3}{4} \tag{4.47}$$

which is independent of the rod diameter  $a$ . This unexpected result is an artifact caused by the negligence of the hydrodynamic interactions among the beads. An approximate analytical calculation considering hydrodynamic interactions can be found in [81, appendix 8.1] and leads to

$$\xi_r = \frac{\pi\eta L^3}{3 \ln\left(\frac{L}{2a}\right)} . \tag{4.48}$$

A more accurate approximation of a rod is to model it as an array of  $N$  interacting spherical elements as exemplarily shown in Fig. 4.11.

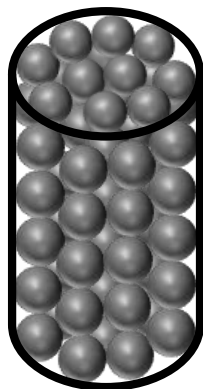


**Figure 4.11:** Cylinder filled up with an array of spheres.

The accuracy of the obtained results increases with  $N$ . Unfortunately, the calculation has to be performed using numerical methods and thus an increase in  $N$  implies increasing

## 4.2 Hydrodynamic properties of Ni nanorods

---

run times. Tirado et al. combined this method with symmetry properties of rodlike particles resulting in a modeling of cylinders as a stack of rings [84–86], Fig. 4.12.



**Figure 4.12:** Cylinder filled up with an array of rings.

This leads to great simplifications implying short run times and thus to an increasing of  $N$  and more accurate results. Tirado et al. calculated a set of rotational friction coefficients as a function of the aspect ratio and described the resulting curve by an analytical expression. For the rotation around the short rod axis

$$\xi_r = \frac{\pi\eta L^3}{3 \left( \ln \left( \frac{L}{a} \right) + \chi \left( \frac{L}{a} \right) \right)} \quad (4.49)$$

where

$$\chi \left( x = \frac{L}{a} \right) = -0.662 + \frac{0.917}{x} - \frac{0.050}{x^2} \quad (4.50)$$

is the end-effect correction was found.

Today’s computer power gives rise to numerical methods providing even more precise results. For example, Aragon used the boundary element method to solve the exact hydrodynamic equations [87] for arbitrarily shaped particles and developed a corresponding software suite called BEST. Later, Aragon solved the exact integral equation for Stokes flow with no slip boundary conditions of cylinders [88]. Similar to Tirado, they provided a high-precision approximate analytical expression for their numerical results which is also described by Eq. (4.49), but with a different end-effect correction:

$$\chi(x) = A - \frac{B}{\sqrt[4]{x}} + \frac{C}{\sqrt{x}} + \frac{D}{x} - \frac{E}{x^2} + \frac{F}{x^3} - \frac{G}{x^4} \quad (4.51)$$

with  $A = -0.372093$ ,  $B = 0.95622$ ,  $C = 1.24792$ ,  $D = 1.23085$ ,  $E = 1.99498$ ,  $F = 1.84201$ ,  $G = 0.664147$ .

Fig.4.13 shows a comparison between the calculated rotational friction coefficient of cylinders with a diameter of 100 nm as a function of its length obtained by the different expressions mentioned above. All expressions that are not based on numerical methods overestimate the rotational friction coefficient significantly. Since Eqs. (4.49) and (4.51) exhibit the highest accuracy, they will be used for all calculations of the rotational friction coefficient in this work. For more information about macromolecular hydrodynamic modeling, reference is made to the review article of Aragon [89].

In the next section, reasons for deviations between the calculated idealized and real rotational friction coefficients will be discussed.

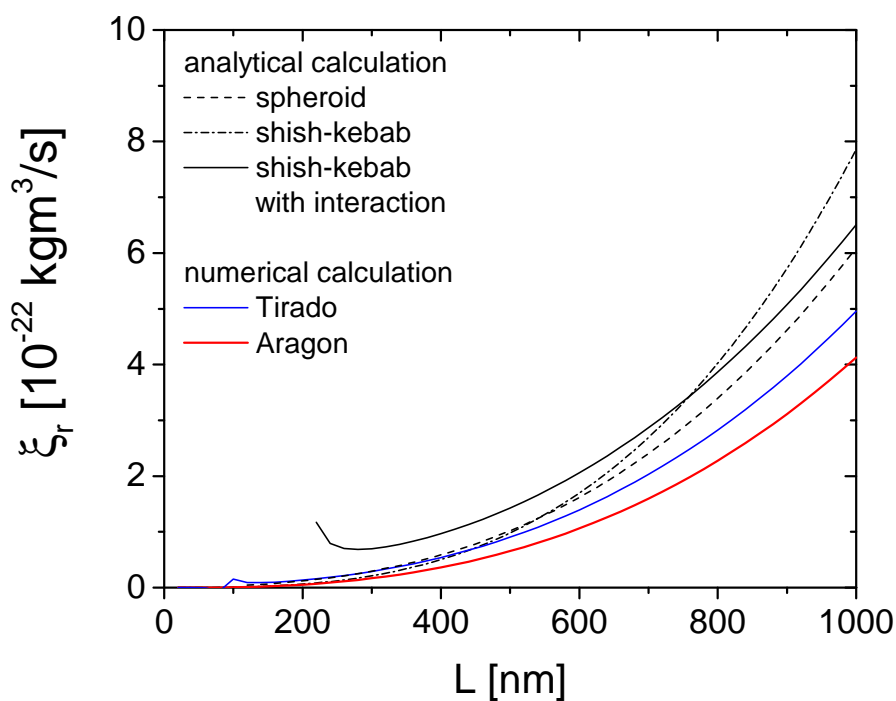


**Figure 4.13:** Calculated rotational friction coefficient  $\xi_r$  as a function of the rod length  $L$  in water ( $\eta = 1$  mPas) for a rod rotating around its short axis with a diameter of 100 nm. The calculations were performed using Eq. (4.44) assuming spheroids (with same volume and aspect ratio as corresponding capped cylinders), Eq. (4.47) using the simple shish-kebab model, Eq. (4.48) using the shish-kebab model with interaction among the beads, Eqs. (4.49), (4.50) using Tirado's results, or Eqs. (4.49), (4.51) using Aragon's results, respectively.

### 4.2.4 Influence of deviations from the considered model

In the present work, all particles are described as capped cylinders, but sometimes differences at the cylinder ends like a non-hemispherical shape are observed. To estimate their influence, the rotational friction coefficient of the same cylinder as used in Fig. 4.13 was calculated by Aragon and Flamik [88] for three different types of cylinders: open, capped and rectangular, Fig. 4.14.

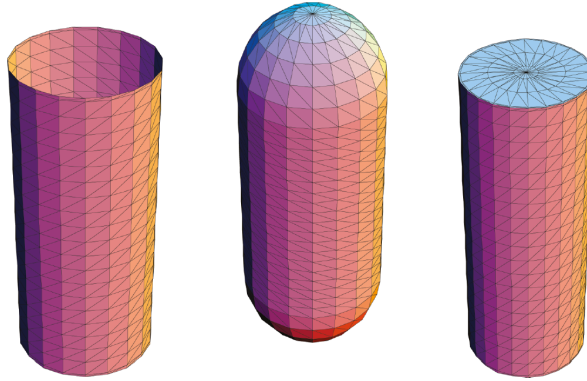


**Figure 4.14:** Triangular tessellations for open, capped, and rectangular cylinders [88].

Except for rod lengths below 200 nm, open and rectangular cylinders exhibit exactly the same behavior within the precision of Fig. 4.15. For small lengths and thus small aspect ratios the values for capped cylinders differ about 40% compared to open and rectangular cylinders. For larger aspect ratios corresponding to  $L = 1000$  nm this difference decreases to  $\sim 17\%$ .

Another perturbation of the shape can be caused by a rough surface. This problem was treated by Yamakawa who compared the rotational diffusion coefficient  $D_r = k_B T / \xi_r$  about the minor axis for a capped cylinder of length  $L$  and diameter  $d$  and a linear array of spherical beads of length  $L$  and diameter  $d'$  (looks similar to the shish-kebab model but is calculated differently) [90]. A good agreement between those models was found if the relation  $d = 0.741d'$  is fulfilled. This result suggests a large influence of the surface roughness, but it has to be mentioned that a linear array of beads is an example of a very rough surface (diameter of the particle varies between 0 and  $d'$ ). The surface roughness of the particles used in this work is much smaller and thus the effect is presumably smaller, too.

The biggest problem when calculating the rotation friction coefficient of a capped cylinder arises from uncertainties in the diameter of the particle which can arise from an unknown thickness of a polymer coating for example.

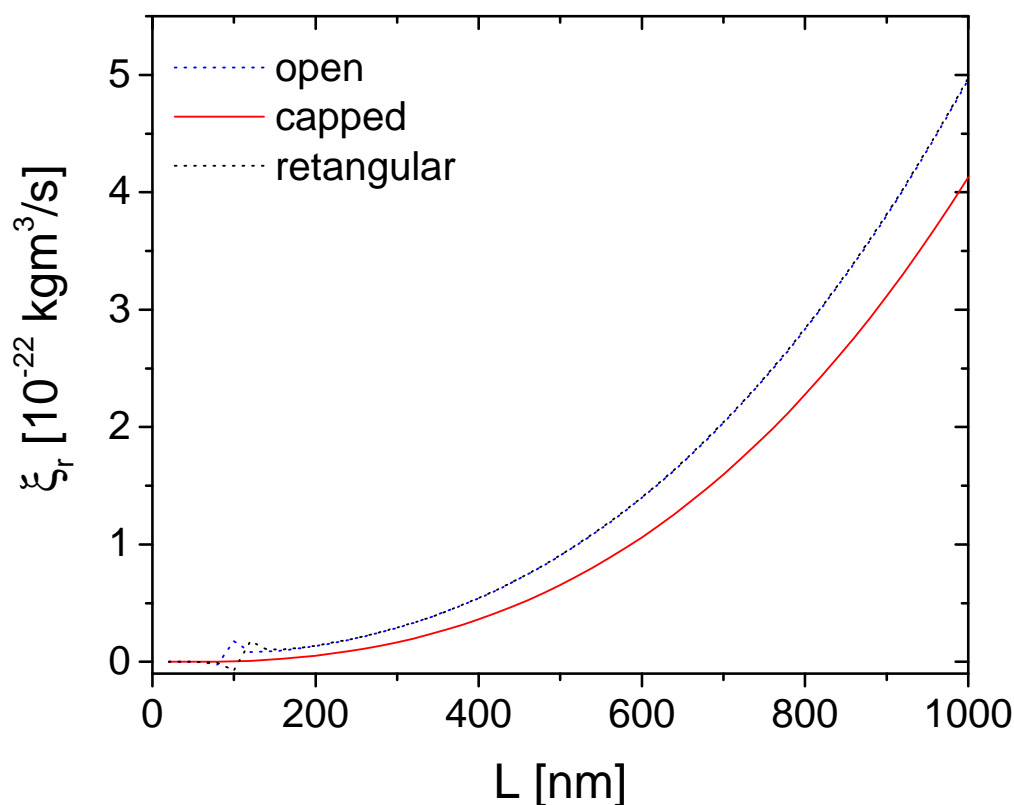


**Figure 4.15:** Same parameters as used in Fig. 4.13. Calculations performed for open, capped, and rectangular cylinders using relations of Aragon et al. [88].

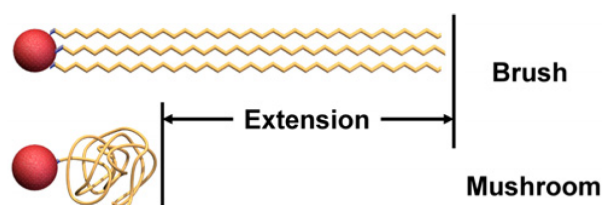


**Figure 4.16:** Thiol terminated linear polystyrene tethered to a nanoparticle surface (top image). Polystyrene in mushroom (random coil) or brush (extended) structure (depending on polymer coverage, bottom image) [91].

Similar effects can be expected for PVP coated Ni nanorods. A. Günther observed a difference of the diameter of PVP coated nanorods when investigated by TEM or SEM, respectively [25]. The difference was attributed to the PVP layer which was not observed in TEM, and determined to  $\approx 4$  nm. It should be noted that this thickness was estimated in vacuum, while the layer is expected to swell in water. In an extreme case, a brush

## 4.2 Hydrodynamic properties of Ni nanorods

---

structure similar as observed for polystyrene could be adopted. Krueger et al. investigated the hydrodynamic size of polystyrene coated spherical Au and CdSe nanoparticles. They discovered that the polymer assumes a brush conformation if the particle is fully covered by the polymer, Fig. 4.16. In this conformation, the polymer is 44% longer than the unbound polymer in solution. All these effects increase the hydrodynamic diameter of the nanorods and may explain the differences (factor 2) between theoretical expected and measured rotational diffusion coefficients  $D_r = k_B T / \xi_r$  observed by Günther [25]. Although swelling was also observed for Stöber particles [92], their change in size is expected to be less dramatically.

In conclusion, the perturbations arising from the differences in the cylinder ends, the surface roughness, and uncertainties in the rod diameter are expected, but it is also expected that they are smaller for silica encapsulated nanorods compared to PVP coated nanorods and will be neglected. The uncertainties in the particle diameter as discussed for PVP coated Ni nanorods should vanish for particles with an additional inorganic silica shell. Finally, the model for capped cylindrical particles proposed by Aragon, Eqs. (4.49) and (4.51), will be used.

In the following, the last fundamental physical aspect concerning the magnetic field-dependent optical transmission through nanorod colloids, i.e. their interaction with linearly polarized light, will be discussed.

## 4.3 Absorption and scattering of light

The following sections (4.3.1 - 4.3.5.3, 4.3.8) summarize chapters 1-3 of the text book *Absorption and scattering of light by small particles* by Bohren and Huffman [93] as far as it is necessary to understand the corresponding physical quantities, especially the optical cross sections used in the presented work. The considerations are limited to a scattering problem where a single particle is hit by an electromagnetic wave within the framework of classical electromagnetic theory and linear optics.

### 4.3.1 Physical basis

In this section the basic physical processes of an obstacle being hit by an electromagnetic wave [93, sections 1.1-1.2] is described. Electric charges inside this obstacle (i.e. electrons) are forced to an oscillatory motion. The accelerated electric charges radiate energy indicating a secondary radiation, which is emitted by the obstacle and is called scattering. Additionally to the reradiated electromagnetic energy, the excited elementary charges can transform a part of the incident electromagnetic energy into other forms of energy, e.g. thermal energy.

In the following, the electromagnetic scattering problem will be confined to the basic problem of interaction of light with an arbitrary wavelength with a single particle that is embedded in a homogeneous medium, meaning that the atomic or molecular heterogeneity is small compared to the wavelength of the incident light. Even though the particles can be complicated in shape and in the composition of their homogeneous components, it is assumed that every point of the particle can be described in macroscopic terms. The analysis is also narrowed down to elastic scattering, which means that the frequency of the scattered wave equals the frequency of the incident wave. In the following, the Maxwell equations which provide the mathematical description of the scattering problem will be introduced [93, section 2.1].

## 4.3 Absorption and scattering of light

---

### 4.3.2 Field vectors and the Maxwell equations

The basic equations to describe the absorption and scattering of electromagnetic waves are the Maxwell equations which are given by

$$\begin{aligned}\nabla \cdot \vec{D} &= \rho_{\text{F}}, \\ \nabla \times \vec{E} + \frac{\partial \vec{B}}{\partial t} &= 0, \\ \nabla \cdot \vec{B} &= 0, \\ \nabla \times \vec{H} &= \vec{J}_{\text{F}} + \frac{\partial \vec{D}}{\partial t}\end{aligned}\tag{4.52}$$

in SI units, where  $\vec{E}$  is the electric field and  $\vec{B}$  the magnetic induction. The electric displacement

$$\vec{D} = \epsilon_0 \vec{E} + \vec{P}\tag{4.53}$$

is related to the electric polarization  $\vec{P}$  (average electric dipole moment per unit volume) by the permittivity  $\epsilon_0$  and the magnetic field

$$\vec{H} = \frac{1}{\mu_0} \vec{B} - \vec{M}\tag{4.54}$$

to the magnetization  $\vec{M}$  (average magnetic dipole moment per unit volume) by the permeability of free space  $\mu_0$ . The quantities  $\rho_{\text{F}}$  and  $\vec{J}_{\text{F}}$  are the charge and current density of free charges.

In order to apply the Maxwell equations to the scattering problem, the Poynting vector [93, section 2.5]

$$\vec{S} = \vec{E} \times \vec{H}\tag{4.55}$$

is defined. It determines direction and magnitude of the rate of transfer of electromagnetic energy at all points of space and has the dimension of energy per area and time. Most instruments cannot follow the rapid oscillations of the Poynting vector, but they can detect the intensity  $I$  which is equal to the time average of the Poynting vector

$$I = \langle \vec{S}(t) \rangle = \frac{1}{\tau} \int_t^{t+\tau} \vec{S}(t') dt',\tag{4.56}$$

where  $\tau$  is a time interval long compared to the inverse angular frequency  $1/\omega$ . The Poynting vector will be used to define the extinction, scattering, and absorption cross section [93, section 3.4].

### 4.3.3 Extinction, scattering, and absorption

Extinction describes the reduction of the detectable rate of electromagnetic energy of light from  $U_0$  to  $U$  hitting a detector caused by the presence of particles in the pathway of the light, Fig. 4.17.

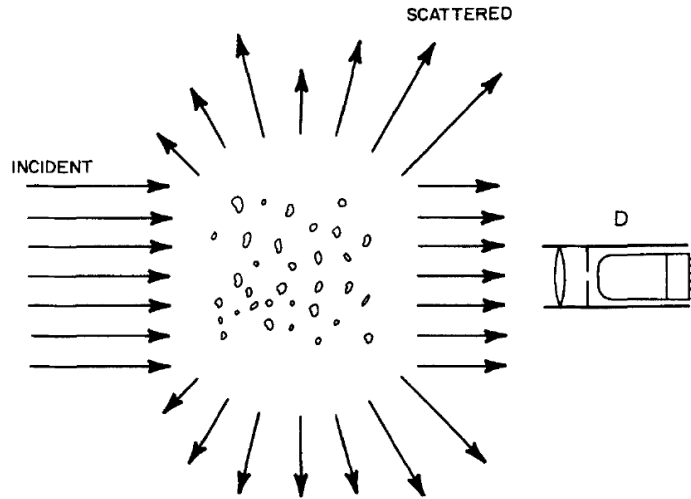


Figure 4.17: Extinction by a collection of particles [93].

Absorption (e.g. transformation of electromagnetic energy into thermal energy) and scattering by the particles has led to the difference  $U_0 - U$ . Fig. 4.18 shows the geometry used to describe the extinction by a single arbitrary particle embedded in a nonabsorbing medium when the particle is illuminated by a plane wave. The net rate at which electromagnetic energy crosses the closed surface  $A$  of an imaginary sphere of radius  $r$  around the particle is

$$W_a = - \int_A \vec{S} \cdot \vec{e}_r \, dA. \quad (4.57)$$

Energy will be absorbed inside the sphere if  $W_a > 0$ . Due to the nonabsorbing medium,  $W_a$  has to be the rate at which the particle absorbs energy. The rate at which energy is extinguished (from the point of view of the detector)  $W_{\text{ext}}$  is the sum of the rate of absorbed and scattered energy

$$W_{\text{ext}} = W_a + W_s, \quad (4.58)$$

where

$$\begin{aligned} W_s &= - \int_A \vec{S}_s \cdot \vec{e}_r \, dA, \\ W_{\text{ext}} &= - \int_A \vec{S}_{\text{ext}} \cdot \vec{e}_r \, dA. \end{aligned} \quad (4.59)$$

### 4.3 Absorption and scattering of light

---

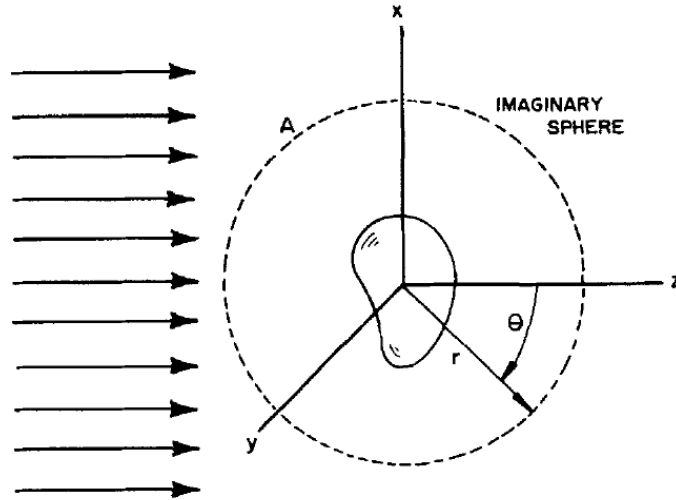


**Figure 4.18:** Extinction by a single particle [93].

The vector  $\vec{S}_s$  is the Poynting vector which is associated to the scattered electromagnetic wave and the vector  $\vec{S}_{\text{ext}}$  can be interpreted as a term arising due to the interaction of the incident and scattered waves.

The ratio of the corresponding rates of energy and incident irradiance  $I_i$

$$\begin{aligned} C_{\text{ext}} &= \frac{W_{\text{ext}}}{I_i}, \\ C_{\text{abs}} &= \frac{W_a}{I_i}, \\ C_{\text{sca}} &= \frac{W_s}{I_i} \end{aligned} \tag{4.60}$$

are quantities with dimension of area and are called the extinction, absorption, and scattering cross section. Following Eq. (4.58), the extinction cross section is the sum of the absorption and scattering cross section:

$$C_{\text{ext}} = C_{\text{abs}} + C_{\text{sca}}. \tag{4.61}$$

Now the general problem of determining the fields required to calculate these optical cross sections will be discussed [93, section 3.1].

#### 4.3.4 General formulation of the problem

The fundamental problem is to determine the electromagnetic field at all points inside the particle which is illuminated by the electromagnetic wave and at all points of the homogeneous medium in which the particle is embedded. Due to the experimental

conditions used in this work, the considerations are limited to a linearly polarized plane monochromatic wave.

If  $(\vec{E}_i, \vec{H}_i)$  and  $(\vec{E}_s, \vec{H}_s)$  are the electric and magnetic fields of the incident and scattered electromagnetic wave, Fig. 4.19, then the field inside the particles  $(\vec{E}_1, \vec{H}_1)$  and the fields inside the surrounding medium  $(\vec{E}_2, \vec{H}_2)$  can be calculated by superposition

$$\begin{aligned}\vec{E}_2 &= \vec{E}_i + \vec{E}_s, \\ \vec{H}_2 &= \vec{H}_i + \vec{H}_s,\end{aligned}\tag{4.62}$$

where

$$\begin{aligned}\vec{E}_i &= \vec{E}_0 \exp(i\vec{k} \cdot \vec{x} - i\omega t), \\ \vec{H}_i &= \vec{H}_0 \exp(i\vec{k} \cdot \vec{x} - i\omega t).\end{aligned}\tag{4.63}$$

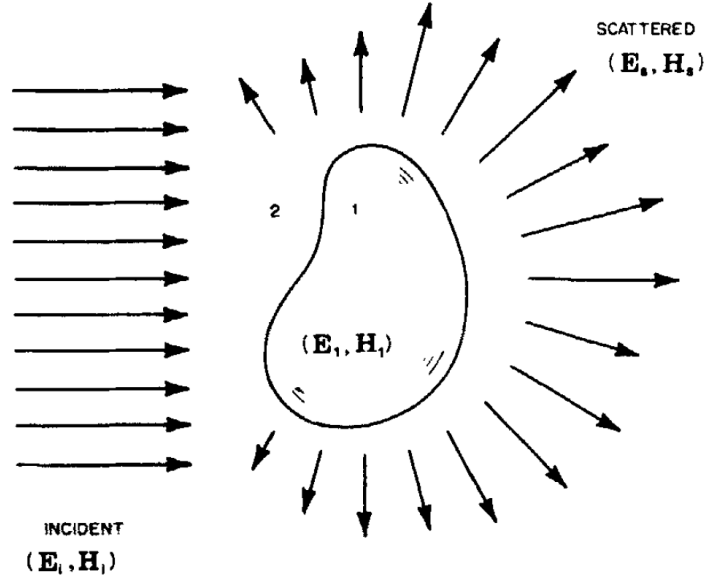


**Figure 4.19:** The incident field  $(\vec{E}_i, \vec{H}_i)$  gives rise to a field  $(\vec{E}_1, \vec{H}_1)$  inside the particle and a scattered field  $(\vec{E}_s, \vec{H}_s)$  in the medium surrounding the particle [93].

Here,  $\vec{k}$  is the wave vector in the surrounding medium. The field must satisfy the Maxwell equations at all points where  $\epsilon$  and  $\mu$  are continuous. However, by crossing the boundary between particle and medium,  $\epsilon$  and  $\mu$  change abruptly implying a macroscopic discontinuity at the boundary. It is required that the tangential components of  $\vec{E}$  and  $\vec{H}$  are continuous at the boundary

$$\begin{aligned}(\vec{E}_2 - \vec{E}_1) \times \vec{n} &= 0, \\ (\vec{H}_2 - \vec{H}_1) \times \vec{n} &= 0,\end{aligned}\tag{4.64}$$

## 4.3 Absorption and scattering of light

---

where  $\vec{n}$  is the outward directed normal to the surface  $S$ .

Our fundamental task is to find a solution of the Maxwell equations (4.52), both inside and outside of the particle that additionally satisfies the boundary conditions (4.64). Using Eqs. (4.57)–(4.60), the absorption, scattering, and extinction cross sections can be calculated from the obtained fields. The simplest geometry of a particle for which the scattering problem can be solved is a sphere which will be addressed in the next section.

### 4.3.5 Solving the scattering problem for spheres

The exact physical description of light scattering by spherical particles of radius  $a$  was derived in 1908 by Gustav Mie [31]. Although the particles used in this work, do not have a spherical shape, a short outline of the Mie theory will be given to illustrate the complexity of solving the scattering problem. The following description gives a resume of the description that can be found in the book of Bohren and Huffman [93, chapter 4] but suppresses a lot of mathematical details to keep the outline as short as possible. Furthermore, approximations for particles small compared to the wave length will be given.

#### 4.3.5.1 Mie theory

The electric and magnetic fields defined in Eqs. (4.62) and (4.63) have to satisfy the Maxwell equations, which can be transformed to

$$\nabla \cdot \vec{E} = 0, \quad (4.65)$$

$$\nabla \cdot \vec{H} = 0, \quad (4.66)$$

$$\nabla \times \vec{E} = i\omega\mu\vec{H}, \quad (4.67)$$

$$\nabla \times \vec{H} = -i\omega\epsilon\vec{E} \quad (4.68)$$

with continuous permittivity  $\epsilon$  and permeability  $\mu$ . The curls of Eqs. (4.67) and (4.68) are

$$\nabla \times (\nabla \times \vec{E}) = i\omega\mu\nabla \times \vec{H} = \omega^2\epsilon\mu\vec{E}, \quad (4.69)$$

$$\nabla \times (\nabla \times \vec{H}) = i\omega\epsilon\nabla \times \vec{E} = \omega^2\epsilon\mu\vec{H}$$

Using the identity

$$\nabla \times (\nabla \times \vec{A}) = \nabla(\nabla \cdot \vec{A}) - \nabla \cdot (\nabla \vec{A}) \quad (4.70)$$

results in

$$\nabla^2 \vec{E} + k^2 \vec{E} = 0, \quad (4.71)$$

$$\nabla^2 \vec{H} + k^2 \vec{H} = 0 \quad (4.72)$$

where  $k^2 = \omega^2 \epsilon \mu$  and  $\nabla^2 \vec{A} = \nabla \cdot (\nabla \vec{A})$ .

A scalar function  $\psi$  and an arbitrary constant vector  $\vec{c}$  can be used to construct a vector valued function  $\vec{M}$

$$\vec{M} = \nabla \times (\vec{c}\psi). \quad (4.73)$$

Since the divergence of a rotation vanishes for every vector function, it follows that

$$\nabla \cdot \vec{M} = 0. \quad (4.74)$$

Using the identities

$$\nabla \times (\vec{A} \times \vec{B}) = \vec{A}(\nabla \cdot \vec{B}) - \vec{B}(\nabla \cdot \vec{A}) + (\vec{B} \cdot \nabla)\vec{A} - (\vec{A} \cdot \nabla)\vec{B}, \quad (4.75)$$

$$\nabla(\vec{A} \cdot \mathbf{B}) = \vec{A} \times (\nabla \times \vec{B}) + \vec{B} \times (\nabla \times \vec{A}) + (\mathbf{B} \cdot \nabla)\vec{A} + (\vec{A} \cdot \nabla)\vec{B}. \quad (4.76)$$

results in

$$\nabla^2 \vec{M} + k^2 \vec{M} = \nabla \times [\vec{c}(\nabla^2 \psi + k^2 \psi)]. \quad (4.77)$$

Thus,  $\vec{M}$  satisfies the vector wave equation if  $\psi$  is a solution of the scalar wave equation

$$\nabla^2 \psi + k^2 \psi = 0. \quad (4.78)$$

Furthermore,  $\vec{M}$  can be used to construct the function

$$\vec{N} = \frac{\nabla \times \vec{M}}{k} \quad (4.79)$$

which is free of divergence and satisfies the vector wave equation  $\nabla^2 \vec{N} + k^2 \vec{N} = 0$ . Furthermore, the relation  $\nabla \times \vec{N} = k \vec{M}$  holds and hence  $\vec{N}$  and  $\vec{M}$  satisfy the attributes of an electromagnetic field. Thus, the problem is reduced to the problem of solving the scalar wave equation, Eq. (4.78).

The vector equation

$$\vec{M} = \nabla \times (\vec{r}\psi) \quad (4.80)$$

where  $\vec{r}$  is the radius vector is a solution of the vector wave equation in spherical coordinates as defined in Eqs. (4.28):

$$\frac{1}{r^2} \frac{\partial}{\partial r} \left( r \frac{\partial \psi}{\partial r} \right) + \frac{1}{r^2 \sin \theta} \frac{\partial}{\partial \theta} \left( \sin \theta \frac{\partial \psi}{\partial \theta} \right) + \frac{1}{r^2 \sin^2 \theta} \frac{\partial^2 \psi}{\partial \varphi^2} + k^2 \psi = 0. \quad (4.81)$$

This equation is separable and the ansatz

$$\psi(r, \theta, \phi) = R(r)\Theta(\theta)\Phi(\varphi) \quad (4.82)$$

### 4.3 Absorption and scattering of light

---

leads to three ordinary differential equations:

$$\frac{d^2\Phi}{d\varphi^2} + m^2\varphi = 0, \quad (4.83)$$

$$\frac{1}{\sin\theta} \frac{d}{d\varphi} \left( \sin\varphi \frac{d\Theta}{d\theta} \right) + \left[ (n(n+1) - \frac{m^2}{\sin^2\varphi}) \right] \Theta = 0, \quad (4.84)$$

$$\frac{d}{dr} \left( r^2 \frac{dR}{dr} \right) + [k^2 r^2 - n(n+1)] R = 0 \quad (4.85)$$

where the separation constants  $m$  and  $n$  are determined by subsidiary conditions that  $\psi$  must satisfy.

Eq. (4.83) represents the  $\varphi$ -dependence and can be solved by the linear independent solutions

$$\Phi_e = \cos m\varphi, \quad \Phi_o = \sin m\varphi \quad (4.86)$$

where  $e$  and  $o$  hint to even and odd functions and  $m \in \mathbb{N}$ .

Eq. (4.84) represents the  $\theta$ -dependence and can be solved by the associated Legendre functions of the first kind  $P_n^m(\cos\theta)$  of degree  $n$  and order  $m$  [94].

Finally, Eq. (4.85) represents the  $r$ -dependence and can be transformed to

$$\rho \frac{d}{d\rho} \left( \rho \frac{dZ}{d\rho} \right) + \left[ \rho^2 - (n + \frac{1}{2})^2 \right] Z = 0 \quad (4.87)$$

by introducing the dimensionless variable  $\rho = kr$  and defining  $Z = R\sqrt{\rho}$ . The linear independent solutions of Eq. (4.87) are the Bessel functions of the first and second kind  $J_{n+1/2}$  and  $Y_{n+1/2}$ . Hence, the linear independent solutions of Eq. (4.85) are

$$j_n(\rho) = \sqrt{\frac{\pi}{2\rho}} J_{n+1/2}(\rho), \quad (4.88)$$

$$y_n(\rho) = \sqrt{\frac{\pi}{2\rho}} Y_{n+1/2}(\rho), \quad (4.89)$$

$$h_n^{(1)}(\rho) = j_n(\rho) + iy_n(\rho), \quad (4.90)$$

$$h_n^{(1)}(\rho) = j_n(\rho) - iy_n(\rho) \quad (4.91)$$

where  $j_n$  and  $y_n$  can be expressed by  $z_n$  which can be calculated using the recurrence relations

$$z_{n-1}(\rho) + z_{n+1}(\rho) = \frac{2n+1}{\rho} z_n(\rho), \quad (4.92)$$

$$(2n+1) \frac{d}{d\rho} z_n(\rho) = n z_{n-1}(\rho) - (n+1) z_{n+1}(\rho), \quad (4.93)$$

where  $z_n$  is either  $j_n$  or  $y_n$ . The first two orders

$$j_0(\rho) = \frac{\sin\rho}{\rho}, \quad j_1(\rho) = \frac{\sin\rho}{\rho^2} - \frac{\cos\rho}{\rho}, \quad y_0(\rho) = -\frac{\cos\rho}{\rho}, \quad y_1(\rho) = -\frac{\cos\rho}{\rho^2} - \frac{\sin\rho}{\rho}, \quad (4.94)$$

allow to generate higher orders.

In conclusion, the solution of the scalar wave equation is

$$\begin{aligned}\psi_{emn} &= \cos(m\varphi)P_n^m(\cos\theta)z_n(kr), \\ \psi_{omn} &= \sin(m\varphi)P_n^m(\cos\theta)z_n(kr)\end{aligned}\tag{4.95}$$

where  $z_n(kr)$  is one of the four Bessel functions. Thus, the spherical harmonic vectors, Eq. (4.73), are

$$\vec{M}_{emn} = \nabla \times (\vec{r}\psi_{emn}), \quad \vec{M}_{omn} = \nabla \times (\vec{r}\psi_{omn})\tag{4.96}$$

and

$$\vec{N}_{emn} = \frac{\nabla \times \vec{M}_{emn}}{k}, \quad \vec{N}_{omn} = \frac{\nabla \times \vec{M}_{omn}}{k}.\tag{4.97}$$

Using the expressions for  $\vec{M}_{emn}$ ,  $\vec{M}_{omn}$ ,  $\vec{N}_{emn}$ , and  $\vec{N}_{omn}$ , a plane wave can be expanded in spherical harmonic waves, which will be done in the following.

### Expansion of a plane wave in vector spherical harmonics

A plane  $x$ -polarized wave that can be represented in spherical coordinates by

$$\vec{E}_i = E_0 e^{ikr \cos\theta} \vec{e}_x \quad \text{with} \quad \vec{e}_x = \sin\theta \vec{e}_r + \cos\theta \cos\varphi \vec{e}_\theta - \sin\varphi \vec{e}_\varphi\tag{4.98}$$

is scattered by an arbitrary sphere. To solve this problem, Eq. (4.98) is expanded in spherical harmonic vectors:

$$\vec{E}_i = \sum_{m=0}^{\infty} \sum_{n=m}^{\infty} (B_{emn} \vec{M}_{emn} + B_{omn} \vec{M}_{omn} + A_{emn} \vec{N}_{emn} + A_{omn} \vec{N}_{omn}).\tag{4.99}$$

The unknown coefficients  $B_{emn}$ ,  $B_{omn}$ ,  $A_{emn}$ , and  $A_{omn}$  can be determined using the orthogonality conditions of  $\sin(m\varphi)$  and  $\cos(m'\varphi)$  leading to  $B_{emn} = A_{omn} = 0$  for all  $m$  and  $n$ . Furthermore, the remaining coefficients vanish unless  $m = 1$  and the superscript  $l$  will be introduced to solve problems related to the misbehavior of  $y_n$  at the origin.

Finally

$$\vec{E}_i = E_0 \sum_{n=1}^{\infty} i^n \frac{2n+1}{n(n+1)} (\vec{M}_{oln}^{(1)} - i\vec{N}_{eln}^{(1)})\tag{4.100}$$

is obtained. Since the expansion of the incident electric field  $\vec{E}_i$  is now determined, the Maxwell equations can be used to obtain the corresponding magnetic fields  $\vec{H}_i$ , too:

$$\vec{H}_i = \frac{-k}{\omega\mu} E_0 \sum_{n=1}^{\infty} i^n \frac{2n+1}{n(n+1)} (\vec{M}_{eln}^{(1)} + i\vec{N}_{oln}^{(1)}).\tag{4.101}$$

Furthermore, the scattered fields  $(\vec{E}_s, \vec{H}_s)$  as well as the fields inside the sphere  $(\vec{E}_1, \vec{H}_2)$  can also be expanded in spherical vectors.

### 4.3 Absorption and scattering of light

---

#### The internal and scattered fields

At the boundary between the sphere and the surrounding medium, the condition

$$(\vec{E}_i + \vec{E}_s - \vec{E}_1) \times \vec{e}_r = (\vec{H}_i + \vec{H}_s - \vec{H}_1) \times \vec{e}_r \quad (4.102)$$

has to be satisfied. These boundary conditions, the orthogonality of the vector harmonics, and the form of the expansion of the incident field determine the expansions for the scattered field and the field inside the sphere. After some mathematical manipulations, it follows that

$$\begin{aligned} \vec{E}_1 &= \sum_{n=1}^{\infty} E_n (c_n \vec{M}_{oln}^{(1)} - id_n \vec{N}_{eln}^{(1)}), \\ \vec{H}_1 &= \frac{-k_1}{\omega \mu_1} \sum_{n=1}^{\infty} E_n (d_n \vec{M}_{eln}^{(1)} + ic_n \vec{N}_{oln}^{(1)}), \\ \vec{E}_s &= \sum_{n=1}^{\infty} E_n (ia_n \vec{N}_{eln}^{(3)} - b_n \vec{M}_{oln}^{(3)}), \\ \vec{H}_s &= \frac{-k}{\omega \mu} \sum_{n=1}^{\infty} E_n (ib_n \vec{N}_{oln}^{(3)} - a_n \vec{M}_{eln}^{(3)}) \end{aligned} \quad (4.103)$$

where  $E_n = i^n E_0 (2n+1)/n(n+1)$  and  $\mu_1$  is the permeability of the sphere. The superscript (3) is appended to vector spherical harmonics for which the radial dependence of the generating functions is specified by  $h_n^{(1)}$ . The orthogonality of sin and cos, the relations between the angle dependent functions  $\pi_n = P_n^l / \sin \theta$  and  $\tau_n = dP_n^l / d\theta$ , the expansion of the incident, particle internal and scattered fields, and the border conditions Eq. (4.102), can be used to generate four linear equations for expansion coefficients whose solutions determine the expansion coefficients inside the particle

$$\begin{aligned} c_n &= \frac{\mu_1 j_n(x) [x h_n^{(1)}(x)]' - \mu_1 h_n^{(1)}(x) [x j_n(x)]'}{\mu_1 j_n(mx) [x h_n^{(1)}(x)]' - \mu h_n^{(1)}(x) [m x j_n(mx)]'}, \\ d_n &= \frac{\mu_1 m j_n(x) [x h_n^{(1)}(x)]' - \mu_1 m h_n^{(1)}(x) [x j_n(x)]'}{\mu m^2 j_n(mx) [x h_n^{(1)}(x)]' - \mu_1 h_n^{(1)}(x) [m x j_n(mx)]'} \end{aligned} \quad (4.104)$$

and the scattering coefficients

$$\begin{aligned} a_n &= \frac{\mu m^2 j_n(mx) [x j_n(x)]' - \mu_1 j_n(x) [m x j_n(mx)]'}{\mu m^2 j_n(mx) [x h_n^{(1)}(x)]' - \mu_1 h_n^{(1)}(x) [m x j_n(mx)]'}, \\ b_n &= \frac{\mu_1 m j_n(x) [x j_n(x)]' - \mu j_n(x) [m x j_n(mx)]'}{\mu_1 j_n(mx) [x h_n^{(1)}(x)]' - \mu h_n^{(1)}(x) [m x j_n(mx)]'}. \end{aligned} \quad (4.105)$$

Here, [...] describes derivatives with respect to the argument inside the parenthesis and

$$x = \frac{2\pi N a}{\lambda} \quad (4.106)$$

is the so called size parameter. It depends on the refractive index of the medium  $N$  and the wave length of the incident light  $\lambda$ . The relative refractive index is related to the refractive index of the particle  $N_1$  by

$$m = \frac{N_1}{N}. \quad (4.107)$$

Introducing the Riccati-Bessel-functions

$$\psi_n(\rho) = \rho j_n(\rho), \quad \xi_n(\rho) = \rho h_n^{(1)}(\rho), \quad (4.108)$$

the scattering coefficients can be simplified to

$$\begin{aligned} a_n &= \frac{m\psi_n(mx)\psi'_n(x) - \psi_n(x)\psi'_n(mx)}{m\psi_n(mx)\xi'_n(x) - \xi_n(x)\psi'_n(mx)}, \\ b_n &= \frac{\psi(mx)\psi'_n(x) - m\psi_n(x)\psi'_n(mx)}{\psi_n(mx)\xi'_n(x) - m\xi_n(x)\psi'_n(mx)}. \end{aligned} \quad (4.109)$$

Using these scattering coefficients, the scattered fields and thus  $W_{\text{ext}}$ ,  $W_{\text{sca}}$ , and  $W_{\text{abs}} = W_{\text{ext}} - W_{\text{sca}}$  can be calculated via Eqs. (4.59), (4.61). Now, the scattering cross section

$$\begin{aligned} C_{\text{sca}} &= \frac{W_s}{I_1} \\ &= \frac{2\pi}{k^2} \sum_{n=1}^{\infty} (2n+1) (|a_n|^2 + |b_n|^2) \end{aligned} \quad (4.110)$$

and the extinction cross section

$$\begin{aligned} C_{\text{ext}} &= \frac{W_{\text{ext}}}{I_1} \\ &= \frac{2\pi}{k^2} \sum_{n=1}^{\infty} (2n+1) \text{Re}(a_n + b_n) \end{aligned} \quad (4.111)$$

of the sphere can be calculated. The absorption cross section is

$$C_{\text{abs}} = C_{\text{ext}} - C_{\text{sca}}. \quad (4.112)$$

To calculate a numerical value of absorption or scattering cross sections, merely the scattering coefficients  $a_n$  and  $b_n$  have to be calculated. However, it turns out that the number of summands necessary for convergence is relatively large. Although this number of summands is no big problem for today's computers, the determination of the scattering coefficients is a challenging numerical task since the coefficients are complicated functions of spherical Bessel functions and their derivatives with complex arguments.

In the case of particles small compared to the wavelength of the incident light, the calculations can be dramatically simplified as will be shown in the following.

## 4.3 Absorption and scattering of light

---

### 4.3.5.2 Spheres small compared to the wave length

The section description gives a resume of the description that can be found in the book of Bohren and Huffman [93, section 5.1]. Expanding the first scattering coefficients to an accuracy of terms of order  $x^6$  results in

$$\begin{aligned}
 a_1 &= -\frac{i2x^3}{3} \frac{m^2 - 1}{m^2 + 2} - \frac{i2x^5}{5} \frac{(m^2 - 2)(m^2 - 1)}{(m^2 + 2)^2} + \frac{4x^6}{9} \left( \frac{m^2 - 1}{m^2 + 2} \right) + O(x^7), \\
 b_1 &= -\frac{ix^5}{45} (m^2 - 1) + O(x^7), \\
 a_2 &= -\frac{ix^5}{15} \frac{m^2 - 1}{2m^2 + 3} + O(x^7), \\
 b_2 &= O(x^7).
 \end{aligned} \tag{4.113}$$

To obtain this representation, it was assumed that the permeability of the sphere is equal to the one of the medium. For  $|m|x \ll 1$  it follows that  $|b_1| \ll |a_1|$  and thus only one term of order three or higher remains:

$$a_1 = -\frac{i2x^3}{3} \frac{m^2 - 1}{m^2 + 2}. \tag{4.114}$$

The scattering cross sections can be determined by inserting this equation into Eq. (4.110)

$$C_{\text{sca}} = \pi a^2 \frac{8}{3} x^4 \left| \frac{\epsilon_1 - \epsilon_m}{\epsilon_1 + 2\epsilon_m} \right|^2. \tag{4.115}$$

Here,  $N = \sqrt{\epsilon}$  was used. The parameter  $\epsilon_1$  is the permittivity of the sphere and the parameter  $\epsilon_m$  the permittivity of the medium. Similar, the extinction cross section can be obtained by inserting Eq. (4.114) into Eq. (4.111) resulting in

$$\begin{aligned}
 C_{\text{ext}} &= \pi a^2 \left[ 4x \operatorname{Im} \left\{ \frac{\epsilon_1 - \epsilon_m}{\epsilon_1 + 2\epsilon_m} \left( 1 + \frac{x^2}{15} \frac{\epsilon_1 - \epsilon_m}{\epsilon_1 + 2\epsilon_m} \frac{m^4 + 27m^2 + 38}{2m^2 + 3} \right) \right\} \right. \\
 &\quad \left. + \frac{8}{3} x^4 \operatorname{Re} \left\{ \left( \frac{\epsilon_1 - \epsilon_m}{\epsilon_1 + 2\epsilon_m} \right)^2 \right\} \right].
 \end{aligned} \tag{4.116}$$

For  $|m|x \ll 1$  the term

$$\frac{x^2}{15} \left( \frac{\epsilon_1 - \epsilon_m}{\epsilon_1 + 2\epsilon_m} \right) \frac{m^4 + 27m^2 + 38}{2m^2 + 3} \tag{4.117}$$

is close to zero and the absorption cross section can be calculated by  $C_{\text{abs}} = C_{\text{ext}} - C_{\text{sca}}$ . Since the corresponding term in the book of Bohren and Huffman seems to have a typing

error, the calculation will be shown in detail:

$$\begin{aligned}
C_{\text{abs}} &= C_{\text{ext}} - C_{\text{sca}} \\
&= \pi a^2 \left( 4x \operatorname{Im} \left\{ \frac{\epsilon_1 - \epsilon_m}{\epsilon_1 + 2\epsilon_m} \right\} + \frac{8}{3} x^4 \operatorname{Re} \left\{ \left( \frac{\epsilon_1 - \epsilon_m}{\epsilon_1 + 2\epsilon_m} \right)^2 \right\} - \frac{8}{3} x^4 \left| \frac{\epsilon_1 - \epsilon_m}{\epsilon_1 + 2\epsilon_m} \right|^2 \right) \\
&= \pi a^2 \left( 4x \operatorname{Im} \left\{ \frac{\epsilon_1 - \epsilon_m}{\epsilon_1 + 2\epsilon_m} \right\} + \frac{8}{3} x^4 \operatorname{Re} \left\{ \left( \frac{\epsilon_1 - \epsilon_m}{\epsilon_1 + 2\epsilon_m} \right)^2 \right\} - \frac{8}{3} x^4 \left( \operatorname{Re} \left\{ \frac{\epsilon_1 - \epsilon_m}{\epsilon_1 + 2\epsilon_m} \right\}^2 \right. \right. \\
&\quad \left. \left. + \operatorname{Im} \left\{ \frac{\epsilon_1 - \epsilon_m}{\epsilon_1 + 2\epsilon_m} \right\}^2 \right) \right) \\
&= \pi a^2 \left( 4x \operatorname{Im} \left\{ \frac{\epsilon_1 - \epsilon_m}{\epsilon_1 + 2\epsilon_m} \right\} + \frac{8}{3} x^4 \operatorname{Re} \left\{ \frac{\epsilon_1 - \epsilon_m}{\epsilon_1 + 2\epsilon_m} \right\}^2 - \frac{8}{3} x^4 \operatorname{Im} \left\{ \frac{\epsilon_1 - \epsilon_m}{\epsilon_1 + 2\epsilon_m} \right\}^2 \right. \\
&\quad \left. - \frac{8}{3} x^4 \operatorname{Re} \left\{ \frac{\epsilon_1 - \epsilon_m}{\epsilon_1 + 2\epsilon_m} \right\}^2 - \frac{8}{3} x^4 \operatorname{Im} \left\{ \frac{\epsilon_1 - \epsilon_m}{\epsilon_1 + 2\epsilon_m} \right\}^2 \right) \\
&= \pi a^2 \left( 4x \operatorname{Im} \left\{ \frac{\epsilon_1 - \epsilon_m}{\epsilon_1 + 2\epsilon_m} \right\} - \frac{16}{3} x^4 \operatorname{Im} \left\{ \frac{\epsilon_1 - \epsilon_m}{\epsilon_1 + 2\epsilon_m} \right\}^2 \right) \\
&= \pi a^2 \left( 4x \operatorname{Im} \left\{ \frac{\epsilon_1 - \epsilon_m}{\epsilon_1 + 2\epsilon_m} \right\} \left( 1 - \frac{4}{3} x^3 \operatorname{Im} \left\{ \frac{\epsilon_1 - \epsilon_m}{\epsilon_1 + 2\epsilon_m} \right\} \right) \right).
\end{aligned} \tag{4.118}$$

Furthermore,  $4/3x^3 \operatorname{Im}\{(\epsilon_1 - \epsilon_m)(\epsilon_1 + 2\epsilon_m)\} \ll 1$  holds for small  $x$  and thus the absorption cross section is approximately

$$C_{\text{abs}} = \pi a^2 4x \operatorname{Im} \left\{ \frac{\epsilon_1 - \epsilon_m}{\epsilon_1 + 2\epsilon_m} \right\}. \tag{4.119}$$

The obtained expressions for the optical cross sections for particles small compared to the wavelength were obtained starting from the results of Mie theory.

In the next section, the same expressions will be deduced by a much simpler approach called the electrostatic approximation.

### 4.3.5.3 Spheres in the electrostatic approximation

The following section summarizes of the description that can be found in the book by Bohren and Huffman [93, section 5.2].

Assuming a wavelength significantly larger than the particle size implies that the field inside the particle depends only on time while it is independent of the position inside the particle, Fig. 4.20. In this electrostatic approximation (also called quasistatic approximation), a homogeneously polarized isotropic sphere is considered to behave like an ideal

### 4.3 Absorption and scattering of light

---

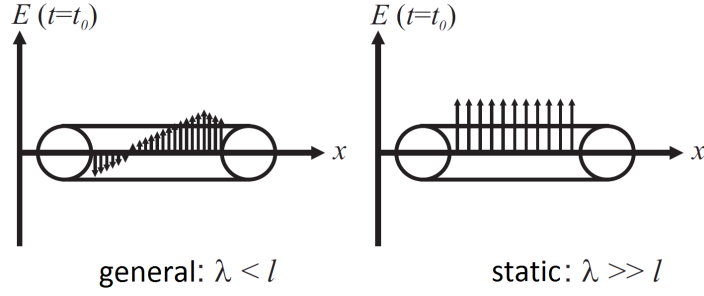


**Figure 4.20:** In general, the electric field inside the illuminated particle depends on location and time. In the electrostatic approximation, it is assumed that the particle is much smaller than the wavelength of the incident light. In this case, the electric field is assumed to be independent on the location inside the particle but still varying with time [25].

dipole. If the permittivities of the medium and the sphere are not equal, a charge will be induced on the surface of the sphere. The electric fields inside and outside of the sphere  $\vec{E}_1$  and  $\vec{E}_2$  can be determined by calculating the negative gradient of the corresponding potentials  $\vec{E}_1 = -\nabla\phi_1$  and  $\vec{E}_2 = -\nabla\phi_2$ .

Considering these differential equations of the electric field and the conditions for potentials at boundaries

$$\phi_1 = \phi_2 \quad (4.120)$$

and

$$\epsilon_1 \frac{\partial\phi_1}{\partial r} = \epsilon_m \frac{\partial\phi_2}{\partial r} \quad (r = a) \quad (4.121)$$

and the fact that the electric field at large distances from the sphere has to be the unperturbed applied field

$$\lim_{r \rightarrow \infty} = -E_0 z, \quad (4.122)$$

the following relations are generated:

$$\phi_1 = -\frac{3\epsilon_m}{\epsilon_1 + 2\epsilon_m} E_0 r \cos\theta, \quad (4.123)$$

$$\phi_2 = -E_0 r \cos\theta + a^3 E_0 \frac{\epsilon_1 - \epsilon_m}{\epsilon_1 + 2\epsilon_m} \frac{\cos\theta}{r^2}. \quad (4.124)$$

Eq. (4.124) determines the field outside of the sphere and consists of one term which is identical to the potential of an ideal dipole

$$\phi = \frac{\vec{p} \cdot \vec{r}}{4\pi\epsilon_m r^3} = \frac{p \cos\theta}{4\pi\epsilon_m r^2} \quad (4.125)$$

with the dipole moment

$$\vec{p} = 4\pi\epsilon_m a^3 \frac{\epsilon_1 - \epsilon_m}{\epsilon_1 + 2\epsilon_m} \vec{E}_0. \quad (4.126)$$

Hence, the applied field induces a dipole moment which is proportional to the field. Using the relation

$$\vec{p} = \epsilon_m \alpha \vec{E}_0, \quad (4.127)$$

the polarizability

$$\alpha = 4\pi a^3 \frac{\epsilon_1 - \epsilon_m}{\epsilon_1 + 2\epsilon_m} \quad (4.128)$$

can be attributed to the sphere.

These considerations are purely electrostatic, but the scattering of a plane wave by a sphere is a dynamical problem. To calculate the scattering, the sphere is replaced by an ideal dipole. Following Eq. (4.126), the dipole moment is assumed to be proportional to the applied field and the permittivities at the frequency of the incident wave. The moment of the ideal dipole oscillates with the frequency of the applied field and thus emits an electric field

$$\vec{E}_s = \frac{e^{ik(r-z)}}{-ikr} \vec{X} E, \quad E = E_0 e^{ikz} \quad (4.129)$$

with

$$\vec{X} = \frac{ik^3}{4\pi} \alpha \vec{e}_r \times (\vec{e}_r \times \vec{e}_x). \quad (4.130)$$

Using these expressions, the corresponding Poynting vectors and thus  $W_{\text{ext}}$ ,  $W_{\text{sca}}$ , and  $W_{\text{abs}} = W_{\text{ext}} - W_{\text{sca}}$  can be calculated by Eqs. (4.59) and (4.60). Now, the absorption cross section

$$\begin{aligned} C_{\text{abs}} &= \frac{W_{\text{abs}}}{I_1} \\ &= k \text{Im}(\alpha) \pi \\ &= a^2 4x \text{Im} \left( \frac{\epsilon_1 - \epsilon_m}{\epsilon_1 + 2\epsilon_m} \right), \end{aligned} \quad (4.131)$$

and scattering cross sections

$$\begin{aligned} C_{\text{sca}} &= \frac{W_s}{I_1} \\ &= \frac{k^4}{6\pi} |\alpha|^2 \\ &= \pi a^2 \frac{8}{3} x^4 \left| \frac{\epsilon_1 - \epsilon_m}{\epsilon_1 + 2\epsilon_m} \right|^2 \end{aligned} \quad (4.132)$$

are determined. These expressions are identical to those obtained for small spheres by aborting the series expansion from the Mie theory, Eqs. (4.115) and (4.119). The main advantage of the electrostatic approximation is not its accuracy, but it gives a physical explanation of the dominant term of scattering by polarization.

## 4.3 Absorption and scattering of light

---

The treatment of the optical properties of spheres is important to understand the scattering problem, but the spherical shape is a completely insufficient description of the cylindrical shape of a nanorod. The simplest anisotropic shape is a spheroid and in the following the determination of its optical cross sections will be outlined.

### 4.3.6 Solving the scattering problem for spheroids

#### 4.3.6.1 The separation of variables method (SVM)

The separation of variables method (SVM) is similar to the Mie theory and provides an exact solution for the Maxwell equations. However, while the Mie theory is limited to spheres, the SVM is applicable to spheroids. Following the introduction to SVM in [95] the basic idea of SVM is to solve the electromagnetic scattering problem for spheroids in the spheroidal coordinate system. It is based on expanding the incident, internal, and scattered fields in vector spheroidal wave functions. The expansion coefficients of the incident field are calculated analytically. Boundary conditions are used to compute the unknown expansion coefficients of the internal and scattered fields. Since the vector spheroidal wave functions are not orthogonal on the spheroidal surface, the determination of the unknown expansion coefficients results in an infinite set of linear algebraic equations. This set has to be truncated and solved by numerical methods.

A method providing very simple analytic expressions to calculate the optical cross sections for spheroids which are small compared to the wavelength of the incident light is the electrostatic approximation which was already presented for the case of a sphere. The idea can be transferred to spheroids.

#### 4.3.6.2 Spheroids in the electrostatic approximation

*A slightly modified version of this section (4.3.6.2) was already part of publication [43], see appendix E.*

As already mentioned in section 4.3.5.3, in the electrostatic approximation (EA), the particle is assumed to be small compared to the wavelength of the incident light in the surrounding medium so that it is instantly and homogeneously polarized by a time-variable, but spatially constant electric field [93]. The polarizabilities along the principal axes of a particle are

$$\alpha_i = V \cdot \frac{\epsilon - \epsilon_m}{\epsilon_m + L_i \cdot (\epsilon - \epsilon_m)} \quad (4.133)$$

where  $\epsilon$  and  $\epsilon_m$  are the permittivities of the particle material and the surrounding medium, respectively,  $V$  is the particle volume and  $L_i$  are the depolarization factors. While in the case of a sphere  $L_i = 1/3$ , for spheroids it has to be distinguished between values of  $L$  along the major ( $i = 1$ ) and minor axes ( $i = 2,3$ ). For a prolate spheroid

$$L_1 = \frac{1}{\Theta^2 - 1} \left( \frac{\Theta}{2\sqrt{\Theta^2 - 1}} \cdot \ln \left( \frac{\Theta + \sqrt{\Theta^2 - 1}}{\Theta - \sqrt{\Theta^2 - 1}} \right) - 1 \right), \quad (4.134)$$

$$L_2 = L_3 = \frac{1}{2} (1 - L_1) \quad (4.135)$$

where  $\Theta$  denotes the aspect ratio of the major to the minor spheroid axis [96]. In this work,  $\epsilon = -12.96 + 16.37i$  [97] for Ni and  $\epsilon_m = 1.75$  [98] for water is used. The corresponding absorption and scattering cross sections are

$$C_{\text{abs}} = k \cdot \text{Im}(\alpha), \quad (4.136)$$

$$C_{\text{sca}} = \frac{k^4}{6\pi} |\alpha|^2, \quad (4.137)$$

where  $k$  is the wave number of the incident light in the medium [93].

Although the EA provides simple expressions for anisotropic particles as used in this study, there are two crude assumptions which might cause considerable inaccuracies. First, the size of particles used in this study are not much smaller than the wavelength of the incident light (sometimes even larger than it) and second, the approximation of the particle shape by spheroids is questionable. The first problem could be solved using the SVM whose greatest advantage is the high accuracy of its results [95]. Unfortunately, the method is still limited to spheroids. To be able to predict the scattering behavior of arbitrarily shaped particles including core-shell particles, simulations using the finite element method (FEM) were performed.

### 4.3.7 Solving the scattering problem for arbitrarily shaped particles by the finite element method (FEM)

The outline of the finite element method (FEM) follows the description in [35]. By inserting the equation of harmonic fields, Eq. (4.63), into the third and fourth Maxwell equations (4.52)

$$\begin{aligned} \nabla \times \vec{E} &= i\omega\mu\vec{H}, \\ \nabla \times \vec{H} &= -i\omega\mu\vec{E}, \end{aligned} \quad (4.138)$$

### 4.3 Absorption and scattering of light

---

is obtained. Applying the curl operator

$$\begin{aligned}\nabla \times (\nabla \times \vec{E}) &= i\omega\mu\nabla \times \vec{H} = \omega^2\epsilon\mu\vec{E}, \\ \nabla \times (\nabla \times \vec{H}) &= -i\omega\mu\nabla \times \vec{E} = \omega^2\epsilon\mu\vec{H}\end{aligned}\tag{4.139}$$

and using the identity

$$\nabla \times (\nabla \times \vec{A}) = \nabla(\nabla \cdot \vec{A}) - \nabla \cdot (\nabla \vec{A})\tag{4.140}$$

results in the Helmholtz equations

$$\begin{aligned}\nabla^2 \vec{E} + k^2 \vec{E} &= 0, \\ \nabla^2 \vec{H} + k^2 \vec{H} &= 0\end{aligned}\tag{4.141}$$

where

$$k^2(\vec{r}) = \omega^2\epsilon(\vec{r})\mu(\vec{r})/c^2.\tag{4.142}$$

The FEM treats the scattering problem in the frequency domain by solving the Helmholtz equations. The basic idea is to divide the whole space into small regions represented by a grid mesh. Although it is not possible to describe every shape exactly, it is possible to use many small elements to obtain a sufficient approximation to arbitrary shapes as shown exemplarily in Fig. 4.21 for a capped cylinder with a length of 100 nm and a diameter of 20 nm.

The electric and magnetic fields inside each region are described by a local function. The runtime depends on the number of finite elements and hence of shape and volume of the particle.

The Helmholtz Eqs. (4.141) are discretized in space and then numerically solved to find

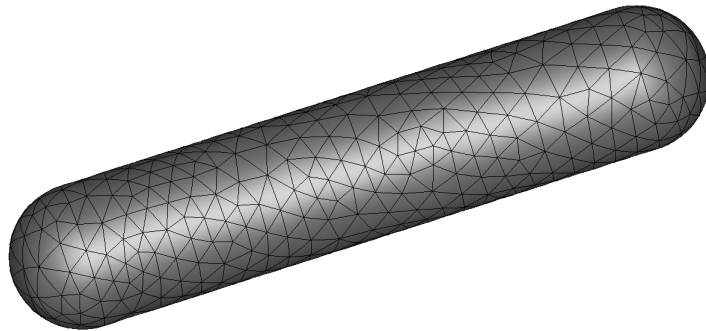


**Figure 4.21:** Mesh of a capped cylinder with a length of 100 nm and a diameter of 20 nm built in CST Microwave 2015. To model the cylinder and the surrounding medium 45774 tetrahedrons were used.

the fields that satisfy the boundary conditions. To reduce the errors induced by the mesh approximation, adaptive mesh refinement procedures are used to refine elements at which the gradients of  $\vec{E}$  and  $\vec{H}$  are largest between adjacent elements.

In the present work, the commercial tool CST Microwave 2015 was used to calculate the optical cross sections for differently shaped particles. The simulations were performed in the frequency domain which provides much shorter run-times compared to simulations performed in the time domain but requires a range of frequencies instead of a single value. The used excitation signal contains frequencies between  $473 \cdot 10^{12}$  Hz and  $475 \cdot 10^{12}$  Hz including the frequency of the HeNe laser ( $473.76 \cdot 10^{12}$  Hz) used in the experimental setup. Adaptive mesh refinement of the tetrahedral mesh was repeated until the obtained extinction cross section varied less than 0.1% in two successive runs or a predefined number of mesh refinements was reached. A value of  $3d/4$  where  $d$  is the diameter of the core of the particle was chosen for the local maximum mesh step width inside the particle for the initial mesh. This provided a sufficient quality of the initial mesh quality for adaptive mesh refinement resulting in converging cross sections.

Fig. 4.22 shows an example of a result of such a FEM simulation. In the next section, the change in the intensity of light before and after passing a slab of particles with known extinction cross sections will be calculated [93, section 3.4.1].

### 4.3.8 The Beer-Lambert law

With regard to the experimental conditions of this work, a beam of light passing a suspension with optical path length  $s$  containing  $N$  identical particles per unit volume, each with an extinction cross section  $C_{\text{ext}}$ , is considered. In order to determine the change in intensity before and after passing the suspension, the illuminated volume is divided into slices of thickness  $ds$ . The differential decrease of intensity is proportional to the intensity, the concentration of the particles, and their extinction cross section:

$$\begin{aligned} dI &= -INC_{\text{ext}} ds \\ \Leftrightarrow \frac{dI}{I} &= -NC_{\text{ext}} ds. \end{aligned} \tag{4.143}$$

This differential equation can be solved by integration with the constant of integration  $\ln(I_0)$  for  $s = 0$  yielding the Beer-Lambert law

$$I = I_0 \exp(-NsC_{\text{ext}}). \tag{4.144}$$

To avoid confusion about the notation of the Beer-Lambert law, it should be noted that the term  $I = I_0 10^{-Nsc\epsilon_\lambda}$ , where  $\epsilon_\lambda = \lg(e)C_{\text{ext}}$  is the attenuation coefficient which can

### 4.3 Absorption and scattering of light

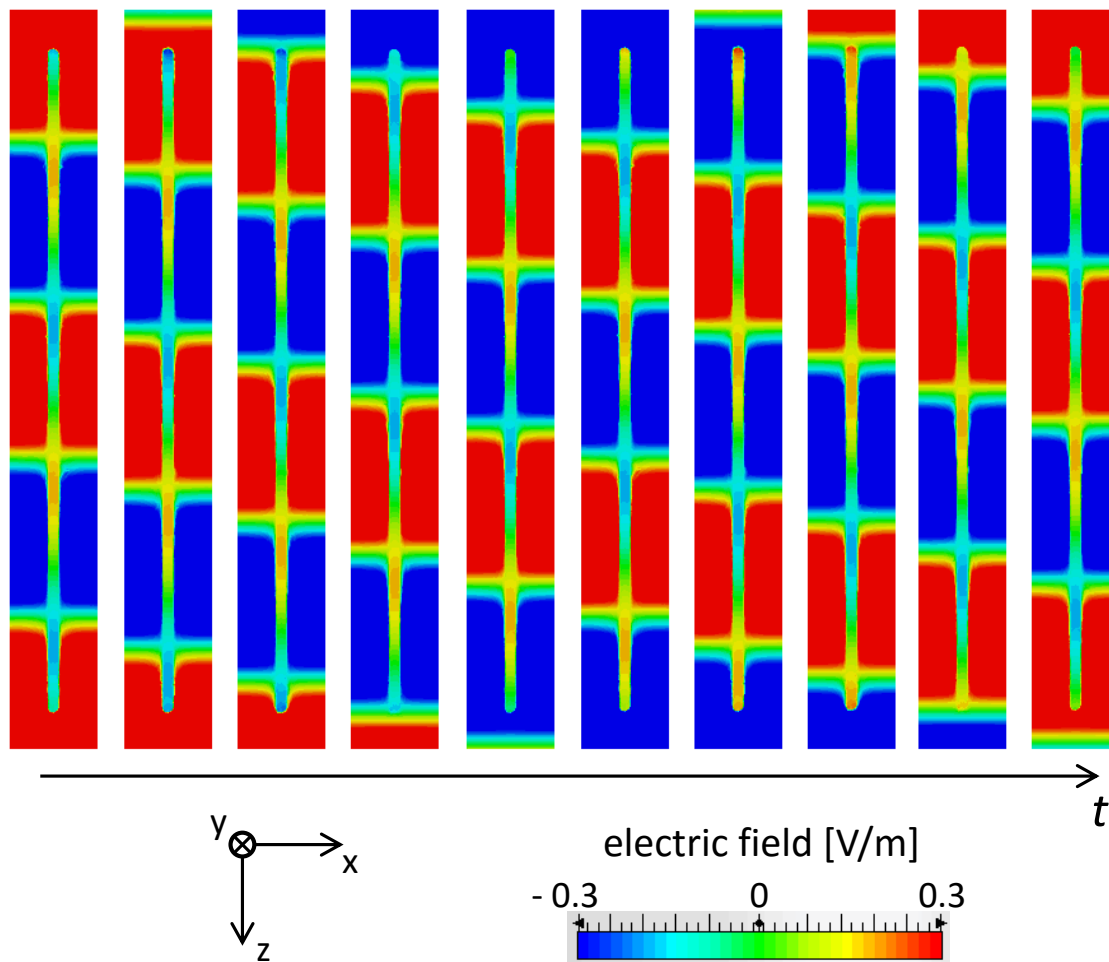


**Figure 4.22:** A capped cylinder (diameter 15 nm, length 1000 nm) is hit by a linearly polarized ( $y$ -direction) electro-magnetic wave (propagating in  $z$ -direction) with a wavelength of 633 nm. The pictures exhibit the time-dependence of the  $y$ -component of the electric field. The field inside the particle is much lower than outside and thus a color scale was chosen that allows to see the differences inside the particle but can not reproduce the full range of the wave outside. The field inside the particle is neither homogeneous nor in phase with the field outside. Especially the latter aspect was also observed for smaller nanorods. The simulation was performed using CST microwave studio.

also often be found in literature.

In this chapter, the theories to describe the magnetic, dynamic, and optical properties of single nanorods were introduced. In the next section, the derived physical parameters will be used for quantitative modeling of the static and dynamic MOT signals of ensembles of nanorods.

# Chapter 5

## Modeling

In this chapter, the combination of the previous theoretical models for the magnetic, hydrodynamic, and optical properties of Ni nanorods to calculate the magnetic field-dependent optical transmission in static as well as in oscillating fields Ni nanorod suspensions will be presented. All procedures described in this chapter were implemented in MATLAB.

### 5.1 Modeling of field-dependent magneto-optical transmission (DC-MOT)

First, the static magnetic field-dependent magneto-optical transmission of an ensemble of monodisperse nanorods will be modeled. *A modified version of this section (5.1) was already part of publication [43], see appendix E.*

As shown in section 4.3.8, extinction  $E$  and transmittance  $\tau$  of a dilute dispersion of small particles can be described by the Beer-Lambert law,

$$E = -\ln \tau = -\ln \frac{I}{I_0} = N s C_{\text{ext}}, \quad (5.1)$$

where  $I_0$  and  $I$  are the intensities of light before and after passing a path of length  $s$  through a dispersion of  $N$  particles per unit volume. The extinction cross section  $C_{\text{ext}}$  depends on the dielectric properties of the particle material and the surrounding medium, the size and shape of the particle, and in case of anisometric particles on their orientation relative to the polarization of the incident light. The basic orientations (longitudinal L and transversal T1 and T2) with respect to the coordinate system of the incident electromagnetic wave are exemplarily shown for a prolate spheroid in Fig. 5.1.

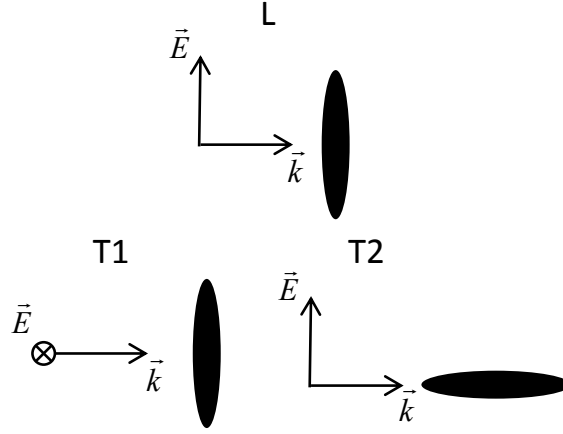


**Figure 5.1:** Basic orientations of a prolate spheroid with respect to the wave vector  $\vec{k}$  and electric field vector  $\vec{E}$  of linearly polarized light: longitudinal L and transversal T1 and T2. For T1 configuration, the electric field vector  $\vec{E}$  is perpendicular to the projection plane.

At an arbitrary orientation, defined by the polar coordinates  $\theta$  and  $\varphi$  of the major particle axis, Fig. 5.2, the extinction cross section is given as [93]

$$C_{\text{ext}} = \cos^2 \theta \cdot C_{\text{ext,L}} + \sin^2 \theta \sin^2 \varphi \cdot C_{\text{ext,T1}} + \sin^2 \theta \cos^2 \varphi \cdot C_{\text{ext,T2}}. \quad (5.2)$$

A macroscopic DC-MOT measurement of a nanorod colloid captures the extinction of a large ensemble of particles with a spatial orientation that can be described by an orientation distribution function  $n(\theta, \varphi)$ . For the particular case of Ni nanorods with or without a silica shell with permanent magnetic moment  $\vec{m}$  along the major rod axis dispersed in a viscous solvent, the distribution function for a superparamagnetic ensemble is used [20, 24, 99],

$$n(\beta) d\beta = \frac{1}{2} \exp\left(\frac{m\mu_0 H}{k_B T} \cos \beta\right) \sin \beta d\beta, \quad (5.3)$$

where  $\beta$  is the angle between the particle axis and the external magnetic field. The magnetic moment per particle  $m = M_s \cdot V$  is assumed to be determined by its core volume  $V = V(l, d)$  and the saturation magnetization  $M_s = 488 \cdot 10^3 \text{Am}^{-1}$  of Ni [63]. For simplification, the length and diameter distributions of the particle ensembles are neglected and it is assumed that the ensemble can be represented by a characteristic particle whose length and diameter correspond to the first moments of its distributions. The angle  $\beta$  in Eq. (5.3) denotes the angle between the external magnetic field and the major axis of the particle. The relation to  $\theta$  and  $\varphi$  depends on the orientation of the

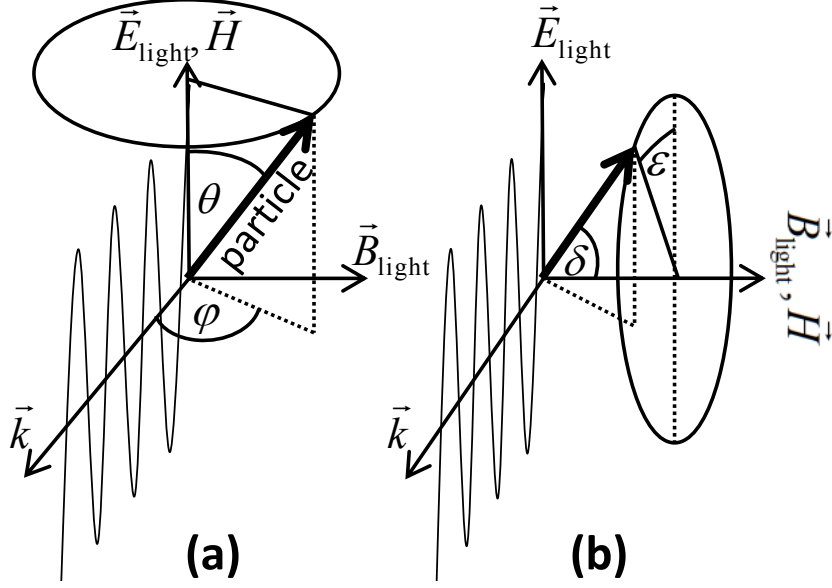


**Figure 5.2:** Definition of angles for a uniaxial anisotropic particle in an external magnetic field  $\vec{H}$  illuminated by linearly polarized light with the electric field vector  $\vec{E}$ , magnetic field vector  $\vec{B}$ , and wave vector  $\vec{k}$ . The two relevant cases are shown: (a)  $\vec{E} \parallel \vec{H} \perp \vec{k}$  and (b)  $(\vec{E} \perp \vec{H}) \perp \vec{k}$ .

magnetic field relative to the electric field vector of the incident light with three cases of particular interest with regard to the experiments performed in this work.

First, the external magnetic field  $\vec{H}$  is assumed to be parallel to the electric field vector of the incident light  $\vec{E}$ , Fig. 5.2 (a). In this case,  $\beta$  in Eq. (5.3) corresponds to  $\theta$  and the distribution function  $n(\theta, \varphi)$  is symmetric with respect to  $\varphi$  so that Eq. (5.2) provides the ensemble average of the extinction cross section as

$$\begin{aligned} \langle C_{\text{ext}} \rangle_{\parallel} &= \langle \cos^2 \beta \rangle C_{\text{ext,L}} + \frac{1}{2} (1 - \langle \cos^2 \beta \rangle) (C_{\text{ext,T1}} + C_{\text{ext,T2}}) \\ &= f_{\parallel} (\langle \cos^2 \beta \rangle). \end{aligned} \quad (5.4)$$

For the distribution function given by Eq. (5.3), the second moment is

$$\langle \cos^2 \beta \rangle = 1 + 2/\zeta^2 - 2 \coth(\zeta)/\zeta \quad (5.5)$$

with  $\zeta(H) = m\mu_0 H/k_B T$ .

If  $\vec{H}$  is perpendicular to  $\vec{E}$ , a particle orientation as shown in Fig. 5.2 (b) has to be considered, with an angle  $\varepsilon$  between the particle axis' projection into the  $(\vec{E}, \vec{k})$ -plane

and  $\vec{E}$ , and an angle  $\delta$  between the particle and the external magnetic field. Here,  $\delta$  coincides with  $\beta$  in Eq. (5.3) and the angles  $\theta, \varepsilon, \delta$ , and  $\varphi$  are related by

$$\cos^2 \theta = \cos^2 \varepsilon \sin^2 \delta \quad (5.6)$$

and

$$\cos^2 \varphi = 1 - \cos^2 \delta / (1 - \cos^2 \varepsilon \sin^2 \delta) . \quad (5.7)$$

The ensemble average extinction cross section for this case can be calculated to

$$\begin{aligned} \langle C_{\text{ext}} \rangle_{\perp} &= \frac{1 - \langle \cos^2 \beta \rangle}{2} C_{\text{ext,L}} \\ &+ \frac{1 + \langle \cos^2 \beta \rangle}{2} C_{\text{ext,T2}} + \langle \cos^2 \beta \rangle (C_{\text{ext,T1}} - C_{\text{ext,T2}}) \\ &= f_{\perp} (\langle \cos^2 \beta \rangle). \end{aligned} \quad (5.8)$$

Finally, the orientation distribution of the particles at  $H = 0$  which is assumed to be isotropic due to thermal rotational diffusion is considered. The orientation averaged extinction cross section is given as [93]

$$\langle C_{\text{ext}} \rangle_{\times} = \frac{1}{3} (C_{\text{ext,L}} + C_{\text{ext,T1}} + C_{\text{ext,T2}}) . \quad (5.9)$$

The transmitted intensity, normalized to the zero-field transmission  $I_{\times}$ , is

$$I(H)_{\perp,\parallel} / I_{\times} = \exp(-Ns(\langle C_{\text{ext}} \rangle_{\perp,\parallel}(H) - \langle C_{\text{ext}} \rangle_{\times})) . \quad (5.10)$$

Thus, taking advantage of the symmetry and the superparamagnetic properties of the nanorods, the problem of modeling the field-dependent optical transmission  $I(H)/I_{\times}$  can be reduced to the calculation of the extinction cross sections  $C_{\text{ext}}$  for the three principal directions.

In the next section, the MOT in oscillating fields will be presented.

## 5.2 Modeling of the response function of magneto-optical transmission in oscillating fields (OF-MOT)

To model the magneto-optical response function in oscillating fields, the magnetic, hydrodynamic, and optical properties of the particles, introduced in chapter 4, will be combined with their equation of motion. A simple model of a rotational oscillator will be used to obtain a differential equation for the rotational motion of axisymmetric particles with a permanent magnetic moment parallel to its axis in an oscillating external magnetic field [15].

### 5.2.1 Equation of rotational motion

The rotational motion of the particles can be described in terms of a periodically driven damped harmonic rotational oscillator:

$$I\ddot{\theta} + \xi_r\dot{\theta} = T(t) + y(t) \quad (5.11)$$

with the moment of inertia  $I$ , the rotational friction coefficient  $\xi_r$ , a time-dependent magnetic torque  $T(t)$ , and a stochastic torque due to the thermal energy  $y(t)$ .

Inertial effects can be neglected since the analysis is limited to frequencies far below  $\tau_l^{-1} = \xi_r/I$ , i.e. to the regime of low Reynold numbers, thus  $I\ddot{\theta} = 0$ . The rotational friction coefficient is calculated by Eq. (4.49), see section 4.2.3.

The magnetic torque depends on the magnetic moment  $m$  of the particle and can be expressed by

$$T(t) = m\mu_0 H_0 \sin[\beta(t) - \theta(t)], \quad (5.12)$$

where  $\beta(t)$  and  $\theta(t)$  are the time dependent angles as defined in Fig.3.2. It is also assumed that the chosen field amplitude is high enough to ensure  $\zeta = \frac{m\mu_0 H}{k_B T} \gg 1$  at all times and hence  $y(t)$  can be neglected. For small rotation angles  $\theta(t)$  and  $\beta(t)$ , the approximation  $\sin x \approx x$  can be applied and Eq. (5.11) can be rewritten to

$$\xi_r\dot{\theta}(t) = m\mu_0 H_0(\beta(t) - \theta(t)). \quad (5.13)$$

Assuming a phase shifted periodic oscillation of the nanorods, the rotation angle as a function of time is written as

$$\theta(t) = \hat{\theta}_0 \exp(i\omega t). \quad (5.14)$$

Solution of Eq. (5.13) yields

$$\hat{\theta}_0 = \frac{\beta_0}{1 + i\omega \frac{\xi_r}{m\mu_0 H_0}}. \quad (5.15)$$

This corresponds to a classical Debye relaxation [100] with the characteristic relaxation time  $\tau_c = 1/\omega_c = \xi_r/(m\mu_0 H_0)$  which is related to the Brownian relaxation time  $\tau_B = \xi_r/(2k_B T)$  by  $\tau_c = 2\tau_B/\zeta$ . The rotational diffusion coefficient of the particles is  $D_r = (\zeta\tau_c)^{-1}$ .

With Eqs. (5.14) and (5.15), the rotation angle of a particle as a function of time can be calculated. Corresponding to the measured response function, Eq. (3.5), the theoretically expected response function can be calculated by

$$\hat{X}_v(\omega) = \hat{\theta}(\omega)/\beta_0 = X'_v(\omega) + iX''_v(\omega). \quad (5.16)$$

For further analysis, it is useful to split it into a real and an imaginary part

$$\hat{X}_v(\omega) = X'_v(\omega) + iX''_v(\omega) \quad (5.17)$$

with

$$\begin{aligned} X'_v(\omega) &= \frac{1}{1 + (\omega\tau_c)^2}, \\ X''_v(\omega) &= \frac{-\omega\tau_c}{1 + (\omega\tau_c)^2}, \end{aligned} \quad (5.18)$$

respectively.

In order to model the OF-MOT signal of an aqueous dispersion of monodisperse Ni nanorods using Eqs. (5.18), the characteristic relaxation time  $\omega_c = 1/\tau_c$  has to be determined.

### 5.2.2 Characteristic frequency of nanorods

The characteristic frequency of a nanorod can be calculated using its magnetic moment and its rotational friction coefficient. While for the former the geometric dimensions of the ferromagnetic Ni core are relevant, the latter depends on the outer dimensions of the whole particle. Due to various contributions like the NiO surface and PVP layer, these geometric dimensions are not equal even without an additional silica shell. Hence, to model the oscillating magnetic field-dependent optical transmission of a particle ensemble, a geometry of a core-shell particle is considered, Fig. 5.3. As a first approximation, any distribution in length and diameter of the ferromagnetic magnetic Ni core ( $l, d$ ) and the whole particle ( $L, D$ ) is neglected. The magnetic moment of the representative

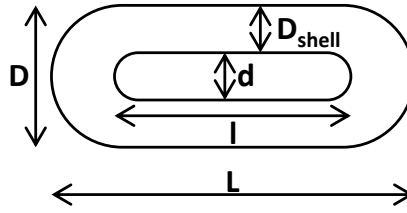


**Figure 5.3:** Definition of lengths and diameters for core-shell capped cylinders.

particle can be calculated by

$$m = V_{\text{mag}} M_s = \left( \frac{\pi}{4} d_{\text{mag}}^2 (l_{\text{mag}} - d_{\text{mag}}) + \frac{4\pi}{24} d_{\text{mag}}^3 \right) M_s, \quad (5.19)$$

where  $l$  and  $d$  are the length and diameter of the Ni core. The rotational friction coefficient  $\xi_r = \xi_r(L, D)$  can be determined by Eqs. (4.49) and (4.51) to obtain the char-

## 5.2 OF-MOT

---

acteristic frequency

$$\omega_c = (\tau_c)^{-1} = \left( \frac{\xi_r}{m\mu_0 H} \right)^{-1}. \quad (5.20)$$

Following Eq.(5.18), the real and the imaginary part of the magneto-optical response function can be determined.

Until now, the modeling of the DC- and the OF-MOT signal was described under the assumption of a monodisperse particle ensemble. In the next section, these models will be extended to consider polydispersity.

### 5.2.3 Modeling of the DC-MOT and the OF-MOT response respecting distributions in the geometric parameters of the particles

The particles used in this work underly a significant distribution in their core lengths and core diameters  $(l,d)$  as well as in their total lengths and total diameters  $(L,D)$ . Consequently, the magnetic moments, the rotational friction coefficients, and the characteristic frequencies of the particles are also distributed.

It is important to notice that larger particles have higher extinction cross sections and thus have a larger influence on the finally transmitted intensity. Since the extinction cross section is not proportional to the particle size, the transmitted intensity is not directly proportional to a moment of the size distribution. Furthermore, it enters  $I/I_0$  in an exponential function. The different optical weights of different particle fractions has to be respected in the following modeling. To consider this polydispersity, characteristic quantities corresponding to the magnetic, hydrodynamic, and optical properties of a large number of particles have to be calculated to model the signal of the entire ensemble.

The field-dependent optical transmission, which takes the polydispersity of the particles into account, can be modeled if a sufficiently large number  $N_c$  of tuples  $(l,d,L,D)$  of geometric parameters of particles (lengths and diameters) representative for the ensemble are known, e.g. from TEM image analysis. For each nanorod with index  $i$ , the magnetic moment  $m_i$  as well as the three principal extinction cross sections ( $C_{\text{ext,L},i}$ ,  $C_{\text{ext,T1},i}$ , and  $C_{\text{ext,T2},i}$ ) are calculated allowing to obtain  $C_{\text{ext},i,\perp,\parallel}(H)$  and  $C_{\text{ext},i,\times}$ . Eq. (5.10) can then be extended to

$$I(H)_{\perp,\parallel}/I_{\times} = \exp \left( -N_s \frac{1}{N_c} \sum_{i=0}^{N_c} (C_{\text{ext},i,\perp,\parallel}(H) - C_{\text{ext},i,\times}) \right). \quad (5.21)$$

To model the optical transmission in oscillating magnetic fields, the rotational friction coefficient of each particle  $\xi_{r,i} = \xi_{r,i}(L_i, D_i)$  has to be calculated, too. With that, the normalized characteristic time constant  $\tau_{c,i}$  can be calculated by Eq. (5.20).

Inserting these quantities into the equation of motion, Eqs. (5.14), the rotation dynamic of every rod depending on the applied frequency  $\omega$  can be described by

$$\theta_{i,\omega}(t) = \frac{\theta_0}{1 + \omega^2 \tau_i^2} (\cos(\omega t) + \omega \tau_{c,i} \sin(\omega t)). \quad (5.22)$$

The external field oscillates around a direction forming an angle of  $45^\circ$  with the electric field vector of the incident light (beneficial condition to increase the resolution of the measurement, section 3.2.2), Fig. 5.4. It is useful to define, the angle

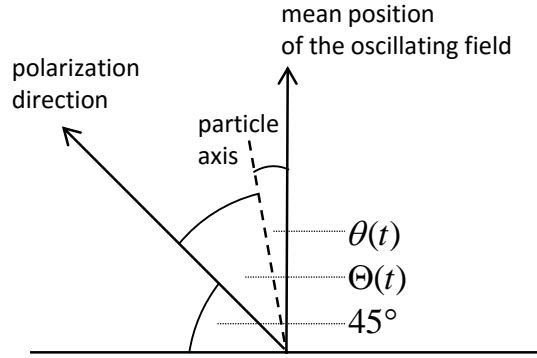


**Figure 5.4:** Illustration of the angles  $\theta(t)$  and  $\Theta(t)$  describing the particle orientation in an OF-MOT measurement.

$$\Theta_{i,\omega}(t) = 45^\circ - \theta_{i,\omega}(t). \quad (5.23)$$

To include the optical properties of each particle, its extinction cross section for arbitrary angles between the electric field vector of the incident light and the particle axis has to be determined:

$$C_{\text{ext},i}(\Theta_i(t)) = \cos^2 \Theta_i(t) C_{\text{ext},L,i} + \sin^2 \Theta_i(t) C_{\text{ext},T1,i}, \quad (5.24)$$

where  $C_{\text{ext},L,i}$  and  $C_{\text{ext},T1,i}$ , as defined in Fig. 5.5, have to be calculated by FEM for the particles. With these preparations, the transmittance as a function of time  $t$  at a given angular frequency  $\omega$  can be calculated using the Beer-Lambert law:

$$T'_\omega(t) = \exp \left( -N'_s s \sum_i (\cos^2(\Theta_{i,\omega}(t)) C_{\text{ext},L,i} + \sin^2(\Theta_{i,\omega}(t)) C_{\text{ext},T1,i}) \right), \quad (5.25)$$

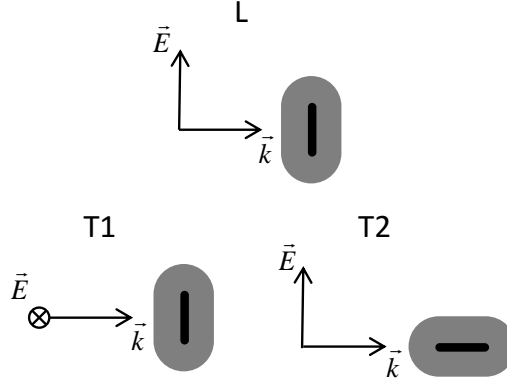


**Figure 5.5:** Basic orientations of the incident linearly polarized light with wave vector  $\vec{k}$  and electric field vector  $\vec{E}$  relative to the principle axes of the particle. For T1, the electric field vector  $\vec{E}$  is perpendicular to the projection plane.

where  $s$  is the optical path length. It is assumed that the particles constitute a representative ensemble which is transferred to real particle densities by multiplication with a factor  $N'_s$ . This factor can be omitted in the modeling of OF-MOT spectra as the dynamical response function is obtained after normalization.

The anisotropic absorption of light results in a small rotation of the polarization direction of the incident light (linear dichroism) while passing the cuvette. This rotation has been experimentally determined to be less than  $5^\circ$  for the highest concentrated sample in this work and was neglected in the modeling.

To remove the offset of the oscillating signal, the time average of the signal is subtracted

$$T_\omega(t) = T'_\omega(t) - \frac{1}{t_0} \int_t^{t+t_0} T'_\omega(t) dt, \quad (5.26)$$

where  $t_0 \gg 1/\omega$ . Using a regression analysis with

$$T_\omega(t) = A_\omega \cos(\omega t + \phi_\omega), \quad (5.27)$$

the amplitude  $A_\omega$  and phase  $\phi_\omega$  of the signal and thus real and imaginary part of the response function are obtained:

$$\begin{aligned} X'_\omega &= A_\omega \cos \phi_\omega, \\ X''_\omega &= A_\omega \sin \phi_\omega. \end{aligned} \quad (5.28)$$

All steps have to be repeated for different frequencies  $\omega$  of the applied magnetic field to obtain  $X'(\omega)$  and  $X''(\omega)$ . Eventually,  $X'(\omega)$  and  $X''(\omega)$  are normalized to the maximum

of  $X'(\omega)$ .

The described procedures allow the simulation of the magneto-optical transmission of the particles in static and oscillating fields including polydispersity, needing merely tabulated lengths and diameters of the particles. This allows us to compare the theoretically expected behavior with the experimentally obtained results.

# Chapter 6

## Results I - Analysis of DC-MOT measurements of colloidal suspensions of PVP coated Ni nanorod

*A modified version of the following sections (6.1-6.5) was already part of the publication [43], see appendix E.*

### 6.1 Structural characterization

Four samples of PVP coated Ni nanorods (pcn-1 – pcn-4) with different sizes were structurally characterized by TEM. The particles exhibit a capped cylindrical shape with slight structural inhomogeneities such as diameter fluctuations and occasionally irregular tip-ends, Fig. 6.1. The PVP layer cannot be explicitly identified.

Due to the invisibility of the PVP layer in TEM micrographs, the overall length  $L$  and diameter  $D$  of the Nanorods could not be measured. However, these parameters are only important for dynamic measurements and this section is limited to static measurements. Hence, it is sufficient to determine the geometric parameters of the Ni cores. The corresponding distributions of the particle core length  $l$  and core diameter  $d$  were obtained by analyzing several TEM images and approximated by log-normal density functions

$$f(x) = \left(\sqrt{2\pi}\sigma x\right)^{-1} \exp\left(-0.5(\ln x - \ln x_c)^2 \sigma^{-2}\right), \quad x > 0, \quad (6.1)$$

Fig. 6.2. The location parameter  $\ln(x_c)$  and scale parameter  $\sigma$  provide the expected value as the first moment of the distribution,  $E_x = x_c \exp(\sigma^2/2)$ . The results for the

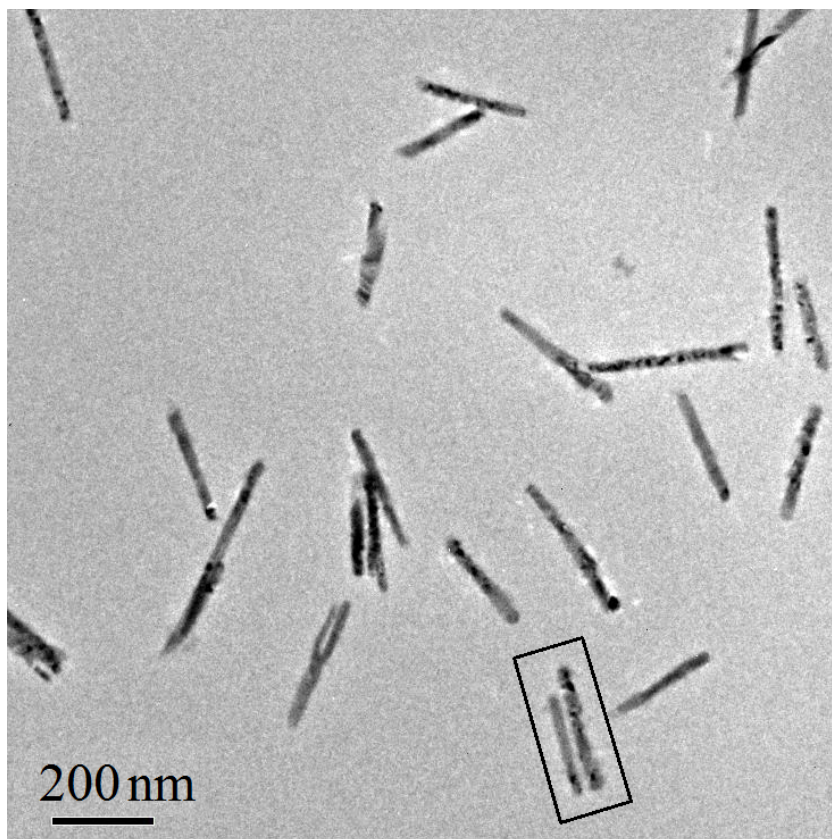


**Figure 6.1:** TEM image of nanorods (sample pcn-3) reveals structural inhomogeneities and the presence of small aggregates, such as dimers (marked). Several such images were analyzed to determine the distribution of length and diameter of the capped cylindrically shaped Ni nanorods for each colloid sample. Additional images can be found in appendix A.

four colloid samples are listed in Tab. 6.1.

Recalling the template based synthesis of the nanorods and assuming a constant volume of Ni deposited into the pores of the alumina layer, one could expect a correlation between the length and diameter of the resulting particles. The length and diameters of the particles were measured and tabulated in a way that allows to correlate every diameter to the length of the same particle. This offers the possibility to investigate a systematic correlation of length and diameter of the particles. A corresponding plot for sample scn-3, Fig. 6.3, does not show any trend and hence it is assumed that length and diameter of the nanorods are uncorrelated.

## 6.1 Structural characterization

---

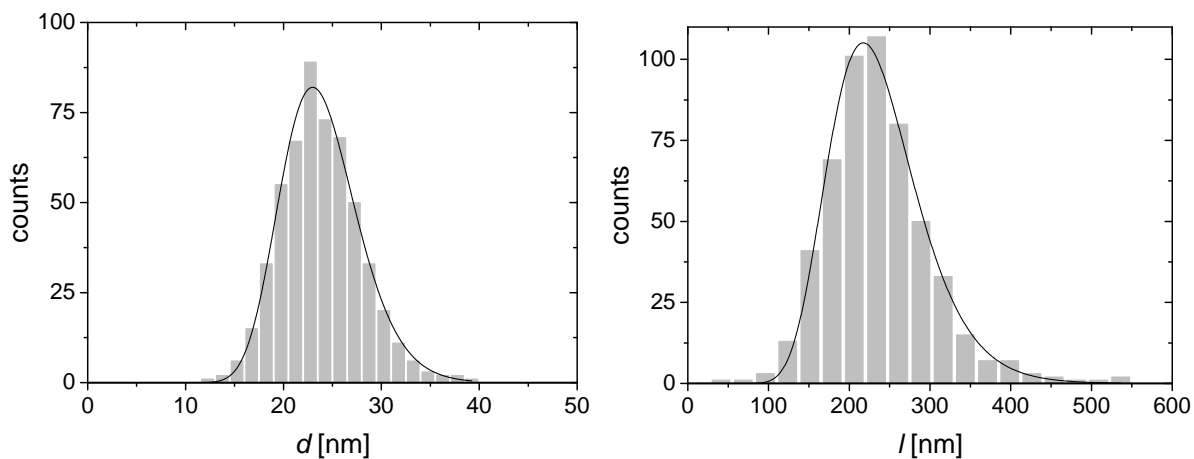


**Figure 6.2:** Distributions of length  $l$  and diameter  $d$  for the nanorods of sample pcn-3 obtained from TEM image analysis. The lines represent least-square fits using a log-normal density function, Eq. (6.1).

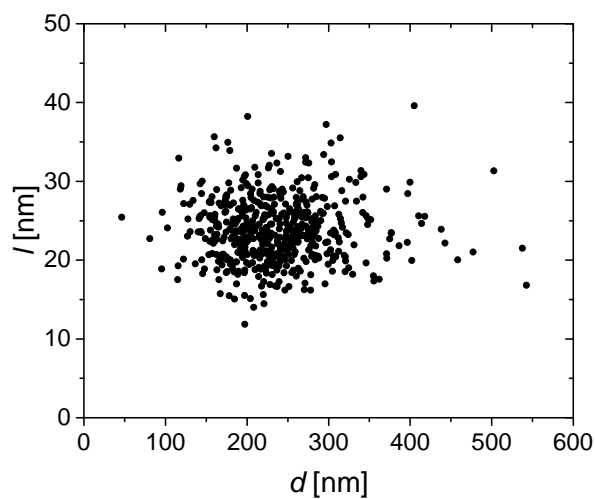


**Figure 6.3:** Plot of length  $l$  versus diameter  $d$  for the nanorods of sample pcn-3 obtained from TEM image analysis reveals absence of a correlation between the two parameters.

## 6 - Results I - Analysis of DC-MOT measurements of colloidal suspensions of PVP coated Ni nanorod

---

Sample	pcn-1	pcn-2	pcn-3	pcn-4
synthesis parameters				
$\#_p$	200	400	500	4000
$t_+$ [ms]	16	4	4	4
$t_-$ [ms]	4	16	16	16
$t_0$ [ms]	200	200	200	400
TEM analysis				
$N_c$	202	250	537	204
$l_c$ [nm]	56.9	181.3	230.7	913.1
$\sigma_l$	0.25	0.17	0.24	0.62
<b><math>E_l</math> [nm]</b>	<b>60.6</b>	<b>186.6</b>	<b>244.4</b>	<b>1106.6</b>
$N_c$	224	250	537	116
$d_c$ [nm]	22.6	24.1	23.6	23.4
$\sigma_d$	0.21	0.17	0.17	0.10
<b><math>E_d</math> [nm]</b>	<b>23.6</b>	<b>24.8</b>	<b>24.3</b>	<b>23.5</b>

**Table 6.1:** Synthesis parameters used for electrodeposition of Ni nanorods: number of current pulses  $\#_p$ , duration of positive current pulse  $t_+$ , negative current pulse  $t_-$  and break  $t_0$ . Parameters of the log-normal density function for the lengths and diameters of the nanorod samples: number of measured nanorods  $N_c$ , location parameters  $l_c$  and  $d_c$ , scale parameters  $\sigma_l$  and  $\sigma_d$ , and the resulting expected values  $E_l$  and  $E_d$ .

### 6.2 Static magnetic field-dependent optical transmission

The collinear magnetic and optical anisotropy of the nanorods is clearly revealed by the field-dependent optical transmission measurements, Fig.6.4. The transmitted intensities, normalized to the zero-field intensity  $I_\times$ , are plotted as a function of the magnetic field perpendicular ( $I(H)_\perp/I_\times$ , upper branch) and parallel ( $I(H)_\parallel/I_\times$ , lower branch) to the polarization direction of the incident light. Optical transmission decreases upon parallel alignment of the nanorods along the polarization direction due to the large longitudinal extinction cross section. Accordingly, the transmittance increases for the perpendicular configuration. Furthermore, since the diameters of the nanorods were sim-

## 6.2 Static magnetic field-dependent optical transmission

ilar, an increasing length implies increasing magnetic moments for the various samples which is reflected in the field-dependence of the alignment against thermal energy. The shorter rods have lower magnetic moments and hence require a higher field strength for magnetic alignment. By contrast, long rods saturate at field strengths as low as  $H \approx 20$  Oe. This signature of the field-dependent optical transmission has been used to extract characteristic quantities, i. e. the particle diameter and particle concentration, for a given nanorod colloid [20]. The underlying analysis, however, relies on a correct physical model for the optical extinction cross sections of the nanorods.

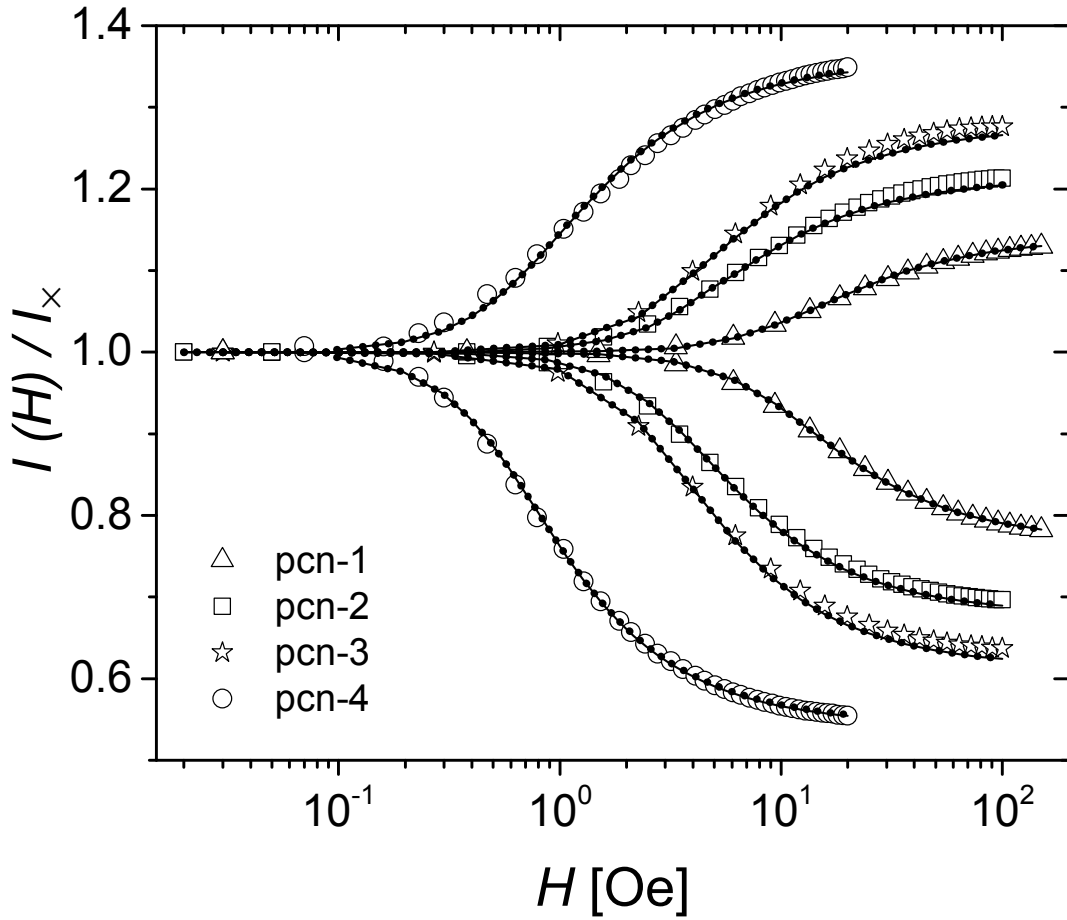


**Figure 6.4:** The transmitted intensity  $I$  of nanorod colloids as a function of the external magnetic field  $H$  parallel (lower branches) or perpendicular (upper branches) to the polarization direction, normalized to the intensity at zero field,  $I_x$ . The dots and the solid lines represent least-square fits using Eq. (5.10) based on extinction cross sections obtained by EA (lines) or FEM (full dots), respectively.

To establish a sound basis for further analysis, the results of the independently obtained least square fits on the transmission measurements for the EA and FEM models will be

compared.

### 6.3 Calculation of optical cross sections

As mentioned in the introduction, there are various methods to calculate optical cross sections. The following comparison includes the EA, SVM and FEM, and is started by focusing on spheroidal particles for two reasons. First, the cross section of spheroids can be obtained analytically in the electrostatic approximation that can be easily implemented in regression analysis of experimental results. Second, the SVM provides a physically exact solution for spheroids which can be used as a reference to evaluate the accuracy of EA and also of FEM calculations performed later in this work.

#### 6.3.1 Spheroids in the electrostatic approximation (EA)

In anticipation of a comparison of the present calculations for spheroids with those of capped cylinders in later sections, it is necessary to make a choice regarding an 'equivalent' size for the two geometries. The length  $l'$  and diameter  $d'$  for the spheroids were chosen to provide the same aspect ratio  $\Theta$  and volume  $V$  as capped cylinders of length  $l$  and diameter  $d$ . The two sets of parameters can be transformed using the relations  $d' = \sqrt[3]{0.5(3 - 1/\Theta)}d$  and  $l' = \sqrt[3]{0.5(3 - 1/\Theta)}l$ , Fig.6.5. Note that both  $l'$  and  $d'$  vary with  $\Theta$  for a given diameter of the cylindrical nanorod. According to Eqs.(4.133), (4.134), and (4.135), the cross sections in the EA are not affected by this transformation as they are completely determined by  $\Theta$  and  $V$ .

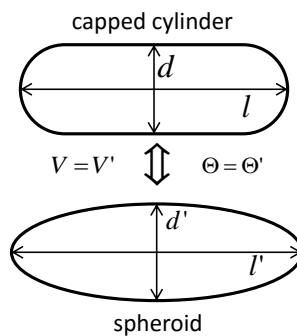


**Figure 6.5:** Transformation of a capped cylinder with aspect ratio  $\Theta = l/d$  and volume  $V = (\pi/4)(l-d)d^2 + (4\pi/3)(d/2)^3$  to a spheroid with  $\Theta' = l'/d' = \Theta$  and  $V' = \pi l' d'^2/6 = V$ . Note that these conditions imply  $l \neq l'$  and  $d \neq d'$ .

### 6.3 Calculation of optical cross sections

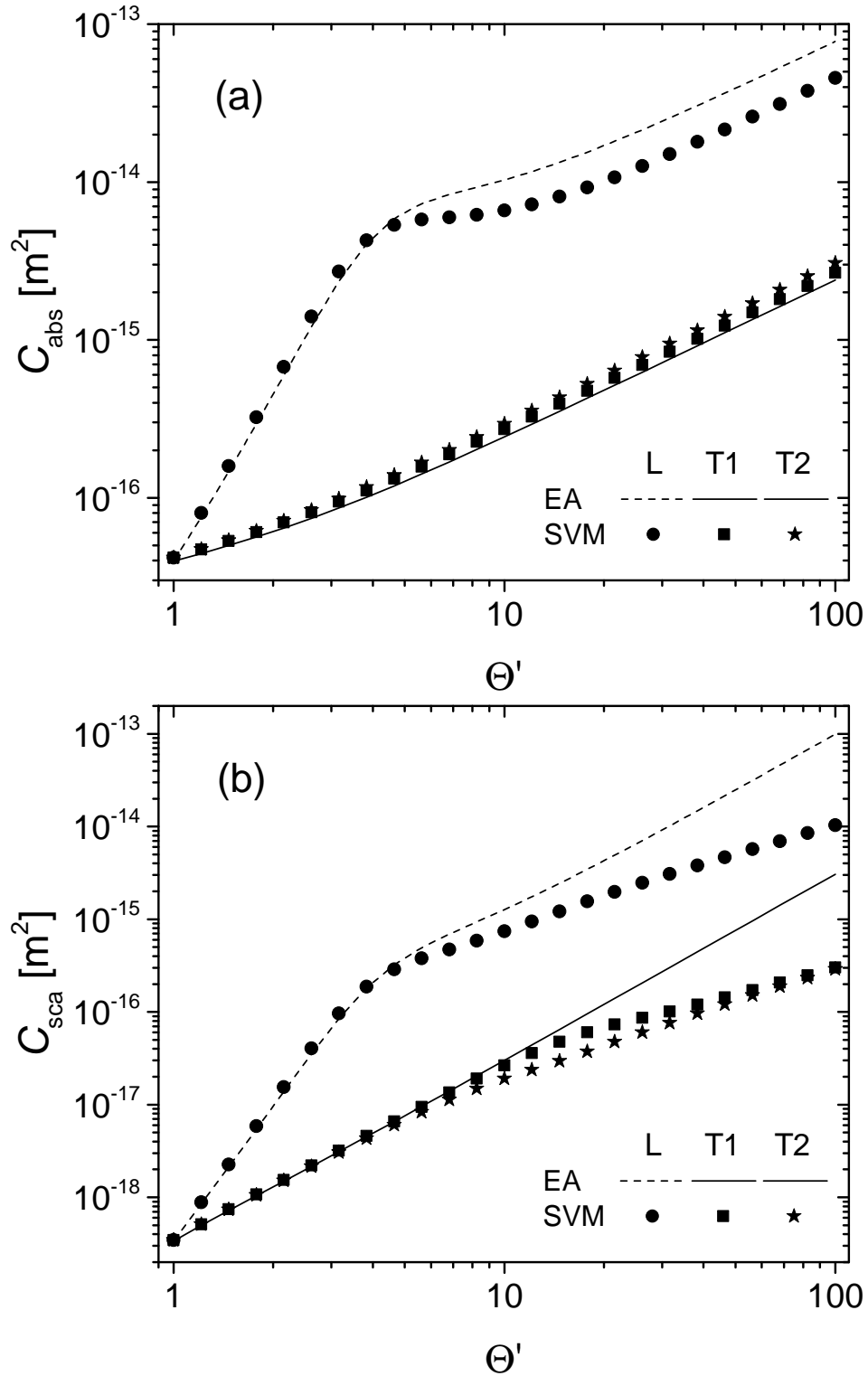


**Figure 6.6:** Absorption cross sections  $C_{\text{abs}}$  (a) and scattering cross sections  $C_{\text{sca}}$  (b) of prolate spheroids for the three basic polarization directions L, T1, and T2 as a function of the aspect ratio  $\Theta'$  obtained by EA and SVM. The values for spherical particles were approximated by  $\Theta' = 1.0001$ .

The absorption and scattering cross sections for prolate Ni spheroids in water as a function of their aspect ratio are shown in Fig.6.6. For longitudinal polarization (L), the absorption cross section increases rapidly by two orders of magnitude until  $\Theta \approx 5$  and then increases with a significantly smaller slope. The observed shoulder is related to the red-shift of the plasmon resonance with increasing aspect ratio. Despite significant damping, Ni exhibits a shallow resonance peak in the plasmon excitation at a wave length of  $\lambda_r \approx 450$  nm (2.76 eV) for spherical particles [101]. With increasing aspect ratio, the depolarization factor  $L_1$  decreases leading to a red-shift of this resonance. Correspondingly, the maximum of  $C_{\text{abs}} = \text{kIm}(\alpha)$  shifts and eventually passes the wave length  $\lambda = 632.8$  nm (1.96 eV) at  $\Theta \approx 5$ . This condition corresponds to the maximum energy dissipation by the particle close to resonance. Regarding the two transversal configurations, the EA provides identical depolarization factors,  $L_2 = L_3$ , Eq. (4.135), implying  $C_{\text{ext},T1} = C_{\text{ext},T2}$  in EA, increasing continuously with the aspect ratio.

The results for the scattering cross sections are shown in Fig.6.6 (b). At low aspect ratios,  $C_{\text{sca}}$  is about two orders of magnitude smaller than  $C_{\text{abs}}$  as expected for small particles [93]. The transversal scattering cross sections increase almost linearly whereas the longitudinal mode exhibits a shoulder at  $\Theta \approx 5$  as remnant of the plasmon resonance. In the following section, these results will be compared with the exact solution obtained by the SVM for prolate spheroids.

### 6.3.2 Spheroids by the separation of variables method (SVM)

The SVM solves the electromagnetic scattering problem for spheroids by expanding the incident, internal, and scattered fields in vector spheroidal wave functions [95]. Using Voshchinnikov's SVM code [34, 102] the absorption and scattering cross sections of prolate spheroids with aspect ratios  $\Theta' = 1..100$  were obtained for the different basic orientations, Fig.6.6. The comparison of the results by the EA and SVM reveals a good agreement with only small deviations  $< 5\%$  for aspect ratios  $\Theta' < 5$ , corresponding to the particle length  $l = 100$  nm. The shoulder in  $C_{\text{abs,L}}$  is more prominent and slightly shifted to lower aspect ratios so that the curve obtained by SVM crosses the corresponding one of the EA at  $\Theta' = 4$ . At larger aspect ratios, the EA overestimates  $C_{\text{abs,L}}$  by up to 70% and underestimates the transversal cross sections by  $\approx 22\%$  at  $\Theta' > 10$ .

The scattering cross sections obtained from the SVM also increase with the aspect ratio, yet with a smaller slope at  $\Theta' > 5$ , Fig.6.6 (b). Accordingly, the deviation between EA and SVM increases continuously reaching a factor of 10 at  $\Theta' = 100$ .

At first glance, the cross sections obtained by EA seem to be unusable for data analysis

### 6.3 Calculation of optical cross sections

because of their meager quantitative agreement with the exact solution for nanorods with  $\Theta' > 5$ , i.e.  $l > 100$  nm. Even the SVM, being limited to spheroids, may not be adequate for modeling cylindrical nanorods. Since there is no closed analytical solution for this geometry, FEM simulations are used to calculate  $C_{\text{abs}}$  and  $C_{\text{sca}}$  for capped cylindrical particles of finite length. But beforehand, the previous results of the exact solution obtained by the SVM are taken as reference to evaluate the accuracy of the FEM calculations of identical spheroids.

#### 6.3.3 Spheroids by the finite element method (FEM)

The results obtained from FEM calculations are very close to the exact solution and hence they are not shown in an separate figure. By contrast, in order to illustrate the accuracy of the FEM, the differences between the exact values of  $C_{\text{abs}}$  and  $C_{\text{sca}}$  obtained by the SVM and the values from FEM simulations for each polarization direction were computed as a function of  $\Theta'$ , Fig. 6.7. The deviations are less than 1% for the absorption cross sections and  $< 5\%$  for the scattering cross sections. Taking the different order of magnitude in the absolute values, i. e.  $C_{\text{sca}} \ll C_{\text{abs}}$ , into account so that  $C_{\text{ext}} = C_{\text{abs}} + C_{\text{sca}} \approx C_{\text{abs}}$ , the accuracy of this computation is sufficient for the purpose of this work and it is safe to proceed with the FEM calculation of the extinction cross sections of nanorods with the geometrical shape of a capped cylinder.

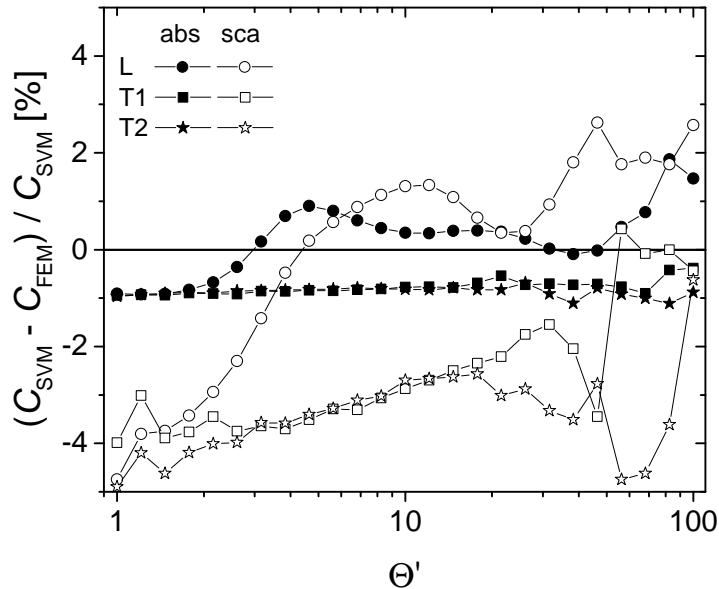


**Figure 6.7:** Relative deviations in  $C_{\text{abs}}$  and  $C_{\text{sca}}$  obtained by FEM as compared to the exact solution by SVM for spheroids as function of aspect ratio  $\Theta'$ .

### 6.3.4 Capped cylinders by FEM

The cross sections  $C_{\text{abs}}$  and  $C_{\text{sca}}$  of capped Ni cylinders with diameter  $d$  (15, 20, and 25 nm) as a function of their aspect ratio  $\Theta = 1..100$  obtained by FEM simulation are shown in Fig.6.8. For all orientations  $C_{\text{abs}}$  and  $C_{\text{sca}}$  increase with increasing  $\Theta$ . The qualitative shape of the curves is very similar to the results for prolate spheroids, Fig.6.6. To point out the influence of the particle shape,  $C_{\text{abs}}$  and  $C_{\text{sca}}$  for both geometries, capped cylinders ( $d = 20$  nm,  $\Theta = 1..100$ ) and equivalent spheroids ( $d', l'$ ), were calculated using the FEM. The differences are moderate, 10% for  $C_{\text{abs}}$  and 20% for  $C_{\text{sca}}$ , Fig.6.9, and smaller than those between the electrostatic approximation and the SVM for spheroids. The maximum deviation occurs at aspect ratios  $4 < \Theta < 10$ . Hence, it is expected that the errors in the data analysis caused by approximating the geometry of the nanorods as spheroids to be less severe than the errors associated with the EA for large nanorods ( $l > 200$  nm) whereas the shape effect dominates for shorter nanorods. The consequences of applying the two approximations on the quantitative analysis of DC-MOT measurements will be addressed in the following section.

## 6.4 Analysis of DC-MOT measurements

Prior to the comparison of the different models, a general aspect of the data analysis needs to be discussed. As shown in the previous sections, the optical properties of a colloidal aqueous suspension of Ni nanorods are determined by several variables, i.e. the length and diameter of the nanoparticles and their number density. The relationship between these parameters and the field dependent transmittance is complex. For instance, the explicit field-dependence and the approach towards saturation of optical transmission depends on the particle's magnetic moment, which is related to its volume  $V \sim ld^2$  whereas the splitting between the parallel and perpendicular branches is determined by the aspect ratio  $\Theta = l/d$ , the volume, and the particle concentration. Furthermore, given three independent variables ( $l$ ,  $d$ , and  $N$ ) the relationship is overdetermined so that there is no unique solution to the inverse problem. Therefore, the analysis of DC-MOT measurements requires an assumption on one of the given colloid variables. The first moment of the length distribution function  $E_l$  was taken as fixed value because it can be determined from TEM images with suitable accuracy.

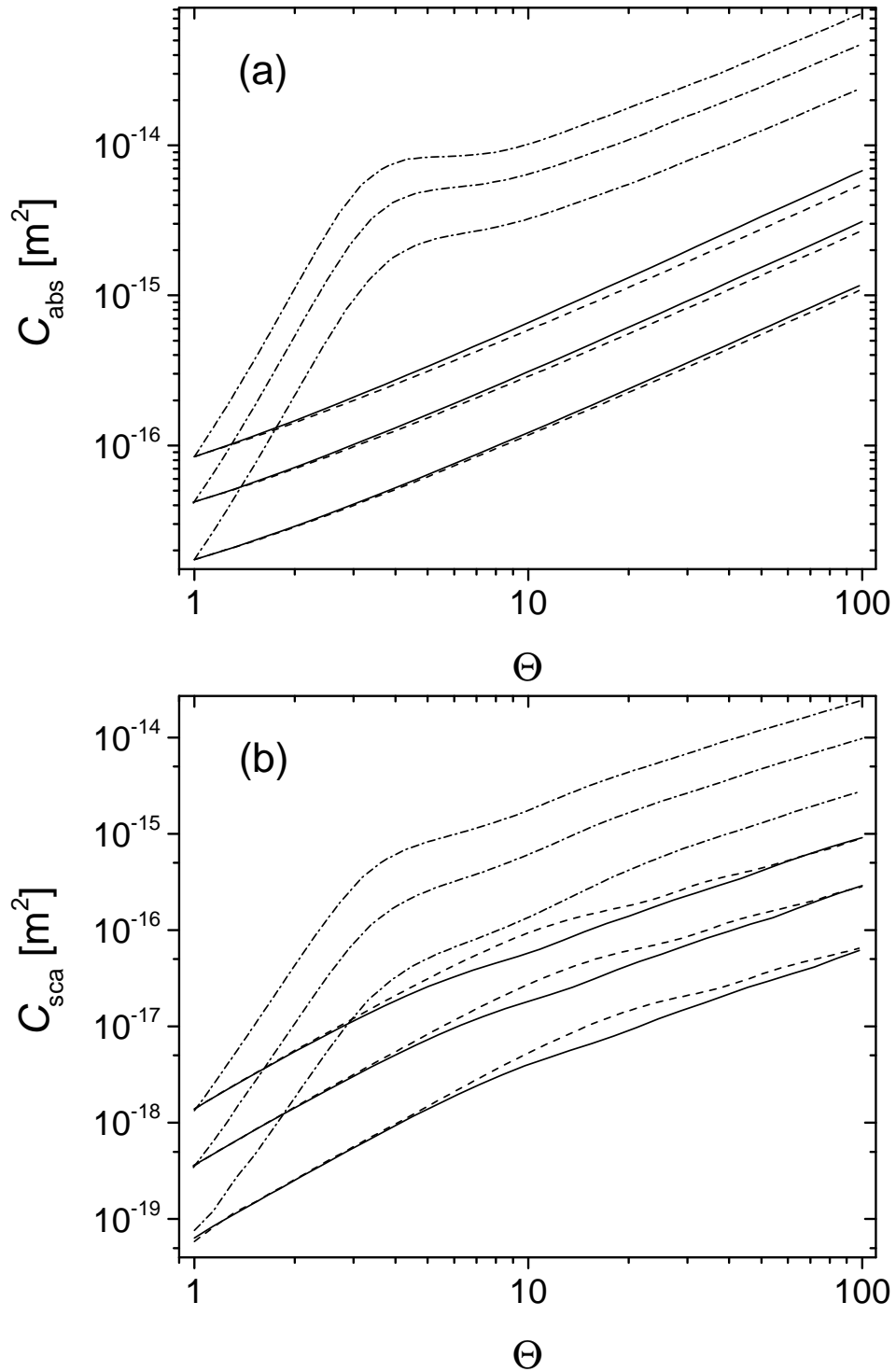


**Figure 6.8:** Absorption cross sections  $C_{\text{abs}}$  (a) and scattering cross sections  $C_{\text{sca}}$  (b) of capped cylinders for longitudinal L (dash-dot), transversal T1 (dashed), and T2 (solid) polarization as a function of their aspect ratio  $\Theta$  for three different diameters  $d = 15$  nm (top curve in each orientation),  $d = 20$  nm (middle), and  $d = 25$  nm (top).

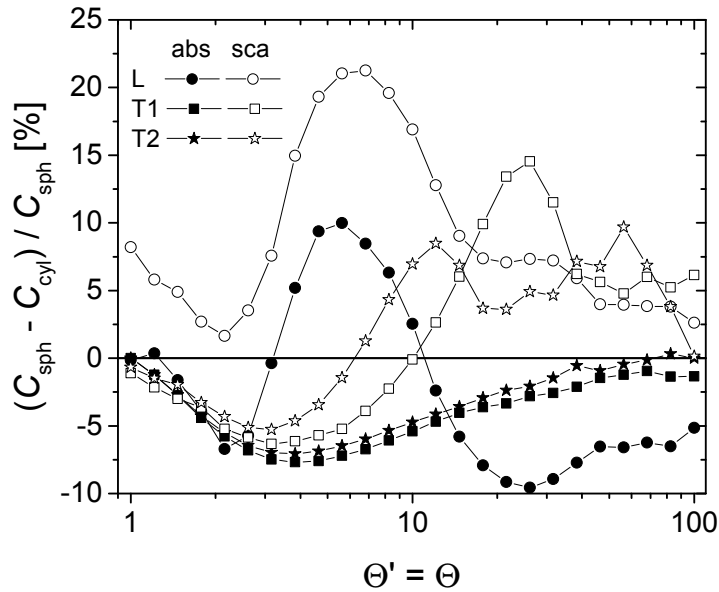


**Figure 6.9:** Normalized differences in the absorption cross sections  $C_{\text{abs}}$  and scattering cross sections  $C_{\text{sca}}$  between capped cylinders ( $d = 20$  nm,  $l = 50..2000$  nm) and the corresponding prolate spheroids with equal volume and aspect ratio.

### 6.4.1 Model A: capped cylinders by FEM

For analysis of DC-MOT measurements, a routine based on Eq. (5.10) describing the field-dependent transmittance, section 5.1,

$$I_{\perp,\parallel}(H)/I_{\times} = \exp(-Ns (\langle C_{\text{ext}} \rangle_{\perp,\parallel}(H) - C_{\text{ext},\times})) \quad (6.2)$$

that fits both branches simultaneously, was implemented. A direct regression analysis would require a FEM recalculation of  $C_{\text{ext}}$  for nanorods during the adjustment of the diameter, which is rather inefficient. Therefore, a data base of extinction cross sections was calculated for discrete combinations of  $d = 10..50$  nm (13 values) and  $l = 50..2000$  nm (25 values, logarithmic sweep) by FEM and intermediate values during regression analysis were computed by cubic spline interpolation. Using the expected length  $E_l$  for each sample as fixed parameter, the regression analysis provided reasonable agreement with the experimental results, Fig.6.4. The obtained values for the particle concentration  $N$  and the diameter  $d_{\text{OT}}$  are summarized in Tab.6.2. For each colloid, the diameter  $d_{\text{OT}}$  obtained from the regression calculation is smaller than the value  $E_d$  from TEM image analysis reflecting a slightly smaller magnetic moment per particle than expected from the geometric size. This deviation has been reported before and can be explained by a thin surface oxide layer [20, 103] with a thickness between 0.6 nm and 2.4 nm for the

## 6.4 Analysis of DC-MOT measurements

---

given samples. The contribution of this surface oxide layer to the extinction cross section was not explicitly considered in the present work. Since an additional encapsulation with silica will not remove the NiO surface layer, a reduced diameter of the Ni core is also expected for silica coated Ni nanorods which will be investigated later.

Sample	pcn-1	pcn-2	pcn-3	pcn-4
TEM analysis				
$E_l$ [nm]	60.6	186.6	244.4	1106.6
$E_d$ [nm]	23.6	24.8	24.3	23.5
DC-MOT analyzed using FEM				
$d_{OT}$ [nm]	22.4	20.4	19.4	19.8
$N$ [ $10^{15}/\text{m}^3$ ]	16.5	8.8	9.8	3.0
DC-MOT analyzed using EA				
$d_{OT}$ [nm]	22.4	20.4	19.4	19.8
$N$ [ $10^{15}/\text{m}^3$ ]	20.9	5.1	6.0	1.3
$z$	1.263	0.583	0.614	0.437
$z'$	1.262	0.582	0.613	0.435
$z'_{\parallel}$	1.262	0.573	0.601	0.429
$z'_{\perp}$	1.262	0.593	0.618	0.445

**Table 6.2:** Characteristic quantities of four different nanorod colloids: expected values for the length  $E_l$  and diameter  $E_d$  obtained from TEM image analysis (repeated from Tab. 6.1) and results of the regression analysis of DC-MOT measurements for the nanorod diameter  $d_{OT}$  and particle concentrations  $N$  based on the extinction cross sections for capped cylinders (Model A: FEM) or equivalent spheroids (Model B: EA). Furthermore, ratio of particle densities  $z$  (Eq. (6.3)), and ratios of extinction cross sections  $z'$  as defined in Eqs. (6.4) and (6.5) are shown.

### 6.4.2 Model B: spheroids by EA

As the extinction cross section calculated for spheroids in the EA deviate noticeably from those of FEM simulations of capped cylinders, one may expect distinct differences in the

## 6 - Results I - Analysis of DC-MOT measurements of colloidal suspensions of PVP coated Ni nanorod

---

numerical results retrieved from the analysis of DC-MOT measurements. To investigate this conjecture, the same data were analyzed based on cross sections for equivalent spheroids in the EA. Surprisingly, the model curves describe the experimental data equally well, Fig. 6.4. The differences between Model A and Model B are indiscernible at the scales of that figure. Furthermore, the diameters  $d_{OT}$  were identical for both models whereas the particle concentrations  $N$  were significantly different, Tab. 6.2. This behavior is caused by an asymmetry in the correlation of the two fit parameters on the calculated field-dependent optical transmission. The characteristic field dependence, i.e. curvature and saturation behavior, of the transmission is entirely determined by the magnetic moment per particle via Eq. (5.5). Hence, a fixed length  $E_l$  for the nanorods implies a distinct value for the diameter  $d_{OT}$  consistent with this magnetic moment. Of course, the extinction cross sections, calculated for capped cylinders of size  $(E_l, d_{OT})$  by FEM and those for equivalent spheroids of size  $(l', d')$  with equal volume (i.e. equal magnetic moment) and aspect ratio, obtained in the EA, are different as shown in the previous sections. Consequently, the splitting in the optical transmission between parallel and perpendicular configuration of the nanoparticles are not identical for the two models. The difference, however, is fully compensated by the second fit parameter, i.e. the particle concentration  $N$ . This is a distinct feature of the particular analysis modality and is plausible from the following argument.

Comparing the particle densities obtained from simultaneous regression analysis of both branches for the two models reveals factors

$$z = \frac{N_{EA}}{N_{FEM}} \quad (6.3)$$

between 0.437 and 1.263, Tab. 6.2. Identical splitting between the two branches of the transmission at saturation (i.e.  $\langle \cos^2 \beta \rangle = 1$ ) is expected when this ratio is equal to – and hence compensates – the ratio

$$z' = \frac{(C_{\text{ext, T1}} - C_{\text{ext, L}})_{FEM}}{(C_{\text{ext, T1}} - C_{\text{ext, L}})_{EA}} \quad (6.4)$$

of the difference in the principal extinction cross section, calculated by FEM and EA, which is readily verified, Tab. 6.2. Furthermore, the virtually identical model curves in Fig. 6.4 imply the same ratios for each branch of the transmission measurements with respect to the zero-field transmission,

$$z'_{\parallel(\perp)} = \frac{(C_{\text{ext, L(T1)}} - C_{\text{ext, } \times})_{FEM}}{(C_{\text{ext, L(T1)}} - C_{\text{ext, } \times})_{EA}}. \quad (6.5)$$

## 6.4 Analysis of DC-MOT measurements

---

Using Eqs. (5.9) and (6.5), recalling  $C_{T1} = C_{T2}$  for the EA, and writing  $C_{L,FEM} = C_L$ ,  $C_{T1,FEM} = C_T$ , and  $C_{T2,FEM} = C_T + \Delta C_T$  for the FEM cross sections, it can be shown that

$$\frac{z'_{\perp}}{z'_{\parallel}} = \frac{C_T - C_L - \Delta C_T}{C_T - C_L + \Delta C_T/2} \approx 1 - \frac{\Delta C_T}{C_T - C_L} \quad (6.6)$$

which is close to unity since the last term on the right hand side is typically of the order of  $10^{-2}$ . This explains why both models provide nearly the same model curve to the measured field-dependent optical transmission (Fig. 6.4) even for simultaneous fitting of both branches. Relevant differences are only expected when  $\Delta C_T$  becomes significant at very large rod sizes.

From these results two important conclusions may be drawn. First, using the expected value for the rod length  $E_l$  obtained from TEM image analysis as fixed parameter in the fitting procedure, the diameter  $d_{OT}$  of the nanorods determined from DC-MOT measurements using analytically derived cross sections for spheroids in the EA is identical to that obtained from the more elaborate FEM model. Second, the concentrations of the nanorods in dispersion obtained from the EA model analysis differ from the reference values of the FEM analysis by well-determined factors. These ratios of optical cross sections for the two models were calculated, Tab. 6.3, and can be employed as correction factors in the analysis of DC-MOT measurements based on the analytic cross sections of equivalent spheroids in the EA.

The performed analysis relies on the Beer-Lambert law which is applicable to dilute suspensions with negligible electromagnetic interactions between the dispersed particles. In order to review the usage of the Beer-Lambert law for colloidal dispersions of finite concentrations, the optical interaction of two particles is investigated in the next section.

**6 - Results I - Analysis of DC-MOT measurements of colloidal suspensions  
of PVP coated Ni nanorod**

---

$\Theta$	$d = 15 \text{ nm}$		$\Theta$	$d = 20 \text{ nm}$		$\Theta$	$d = 25 \text{ nm}$	
	$\parallel$	$\perp$		$\parallel$	$\perp$		$\parallel$	$\perp$
1.13684	1.00484	1.01332	1.15948	1.03605	1.04527	1.0817	1.0492	1.06232
1.32572	1.04247	1.04762	1.25	1.05369	1.06318	1.26142	1.08901	1.10294
1.54598	1.07617	1.08081	1.35213	1.07737	1.08647	1.471	1.14407	1.15643
1.66667	1.09427	1.09816	1.57678	1.12323	1.13074	1.7154	1.20629	1.21629
1.80284	1.1146	1.11834	1.83875	1.16973	1.17576	2	1.26644	1.27432
2.10237	1.1463	1.14909	2.14425	1.21563	1.22029	2.33229	1.30921	1.3152
2.45167	1.16173	1.1638	2.5	1.22935	1.23291	2.71979	1.29651	1.30089
2.859	1.14644	1.14804	2.91536	1.19535	1.198	3.17167	1.17503	1.1783
3.33333	1.08086	1.0821	3.39973	1.09795	1.1	3.69862	0.96802	0.97058
3.88715	0.98801	0.98906	3.96458	0.9474	0.94909	4.31313	0.77011	0.77228
4.53298	0.88472	0.88569	4.62328	0.80902	0.81056	5.02973	0.62978	0.63179
5.28611	0.80863	0.80959	5.39141	0.70714	0.70866	5.8654	0.54546	0.54742
6.16437	0.76005	0.76108	6.28717	0.64855	0.65008	6.8399	0.49936	0.50131
7.18855	0.73411	0.73519	7.33175	0.6135	0.6151	7.97632	0.47059	0.47255
8.38289	0.72378	0.72494	8.54988	0.59627	0.5979	9.30154	0.46119	0.46324
9.77566	0.72423	0.72543	9.9704	0.59115	0.59279	10.84695	0.46	0.46228
11.39984	0.73171	0.73289	11.62693	0.59356	0.59525	12.64911	0.46051	0.46331
13.29386	0.74164	0.74286	13.55868	0.59456	0.59644	14.7507	0.45684	0.46031
15.50257	0.74566	0.74688	15.81139	0.5931	0.59529	17.20145	0.44516	0.44925
18.07824	0.74223	0.74358	18.43837	0.58461	0.58726	20.05938	0.43044	0.43493
21.08185	0.73466	0.73615	21.50181	0.56761	0.57064	23.39214	0.4109	0.41571
24.58449	0.72753	0.72934	25.07422	0.55804	0.56149	27.27863	0.38625	0.39112
28.66908	0.71992	0.72206	29.24018	0.53754	0.54121	31.81083	0.36069	0.36551
33.4323	0.70254	0.70487	34.09828	0.51143	0.51509	37.09603	0.33455	0.3394
38.9869	0.68375	0.68614	39.76354	0.48566	0.48931	43.25935	0.31139	0.31633
45.46438	0.6629	0.66548	46.37004	0.45893	0.4628	50.44667	0.28618	0.29116
53.01805	0.639	0.64149	54.07419	0.43202	0.43563	58.82812	0.26099	0.26579
61.82672	0.61211	0.61448	63.05834	0.4033	0.40711	68.60211	0.23604	0.24061
72.09892	0.59015	0.59276	73.53515	0.37403	0.3779	80	0.21285	0.21721
84.07778	0.56166	0.56442	85.75264	0.3451	0.34869	93.312	0.19149	0.19551
98.04687	0.53181	0.53436	100	0.31538	0.31891	100	0.18219	0.18602

**Table 6.3:** Calculated values of  $z'$  for  $\parallel$  and  $\perp$  orientation as function of aspect ratio  $\Theta$  for three different diameters  $d$ .

## 6.5 Optical interaction of two particles

Making use of the flexibility of FEM simulations regarding the geometry of the considered object, the optical cross sections of nanorod pairs will be determined. In particular, the focus lies on the absorption and scattering efficiencies of two nanorods with parallel end-to-end (Fig.6.10) and side-by-side (Fig.6.11) configuration in the major orientations with respect to the field- and propagation vectors of the incident light.

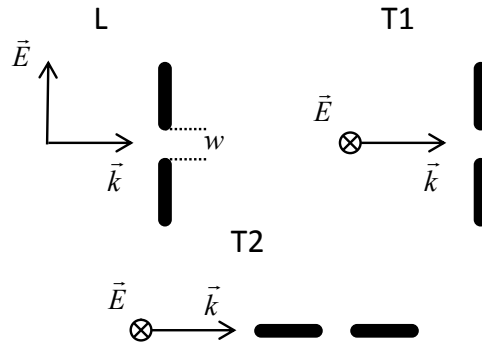


**Figure 6.10:** Geometries simulated for two nanorods in end-to-end configuration separated by a distance  $w$ . The  $\otimes$ -symbol indicates a vector perpendicular to the projection plane.

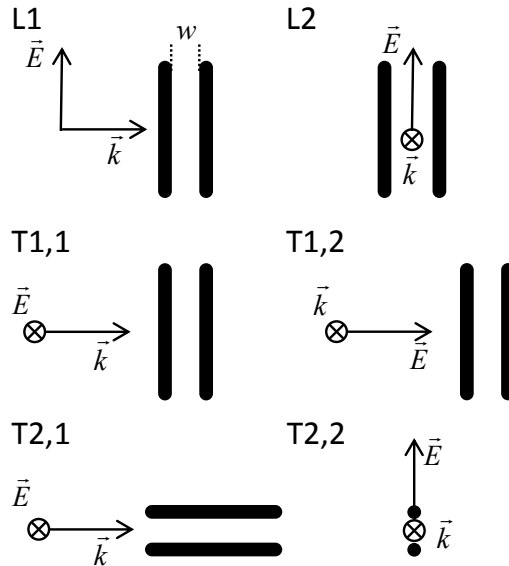


**Figure 6.11:** Geometries simulated for two nanorods in side-by-side configuration separated by a distance  $w$ . The  $\otimes$ -symbol indicates a vector perpendicular to the projection plane.

## 6 - Results I - Analysis of DC-MOT measurements of colloidal suspensions of PVP coated Ni nanorod

---

The end-to-end configuration is of interest because it represents the building unit of a nanorod chain which may form in a homogeneous external field at high particle concentrations [104]. The absorption cross sections for two capped cylinders of diameter  $d = 20$  nm and length  $l = 200$  nm in end-to-end configuration as a function of the distance  $w$  between the particles are shown in Fig.6.12 and compared with the corresponding value of two individual nanorods (horizontal lines) in order to highlight the influence of the near-field electromagnetic interaction.

The absorption cross sections converge to those of individual rods at large distances  $w > 100$  nm. For all geometries the absorption decreases upon reduction of interparticle distance whereas the scattering cross sections increases. The observed changes at the shortest separation are quantitatively consistent with the differences between single nanorods of length  $l = 200$  nm and of doubled length  $l = 400$  nm. Computing the combined extinction cross sections, the deviations partially compensate, yielding  $\Delta C_{\text{ext}} = -6.3\%$  for longitudinal,  $-2.8\%$  for the T1, and  $-0.6\%$  for the T2 transversal orientations, respectively.

The changes in the absorption and scattering cross sections of two nanorods in side-by-side configurations caused by decreasing interparticle distance are shown in Fig.6.13. Similar to the end-to-end configuration, electromagnetic interaction was found to be negligible for particle spacings  $w > 100$  nm. Assuming this distance as a characteristic threshold value for arbitrary orientation of the two particles, a particle concentration  $N \approx (L + 100 \text{ nm})^{-3} = 4 \cdot 10^{19} \text{ m}^{-3}$ , below which near-field electromagnetic interaction is negligible, can be estimated. By comparison with the highest concentration of  $\sim 10^{16} \text{ m}^{-3}$  used in experiments, it can be concluded that this condition is clearly fulfilled in the DC-MOT measurements of the present study.

The two dominating contributions to  $C_{\text{abs}}$  ( $L_1$  and  $L_2$ ) both decrease by 15% whereas positive and negative deviations were found for the other orientations. Large relative changes were obtained for the T<sub>1,2</sub> and T<sub>2,2</sub> configuration where the electric field vector  $\vec{E}$  is parallel to the interparticle axis. The scattering cross sections increase significantly by  $\sim 60\%$  for longitudinal polarization. This large increase complies with a blue-shift of the plasmon resonance reported for pairs of gold nanorods in side-by-side configuration [105, 106]. For Ni nanorods with aspect ratio  $\Theta > 5$  such a blue-shift of the shoulder is expected to result in an increasing intensity.

Depending on the geometry of the measurement, various contributions combine to the total extinction cross section. One particular example is given by the average of all six configurations  $\tilde{C}_{\text{ext}, \times}$  which resembles the extinction cross section of an isotropic disper-

## 6.5 Optical interaction of two particles

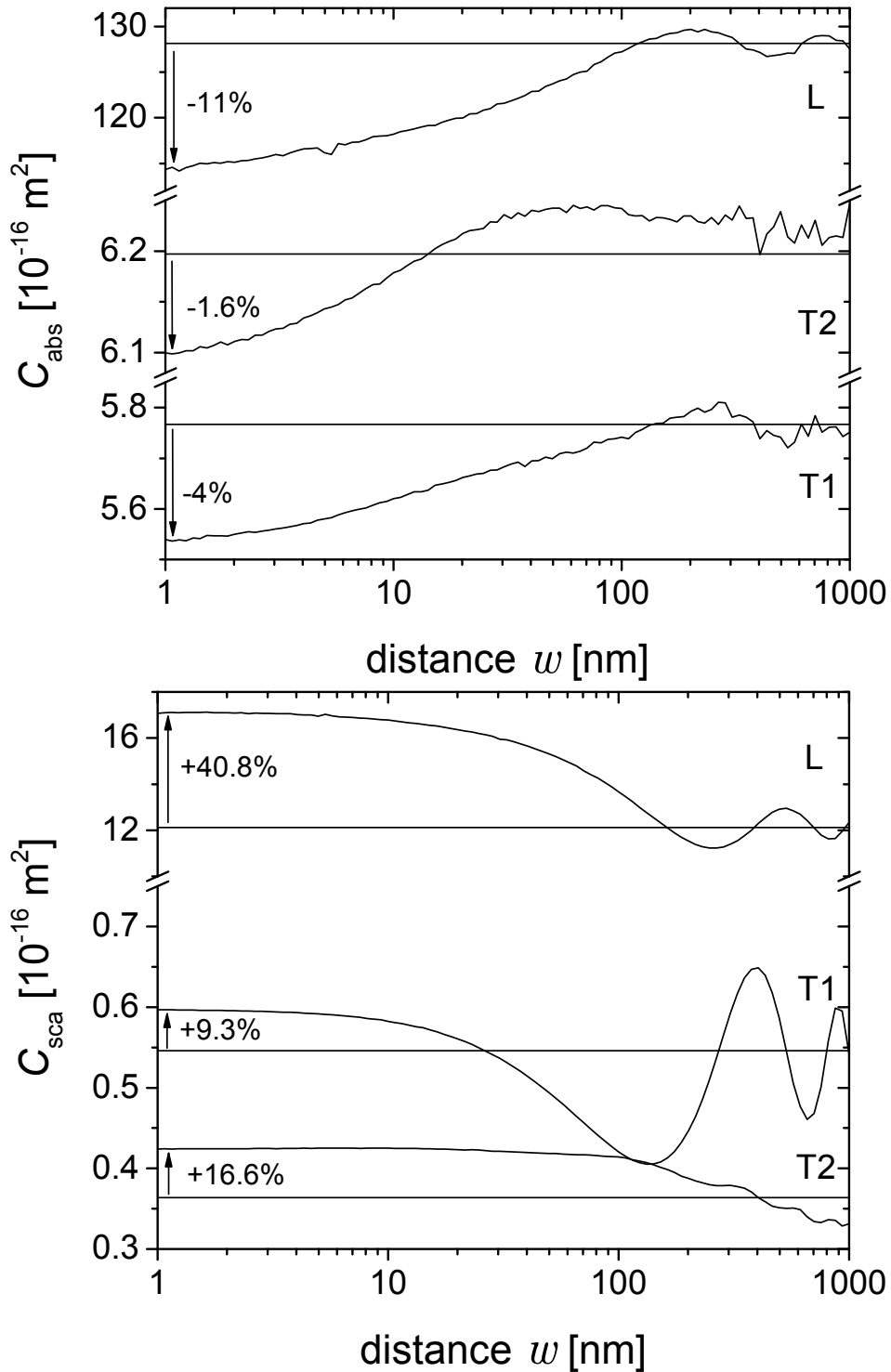


**Figure 6.12:** Absorption and scattering cross sections for two capped cylinders ( $l = 200$  nm,  $d = 20$  nm) in end-to-end configuration as a function of their distance  $w$  for different polarization directions as defined in Fig. 6.10. The horizontal lines represent the corresponding values for two individual particles.

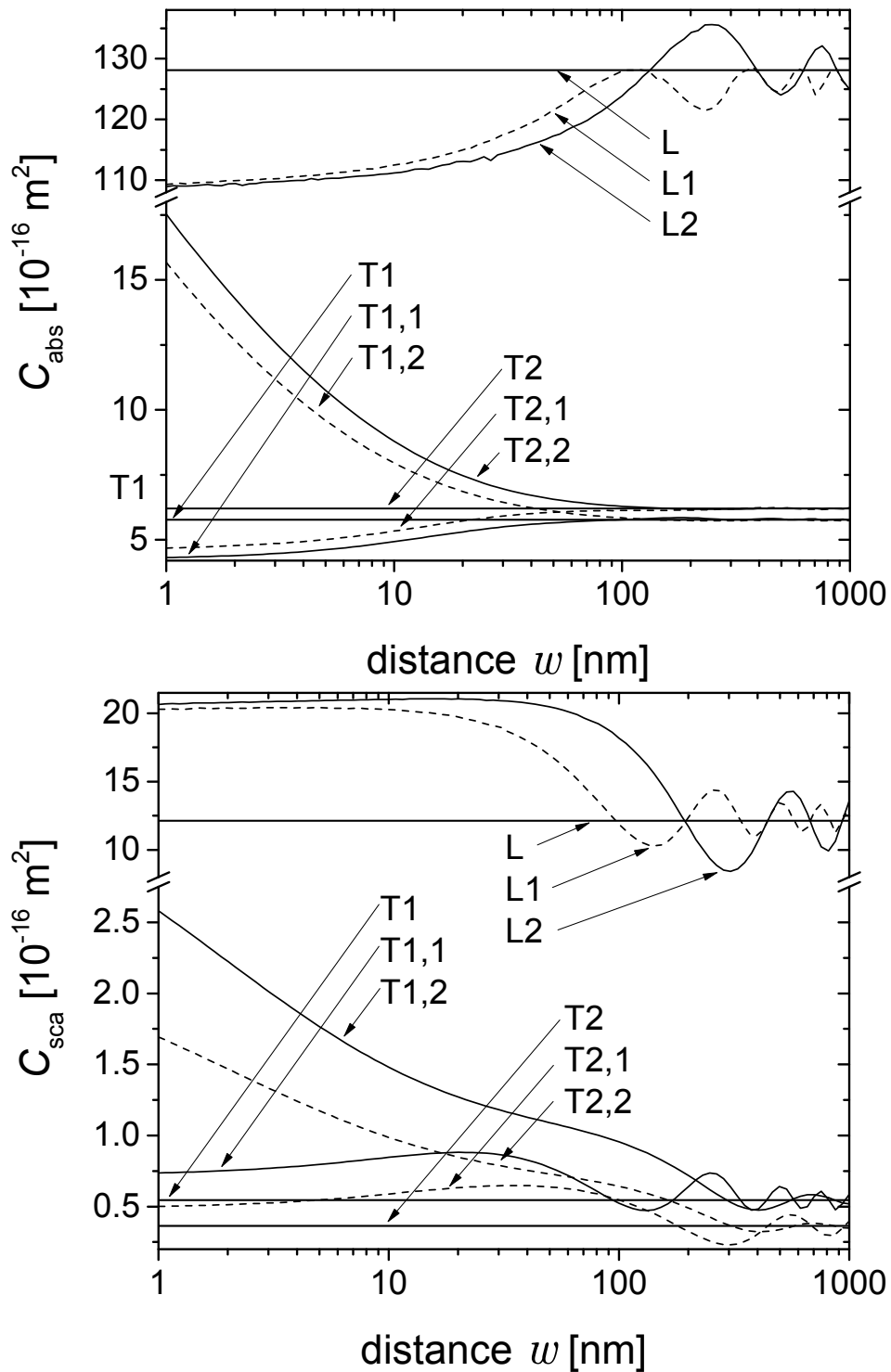


**Figure 6.13:** Absorption and scattering cross sections for capped cylinders ( $l = 200 \text{ nm}$ ,  $d = 20 \text{ nm}$ ) in side-by-side configuration as a function of their distance  $w$  for different polarization directions and orientations as defined in Fig.6.11. The horizontal lines represent the corresponding values for two individual particles.

## 6.5 Optical interaction of two particles

---

sion of side-by-side nanorod dimers, Fig. 6.14. This superposition reveals a maximum deviation of only  $\sim -4\%$  in a range of interparticle distance of  $w \sim 5 - 20$  nm for two nanorods with  $d = 20$  nm and  $l = 200$  nm.

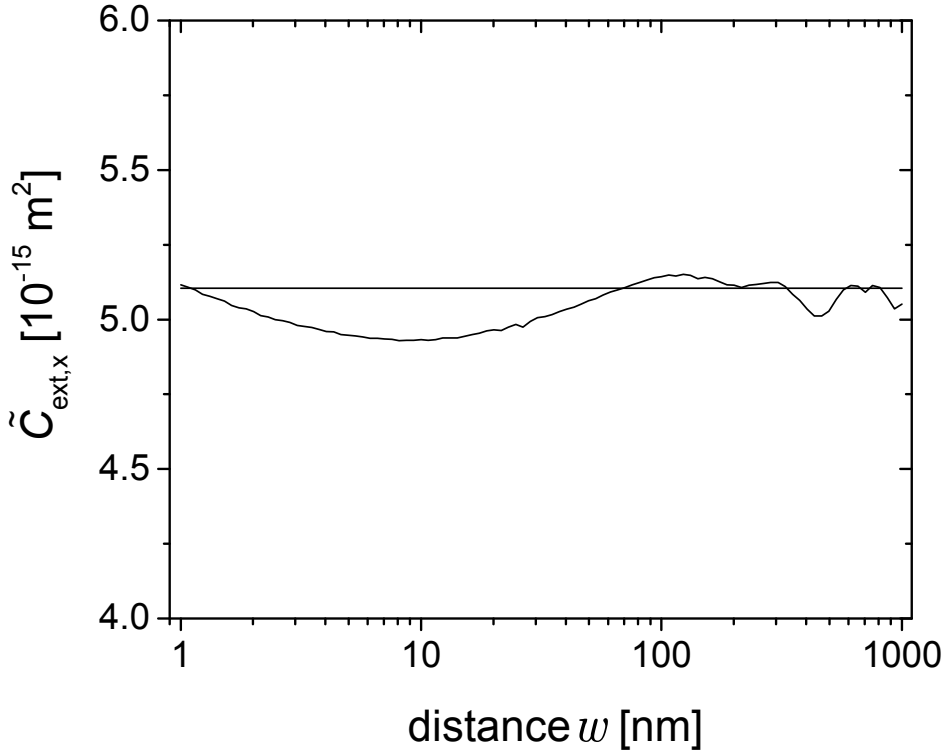


**Figure 6.14:** Average extinction cross section  $\tilde{C}_{\text{ext},x}$  for two agglomerated particles ( $l = 200$  nm,  $d = 20$  nm) in side-by-side configuration as a function of their distance  $w$  compared to the corresponding value  $2 \cdot C_{\text{ext},x}$  for two individual nanorods (horizontal line).

The side-by-side configuration with anti-parallel orientation of their magnetic moments represents the minimum energy state of two uniaxial ferromagnetic nanorods and is frequently observed in TEM images, Fig. 6.1. As their magnetic moments cancel each other out, such dimers exhibit purely statistically determined rotational diffusion at the low external magnetic fields applied during DC-MOT measurements and generate a constant extinction background. In a recent study, the contribution of these dimers to optical extinction was investigated by controlled destabilization of the colloidal nanorod suspension [103]. By increasing the ionic strength of the colloid, the magnetic field-dependent optical response due to individual nanorods was found to decrease with time while a continuous increase of the field-independent background was observed. The

## 6 - Results I - Analysis of DC-MOT measurements of colloidal suspensions of PVP coated Ni nanorod

---

analysis suggested an optical extinction for each nanorod in a dimer configuration equivalent to  $(0.8 \pm 0.2) \cdot C_{\text{ext},\times}$  in accordance with the results of the FEM simulations  $\tilde{C}_{\text{ext},\times} \approx 0.96C_{\text{ext},\times}$ .

At this point, the treatment of the DC-MOT of colloidal suspensions of PVP coated Ni nanorods is completed. In the next chapter the properties of silica coated nanorods using DC-MOT and additionally OF-MOT measurements will be investigated.

# Chapter 7

## Results II - Quantitative modeling of DC- and OF-MOT signals of silica coated Ni nanorods colloids

PVP coated Ni nanorods exhibit significant deviations between theoretically expected and measured rotational diffusion coefficients [24] which is mainly attributed to the ill-defined boundary between the particle and the liquid matrix and the concomitant unknown thickness of the organic PVP layer. This uncertainty limits their suitability as model particles for investigation on particle-matrix interaction significantly. To obtain a well-defined particle-matrix-interface, the PVP rods were encapsulated with an additional inorganic silica shell as described in section 2.3. In the following, colloidal suspensions of these particles will be investigated using static and dynamic MOT. The comparison of measurements and theoretical models will serve as a benchmark for using such core-shell nanorods as model objects for ferromagnetic probe particles.

### 7.1 Structural characterization

The silica encapsulated Ni nanorods were structurally characterized by bright field TEM images. Fig. 7.1 exhibits micrographs of the samples (scn-1 – scn-3) which were investigated in the present work. The Ni nanorods of different sizes are clearly discernible as dark cores. These Ni cores exhibit the same structural inhomogeneities as the PVP coated Ni nanorods, section 6.1, and are covered with amorphous silica (as verified by EDX chemical analysis, not shown) which appears as lighter outer layer. However, as observed in former studies where nanoparticles were covered with silica, various struc-

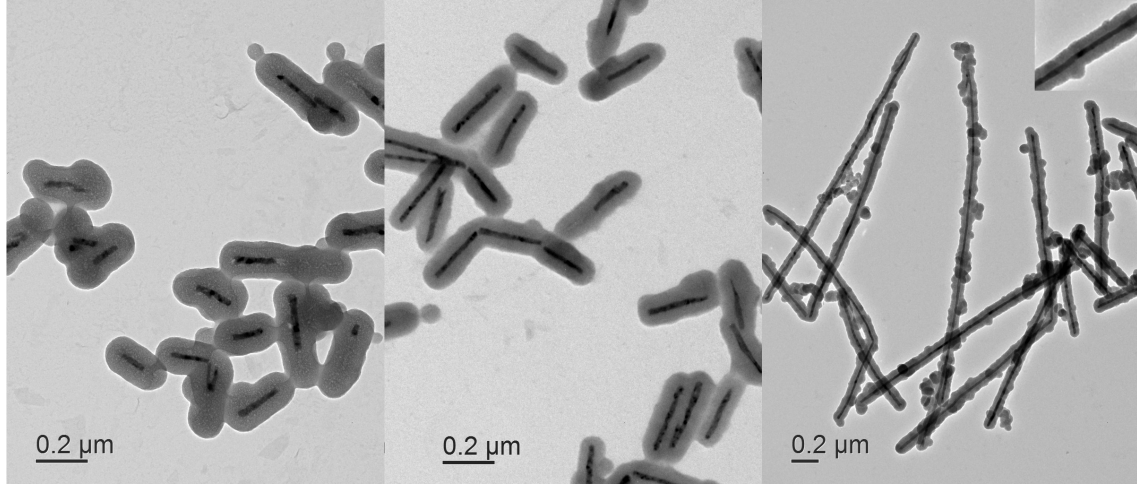


**Figure 7.1:** TEM images of silica-encapsulated Ni nanorods: Sample scn-1 (left), scn-2 (middle), and scn-3 (right, with insert at double magnification). Individual core-shell nanorods as well as multi-core particles, extended chains and adherent silica spheres are found. Additional images can be found in appendix B.

tural defects and irregularities such as bumps in the silica shell, multi-core particles, and fused particle chains are observed [26, 28, 59]. Also, pure silica spheres sticking at nanorods were found, in particular in sample scn-3. It remains unclear to which extent these structures are present in the colloid or may have formed during drying of the colloid on the TEM grid.

The shape of individual core-shell particles can be described as capped cylinders. The characteristic geometric dimensions of these single core particles, i.e. length  $l$  and diameter  $d$  of the Ni core as well as overall length  $L$  and diameter  $D$  (definitions in Fig. 5.3), of more than 200 nanorods were measured. The corresponding histograms derived for sample scn-2 are shown in Fig. 7.2. Furthermore, the thickness of the silica shell  $D_{\text{sh}}$  was determined by  $D_{\text{sh}} = (D - d)/2$ . The distribution of each quantity was approximated by log-normal density functions, Eq. (6.1),

$$f(x) = \left(\sqrt{2\pi}\sigma x\right)^{-1} \exp\left(-0.5(\ln x - \ln x_c)^2 \sigma^{-2}\right), \quad x > 0, \quad (7.1)$$

with location parameter  $x_c$ , scale parameter  $\ln(\sigma_x)$  and expected values  $E_x$ , Tab. 7.1.

## 7.1 Structural characterization

---

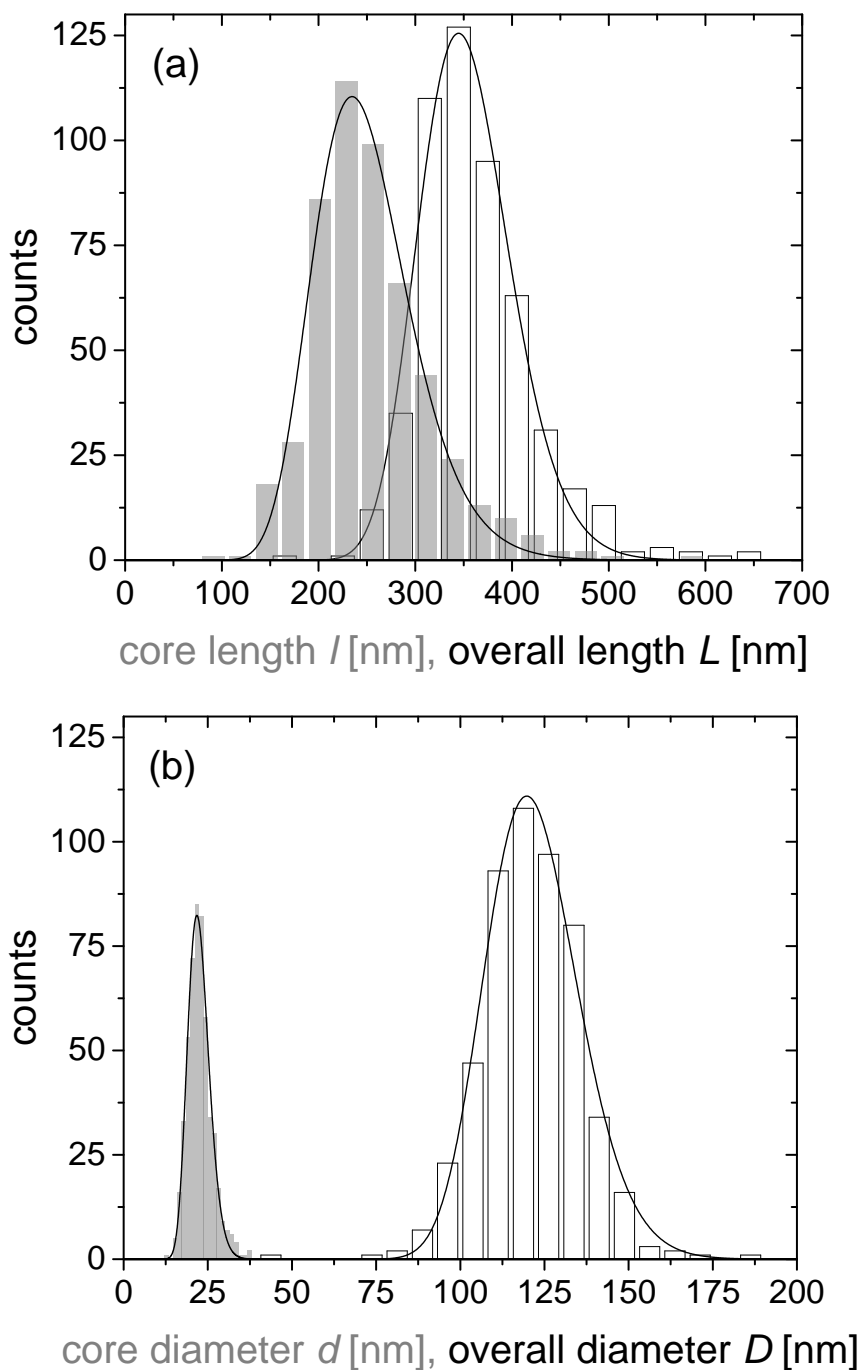


**Figure 7.2:** Distributions of (a) Ni core length  $l$  (grey), overall length  $L$  (open bars), (b) Ni core diameter  $d$  (grey), and overall diameter  $D$  (open bars) for sample scn-2. The lines represent the results of a regression analysis using a log-normal density function, Eq. (6.1).

## 7 - Results II - Quantitative modeling of DC- and OF-MOT signals of silica coated Ni nanorods colloids

---

Sample	scn-1	scn-2	scn-3
$N_c$	205	516	206
$l_c$ [nm]	144.4	244.6	890.1
$\sigma_l$	0.29	0.20	0.47
<b><math>E_l</math> [nm]</b>	<b>150.8</b>	<b>249.5</b>	<b>991.7</b>
$d_c$ [nm]	22.5	22.2	20.6
$\sigma_d$	0.18	0.14	0.16
<b><math>E_d</math> [nm]</b>	<b>22.9</b>	<b>22.4</b>	<b>20.8</b>
$L_c$ [nm]	310.2	351.1	953.9
$\sigma_L$	0.16	0.14	0.45
<b><math>E_L</math> [nm]</b>	<b>314.3</b>	<b>354.6</b>	<b>1057.0</b>
$D_c$ [nm]	149.2	121.3	80.2
$\sigma_D$	0.05	0.11	0.10
<b><math>E_D</math> [nm]</b>	<b>149.3</b>	<b>122.0</b>	<b>80.6</b>
<b><math>E_{D_{sh}}</math> [nm]</b>	<b>63.2</b>	<b>49.8</b>	<b>30.2</b>

**Table 7.1:** For each sample of silica coated nanorods (scn),  $N_c$  particles were measured by TEM image analysis. The location parameter  $x_c$ , scale parameter  $\sigma_x$ , and expected values  $E_x$  of the log-normal density functions, Eq. (6.1), which approximate the distributions of the length  $l$  and diameter  $d$  of the Ni core and overall length  $L$  and diameter  $D$  of the core-shell particles, were obtained. The values for the silica shell thickness were calculated by  $D_{sh} = (D - d)/2$ .

### 7.2 Static magnetic field-dependent optical transmission (DC-MOT)

The collinear magnetic and optical anisotropy of the silica coated Ni nanorods is confirmed by the static field-dependent optical transmission, Fig. 7.3. The transmitted intensities for magnetic field perpendicular,  $I_{\perp}(H)$  (upper branches), and parallel,  $I_{\parallel}(H)$  (lower branches), are normalized by the zero-field intensity  $I_{\times}$  and exhibit the same qualitative behavior as the PVP coated Ni nanorods, section 6.2. The reduced transmission upon parallel alignment complies with a larger extinction cross section of core-shell parti-

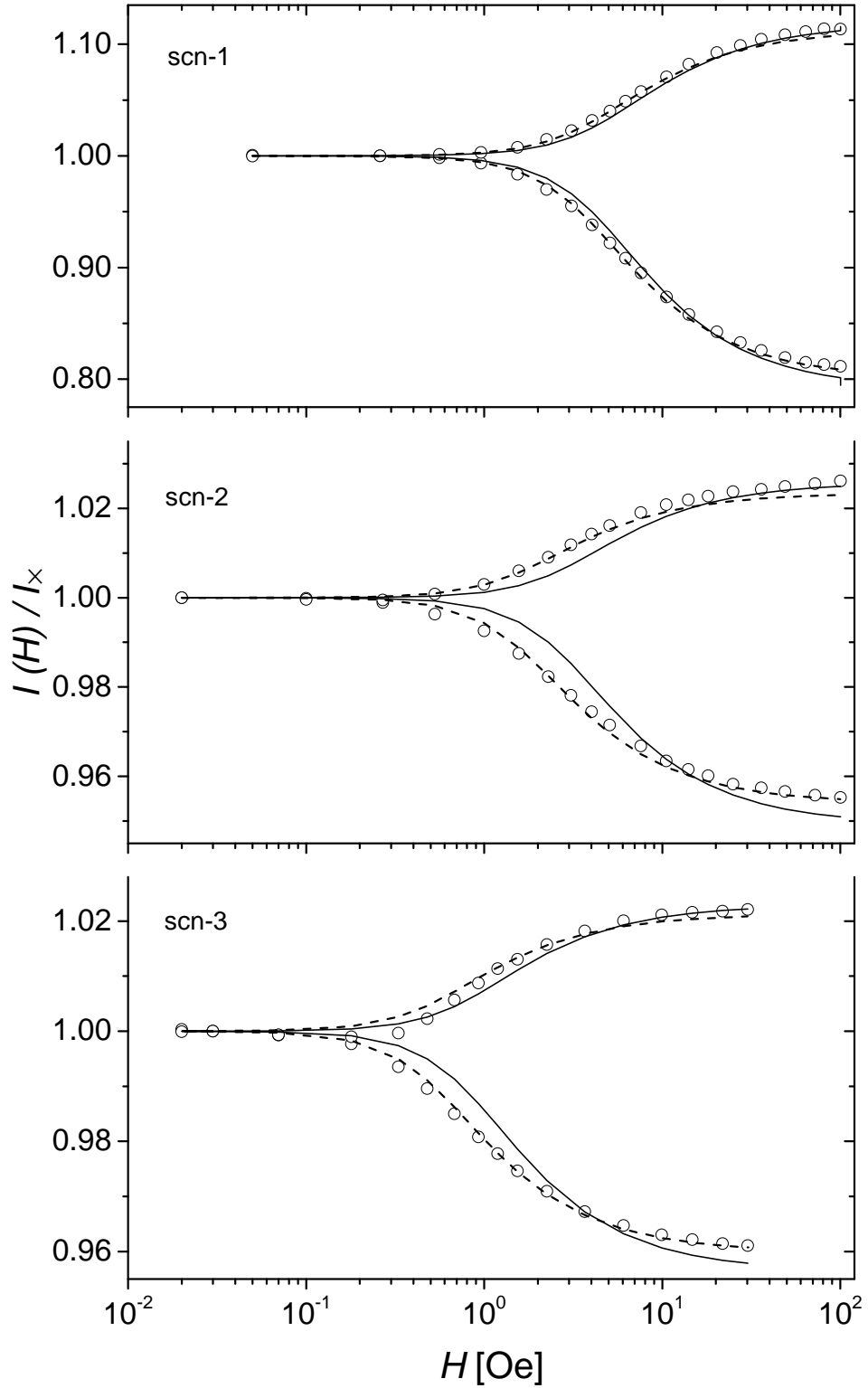


**Figure 7.3:** Measured transmitted intensity  $I(H)$  as a function of the external magnetic field normalized to the intensity at zero field  $I_x$  (circles). The lines represent least-square fits using Eq. (5.10) where  $d$  was a free parameter (dashed) or  $d_{OT}$  was fixed to  $E_d - 2d_{ox}$  obtained by TEM analysis.

## 7 - Results II - Quantitative modeling of DC- and OF-MOT signals of silica coated Ni nanorods colloids

---

cles for longitudinal polarization as compared to transversal polarization. Increasing size of the Ni core entails increasing magnetic moments and enables field-alignment against thermal energy at lower fields. Hence, the transmission of sample scn-3 nearly saturates at a field strength of  $H \approx 20$  Oe while shorter rods with comparable diameters (sample scn-1 and scn-2) and thus lower magnetic moments require higher magnetic fields. This field-dependence has been analyzed to extract characteristic quantities of PVP coated Ni nanorod colloids, i. e. the mean diameter per particle and the particle concentration in the colloid in the previous chapter. In the following, this approach will be adapted for the analysis of Ni/SiO<sub>2</sub> core-shell nanorods.

As described in section 5.1, the field-dependent transmittance can be described by

$$I_{\perp,\parallel}(H)/I_{\times} = \exp(-Ns (\langle C_{\text{ext}} \rangle_{\perp,\parallel}(H) - C_{\text{ext}, \times})) . \quad (7.2)$$

The protocol of the analysis is exactly the same as for PVP coated nanorods. The analysis of field-dependent optical transmission is essentially reduced to modeling of the extinction cross sections along the principle axes of the core-shell nanorods. For this purpose, FEM simulations as described in section 4.3.7 were used to solve the Maxwell equations. The required value of the permittivity of silica  $\epsilon_{\text{silica}} = 2.15502$  was taken from [107].

In order to illustrate the influence of the silica shell on the optical properties, the absorption and scattering cross sections of bare capped Ni nanocylinders with a diameter of  $d = 20$  nm, length  $l = 50 \dots 2000$  nm and of the same Ni nanorods encapsulated by a silica shell with a thickness of  $D_{\text{sh}} = 50$  nm are shown in Fig. 7.4.

The absorption cross sections of the bare nanorods are significantly larger than the scattering components, as already shown in section 6.3.1 and 6.3.4. For longitudinal polarization,  $C_{\text{abs}}$  exhibits a shoulder at  $L \sim 80$  nm related to the red-shift of the plasmon resonance with increasing aspect ratio [43, 101]. For rod lengths  $L > 300$  nm,  $C_{\text{abs}, L}$  increases with a slope  $\sim 1$ , Fig. 7.4(a). The same proportional increase – yet at much smaller values – is found for the absorption cross sections at transversal polarization. The additional silica layer has a minor impact on the absorption component whereas the scattering cross sections are significantly changed, Fig. 7.4(b). In particular, the scattering cross section for the transversal polarizations are increased significantly while for the longitudinal polarization a moderate decrease is found so that the optical anisotropy nearly vanishes with respect to scattering. A variation of the silica shell thickness mainly affects the scattering cross sections, Fig. 7.5. For a given core length of  $L = 250$  nm, the absorption cross sections change by less than 20% whereas  $C_{\text{sca}, T2}$  increases by a factor

## 7.2 Static magnetic field-dependent optical transmission (DC-MOT)

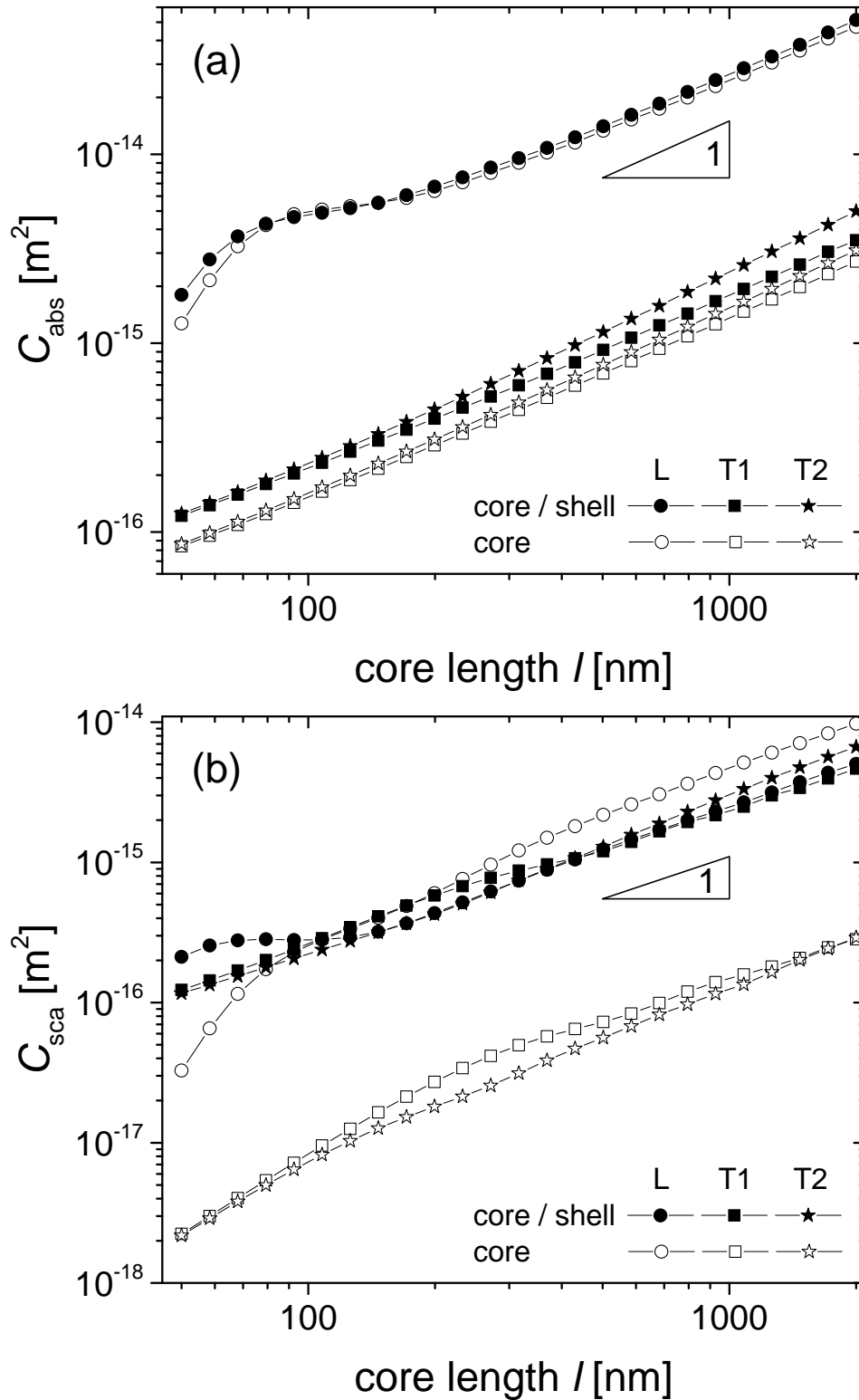


**Figure 7.4:** Absorption (a) and scattering (b) cross sections of bare capped Ni cylinders (empty symbols) and silica coated capped Ni cylinders (full symbols) as a function of the core length  $l$ . The core diameter was  $d = 20$  nm and the thickness of the silica shell was  $D_{\text{sh}} = 50$  nm.

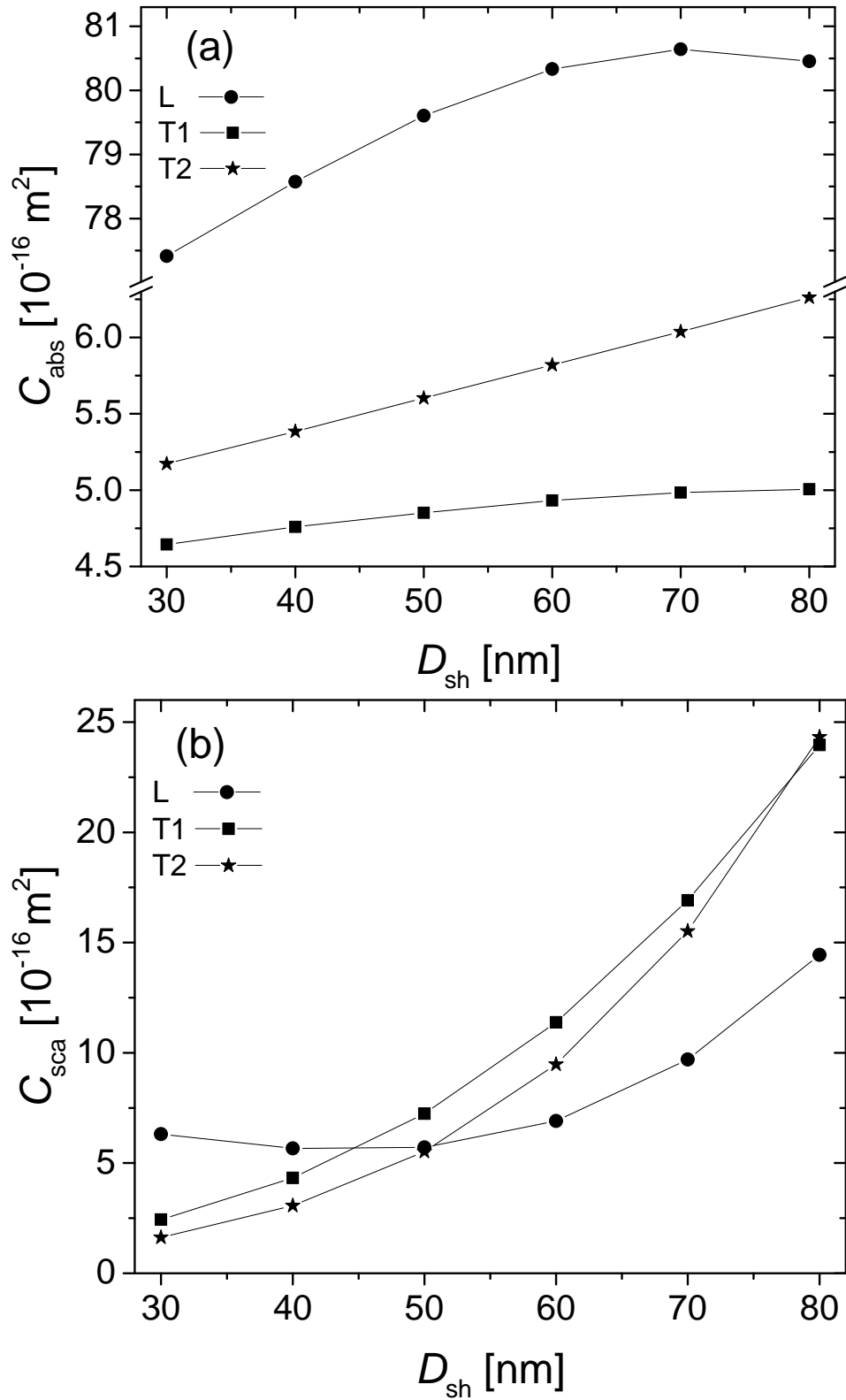


**Figure 7.5:** Absorption (a) and scattering (b) cross sections of silica encapsulated capped Ni cylinders with core diameter  $d = 20$  nm and core length  $l = 250$  nm as a function of the thickness of the silica shell  $D_{sh}$ .

## 7.2 Static magnetic field-dependent optical transmission (DC-MOT)

---

of  $\sim 12$  upon variation of the thickness of the silica shell in the range of  $D_{\text{sh}} = 30..80$  nm, even rising above the longitudinal contribution. Obviously, the distinct optical anisotropy of the Ni core drops away when the particles are encapsulated in a silica shell with a thickness close to the length of the core particle.

After these considerations regarding the optical properties of the silica coated Ni nanorods, the focus can be returned to the analysis of the DC-MOT measurements, Fig. 7.3. The splitting between the two branches of parallel and perpendicular measurement depends on the optical anisotropy of the nanorods as well as on their concentration  $N$ , as reported for PVP coated Ni nanorods in the previous chapter. The field-dependence of this splitting is characteristic for the magnetic moment of the Ni core because this moment determines the alignment in field-direction against thermal energy. However, cylindrical particles of equal volume and hence equal magnetic moment can be realized with arbitrary aspect ratio, which in turn also implies varying optical anisotropy. So, as for bare nanorods, the relationship between three independent variables ( $l$ ,  $d$ , and  $N$ ) and the field-dependent transmission is overdetermined so that there is no unique solution to the inverse problem. Therefore, the analysis of DC-MOT measurements of Ni nanorod suspensions requires assumptions on all but two colloid variables. For bare Ni nanorods, the first moment of the length distribution function  $E_l$  was taken as fixed value because it can be determined from TEM images with suitable accuracy. For the silica coated nanorods, the thickness of the silica shell  $E_{D_{\text{sh}}}$ , determined for each colloid from TEM images, Tab. 7.1, was also taken as fixed quantity and only the diameter  $d$  of the Ni core and the concentration  $N$  of the colloidal particles served as free variables. The results of the regression analysis using the model described in section 5.1 are shown in Fig. 7.3 (dashed lines). The field-dependent splitting into the two branches and its shift to a lower field strength with increasing size of the Ni core is correctly reproduced by the model. The curvature and convergence to the saturation values of the transmission is also well described with some small deviations for sample scn-2. However, the obtained values for the diameter of the Ni core  $d_{\text{OT}}$  tended to be larger than the expected values  $E_d$  from TEM image analysis, Tab. 7.2. This result is in contrast to the studies in section 6.4 on PVP coated Ni nanorods which provided slightly smaller diameters caused by a non-ferromagnetic surface oxide layer of 1–2 nm thickness. To evaluate whether such a small variation in the diameter is significant with regard to the measurement, a second regression analysis was performed with the length as well as the diameter of the Ni cores

## 7 - Results II - Quantitative modeling of DC- and OF-MOT signals of silica coated Ni nanorods colloids

---

being fixed at  $E_l$  and  $E_d - 2d_{\text{ox}}$  with  $d_{\text{ox}} = 1.5 \text{ nm}^1$ , respectively. Hence, the concentration of the particles in the colloid was the only free fit parameter. The solid lines in Fig. 7.3 show that such a small difference in the diameter of the nanorods is indeed significant and results in a clear shift of the field-dependent splitting to higher values. The question whether the larger diameter or other factors may be responsible for this discrepancy is left open for now and will be addressed later again. In order to gather more information, the focus will be turned to the dynamical properties of the particles in the following section.

	Sample	scn-1	scn-2	scn-3
TEM analysis (repeated from Tab. 7.1)	$E_d$ [nm]	22.9	22.4	20.8
DC-MOT analysis, free parameters: $d, N$	$d_{\text{OT}}$ [nm] $N$ [ $10^{15} \text{ m}^{-3}$ ]	21.9 5.5	25.5 0.68	22.1 0.204
DC-MOT analysis, free parameter: $N$	$N$ [ $10^{15} \text{ m}^{-3}$ ]	6.9	1.1	0.306

**Table 7.2:** First moment of the core diameter distribution  $E_d$  obtained by TEM and core diameters  $d_{\text{OT}}$  as well as particle concentrations  $N$  obtained by the regression analysis of DC-MOT measurements assuming monodisperse particle ensembles, Fig.7.3.

### 7.3 Dynamic magnetic field-dependent optical transmission (OF-MOT)

The dynamical properties of the silica coated Ni nanorods in aqueous suspension were investigated using oscillating magnetic fields. An experimental setup as described in section 3.2.2 was used for all dynamic measurements in this work. A field amplitude of  $H_0 = 60 \text{ Oe}$  was used to ensure sufficiently large Langevin parameters ( $\zeta > 10$ ) resulting in a nearly parallel alignment of the particles with the field as shown in section 4.1.3. The imaginary part of the response function  $X''(\omega)$  is shown in Fig. 7.6 (dotted lines). The relaxation peaks for the silica coated nanorods dispersed in water are found at angular

---

<sup>1</sup>Referring to section 6.4 and [20, 103], 1.5 nm can be assumed as a typical value of  $d_{\text{ox}}$ .

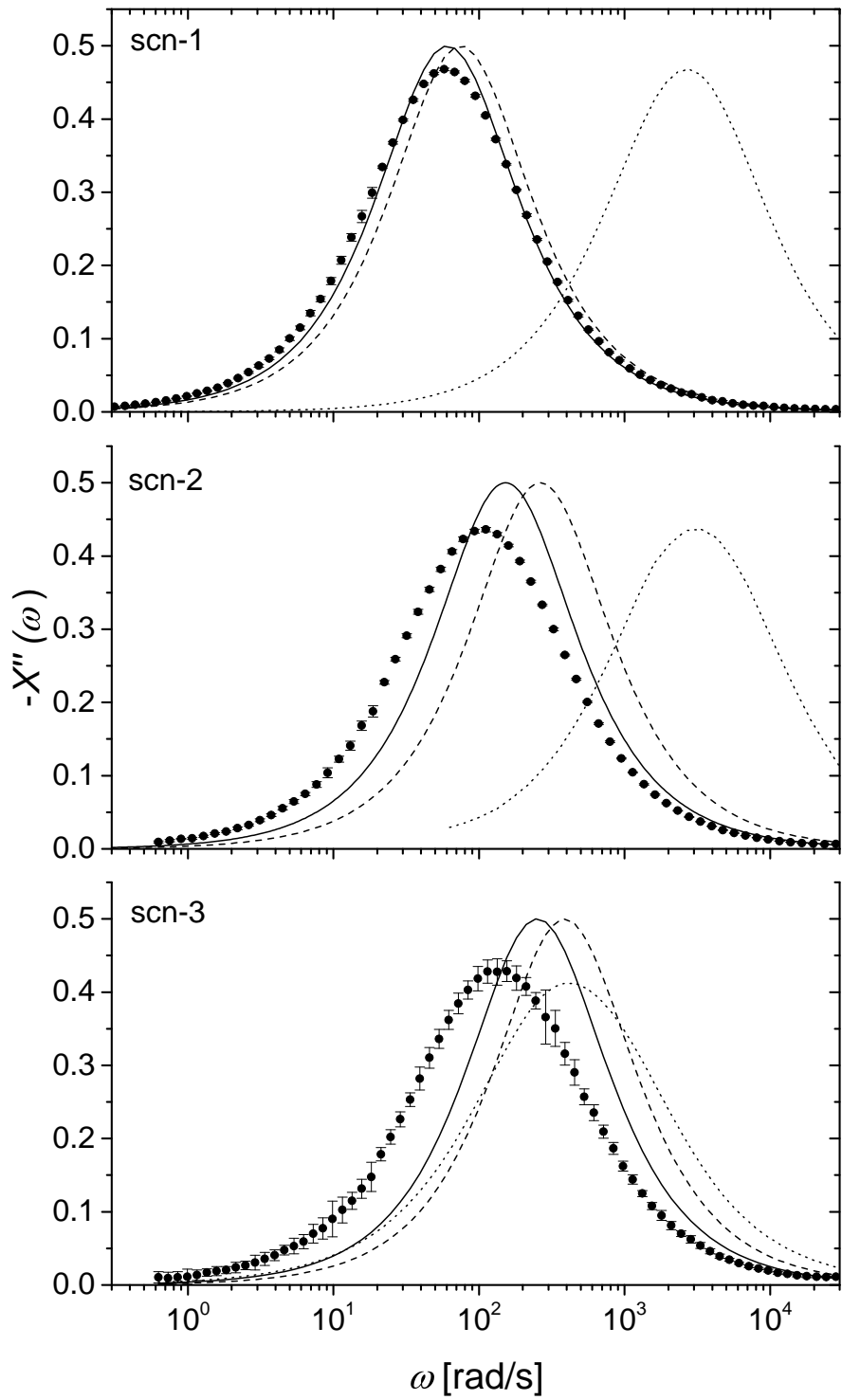


**Figure 7.6:** Measured imaginary part of the response function  $-X''(\omega)$  as a function of the angular frequency of the applied magnetic field in water (dotted lines) and in a glycerol-water mixture (full dots). The other lines are calculated following Eq. (5.18) assuming a monodisperse particle ensemble with a core diameter obtained from DC-MOT measurements (dashed) or a core diameter  $d = E_d - 2d_{\text{ox}}$  obtained by TEM (solid), respectively.

## 7 - Results II - Quantitative modeling of DC- and OF-MOT signals of silica coated Ni nanorods colloids

---

frequencies  $\omega > 1000$  rad/s with tails exceeding the accessible frequency range of the OF-MOT setup ( $\omega_{\max} = 3 \cdot 10^4$  rad/s). Mixing glycerol into the suspension medium increased its viscosity  $\eta$ , Tab.7.3, and resulted in a shift of the relaxation peaks into the accessible frequency window, Fig.7.6 (full dots). Assuming a monodisperse particle ensemble allows the modeling of the relaxation peaks. The core lengths as well as the overall lengths and diameters of the particle representing the ensemble were chosen to the first moment of their distributions obtained by TEM ( $l = E_l$ ,  $L = E_L$ , and  $D = E_D$ ). This model calculation was performed for the two scenarios discussed in the analysis of DC-MOT measurements, i. e. for the diameters  $d_{\text{OT}}$  obtained from the regression analysis as free parameter (dashed lines in Fig.7.6) and for the smaller diameters fixed at  $E_d - 2d_{\text{ox}}$  (solid lines). The former which showed better agreement between measured and modeled DC-MOT signals revealed a larger deviation from the relaxation peak in the OF-MOT experiment than the latter, Tab.7.3. Therefore, it is assumed that the increased values of  $d_{\text{OT}}$  are the result of a yet untreated contribution of multi-core particles to the measured optical transmission. The value of the imaginary part at peak maximum is  $-X''(\omega)_{\max} = 0.5$  for a relaxation following Eq.(5.18) with a single time constant. The measured response functions have maximum values  $\leq 0.47$ , Tab.7.3, in combination with a slight peak broadening. This effect is commonly attributed to a distribution of relaxation times, which will be addressed in the next section.

### 7.4 Polydispersity

In order to investigate whether the observed peak broadening is consistent with the size distribution of the core-shell particles revealed by TEM image analysis, the oscillating field optical transmission of the polydisperse particle ensembles is computed as described in section 5.2.3. The model calculations are based on the tabulated values of the Ni cores ( $l_i$  and  $d_i$ ) and overall size ( $L_i$  and  $D_i$ ) for a large number of core-shell particles which already served as a basis for the determination of the distribution functions, Fig.7.2.

Furthermore, the extinction cross sections for each counted particle dispersed in a glycerol-water-mixture was calculated by FEM<sup>2</sup>. The values for the permittivity of this solvent were taken from [108] and can be found in Tab.7.3. The result of this calculation is shown in Fig.7.7 together with the measured imaginary part of the response function

---

<sup>2</sup>The computation time for this step substantial since  $C_{\text{ext}}$  of about 900 particles for the L and T1 mode had to be calculated. This resulted in about 1800 FEM simulations to calculate the cross sections needed to model the polydisperse OF-MOT signal.

## 7.4 Polydispersity

sample		scn-1	scn-2	scn-3
	$\eta$ [mPa s]	48.1	27.7	4.9
	$\epsilon_r$	2.0731	2.0474	1.9384
measurement	$-X''_{\max}$	0.47	0.44	0.43
	$\omega(-X''_{\max})$ [rad/s]	57.9	111.5	133.2
calculation based on				
$E_l$ (TEM) and $d = d_{OT}$ from Tab. 7.2	$-X''_{\max}$	0.5	0.5	0.5
	$\omega_c$ [rad/s]	74.6	263.4	386.5
$E_l$ (TEM) and $d = E_d - 2d_{ox}$ (TEM)	$-X''_{\max}$	0.5	0.5	0.5
	$\omega_c$ [rad/s]	60.6	152.2	251.2

**Table 7.3:** Parameters of  $-X''(\omega)$  obtained by measurements or calculations assuming monodisperse particle ensembles (using Eqs. (5.20) and (5.18)). The values for relative permittivity  $\epsilon_r$  and the viscosity  $\eta$  were calculated from the percentage of glycerol [108, 109].

$-X''(\omega)$ . As expected, the polydispersity of the core-shell nanorods results in a moderate broadening of the relaxation peak and a corresponding reduction of the peak maximum rather close to the measured ones, Tab. 7.4. Consequently, the differences between the measured and modeled relaxation peak observed in section 7.3 can be partially explained by the polydispersity of the particles.

However, including the polydispersity has only a marginal influence on the position of the relaxation peak. The observed lower frequency of the relaxation peak might be caused by an additional hydrodynamic layer at the silica surface but the sample scn-1 with the shortest nanorods for which this effect is expected to be most prominent shows the best agreement between the measured and modeled peak position. Therefore, this hypothesis can be excluded. In the next step, the contribution of agglomerates to the measured magnetic field-dependent optical signals will be included. But beforehand, the impact of polydispersity on DC-MOT shall be investigated.

Similar to the construction of the OF-MOT signal, the model is based on the tabulated values of  $l_i$ ,  $d_i$ ,  $L_i$ , and  $D_i$  but additionally has to consider the overall particle concentration as the splitting of the DC-MOT curves depends on the absolute concentration of nanorods in the colloid and is required for a quantitative modeling of the

## 7 - Results II - Quantitative modeling of DC- and OF-MOT signals of silica coated Ni nanorods colloids

---

DC-MOT signal. In Fig. 7.8, the obtained modeled curves are shown. Compared to the corresponding curve for a monodisperse particle ensemble (solid line in Fig. 7.3), the agreement with the measured data is slightly improved for all samples but there are still significant deviations from the measured data especially in the region where the upper and lower branches disjoin as well as at saturation. The concentrations obtained from both analysis models are similar, Tab. 7.5.

In conclusion, neither the monodisperse modeling with diameters from static MOT measurements nor reduced diameters from TEM analysis nor the polydisperse modeling of OF-MOT signals resulted in a quantitative agreement with the measured signal for all samples. The calculated peak positions were higher than measured. This suggests a second particle fraction with a characteristic relaxation frequency that is significantly lower than those of the so far treated single core particles. The next section focuses on the identification of these particles and, by extending the used model, their influence on the MOT.

	sample	scn-1	scn-2	scn-3
measurement	$-X''_{\max}$	0.47	0.44	0.43
	$\omega(-X''_{\max})$ [rad/s]	57.9	111.5	133.2
polydisperse modeling based on TEM data	$-X''_{\max}$	0.46	0.47	0.41
	$\omega(X''_{\max})$ [rad/s]	62.8	163.7	211.9

**Table 7.4:** Parameters of  $-X''(\omega)$  obtained by measurement and calculation of the MOT respecting the polydispersity of the particles.

	Sample	scn-1	scn-2	scn-3
DC-MOT analysis (monodisperse), free parameter: $N$ (repeated from Tab. 7.2)	$N$ [ $10^{15} \text{ m}^{-3}$ ]	6.9	1.1	0.306
DC-MOT analysis (polydisperse) (free parameter: $N$ shown in Fig. 7.8)	$N$ [ $10^{15} \text{ m}^{-3}$ ]	6.9	1.07	0.3

**Table 7.5:** Particle concentrations obtained by regression analysis of DC-MOT measurements assuming a monodisperse particle ensemble with  $d_{\text{OT}} = E_d - 2d_{\text{ox}}$  or a polydisperse particle ensemble.

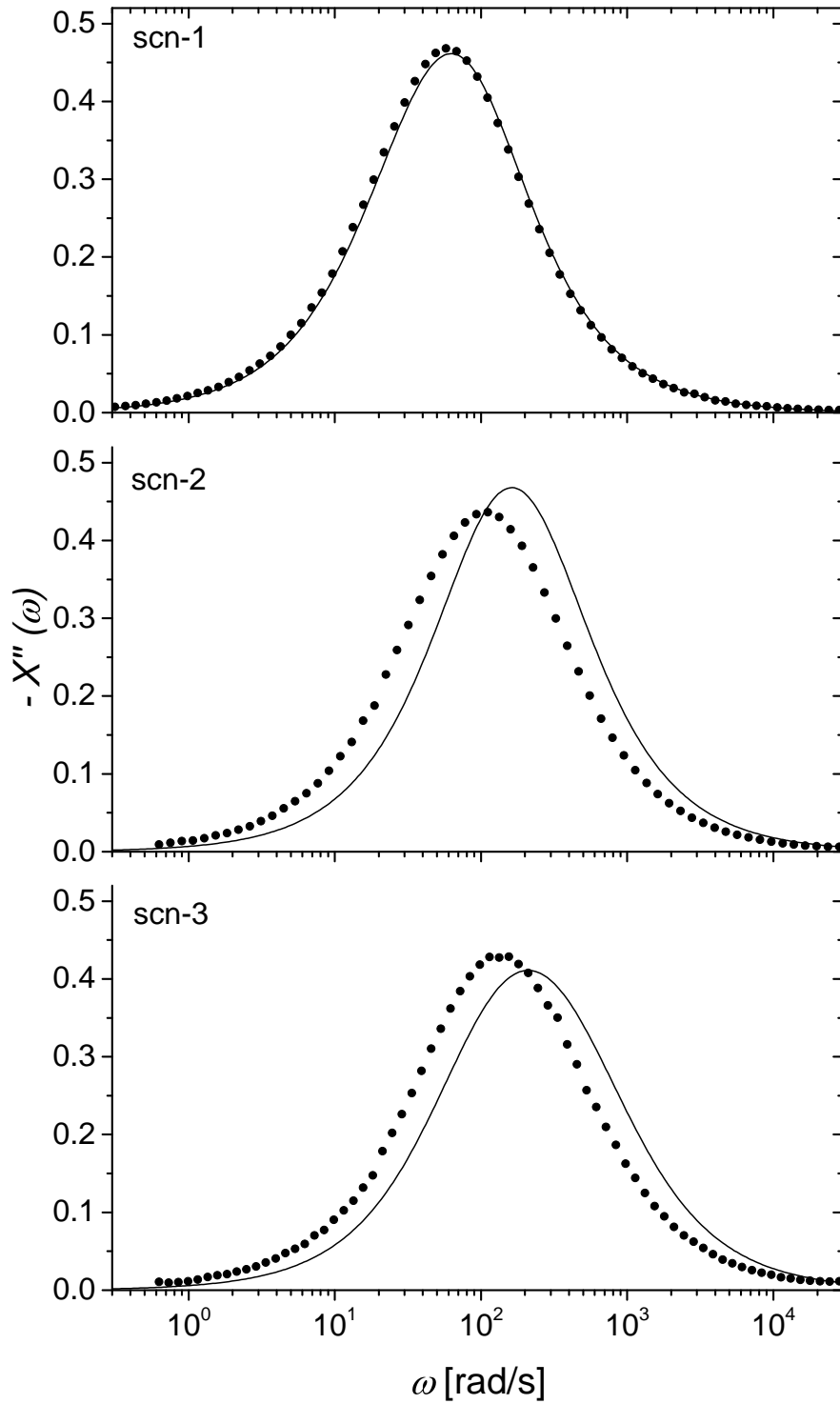


**Figure 7.7:** Measured (points) and modeled (considering the size distribution of the particles, solid lines) imaginary part of the response function  $-X''(\omega)$ . In the model calculation, the core diameter was chosen to  $d_i - 2d_{ox}$ .

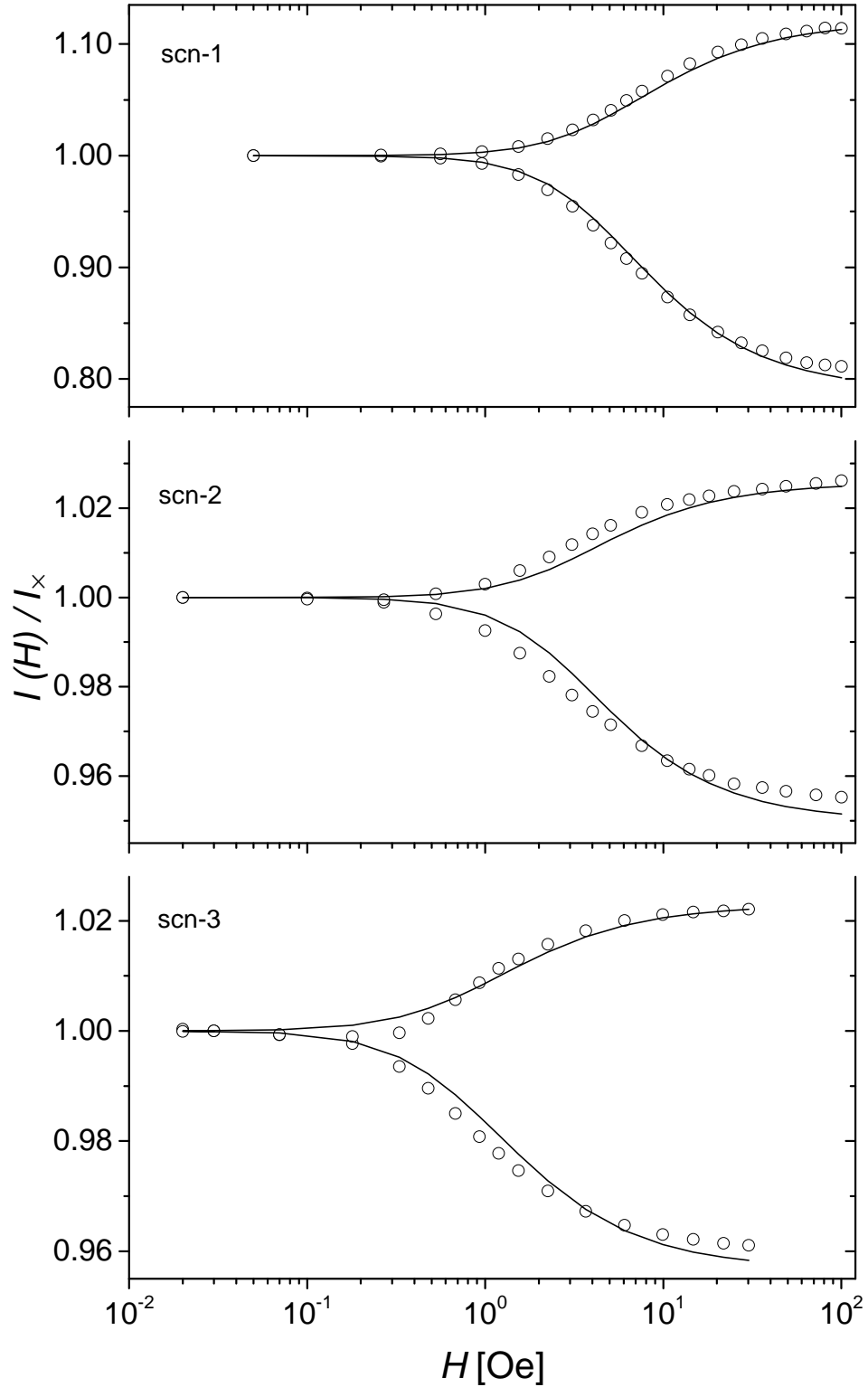


**Figure 7.8:** Measured normalized transmitted intensity  $I(H)/I_x$  (open circles). The solid lines represent least-square fits following Eq. (5.21) for given particle lengths and diameters and respecting the polydispersity of the particle ensemble. The core diameter of every particle was chosen to  $d_i - 2d_{ox}$ .

## 7.5 Contributions of multi-core particles to the MOT

Figure 7.1 shown at the beginning of this chapter displays TEM images of particles containing more than one Ni core. These multi-core particles exhibit different structures like linear and zig-zag chains or curved arc segments. Until now, these particles were neglected in the modeling of the MOT. Due to the multitude of possible configurations, a detailed modeling of the various multi-core structures is not feasible so that the objective of the present study was to identify a representative aggregate that effectively captures the contribution of these structures.

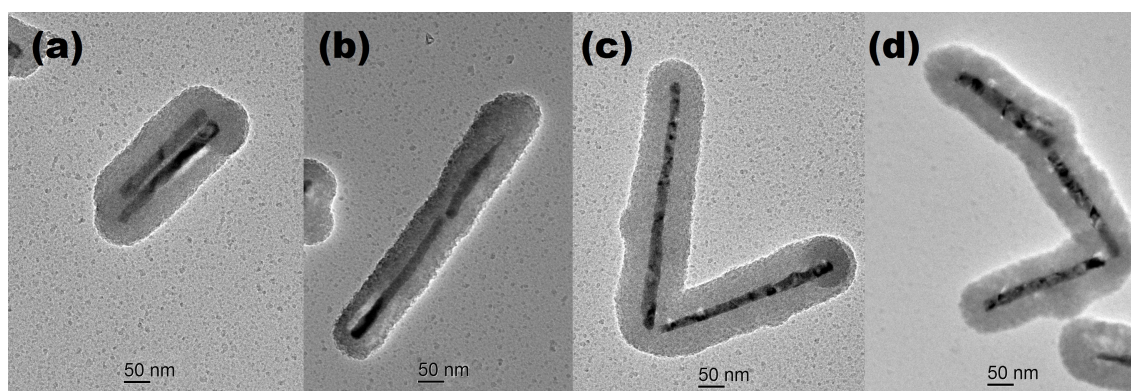


**Figure 7.9:** Typical examples of multi-core particles observed in TEM images such as silica encapsulated dimers of two Ni nanorods in side-by-side configuration (a), two collinear cores (b), two tilted cores (c) and particles with three cores (d).

Fig. 7.9 shows typical examples for multi-core particles. Dimers of nanorods, Fig. 7.9(a), in parallel side-by-side alignment are commonly observed in the present samples as well as in colloids of PVP coated Ni nanorods [103]. In the ground state, the magnetization of two nanorods in parallel configuration point into opposite directions and compensate each other. Due to the vanishing net magnetic moment, such dimers do not contribute to the field-dependent transmission but add a field-independent extinction background [103]. They do not participate in the field-modulated OF-MOT measurement and their contribution to the DC-MOT is blanked out by normalization to the zero-field transmittance and thus are not considered further.

A particular structural defect are single core-shell particles fused together into extended chains by the silica coating. Different conformations (e.g. linear, curved, zig-zag) of such chains can be identified. Linear chains containing two or more Ni cores, Fig. 7.9(b), exhibit the highest magnetic moment and optical anisotropy. These particles are expected to have a high influence on static and dynamical MOT measurements and can be readily

## 7 - Results II - Quantitative modeling of DC- and OF-MOT signals of silica coated Ni nanorods colloids

modeled due to their axisymmetric shape.

The influence of particles with tilted cores, Fig. 7.9(c), depends on the angle between the cores with the limiting cases shown in Fig. 7.9(a) and Fig. 7.9(b). As an example, a particle containing two Ni cores that are oriented perpendicular to each other is assumed, Fig. 7.10. To calculate its orientation dependent extinction cross section in a first approximation, the particle is divided into two single core particle and the extinction cross section is calculated by summation of the extinction cross sections of these single core particles, hence electromagnetic interaction is neglected..

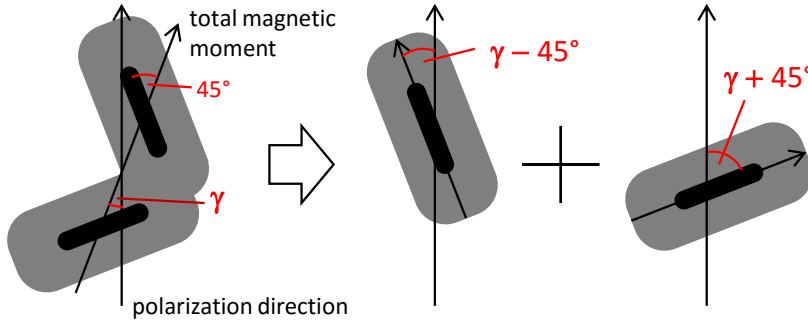


**Figure 7.10:** Analysis of a multi-core particle with two cores perpendicular to each other. The angle  $\gamma$  is the angle between the resulting magnetic moment of the particle and the polarization direction of the incident light.

To obtain the effective extinction cross section when the polarization direction of the incident light is parallel or perpendicular to the external magnetic field, as experimentally realized in DC-MOT measurements, the argumentation is focused on the simple case of saturation. In this case, the external magnetic fields are high enough for a parallel alignment of the resulting moment against thermal energy ( $\zeta > 10$ ) but small enough to avoid significant rotations of the magnetic moments out of the core axes. Then, thermally activated rotations around the axis of the resulting magnetic moment have to be considered and the effective extinction cross section for the parallel  $C_{\text{ext, eff, ||}}$  and for the perpendicular  $C_{\text{ext, eff, \perp}}$  case can be calculated by averaging  $C_{\text{ext}}$  over all states of rotation consistent with the field alignment. Hence for  $\gamma = 0$ , both rods include an angle of  $\theta = 45^\circ$  with the external magnetic field, Fig. 5.2(a). The orientation-averaged extinction cross section of the whole multi-core particle can be calculated applying Eq. (5.2) on both single core particles with the extinction cross sections  $C_{\text{ext, L}}$ ,  $C_{\text{ext, T1}}$ ,  $C_{\text{ext, T2}}$  :

$$\begin{aligned} C_{\text{ext, eff, ||}} &= 2 \left( \frac{1}{2} C_{\text{ext, L}} + \frac{1}{2} \langle \sin^2 \phi \rangle C_{\text{ext, T1}} + \frac{1}{2} \langle \cos^2 \phi \rangle C_{\text{ext, T2}} \right) \\ &= C_{\text{ext, L}} + \frac{1}{2} C_{\text{ext, T1}} + \frac{1}{2} C_{\text{ext, T2}} . \end{aligned} \quad (7.3)$$

## 7.5 Multi-core particles

For  $\gamma = 45^\circ$ , both rods include an angle of  $\delta = 45^\circ$  with the external magnetic field, Fig. 5.2 (b). Using Eqs. (5.2), (5.6), and (5.7)  $C_{\text{ext, eff, } \perp}$  can be calculated to

$$\begin{aligned}
 C_{\text{ext, eff, } \perp} &= 2 \left( \langle \cos^2 \epsilon \rangle \sin^2 \delta C_{\text{ext, L}} + (1 - \langle \cos^2 \epsilon \rangle \sin^2 \delta) \frac{\langle \cos^2 \epsilon \rangle}{1 - \langle \cos^2 \epsilon \rangle \sin^2 \delta} C_{\text{ext, T1}} \right. \\
 &\quad \left. + (1 - \langle \cos^2 \epsilon \rangle \sin^2 \delta) \left( 1 - \frac{\langle \cos^2 \epsilon \rangle}{(1 - \langle \cos^2 \epsilon \rangle \sin^2 \delta)} \right) C_{\text{ext, T2}} \right) \\
 &= \frac{1}{2} C_{\text{ext, L}} + C_{\text{ext, T1}} + \frac{1}{2} C_{\text{ext, T2}}.
 \end{aligned} \tag{7.4}$$

For a particle containing two perpendicular arranged Ni cores with  $d = 20$  nm,  $l = 200$  nm and  $D_{\text{sh}} = 50$  nm, a ratio  $C_{\text{ext, eff, } \parallel} / C_{\text{ext, eff, } \perp} = 1.6$  is found while for linear multi-core particles  $C_{\text{ext, } \parallel} / C_{\text{ext, } \perp} = 7.3$ . This example shows that particles with tilted cores have lower optical anisotropy and hence a smaller contribution to DC- as well as OF-MOT measurements.

With the same reasoning, multi-core particles with three or more cores are also expected to have the highest influence when the cores are aligned in a linear chain. With these preliminary considerations, it was decided to model the influence of multi-core particles on DC- and on OF-MOT using the simple linear multi-core particles as schematically illustrated for a particle containing three cores in Fig. 7.11.

While the diameter  $D$  is assumed to be the same as observed for single core particles,

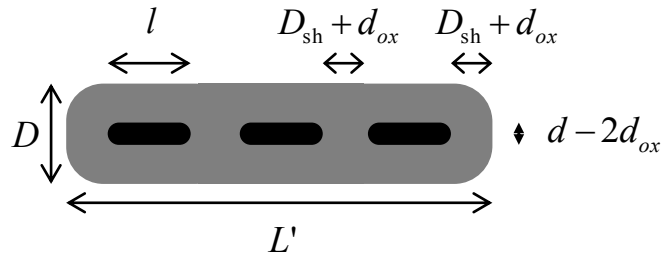


**Figure 7.11:** Example for a multi-core particle containing  $n_c = 3$  collinear Ni cores.

the length  $L'$  depends on the number of Ni cores. For a particle consisting of  $n_c$  Ni cores, the resulting magnetic moment is expected to be  $n_c$  times the moment of a single core particle. The whole structure is assumed to be covered with a silica shell with  $D_{\text{shell}} = 50$  nm.

Before estimating the influence of these particles on the MOT, their optical properties in terms of their extinction cross section need to be simulated by FEM. In the present calculations particles containing up to ten Ni cores, each represented by a capped cylinder

## 7 - Results II - Quantitative modeling of DC- and OF-MOT signals of silica coated Ni nanorods colloids

with a length of  $l = 250$  nm and a diameter of  $d = 22.5$  nm, were treated.

Fig.7.12 shows the extinction cross section of such a linear multi-core particle as a function of the number of Ni cores. The extinction is the highest for the L mode followed by the T1 and T2 modes. The extinction cross sections increase linearly with the number of cores  $n_c$  (the lines in Fig.7.12 are lines through origin with slope equal to  $C_{\text{ext}}$  of a single core particle). This relation may be used as an approximation and is reasonable for the L mode and the isotropic case but less accurate for the transversal modes.

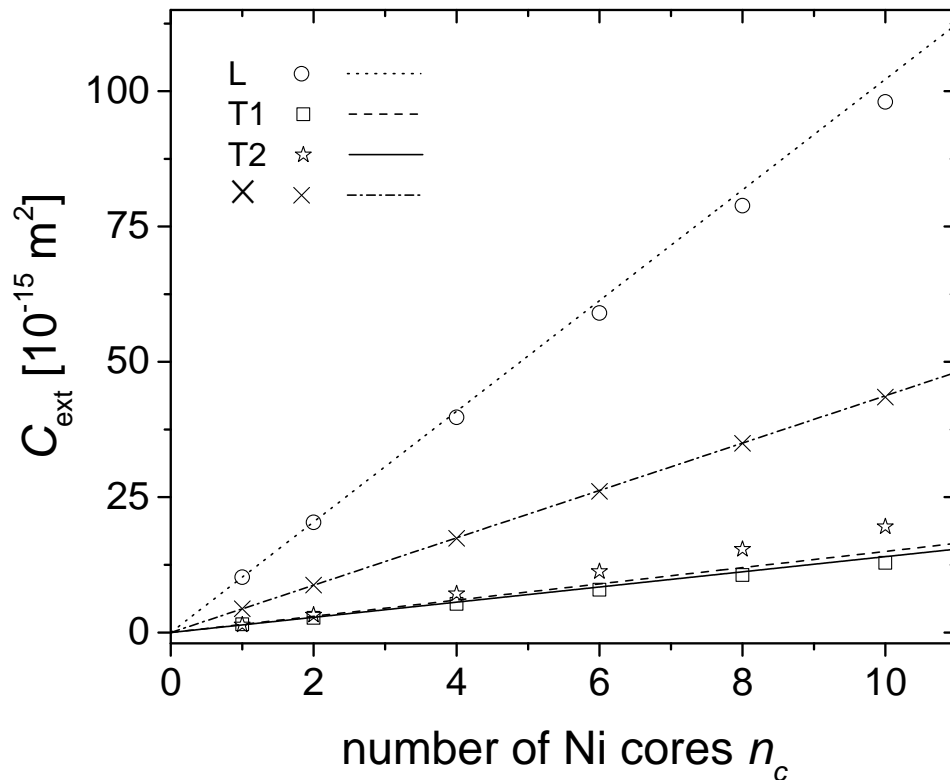


**Figure 7.12:** Extinction cross sections  $C_{\text{ext}}$  of linear multi-core particles with a shell thickness of  $D_{\text{sh}} = 50$  nm as a function of the number of Ni cores. Each core has a diameter of  $d = 22.5$  nm and a length of  $l = 250$  nm. The symbols represent values obtained by FEM for the L, T1, and T2 mode as well as for the isotropic case ( $\times$ ). The lines are drawn through the origin with a slope equal to the corresponding  $C_{\text{ext}}$  of the single core particle.

## 7.5 Multi-core particles

---

### 7.5.1 Modeling OF-MOT using polydisperse single core and linear multi-core particles

Up to this point, the modeling of DC- as well as OF-MOT signals was limited to the contributions of polydisperse single core particles. This treatment is insufficient and has to be extended by linear multi-core particles. The first approach to model the relaxation peaks of the composed system of particles is a simple superposition of peaks of different particle fractions, i.e. polydisperse single-core and monodisperse linear multi-core particles. This method neglects the different optical weighting of different particle fractions but provides a simple and fast analysis.

#### Direct superposition of relaxation peaks

The superposition of relaxation peaks corresponding to single core-shell particles and multi-core particles to the OF-MOT response function can be expressed by

$$X''(\omega) = R'_{sc} X''_{pd\_scp}(\omega) + (1 - R'_{sc}) X''_{mc}(\omega), \quad (7.5)$$

where  $R'_{sc}$  is the ratio of single core particles,  $X''_{pd\_scp}(\omega)$  the peak of the polydisperse single core particles and  $X''_{mc}(\omega)$  the peak resulting from linear multi-core aggregates. The length and diameter per core as well as the thickness of the silica shell for the multicore aggregates were chosen to corresponding values of the first moment of the distribution of these parameters obtained by TEM image analysis of the single core particles.

Using Eq. (7.5) and the relaxation peak  $X''_{pd\_scp}(\omega)$  obtained by modeling the peak for polydisperse single core particles, section 7.4, and peaks obtained for monodisperse multi-core particles  $X''_{mc}$ , a good approximation of the measured spectra can be obtained when the mixing ratio is variable, Fig. 7.13.

For the two samples scn-1 and scn-3, a good agreement between the measured and modeled data was found for a combination of polydisperse single core particles and monodisperse two-core particles, Tab. 7.6.

For sample scn-2, a good agreement between the measured and modeled data was found for a combination of polydisperse single core particles with monodisperse two-core and three-core particles.

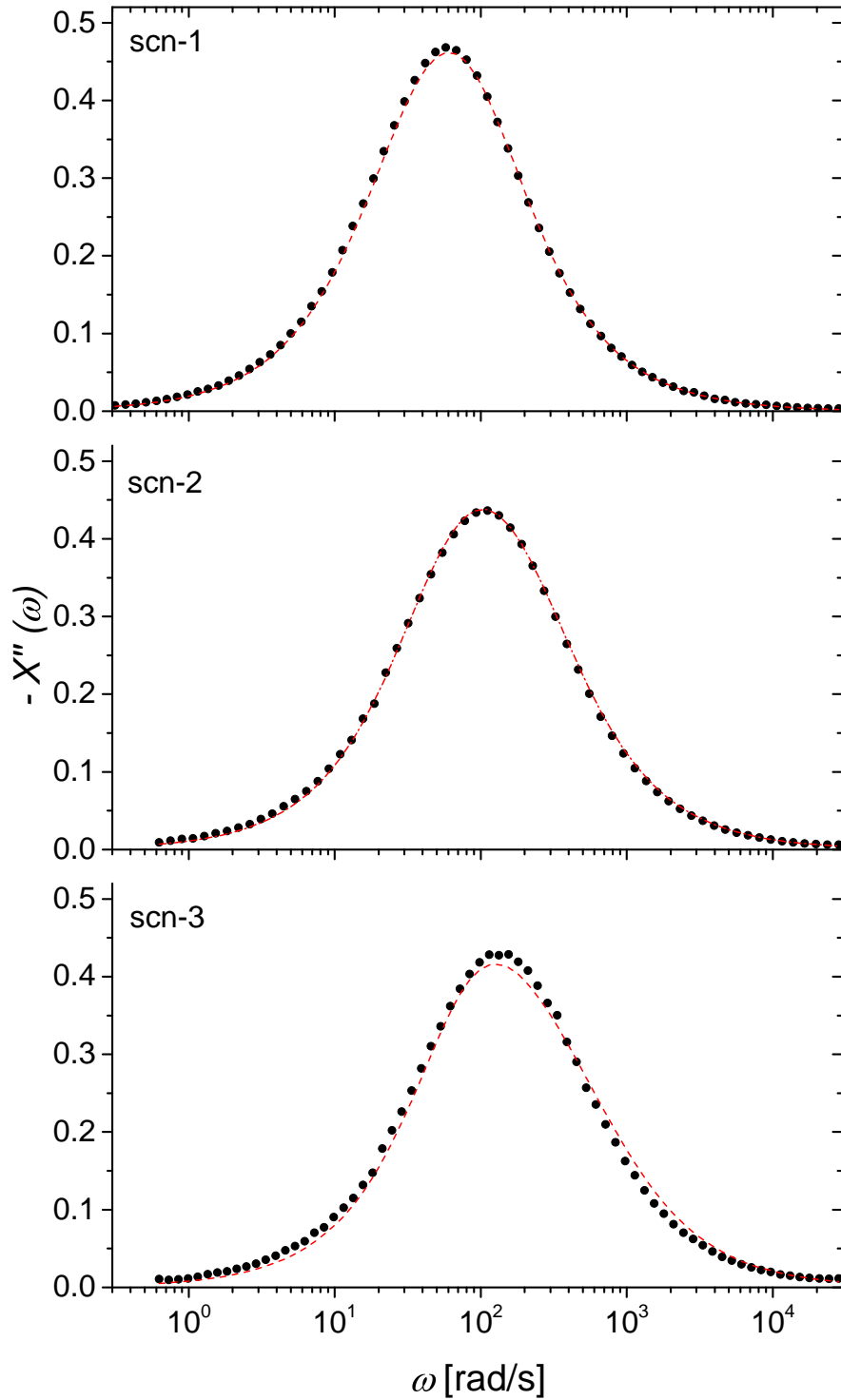


**Figure 7.13:** Measured imaginary part of the OF-MOT response function  $-X''(\omega)$  (full dots) as well as  $-X''(\omega)$  calculated by superposition of the relaxation peaks of single core particles and linear multi-core particles with two (red dashed lines) or two and three (red dash-dot lines) Ni cores. The mixing ratios for the superposition of relaxation peaks were free parameters, Tab. 7.6.

## 7.5 Multi-core particles

	sample	scn-1	scn-2	scn-3
best agreement	$R'_{sc}$ [%]	92.5	55.0	62.0
for superposition of peaks	$R'_{mc-2}$ [%]	7.5	32.0	38.0
	$R'_{mc-3}$ [%]	-	13.0	-

**Table 7.6:** Mixing ratios for the calculation of  $X''(\omega)$  by supersposition of peaks of polydisperse single core particles and monodisperse linear multi-core particles.

Since the transmitted intensity which is determined by the Beer-Lambert law is not an extensive quantity such as e.g. the magnetic moment, the superposition of peaks is not adequate. The magnetic, hydrodynamic, and optical properties of the particles have to be combined in one model to obtain a quantitatively sufficient and reliable theoretical signal of DC-MOT and OF-MOT signals. Simplified models can lead to significant deviations and regarding the OF-MOT, the question about the reliability of the mixing ratios of the particle fractions obtained by a simple superposition of peaks for single and multi-core particles arises. To investigate this issue a correct calculation which is based on a superposition of orientation dependent extinction cross sections will be performed in the following.

### Time-dependent superposition of orientation dependent cross sections

In order to investigate the influence of linear multi-core particles on the imaginary part of the response function  $-X''(\omega)$ , the time-dependent superposition of orientation dependent cross sections used to model the response of polydisperse ensembles is extended to include the contributions of linear multi-core particles. The resulting transmittance can be expressed by

$$T'_\omega(t) = \exp \left[ -N_s s \left( \left( R_{sc}/N_c \sum_i^{N_c} \left( \cos^2(\theta_{i,\omega}(t)) C_{\text{ext,L},i} + \sin^2(\theta_{i,\omega}(t)) C_{\text{ext,T1},i} \right) \right) + (1 - R_{sc}) \left( \cos^2(\theta_{mc,\omega}(t)) C_{\text{ext,L,mc}} + \sin^2(\theta_{mc,\omega}(t)) C_{\text{ext,T1,mc}} \right) \right) \right], \quad (7.6)$$

where  $\theta_{mc,\omega}(t)$  is the time and frequency dependent angle between the mean oscillating axis and the particle axis. The extinction cross sections of the linear multi-core particle for the L and T1 mode are  $C_{\text{ext,L,mc}}$  and  $C_{\text{ext,T1,mc}}$ . They were calculated by FEM for particles as described in Fig. 7.11 with  $d$ ,  $l$ ,  $D$  and  $D_{sh}$  chosen to the first moments of their distribution obtained by TEM for single core particles. The ratio of single core

## 7 - Results II - Quantitative modeling of DC- and OF-MOT signals of silica coated Ni nanorods colloids

---

particles  $R_{sc}$  was the only free parameter in the following model.

Furthermore, the number of Ni cores inside the linear multi-core particle will be increased in order to show the influence of the chain size on the modeled peaks. The OF-MOT spectra were modeled for three different combinations of polydisperse single core particles and monodisperse linear multi-core particles with two, three, or four Ni cores, respectively. The results of these calculations are shown in Fig. 7.14 and the obtained ratios as well as observed peak parameters can be found in Tab. 7.7.

For sample scn-1, the best result was found for a combination of 92.5% single core particles and 7.5% linear multi-core particles containing two Ni cores. For these parameters, the agreement between the calculated and measured maximum value of the peak was  $> 98\%$ . The agreement for the peak position was  $\geq 99.8\%$ . Further, an excellent agreement of the peak shape was found, as for all other samples. A combination with multi-core particles containing more than two cores resulted in very low fractions of these particles and an increasing deviation of the peak height.

For sample scn-2, the best combination of single core and linear two-core particles resulted in a curve slightly overestimating the peak maximum while the best combination with three-core particles resulted in a slightly underestimated maximum. The combination of single core particles with four-core particles resulted in a curve exhibiting a distinct shoulder and an insufficient description of the peak shape. A combination of single core particles with two fractions of multi-core particles containing two cores and multi-core particles containing three cores results in an improved agreement with the measured data, Fig. 7.15. For a mixture of 73% single core, 20% two-core, and 7% three-core particles, Tab. 7.7, this resulted in an agreement of 98.8% for the peak maximum and 99.9% for the peak position.

For sample scn-3, all combinations resulted in maxima below the measured one. The best agreement was found for a mixture of 77% single core particles and 23% multi-core particles with two cores. The corresponding agreement with the measured values was  $> 96.8\%$  for the peak height and 99.9% for the peak position.

It turns out that the first approach which was a simple superposition of peaks, leads to fits that show a comparable agreement with the measured data but also leads to significant differences in the obtained mixing ratios, Tab. 7.8. Hence, adequate modeling of the MOT signals of a mixture of different particle fractions requires the superposition of time modulated extinction cross sections in the Beer-Lambert law.

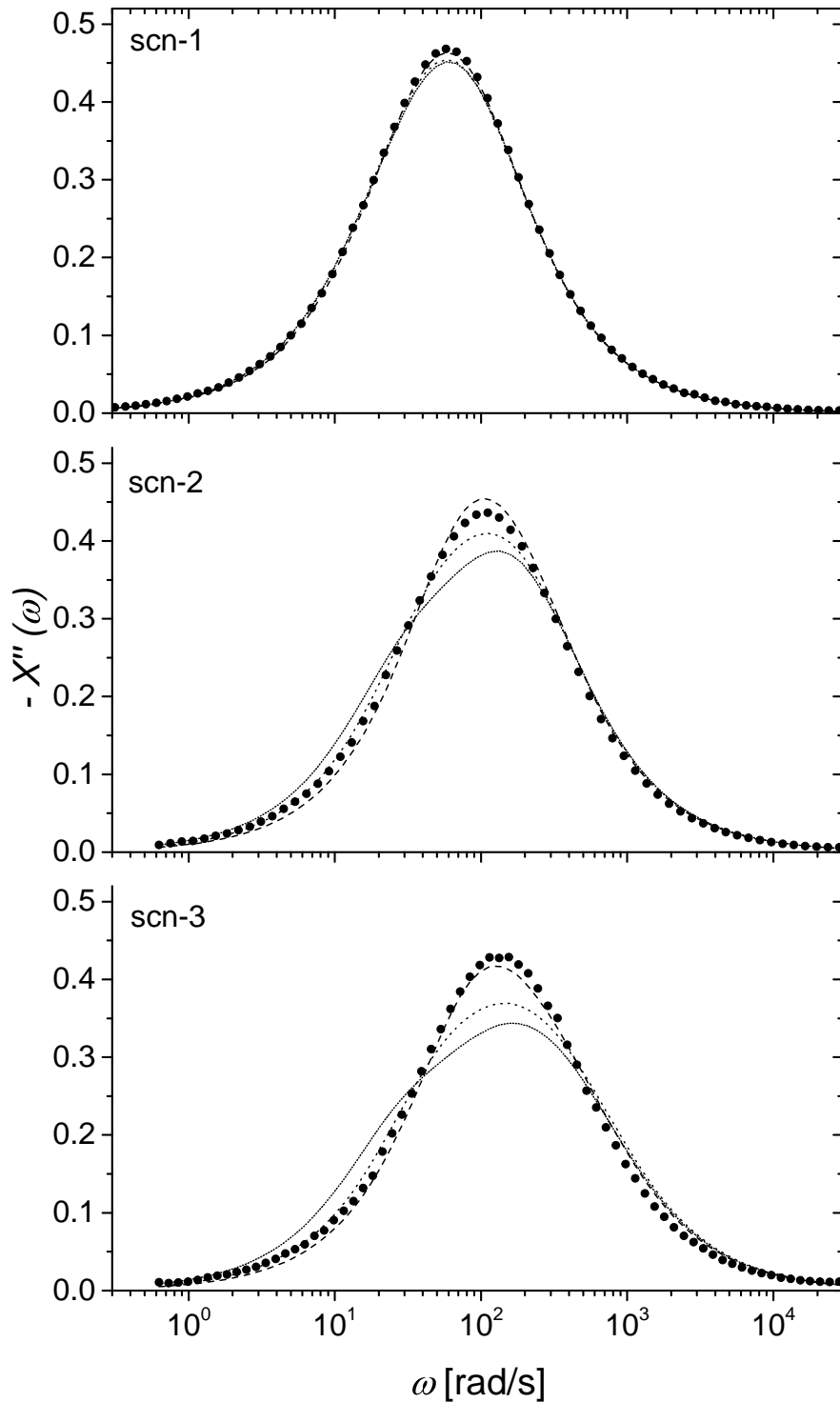


**Figure 7.14:** Measured imaginary part of the response function  $-X''(\omega)$  (full dots). The lines represent calculated signals resulting from a combination of polydisperse single core particles and monodisperse linear multi-core particles with two (dashed), three (dots) or four (small dots) Ni cores. The mixing ratio between single core and multi-core particles was the only free parameter, Tab. 7.7.

## 7 - Results II - Quantitative modeling of DC- and OF-MOT signals of silica coated Ni nanorods colloids

sample		scn-1	scn-2	scn-3
measurement	$X''_{\max}$	0.47	0.44	0.43
	$\omega(X''_{\max})$ [rad/s]	57.9	111.5	133.2
modeling including polydisperse single core particles and linear multi-core particles				
with two cores	$-X''_{\max}$	0.463	0.454	0.417
	$\omega(-X''_{\max})$ [rad/s]	57.8	111.7	133.3
	$R_{\text{sc}} \%$	92.5	68.0	77.0
	$R_{\text{mc-2}} \%$	7.5	32.0	23.0
with three cores	$-X''_{\max}$	0.454	0.410	0.369
	$\omega(-X''_{\max})$ [rad/s]	57.9	111.4	143.3
	$R_{\text{sc}} \%$	97.0	85.0	90.0
	$R_{\text{mc-3}} \%$	3.0	15.0	10.0
with four cores	$-X''_{\max}$	0.451	0.387	0.344
	$\omega(-X''_{\max})$ [rad/s]	57.9	133.4	155.5
	$R_{\text{sc}} \%$	98.5	90.0	92.0
	$R_{\text{mc-4}} \%$	1.5	10.0	8.0
with two and three cores	$-X''_{\max}$	-	0.435	-
	$\omega(-X''_{\max})$ [rad/s]	-	111.4	-
	$R_{\text{sc}} \%$	-	73.0	-
	$R_{\text{mc-2}} \%$	-	20.0	-
	$R_{\text{mc-3}} \%$	-	7.0	-

**Table 7.7:** Parameters of  $-X''(\omega)$  obtained by measurement and modeling assuming a combination of polydisperse single core particles and monodisperse linear multi-core particles with different numbers of Ni cores.

Having identified a satisfying model for OF-MOT measurements, the same method, i.e. the superposition of orientation dependent extinction cross sections, will be used to analyze the DC-MOT measurements.

## 7.5 Multi-core particles

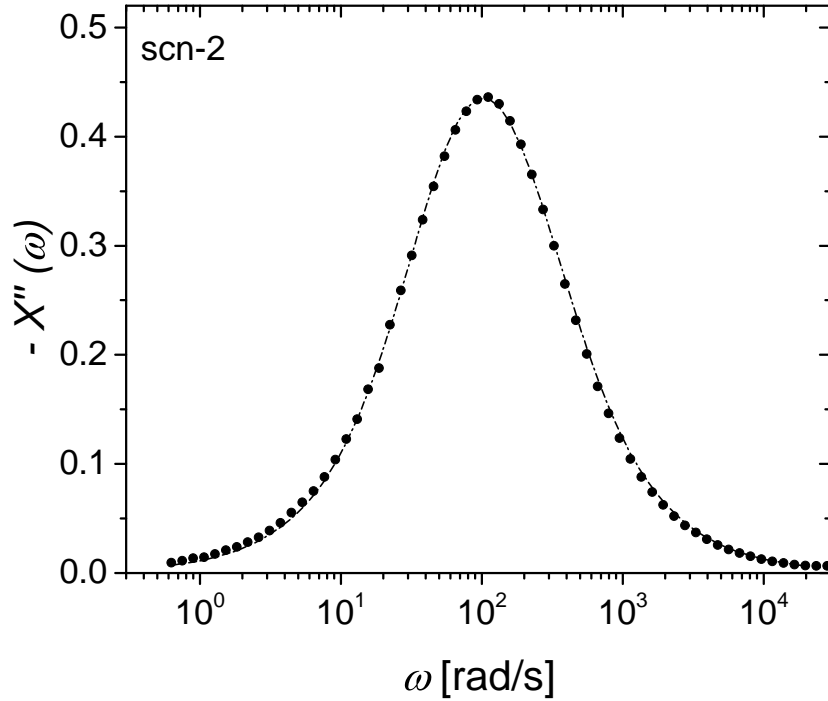


**Figure 7.15:** Measured imaginary part of the response function  $-X''(\omega)$  (points) of sample scn-2. The dash-dot line represents a calculated signal resulting from a combination of polydisperse single core particles and linear multi-core particles with two and three Ni cores. The mixing ratio between single core and multi-core particles was the only free parameter, Tab. 7.7.

	sample	scn-1	scn-2	scn-3
results repeated from Tab. 7.7	$R'_{sc}$ [%]	92.5	73.0	77.0
	$R'_{mc-2}$ [%]	7.5	20.0	23.0
	$R'_{mc-3}$ [%]	-	7.0	0.0
best agreement for superposition of peaks	$R'_{sc}$ [%]	92.5	55.0	62.0
	$R'_{mc-2}$ [%]	7.5	32.0	38.0
	$R'_{mc-3}$ [%]	-	13.0	-

**Table 7.8:** Mixing ratios for the calculation of  $X''(\omega)$  by supersposition of peaks of polydisperse single core particles and monodisperse linear multi-core particles.

### 7.5.2 Modeling DC-MOT using polydisperse single core and linear multi-core particles

Modeling the MOT of a combination of polydisperse single core particles and linear multi-core particles in static magnetic fields requires an extension of Eq. (5.21) to

$$I(H)_{\perp,\parallel}/I_{\times} = \exp \left[ - N s \frac{1}{N_c} \sum_{i=0}^{N_c} (C_{\text{ext}, i, \perp, \parallel}(H) - C_{\text{ext}, i, \times}) - N_{\text{mc}} s (C_{\text{ext}, \text{mc}, \perp, \parallel}(H) - C_{\text{ext}, \text{mc}, \times}) \right], \quad (7.7)$$

where  $N_{\text{mc}}$  is the concentration of linear multi-core particles,  $C_{\text{ext}, \text{mc}, \perp, \parallel}(H)$  their field dependent, and  $C_{\text{ext}, \text{mc}, \times}$  their orientation averaged extinction cross section which were individually calculated for every sample by FEM.

With  $N$  and  $N_{\text{mc}}$  as the only free parameters, the DC-MOT was modeled for a combination of polydisperse single core particles and monodisperse linear multi-core particles with  $n_c = 2$  (dashed), 3 (dotted) or 4 Ni cores (not shown), Fig. 7.16. A good agreement was found for all three combinations with small deviations in the saturation behavior, Tabs. 7.7 and 7.9. For sample scn-3, the experimental data for a perpendicular field (upper branch) were below the calculated curve. The initial slope of the first data points is apparently negative which suggests a small misalignment of the field direction in the experiment. In contrast to the modeling of the OF-MOT signals where the number of cores inside the multi-core particles had a significant influence, the modeled DC-MOT does not exhibit a strong dependence on the number of cores. However, the mixing ratios which were free parameters in the modeling of the DC- as well as the OF-MOT show the same trend for both measurement modes, i.e. the amount of single core particles is highest for sample scn-1 and lowest for scn-2.

It should be noted, that the curves obtained by a regression analysis assuming a monodisperse single core particle ensemble with diameter as a free variable, Fig. 7.3, resulted in a similar agreement. However, this regression analysis did not reveal the presence of aggregates which is the real reason for the increased field dependence of the measured signal and not as implicated first in section 7.2 the increased diameter of the single core particles.

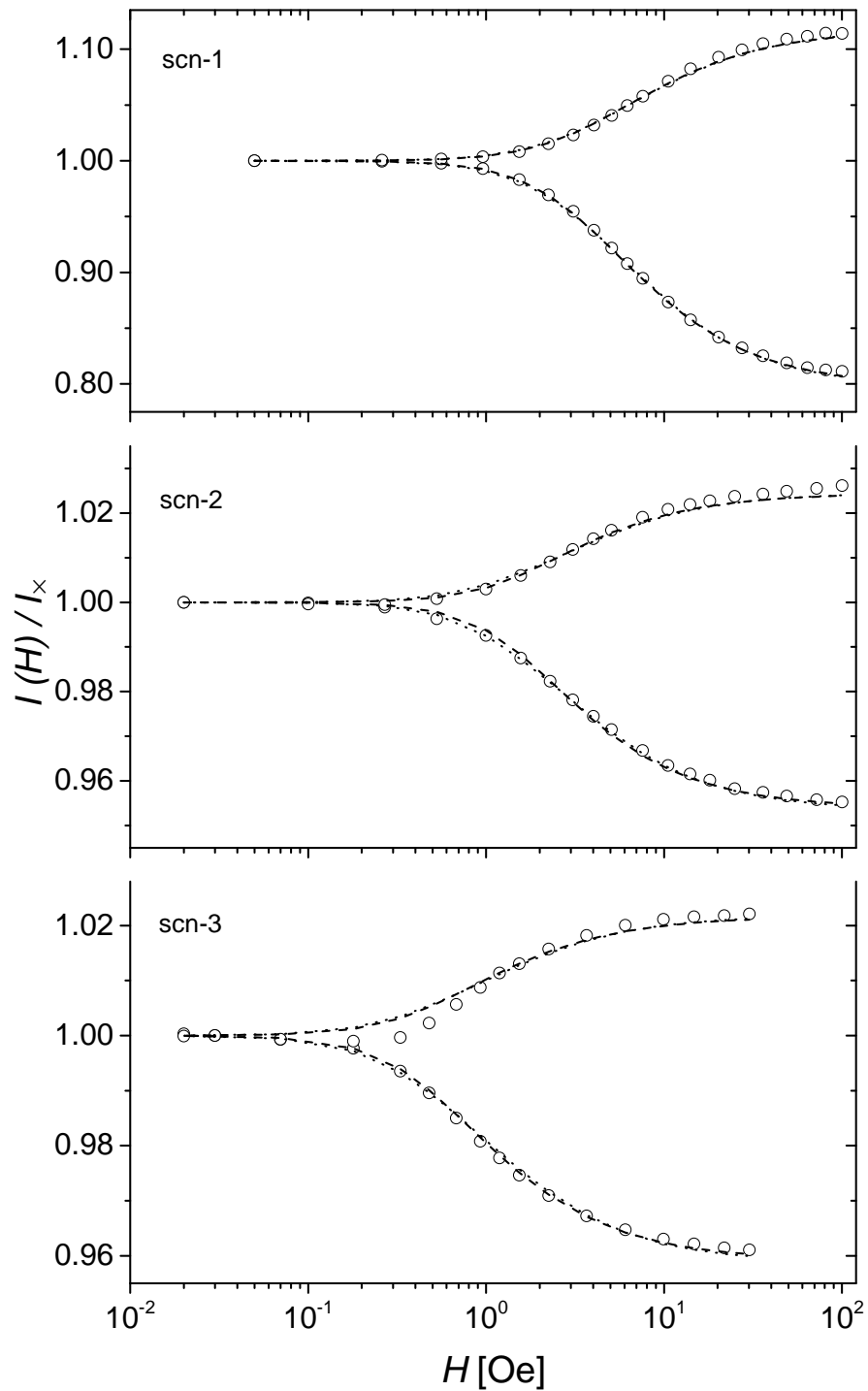


**Figure 7.16:** Measured normalized intensity  $I(H)/I_x$  as a function of the applied external magnetic field (open circles). The lines represent calculated signals resulting from a combination of polydisperse single core particles and monodisperse linear multi-core particles with two (dashed) or three (dots) Ni cores.

## 7 - Results II - Quantitative modeling of DC- and OF-MOT signals of silica coated Ni nanorods colloids

---

In conclusion, DC- as well as OF-MOT measurements of silica encapsulated Ni nanorod colloids can be quantitatively modeled with a combination of polydisperse single core particles and monodisperse linear multi-core particles with two (scn-1 and scn-3) or two and three (scn-2) Ni cores. The used models, especially for the multi-core particles, are rather simple and widely based on independent determined variables. This allowed to keep the number of free parameters low (one for OF-MOT and two for DC-MOT) and resulted in very good agreements between theoretically expected and measured signals. For comparison, in former studies performed on PVP coated Ni nanorod colloids, the measured values of rotational friction coefficients were twice as large as theoretically expected [24]. This indicates that silica encapsulated Ni nanorods are well suited as probe particles in both static and dynamic MOT measurements. The superior properties with respect to the well-defined particle-matrix boundary, however, are partially deteriorated by the presence of chain-like aggregates. If their formation during the Stöber process could be inhibited or their fraction in the colloid be significantly reduced by separation post-processing, the silica encapsulated Ni nanorods would be excellent model particles to investigate particle matrix interactions in soft materials.

Furthermore, the silica coating offers the possibility for various particle functionalizations like fluorescence labeling which was used to observe the cellular uptake of silica-encapsulated Ni nanorods by confocal laser scanning microscopy, appendix C, and increases the colloidal stability of the particles in solvents of high ionic strength significantly, appendix D.

## 7.5 Multi-core particles

---

Sample		scn-1	scn-2	scn-3
DC-MOT analysis (polydisperse), free parameter: $N$	$N$ [ $10^{15} \text{ m}^{-3}$ ]	6.9	1.07	0.3
model including polydisperse single core particles and linear multi-core particles				
with two cores	$N_{\text{sc}}$ [ $10^{15} \text{ m}^{-3}$ ]	5.08	0.295	0.153
	$N_{\text{mc-2}}$ [ $10^{15} \text{ m}^{-3}$ ]	0.79	0.359	0.07
	$R_{\text{sc}}$ [%]	86.5	45.1	68.6
	$R_{\text{mc-2}}$ [%]	13.5	54.9	31.4
with three cores	$N_{\text{sc}}$ [ $10^{15} \text{ m}^{-3}$ ]	5.78	0.592	0.225
	$N_{\text{mc-3}}$ [ $10^{15} \text{ m}^{-3}$ ]	0.3	0.141	0.024
	$R_{\text{sc}}$ [%]	95.0	80.8	90.4
	$R_{\text{mc-3}}$ [%]	5.0	19.2	9.6
with four cores	$N_{\text{sc}}$ [ $10^{15} \text{ m}^{-3}$ ]	6.02	0.689	0.247
	$N_{\text{mc-4}}$ [ $10^{15} \text{ m}^{-3}$ ]	0.18	0.084	0.013
	$R_{\text{sc}}$ [%]	97.1	89.1	95.0
	$R_{\text{mc-4}}$ [%]	2.9	0.9	5.0

**Table 7.9:** Parameters obtained by the regression analysis of DC-MOT measurements assuming polydisperse single core particles only (repeated from Tab. 7.5) and assuming a combination of polydisperse single core particles and monodisperse linear multi-core particles with two, three or four Ni cores, Fig. 7.16.

## 7 - Results II - Quantitative modeling of DC- and OF-MOT signals of silica coated Ni nanorods colloids

---

# Chapter 8

## Summary

*The first part of this summary concerning the static magnetic field-dependent optical transmission of suspensions of PVP coated Ni nanorods corresponds to the related section in publication [43], see appendix E.*

The objective of this work was to investigate the dynamic properties of silica coated Ni nanorods in colloidal suspensions and to derive a quantitative model for optical transmission measurements of rotational relaxation in oscillating magnetic fields. Because the field dependent optical response involves magnetic, hydrodynamic, and optical properties of non-spherical core-shell particles, the complexity of the modeling was increased step-by-step aiming at a description which is sufficient to correctly capture all signal features quantitatively, yet with the lowest possible number of unknown variables.

In the first step, PVP coated Ni nanorods of different length were synthesized by the AAO-template method and their structure was characterized by transmission electron microscopy. The collinear magnetic and optical anisotropy was revealed by the static field-dependent optical extinction of linearly polarized light, depending on the orientation between the magnetic field and optical polarization. The experimental data were analyzed by assuming a superparamagnetic orientation distribution function for the nanorod magnetic dipoles. As compared to earlier studies, different models for the optical cross-sections were investigated in detail. The consequences of two common approximations, i. e. (i) the electrostatic approximation for the polarizability of the particles at optical frequencies, and (ii) approximation of the particle shape as prolate spheroid, were of particular interest. For comparison, extinction cross sections were calculated for spheroidal particles by the electrostatic approximation (EA), the separation of variables method

(SVM), and FEM simulation. Using the latter, the optical cross sections were also determined for capped cylindrical particles. The approximations regarding the polarization (homogeneous and quasistatic vs. inhomogeneous and dynamic) and the shape (spheroidal vs. cylindrical) of the different approaches resulted in significant differences in the optical cross sections. In a regression analysis, the various models were applied to field-dependent optical transmission data using the average length of the nanorods obtained from TEM image analysis as fixed and the diameter and concentration of the nanorods as variable parameters. The results for the diameter were identical for EA and the FEM-based models whereas the expected differences were all captured in the concentration parameter. This asymmetry was attributed to the particular correlation of the two model parameters to the relevant physical quantities. The characteristic field dependence of the transmission was directly related to the magnetic moment per nanorod. Given a fixed length of the nanorods, regression analysis provided the same diameter – and hence the same particle volume – consistent with this magnetic moment. The differences in the optical cross sections between the two calculation methods of the extinction cross section (EA vs. FEM) were compensated in the regression analysis by the particle concentrations. A convenient procedure was suggested for modeling the optical properties of Ni nanorods by using analytical cross sections for spheroids in the EA and tabulated factors to compute corrected particle densities. This approach is restricted to dilute nanorod colloids in which the concentration is low enough to neglect near-field electromagnetic interaction which was verified for the present work by FEM simulation of extinction cross sections for pairs of nanorods in end-to-end configuration and side-by-side configuration as a function of their spacing.

In the second step, Ni nanorods were coated with a silica layer using the Stöber process. The length and diameter of the Ni core and of the overall core-shell particles were determined from TEM image analysis. The tabulated values of these parameters were used as a complementary data base for modeling the magnetic, hydrodynamic, and optical properties of the polydisperse nanorods in suspension. Similar to the procedure used for the PVP coated Ni nanorods, the superparamagnetic orientation distribution served as the basis to model the field-dependent static MOT. In order to model the oscillating magnetic field-dependent optical transmission, the time resolved orientation of the particles which is determined by their rotational friction coefficient and their magnetic moment was calculated by the equation of motion in oscillating magnetic fields. Using the time dependent orientation of the particles, the orientation dependent extinction

---

cross section and thus the transmitted intensity could be calculated. By variation of the magnetic field oscillating frequency, the magnetic field-dependent optical response function was obtained.

As a first approach, the diameter of the Ni core was set as a free parameter in the modeling of the DC-MOT signal. Although the obtained fitting curves showed a reasonable agreement with the measured data, the obtained diameters were larger than those observed in TEM. This result was not expected as similar measurements on PVP coated Ni nanorods typically provide smaller diameters of the magnetic core due to the presence of a surface oxide layer. Comparison with a second analysis based on a diameter fixed at the expected value clearly showed that the deviation of a few nanometers was significant. Additional information was obtained from the dynamical properties of the particles measured in oscillating magnetic fields. The relaxation frequencies were closer to the measured signal for the smaller core diameter. In addition, the measured relaxation peaks exhibited a slight reduction in the peak maximum as well as some broadening which is related to the polydispersity of the nanorods.

In the third step, polydispersity was taken into account by calculating the physical properties of each silica/Ni core-shell nanorod tabulated in the TEM image analysis database. Assuming this sample of particles to be representative for the ensemble, the measured field-dependent transmission signals were computed. As expected, the inclusion of polydispersity resulted in a reduction in peak maximum as well as the observed broadening. However, the calculated relaxation frequencies were still higher than measured.

Inspired by TEM micrographs exhibiting single core particles as well as several types of multi-core particles, the used models were extended again. Combining polydisperse single core particles with an additional particle fraction, i.e. linear multi-core particles, resulted in models which show very good quantitative agreements with the measured data for static and dynamic MOT. Using tabulated values for the size of the nanoparticles obtained from TEM image analysis as a complementary source of information only one (OF-MOT) or two (DC-MOT) free variables were needed.

In conclusion, the particles have well-defined magnetic, optic, and hydrodynamic properties and are suitable as probe particles in microrheological experiments. If the contribution of chain-like agglomerates could be suppressed, they could be used as model particles. Furthermore, the silica coating offers the possibility for various particle func-

tionalizations like fluorescence labeling, appendix C, and increases the colloidal stability of the particles in solvents of high ionic strength significantly, appendix D.

# Chapter 9

## Outlook

As shown in the present work, silica-encapsulated Ni nanorods exhibit well-defined hydrodynamic properties compared to PVP stabilized nanorods. This implies an almost perfect suitability to study particle-matrix-interactions. This holds particularly in the case of dispersions of single core particles, as shown by sample scn-1. In order to benefit from the superior properties in microrheological standard measurements, it would be necessary to minimize the concentration of multi-core particles.

A decreased concentration of multi-core particles can be achieved either by improvement of the synthesis protocol or additional separation steps like fractionation in magnetic field gradients or centrifugation.

Regardless of the success of further optimizations, the particles are very well suited as probes for microrheological studies since the ensemble averaged hydrodynamic properties, including the contribution of multi-core particles, can be readily characterized by a reference measurement in a matrix with known rheological properties. For this purpose, a purely viscous matrix like the glycerol water mixture used in this work can be used for example. As long as the silica surface of the particles is not modified in the biological or chemical environment of the investigated sample, it is expected that the geometrical factor in the rotational friction coefficient of the nanorods stay constant. With the correct calibration, magnetic field-dependent optical transmission measurements in rotating, alternating, or as used in this work, oscillating magnetic fields can be used to study viscoelastic properties of complex soft matter on length scales that are determined by the size of the nanorods. An interesting and yet open question is the characteristic length scale of such substances that separates the regime of macroscopic properties from the regime in which the molecular structures can be resolved. An example for which this question is of practical importance is mucus which is a biological substance that

covers the luminal surfaces of e.g. gastrointestinal and pulmonary tissue in humans and most animals. On a macroscopic scale, mucus exhibits highly viscous or viscoelastic properties. However, the more interesting behavior is observed on a microscopic scale. On this scale, mucus allows the transport of nutrients and at the same time suppresses the passage of pathogens. This selective barrier behavior is achieved by a special combination of a particular cellular structure of the mucin network and its physico-chemical properties. A detailed understanding of the transport properties of mucus is of great importance for the drug administration and could be investigated using nanorods as size variable probe particles.

The silica coating also enables further functionalization of the Ni nanorods. Incorporation of fluorescence label such as Rhodamine B offers the possibility to observe single particles using confocal laser-scanning microscopy. This modification was successfully integrated in the synthesis of the core shell particles. The resulting particles were used to investigate the magnetic field induced rotation of individual nanorods in elastic hydrogels and the incorporation of Ni nanorods in cell cultures of human brain microvascular endothelial cells (HBMEC), appendix C. The latter one was performed in a cooperation with the group of Dr. J. Clement at the Department of Hematology and Oncology of the Jena University Hospital. The corresponding studies focus on the global cytotoxicity and the details of intracellular processes which are initiated by the penetration of the nanorods into the cell. Hereby, first details of the pro-survival as well as stress and inflammation associated signaling pathways were found.

For studies of biological samples, an additional advantage of silica encapsulated nanorods as compared to the PVP coated nanorods has turned out and is of great importance. The large shell thickness of typically 50 nm increases the stability of the nanorod colloid against coagulation. Due to long range dipolar interactions, the colloidal stability of the PVP coated nanorods is at risk and requires an efficient electrostatic stabilization. At the high ionic strength of typical biological systems, the electrostatic screening length is reduced to a few nanometers. This results in a fast agglomeration of the nanorod colloids. As shown in appendix D, the silica coating which acts as additional space between the magnetic Ni cores increases the colloidal stability of the Ni nanorod colloid significantly. The positive effect of the silica shell regarding the coagulation is accompanied by a faster sedimentation of the core-shell particles due to their larger size. The coagulation of the nanorods at high ionic strength was not completely suppressed but the agglomerates were only weakly bonded. This enables a complete redispersion using ultrasonication. The coagulation of the silica encapsulated nanorods at different ionic strength and pH

---

values should be investigated systematically to determine the time frame of an individual dispersion of the nanorods in biological systems.



## Appendix A

### Additional TEM micrographs of PVP coated Ni nanorods

In this appendix, some additional TEM micrographs of PVP coated Ni nanorods used in this work are shown.

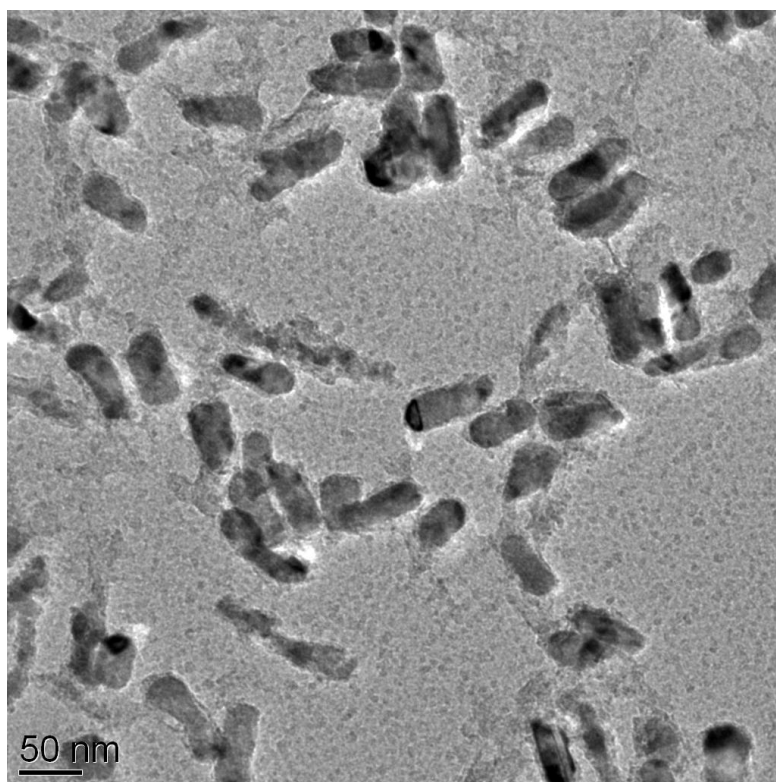


**Figure A.1:** TEM micrographs of sample pcn-1.

A - Additional TEM micrographs of PVP coated Ni nanorods

---

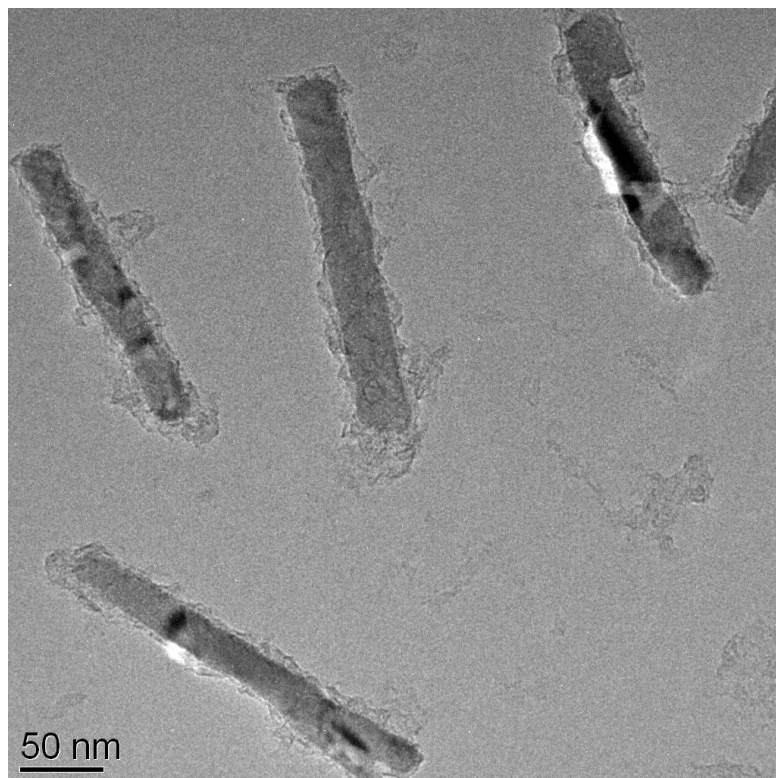
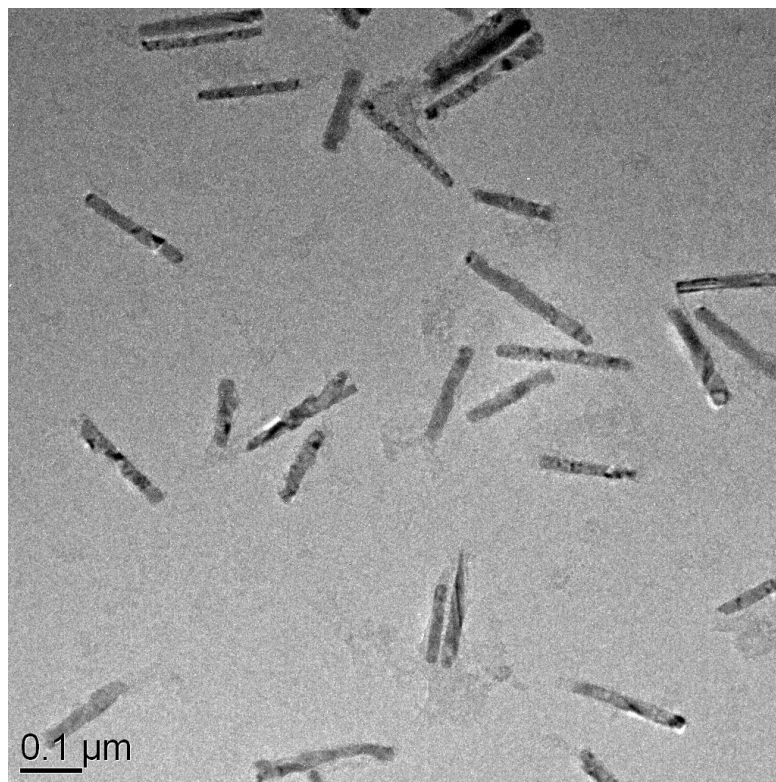


**Figure A.2:** TEM micrographs of sample pcn-2.

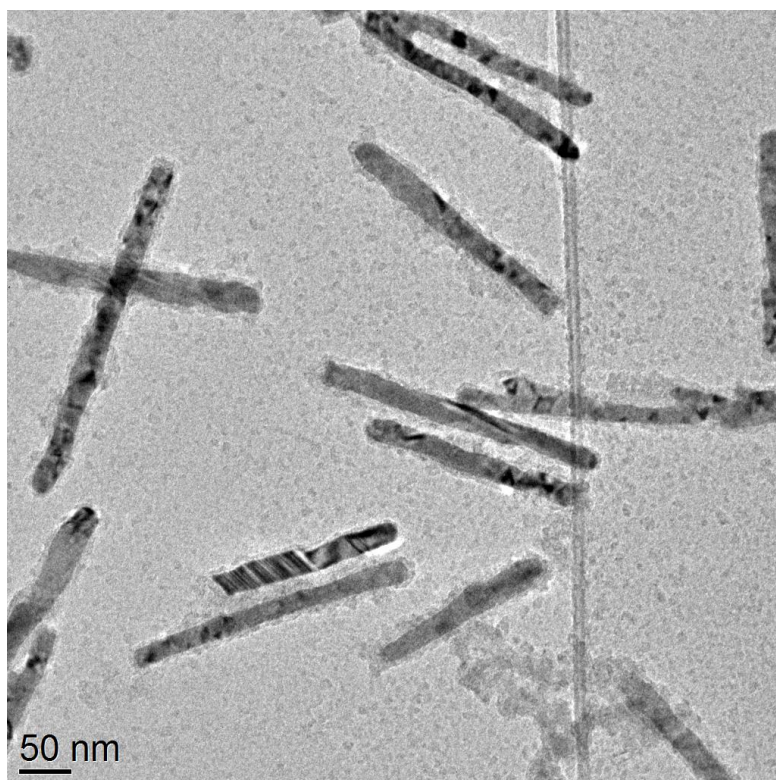
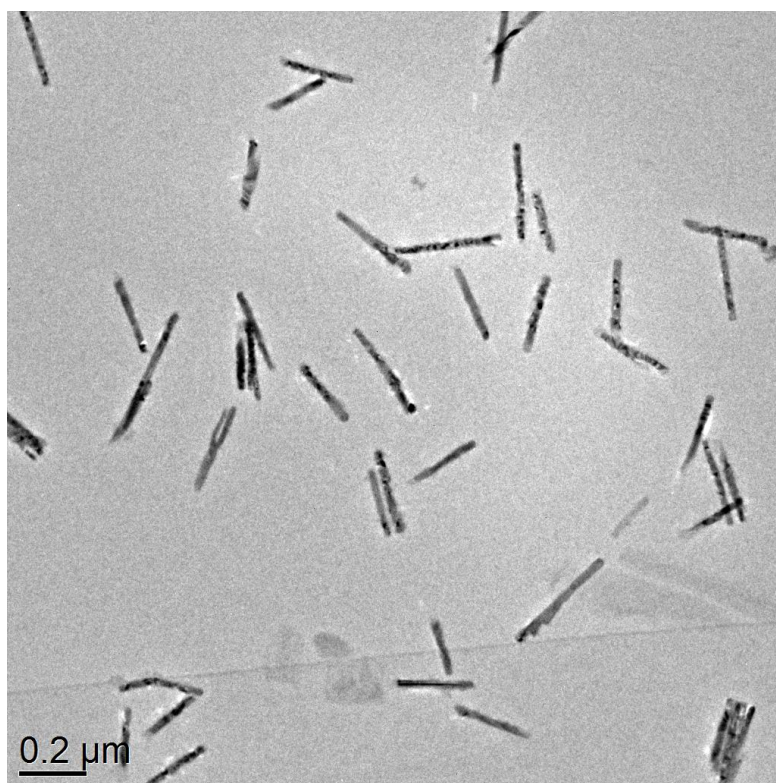


**Figure A.3:** TEM micrographs of sample pcn-3.

A - Additional TEM micrographs of PVP coated Ni nanorods

---

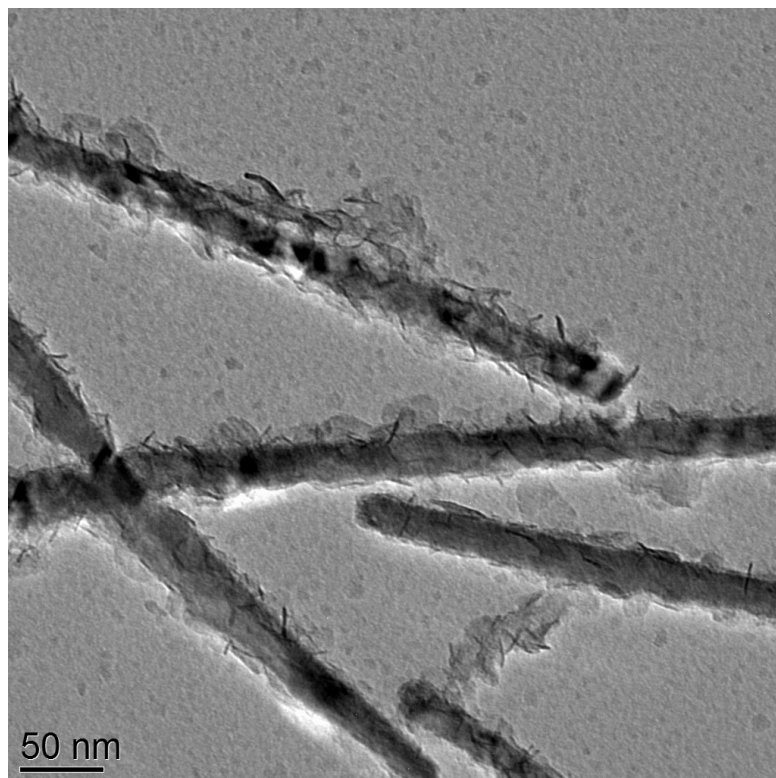
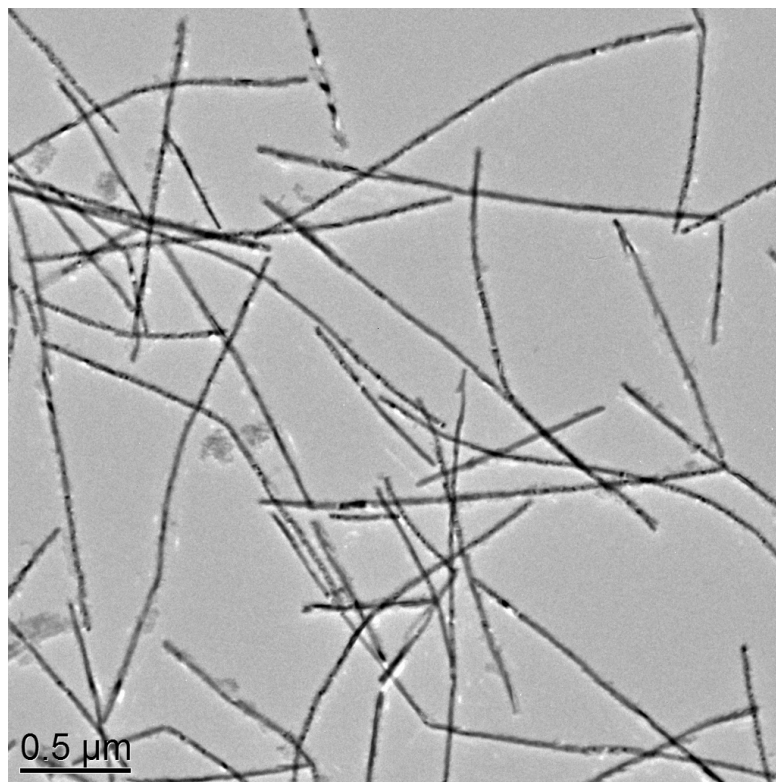


**Figure A.4:** TEM micrographs of sample pcn-4.

## Appendix B

### Additional TEM micrographs of silica coated Ni nanorods

In this appendix, some additional TEM micrographs of silica coated Ni nanorods used in this work are shown.

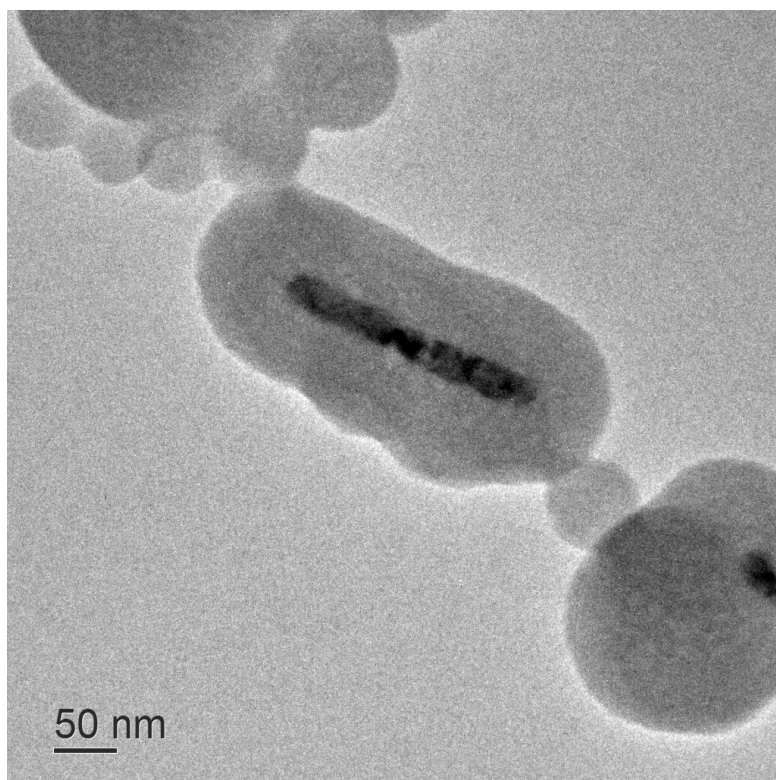


**Figure B.1:** TEM micrographs of sample scn-1.

B - Additional TEM micrographs of silica coated Ni nanorods

---

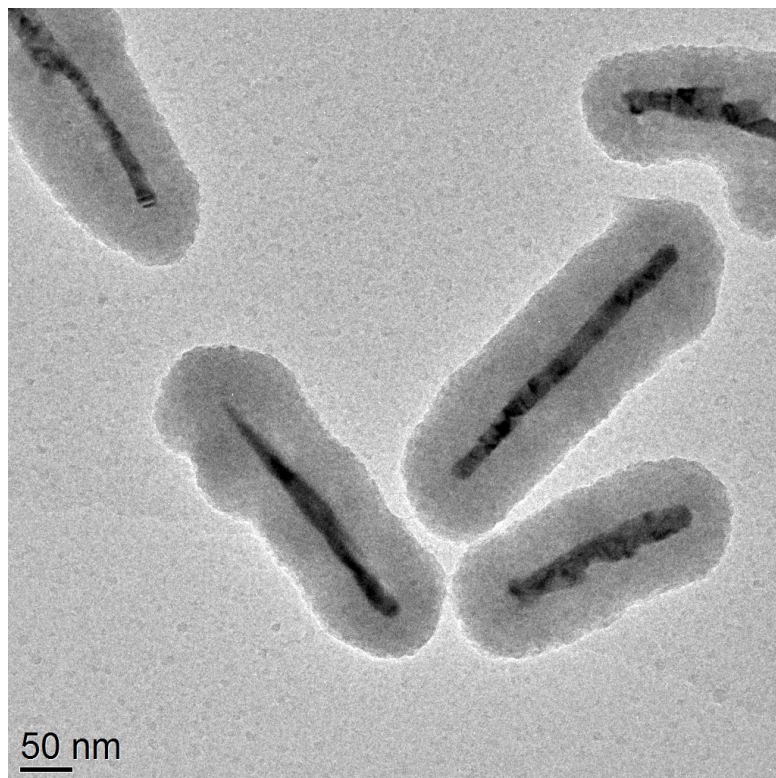
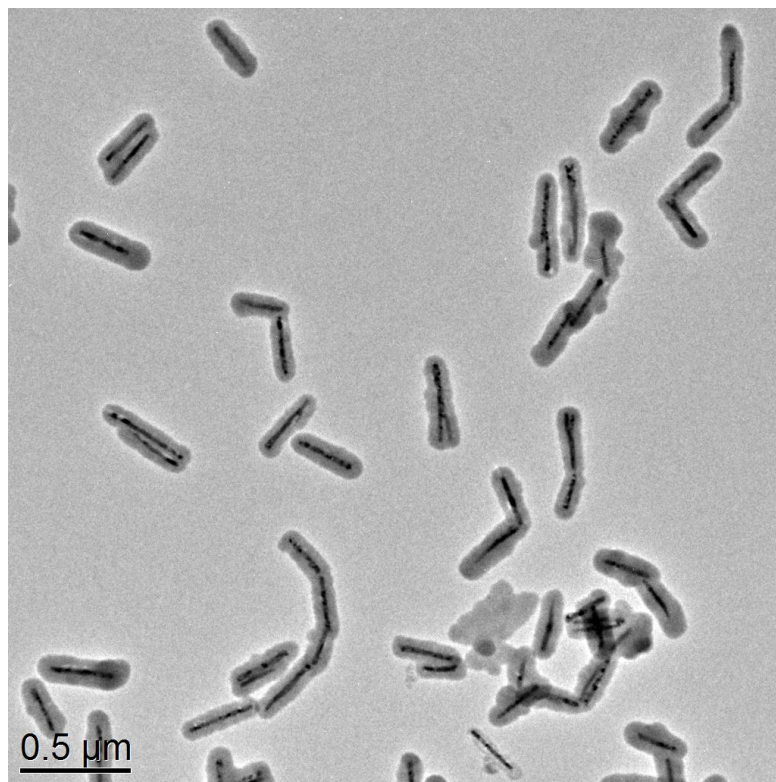


**Figure B.2:** TEM micrographs of sample scn-2.

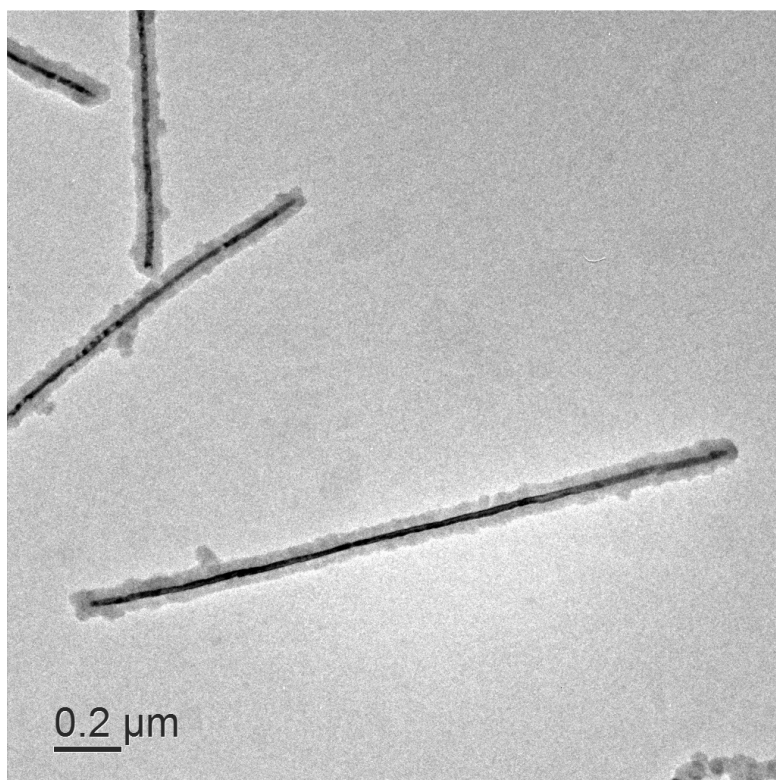
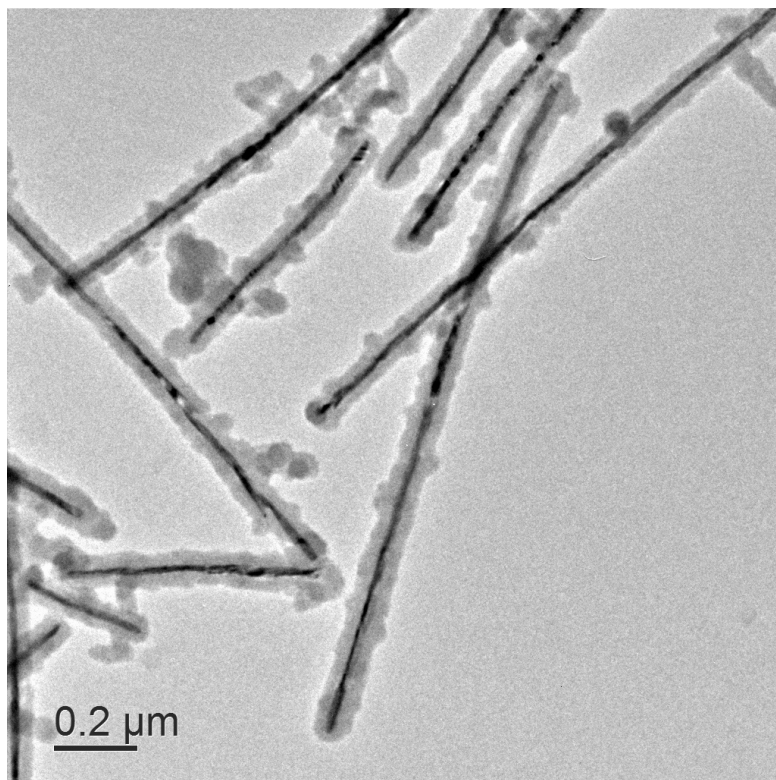


**Figure B.3:** TEM micrographs of sample scn-3.

## B - Additional TEM micrographs of silica coated Ni nanorods

## Appendix C

# Vitality of human cells interacting with differently coated Ni nanorods

In the following, some results on the interaction of Ni nanorods with human brain microvascular endothelial cells (HBMEC) obtained in cooperation with the group of J.H. Clement, Department of Hematology and Oncology, Jena University Hospital, will be summarized. The results have been published at conferences [110] and for more information, reference is made to the master thesis of A.-K. Schmidt [111].

Magnetic nanomaterials are a subject of current biomedical research. Spherical iron oxide nanoparticles are widely used due to their comprehensively tested biocompatibility and their biodegradability. Although the usability of Ni nanoparticles in biomedical applications, e.g. for gene or drug delivery were investigated [112, 113], Ni ions exhibit a low biocompatibility. To enable a reasonable usage in biomedical research, Ni particles have to be encapsulated with a material of higher biocompatibility. The effect of different coatings of Ni nanorods on cell viability of human brain microvascular endothelial cells (HBMEC) which are a commonly used model for the blood brain barrier [114] was investigated. For this purpose, colloidal dispersions of Ni nanorods with different coatings (PVP, silica, silica with rhodamine B, and gelatine) were synthesized.

To ensure an interaction of the nanorods with the cells, the cellular uptake was investigated first. For this purpose, silica coated Ni nanorods with an additional Rhodamine B labeling were synthesized by varying a procedure provided by Günter Auernhammer, Max Planck institute for polymer research, Mainz, in personal communication, as follows. First, a beaker with 10 ml 2-propanol was placed on a magnetic stirrer. After addition of 0.0938 g 3-(Aminopropyl)triethoxysilan and a short waiting time of about

## C - Vitality of human cells interacting with differently coated Ni nanorods

2 min, 0.1178 g rhodamine B isothiocyanat was added. The beaker with the mixture was closed and wrapped into Al foil to preserve photo-stability and the mixture was stirred overnight. Then a Stöber process as described in section 2.2 was carried out, with a volume of 0.28  $\mu\text{l}$  per 100 ml isopropanol of the mixture. The obtained rhodamine B labeled silica coated Ni nanorods suspensions were stored in a dark environment to preserve photo stability of the nanorod solution.

To perform the cellular uptake experiments, the rhodamine B labeled silica coated Ni nanorods suspensions were added to HBMEC's. After a incubation time of 0.5 h, 3 h, and 24 h, the cell nuclei and the actin cytoskeleton were stained with DAPI (blue) and phalloidin-Alexa fluor 488 (green), respectively, and the particle uptake of the cells was investigated using a confocal laser scanning microscope, Fig. C.1.

In the next step, the cytotoxicity of the differently coated particles were investigated. The vitality of HBMEC's after 3 h and 24 h incubation time was studied using PrestoBlue Cell Viability Assay (Invitrogen, Germany) and flow cytometry (Annexin V / Propidium iodide staining). Furthermore, Real-Time Cell Analysis (RTCA) (ACEA Biosciences, USA) was applied for long term studies. The results of these investigations are shown in Tab.C.1. For time periods  $\leq 24$  h, independent on the particle coating, the cell viability of HBMEC was not dramatically perturbed for the used particle concentrations. Rergarding longer timeperiods, the viability of HBMEC cells was affected at higher concentrations of Ni nanorods. In these experiments, the viability was best for silica coated Ni nanorods, followed by gelatine coated and PVP coated nanorods.

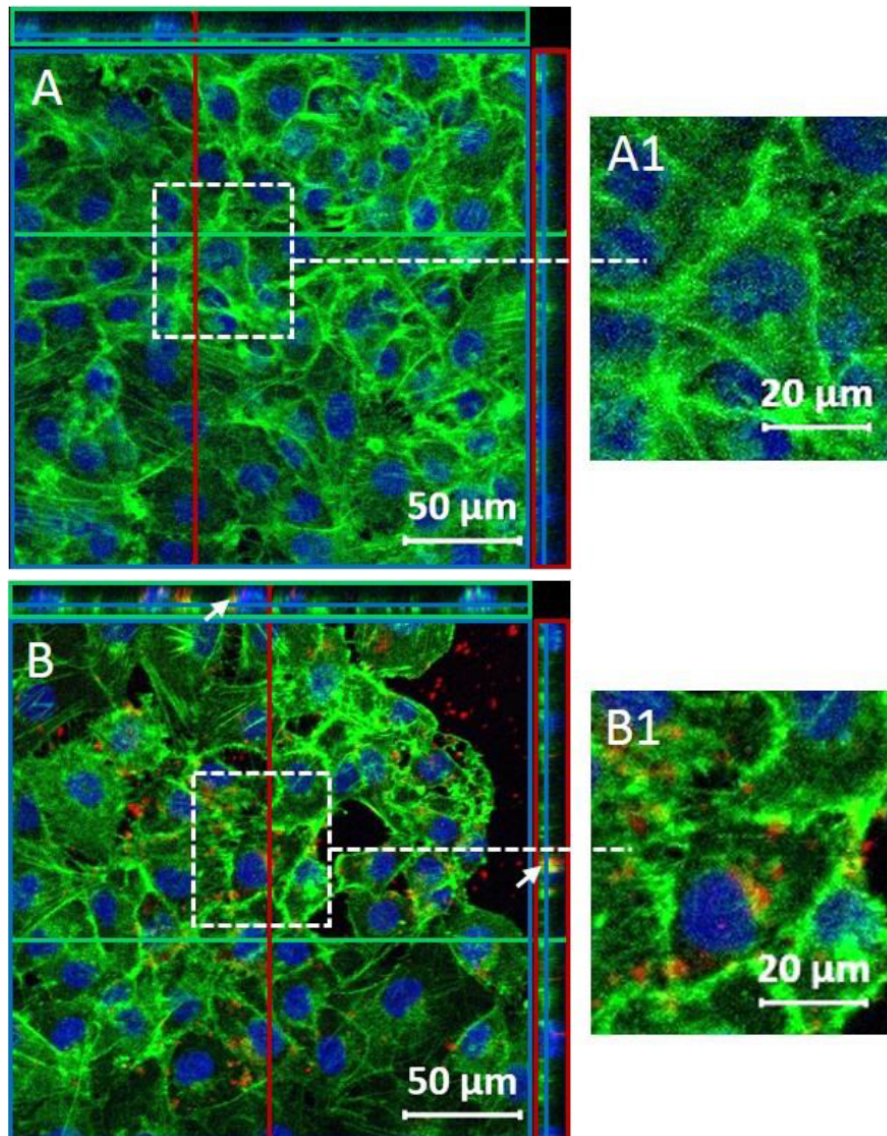


**Figure C.1:** Localization and quantification of internalized silica rhodamine B coated Ni nanorods into HBMEC after 24 hours of exposure: 200000 HBMEC were seeded onto flamed coverslips which were placed into the wells of a 4-well cell culture plate. After overnight cultivation, the cells were exposed to silica rhodamine B coated Ni nanorods in a final Ni concentration of  $1.5 \mu\text{g}/\text{cm}^2$  for 24 hours (B, B1). A, A1 indicate control cells without nanoparticle incubation. After cell fixation and permeabilization, the cell nuclei and the actin filaments were stained with DAPI I counterstain (blue) and Alexa Fluor<sup>®</sup> 488 phalloidin (green), respectively. Representative images were recorded with the confocal laser scanning microscope LSM 510 Meta (Zeiss, Germany). The  $x$ - (green lines),  $y$ - (red lines), and  $z$ -levels (blue lines) are depicted simultaneously in the images A and B. White arrows indicate internalized nanoparticles. A1 and B1 are magnifications of a part of the images A and B, image and text from [111].

## C - Vitality of human cells interacting with differently coated Ni nanorods

---

coating	concentration	vitality assay							
		PrestoBlue		flow cytometry		RTCA			
		3h	24h	3h	24h	3h	24h	48h	96h
PVP	1	green	green	green	green	green	green	green	green
	10	green	green	yellow	green	green	green	yellow	red
	25	green	green	red	green	yellow	yellow	red	red
gelatine	1	green	green	green	green	green	green	green	green
	10	green	green	green	green	green	green	green	green
	25	green	green	yellow	green	yellow	yellow	yellow	yellow
silica	1	green	green	green	green	green	green	green	green
	10	green	green	green	green	green	green	green	green
	25	green	green	green	green	green	green	green	red

**Table C.1:** Influence of Ni nanorods on the vitality of HBMECs: Ni nanorods with 3 different coatings were applied to HBMEC cultures in different concentrations and for up to 96 hours. Cell vitality was monitored with 3 assays independently and rated as follows: green: cell vitality  $\geq 70\%$  of control, yellow: cell vitality  $30\% - 70\%$  of control, red: cell vitality  $\leq 30\%$  of control, table and text from [110].

## Appendix D

# Colloidal stability of silica encapsulated nanorods in aqueous dispersions

In [103], the DC-MOT measurements on colloidal suspensions of PVP coated Ni nanorods were performed and the obtained transmitted intensities  $I(H)$  were normalized to the intensity of the zero-field transmission  $I_{\times}$ , Fig.D.1 (full dots). A regression analysis based on the same model as used in section 6.4.2 was applied and resulted in a reasonable agreement with the measured data, Fig.D.1 (solid line).

The obtained particle lengths, diameters, and particle concentrations also allowed the calculation of the absolute transmitted intensity  $I(H)$  normalized to a reference measurement of pure water  $I_0$ , Fig.D.1 (dashed line). Comparison with the corresponding measured values of  $I(H)/I_0$  revealed significant differences indicating an additional field-independent contribution to the optical extinction. Due to the dipolar nature of the nanorods, flux-closing structures such as nanorod dimers without magnetic field-dependent optical activity were expected to be the primary reason for the field-independent extinction contribution. This assumption is supported by the observation of such aggregates in TEM micrographs, Fig.D.2. The basic idea in [103] was to use the difference between the theoretically expected and measured  $I/I_0$  to determine the concentration of agglomerated particles in addition to the concentration of individually dispersed nanorods. This quantity was used to characterize the colloidal stability of Ni nanorod dispersions. Taking into account the long-range magnetic dipolar interaction between the magnetic nanorods, colloidal stability relies on an efficient long-range electrostatic repulsion between the nanorods originating from their positive surface charge. Increas-

## D - Colloidal stability of silica encapsulated nanorods in aqueous dispersions

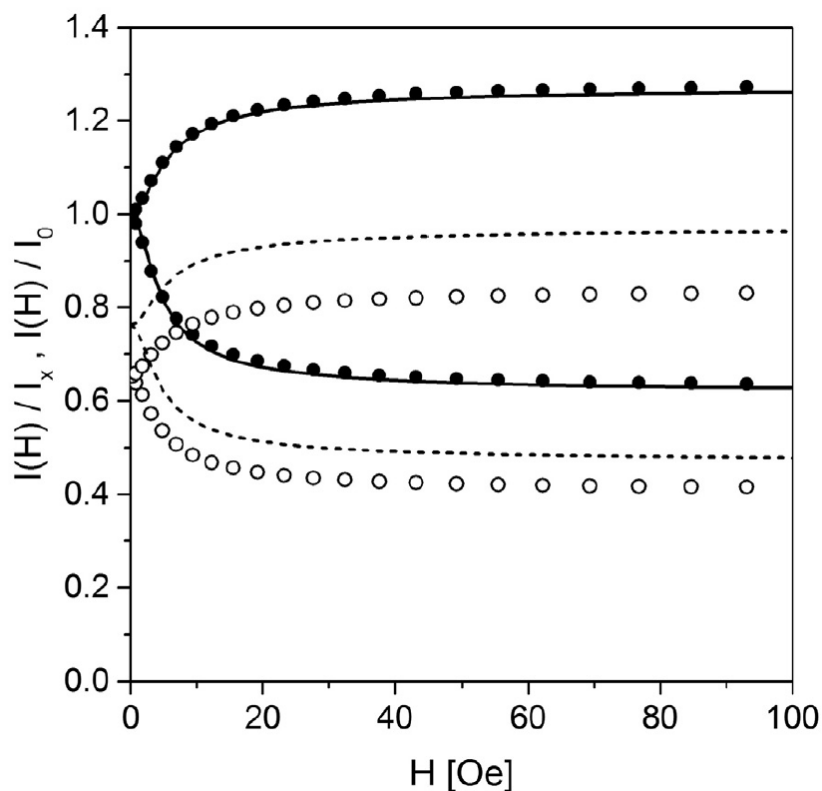


**Figure D.1:** Transmitted laser intensity as a function of the magnetic field parallel (lower branches) or perpendicular (upper branches) to the polarization direction, normalized to the zero-field transmission  $I_x$  (full dots). Data analysis of the zero-field normalized measurements (solid line) provided the concentration of singly dispersed particles  $N_s$ . The discrepancy between the calculated absolute transmittance (dashed line) and the experimental data normalized to a reference measurement of pure water (open circles) points to the presence of a magneto-optically inactive contribution to optical extinction, image and text from [103].

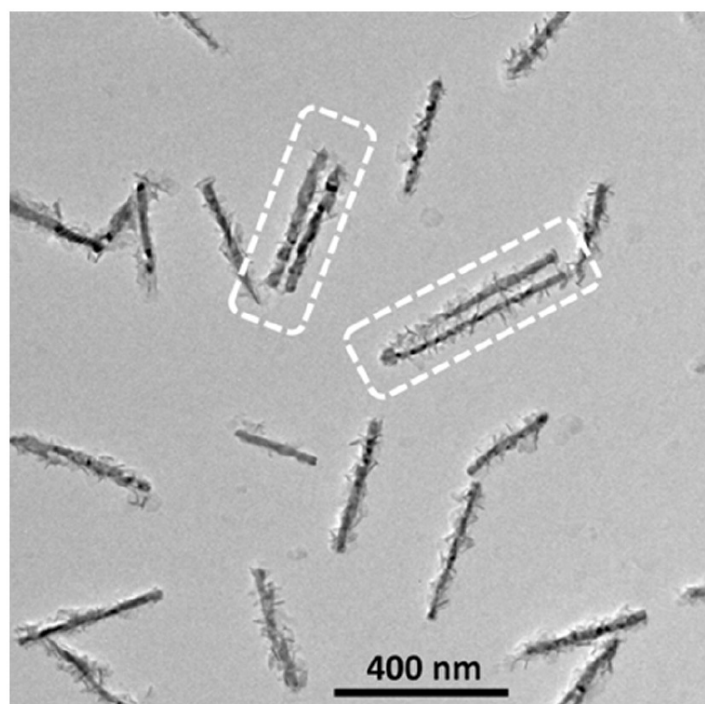


**Figure D.2:** A TEM image reveals individual Ni nanorods as well as aggregates such as dimers of parallel nanorods (marked by dashed white frame), image and text from [103].

## D - Colloidal stability of silica encapsulated nanorods in aqueous dispersions

ing the ionic strength implies decreasing screening length and is expected to result in an increasing coagulation rate of the nanorods. In [103], NaCl was used for a deliberate destabilization of the dispersion and, by analyzing  $I/I_\times$  from a series of DC-MOT measurements, the concentration of singly dispersed particles  $N_s$  was monitored as a function of time. Furthermore, an additional analysis of  $I/I_0$  was used to obtain the concentration of Ni nanorods trapped in magneto-optically inactive agglomerates  $N_a$  as a function of time. It was found that a decrease of  $N_s(t)$  is accompanied by an increase of  $N_a(t)$ . Using a model involving extinction contributions of  $N_s$  dispersed single nanorods as well as  $N_a$  magneto-optically inactive nanorods in agglomerates, resulted in a good agreement of theoretically calculated and measured  $I(H)/I_0$  curves (not shown).

In [103], time constants for the coagulation process for PVP coated Ni nanorods were determined. The short time constant of  $310 \pm 40$  min in a 22 mM NaCl solution shows that PVP coated Ni nanorods are not suitable as probe particles in environments of higher ionic strength, e.g. biological systems which exhibit typical NaCl concentrations of 100 mM if the measurement time typically exceeds the time constant of the coagulation process.

In the present work, the influence of the silica shell on the colloidal stability will be studied, performing the same experiments as described in [103], but using silica encapsulated Ni nanorods instead of PVP coated Ni nanorods. The colloidal stability of the silica encapsulated Ni nanorods is expected to be improved by steric repulsion due to the silica shell. However, as for PVP coated Ni nanorods, the colloidal stability relies mainly on electrostatic repulsion.

To investigate the colloidal stability of silica encapsulated Ni nanorods, an aqueous suspension was deliberately destabilized by addition of NaCl to reduce the electrostatic repulsion between the particles. As observed for PVP coated Ni nanorods, the particles aggregate, Fig.D.3(a), presumably forming dimers of two parallel aligned single core particles, Fig.D.3(b), with a vanishing resulting magnetic moment. These particles lose their magnetic field-dependent optical activity and thus they are ignored when analyzing DC-MOT measurements normalized to the intensity measured for an isotropic orientation distribution  $I_\times$ . Thus, agglomerating particles apparently vanish from the measurement signal and  $N_s$  decreases.

A series of DC-MOT measurements (measurement time  $< 10$  min) was performed to monitor the concentration of singly dispersed particles  $N_s$  as a function of time as described in section 7.2, assuming monodisperse single core particles with given core length

$l$ , shell thickness  $D_{\text{sh}}$ , free diameter  $d_{\text{OT}}$ , and free particle concentration  $N_s$ , neglecting multi-core particles. For colloids stored for several days, a change in their transmittance was observed which was attributed to particle sedimentation. To avoid sedimentation effects, the closed cuvette was shaken by hand for some seconds prior to each measurement. The agitation of the colloid is expected to be too weak to break agglomerates. Fig.D.4 shows the concentration of singly dispersed rods  $N_s$  as a function of time elapsed since addition of NaCl for silica encapsulated Ni nanorods ( $c = 10.8 \text{ mM NaCl}$ , sample scn-2) and corresponding PVP coated nanorods ( $c = 10 \text{ mM NaCl}$ , sample pcn-3) with comparable core length, diameter, and particle concentration. For the silica coated

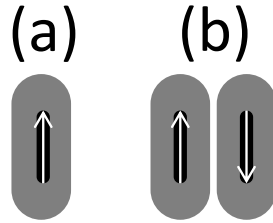


**Figure D.3:** Schematic illustration of (a) a single core particle, and (b) a dimer consisting of two single core particles. The white arrows indicate magnetic moments of the individual Ni cores. Only (a) has a resulting magnetic moment.

core-shell particles, the particle concentration  $N_s$  was nearly constant for  $\sim 4 \text{ h}$ . Only for very long incubation times  $\geq 200 \text{ h}$ , a slight decrease in  $N_s$  was found.

In contrast, the concentration of PVP coated Ni nanorods decreased rapidly within the first few measurements and the particles were almost completely agglomerated after 3 h. Thus, the colloidal stability of Ni nanorods was dramatically increased by the additional silica shell.

In order to estimate the dependence of the time constant of the aggregation process on NaCl concentrations, the measurements were repeated for higher NaCl concentrations. Fig.D.5 shows  $N_s$  as a function of time for an aqueous suspension of silica coated nanorods (scn-2) with a 50 mM NaCl concentration.

The fraction of singly dispersed rods decreased from  $4.2 \cdot 10^{15} \text{ m}^{-3}$  to  $1.4 \cdot 10^{15} \text{ m}^{-3}$  within seven hours and reached a value of  $7.5 \cdot 10^{14} \text{ m}^{-3}$  after more than 60 h. The rate of the coagulation process could be characterized by a half-life  $t_{50}$  which was directly obtained from the observed data. The measurement was repeated three times for two different NaCl concentrations. Half-lives of  $\langle t_{50} \rangle = 163 \text{ h}$  (standard deviation 16 min) in a 50 mM and  $\langle t_{50} \rangle = 134 \text{ h}$  (standard deviation 59 min) in a 100 mM NaCl solution were received. Since  $t_{50}$  is much larger than the typical measurement time ( $\sim 10 \text{ min}$ ) even in 100 mM

## D - Colloidal stability of silica encapsulated nanorods in aqueous dispersions

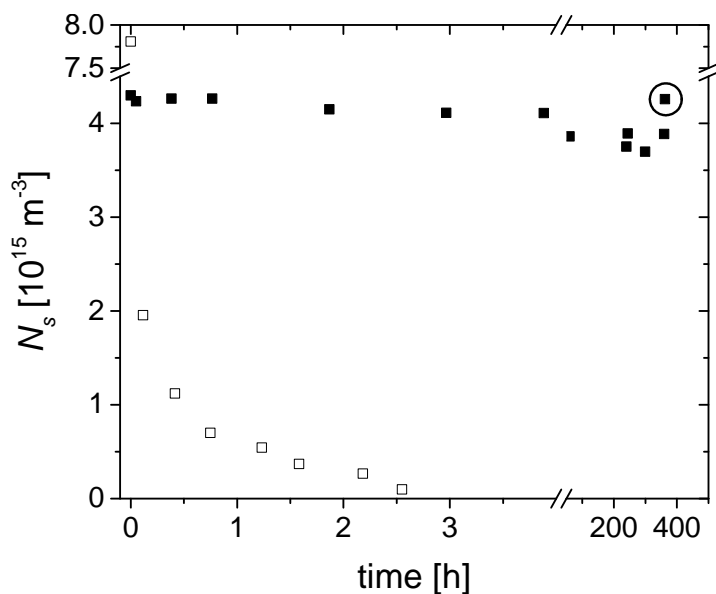


**Figure D.4:** Concentration of singly dispersed particles  $N_s$  as a function of time since addition of NaCl for silica (full squares, 10.8 mM NaCl, sample scn-2) and PVP coated Ni rods (empty squares, 10 mM NaCl). The circle indicates a 1 min sonication before the point was captured.

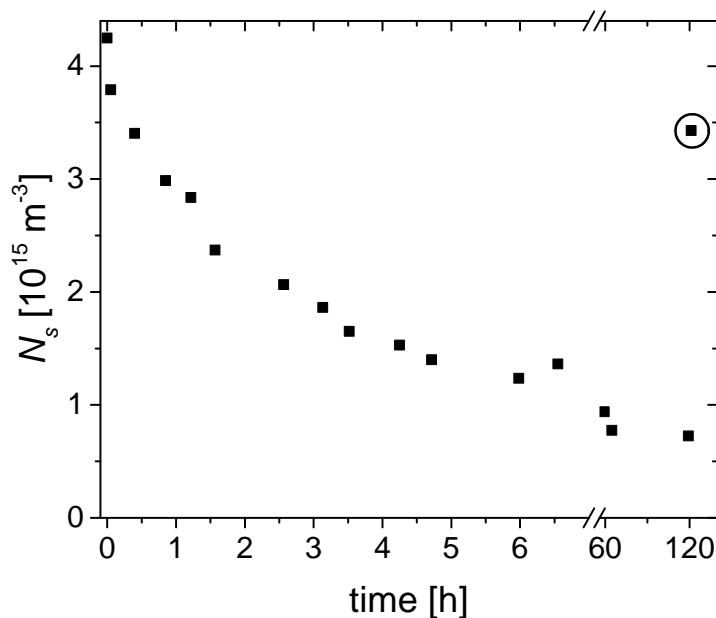


**Figure D.5:** Sample scn-2, 50 mM NaCl:  $N_s$  as a function of time since addition of NaCl. The circle indicates a 1 min sonication treatment before the point was captured.

---

NaCl solutions, silica encapsulated Ni nanorods are promising candidates to act as probes in systems of high ionic strength, for example in biological environments.

In conclusion, it was shown that due to the larger spacing between the magnetic cores, the colloidal stability of silica coated Ni nanorods is significantly increased as compared to PVP coated Ni nanorods. Furthermore, the larger spacing reduces the stability of formed aggregates, Fig.D.3 (b), as shown by the last measurement point in Figs.D.4 and D.5, which was captured after performing a 1 min redispersion in an ultrasonic bath which resulted in values for  $N_s$  comparable to the initial values. The possibility to break agglomerates of silica encapsulated rods is a great advantage with regard to a long term storage of the samples.

**D - Colloidal stability of silica encapsulated nanorods in aqueous dispersions**

# Appendix E

## Legal notice

Some parts of this work were already published in the *Journal of Applied Physics* under the title *Analysis of the static magnetic field-dependent optical transmission of Ni nanorod colloidal suspensions* (2016). This publication is equal to reference [43]. Every time text from this publication was reused in the present work, a corresponding note is given.

In the following, the contributions of the first and the co-authors to this publication will be described. The samples were synthesized by MG (pcn-1 and pcn-2) and FK (pcn-3 and pcn-4). The structural characterization of the particles using TEM as well as analysis of the resulting micrographs were performed by MG (pcn-1 and pcn-2) and FK (pcn-3 and pcn-4). Magnetic field-dependent optical transmission measurements on the colloids were carried out by FK. All calculations including the determination of the optical cross section by EA, SVM, and FEM as well as all the implementation and execution of all regression analyses were done by FK. The first version of the manuscript was written by FK. The final manuscript was generated jointly by FK and AT.



# Appendix F

## Publications

### F.1 Papers

Published:

- **Analysis of the static magnetic field-dependent optical transmission of Ni nanorod colloidal suspensions**  
F. Krämer, M. Gratz, and A. Tschöpe  
Journal of Applied Physics, 120, 044301, July 2016
- **Influence of dipolar interactions on the angular-dependent coercivity of nickel nanocylinders**  
P. Bender, F. Krämer, A. Tschöpe, and R. Birringer  
Journal of Physics D: Applied Physics, Volume 48, Number 14, March 2015
- **Quantification of magneto-optically active nanorods and inactive aggregates in nickel nanorod colloids**  
Andreas Tschöpe, Florian Krämer, Kerstin Birster, Micha Gratz, and Rainer Birringer  
Colloids and Interface Science Communications, Volumes 10 – 11, January – March 2016, Pages 11 – 14, April 2016

Prepared:

- **Static and dynamic magneto-optical properties of silica-coated nickel nanorod colloidal suspensions**  
F. Krämer and A. Tschöpe

- **Ni nanorods interact with human cells and induce changes in intracellular signalling and gene expression**

A-K Schmidt, C Gräfe, F Krämer, A Tschöpe, R Birringer, A Hochhaus, and J H Clement

## F.2 Conference contributions

As first and presenting author:

- **Examination of the Switching Field Distribution (SFD) and the shape anisotropy constant of nickel nanorods**

F Krämer, P Bender, A Tschöpe, and R Birringer  
DPG Frühjahrstagung 2011, Dresden

- **Investigation of the influence of dipolar interactions on the magnetic behavior of Ni nanorods**

F Krämer, P Bender, A Tschöpe, and R Birringer  
DPG Frühjahrstagung 2012, Berlin

- **Synthesis and characterization of silica-encapsulated Ni nanorods**

F Krämer, A Tschöpe, and R Birringer  
DPG Frühjahrstagung 2013, Regensburg

- **Influence of Silica-Encapsulation on the Hydrodynamical Properties of Ni Nanorods**

F Krämer, D Pieter, P Bender, A Tschöpe, and R Birringer  
13th German Ferrofluid Workshop, Benediktbeuern, 2013

- **Silica-Encapsulated Ni Nanorods as Model Particles for Stroboscopic Small Angle X-Ray Scattering (S-SAXS)**

F Krämer, P Bender, S Disch, M Kundt, D Honecker, A Tschöpe, and R Birringer  
14th German Ferrofluid Workshop, Ilmenau, 2014

- **Colloidal Stability of Silica-Encapsulated Ni Nanorods in Moderate Electrolytes and their Biocompatibility to Human Brain Microvascular Endothelial Cells**

F Krämer, C Gräfe, A Tschöpe, J Clement, R Birringer, and A Hochhaus

## F.2 Conference contributions

---

10th International Conference on the Scientific and Clinical Applications of Magnetic Carriers, Dresden, 2014

As co-author:

- **Coated superparamagnetic nickel nanorods affect cell vitality and intracellular signalling**

A-K Schmidt, C Gräfe, F Krämer, K Birster, A Tschäpe, A Hochhaus, J H Clement  
15th German Ferrofluid Workshop, Rostock, 2015

- **Ni nanorods interact with human cells and induce changes in intracellular signalling and gene expression**

A-K Schmidt, C Gräfe, F Krämer, A Tschöpe, R Birringer, A Hochhaus, J H Clement

11th International Conference on the Scientific and Clinical Applications of Magnetic Carriers, Vancouver, 2016



# Danksagung

**Prof. Dr. Rainer Birringer** danke ich für die Möglichkeit der Promotion an seinem Lehrstuhl sowie für die vielen physikalischen und philosophischen Ratschläge.

**Prof. Dr. Christian Wagner** danke ich für die Erstellung des Zweitgutachtens meiner Arbeit.

**Dr. Andreas Tschöpe** danke ich für die konzeptionelle Betreuung meiner Arbeit, die vielen Stunden Detailarbeit beim Feinschliff und die immer offene Tür für alle Belange.

**Dr. Philipp Bender** danke ich für die Zusammenarbeit und Hilfen in diversen Projekten und die spannende gemeinsame Zeit.

**Prof. Dr. Carl Krill** danke ich für die netten Besuche in Ulm und die Leihgabe des ALD-Reaktors, auch wenn dieser letztendlich nicht benutzt wurde.

**Jörg Schmauch** danke ich für seine Hilfe an REM und TEM.

**Jörg Schwarz** danke ich für seine Hilfe bei technischen Realisierungen von Versuchen sowie für die vielen Gespräche und Diskussionen.

**Christine Joerg** danke ich für die schnelle Bearbeitung bürokratischer Fragen.

**Michael Deckarm, Micha Gratz, Christoph Schopphoven, Andreas Leibner, Christian Braun, Manuel Grewer und Kerstin Birster** danke ich für die schöne Zeit voller fachlicher und fachfremder Diskussionen, Grillfeste und Unternehmungen am Lehrstuhl und darüber hinaus. Besonderen Dank gilt all jenen, die zum Gelingen dieser Arbeit (beispielsweise durch Korrekturlesen oder Hilfe im Labor) beigetragen haben.

**Konstantin Eckle** danke ich fürs Korrekturlesen der Arbeit.

**Meiner Frau und meinen Kindern** danke ich dafür, dass sie **alle** genauso sind, wie sie sind. Da könnte ich mir nichts Besseres wünschen.

**Meinen Eltern** danke ich dafür, dass sie mir immer die Freiheit ließen, zu tun was ich wollte, und mich in meinen Vorhaben bestärkt haben.

# Bibliography

- [1] Robert Brown. XXVII. A brief account of microscopical observations made in the months of June, July and August 1827, on the particles contained in the pollen of plants; and on the general existence of active molecules in organic and inorganic bodies. *Philosophical Magazine Series 2*, 4(21):161–173, 1828.
- [2] Albert Einstein. Über die von der molekularkinetischen Theorie der Wärme geforderte Bewegung von in ruhenden Flüssigkeiten suspendierten Teilchen. *Annalen der Physik*, 322(8):549–560, 1905.
- [3] T A Waigh. Microrheology of complex fluids. *Reports on Progress in Physics*, 68(3):685, 2005.
- [4] Thomas G Mason. Estimating the viscoelastic moduli of complex fluids using the generalized Stokes–Einstein equation. *Rheologica Acta*, 39(4):371–378, 2000.
- [5] A. Ashkin. Acceleration and trapping of particles by radiation pressure. *Phys. Rev. Lett.*, 24:156–159, Jan 1970.
- [6] R R Brau, J M Ferrer, H Lee, C E Castro, B K Tam, P B Tarsa, P Matsudaira, M C Boyce, R D Kamm, and M J Lang. Passive and active microrheology with optical tweezers. *Journal of Optics A: Pure and Applied Optics*, 9(8):S103, 2007.
- [7] LG Wilson, AW Harrison, AB Schofield, J Arlt, and WCK Poon. Passive and active microrheology of hard-sphere colloids. *The Journal of Physical Chemistry B*, 113(12):3806–3812, 2009.
- [8] H Freundlich and W Seifriz. Über die Elastizität von Solen und Gelen. *Z. phys. Chem*, 104:233–261, 1922.
- [9] Alfred Heilbronn. Eine neue Methode zur Bestimmung der Viskosität lebender Protoplasten. *Jahrb. Wiss. Bot*, 61:284, 1922.

- [10] F H C Crick and A F W Hughes. The physical properties of cytoplasm: A study by means of the magnetic particle method Part I. Experimental. *Experimental Cell Research*, 1(1):37–80, 1950.
- [11] Malcolm King and Peter T Macklem. Rheological properties of microliter quantities of normal mucus. *Journal of Applied Physiology*, 42(6):797–802, 1977.
- [12] Ken S Zaner and Peter A Valberg. Viscoelasticity of f-actin measured with magnetic microparticles. *Journal of cell biology*, 109(5):2233–2243, 1989.
- [13] Andreas R Bausch, Florian Ziemann, Alexei A Boulbitch, Ken Jacobson, and Erich Sackmann. Local measurements of viscoelastic parameters of adherent cell surfaces by magnetic bead microrheometry. *Biophysical journal*, 75(4):2038–2049, 1998.
- [14] Andreas R Bausch, Winfried Möller, and Erich Sackmann. Measurement of local viscoelasticity and forces in living cells by magnetic tweezers. *Biophysical journal*, 76(1):573–579, 1999.
- [15] A. Tschöpe, K. Birster, B. Trapp, P. Bender, and R. Birringer. Nanoscale rheometry of viscoelastic soft matter by oscillating field magneto-optical transmission using ferromagnetic nanorod colloidal probes. *Journal of Applied Physics*, 116(18):184305, 2014.
- [16] Anne K Bentley, Arthur B Ellis, George C Lisensky, and Wendy C Crone. Suspensions of nickel nanowires as magneto-optical switches. *Nanotechnology*, 16(10):2193–2196, 2005.
- [17] Prajnaparamita Dhar, Yanyan Cao, Thomas M. Fischer, and J. A. Zasadzinski. Active interfacial shear microrheology of aging protein films. *Phys. Rev. Lett.*, 104:016001, Jan 2010.
- [18] Alexander Tokarev, Alexey Aprelev, Mikhail N. Zakharov, Guzeliya Korneva, Yury Gogotsi, and Konstantin G. Kornev. Multifunctional magnetic rotator for micro and nanorheological studies. *Review of Scientific Instruments*, 83(6), 2012.
- [19] Pavel Aprelev, Yu Gu, Ruslan Burtovyy, Igor Luzinov, and Konstantin G. Kornev. Synthesis and characterization of nanorods for magnetic rotational spectroscopy. *Journal of Applied Physics*, 118(7), 2015.

## BIBLIOGRAPHY

---

- [20] Tobias Klein, Aleksej Laptev, Annegret Günther, Philipp Bender, A. Tschöpe, and R. Birringer. Magnetic-field-dependent optical transmission of nickel nanorod colloidal dispersions. *Journal of Applied Physics*, 106(11):114301, 2009.
- [21] Taeg M. Kwon, Paul L. Frattini, Lachmi N. Sadani, and Myung S. Jhon. Rheo-optical study of magnetic particle orientation under external fields. *Colloids and Surfaces A: Physicochemical and Engineering Aspects*, 80(1):47–61, 1993.
- [22] Alejandro J. Gimenez, Diana G. Ramirez-Wong, Sarai E. Favela-Camacho, Isaac C. Sanchez, J.M. Yañez-Limón, and Gabriel Luna-Bárceñas. Optical detection of magnetic nanoparticles in colloidal suspensions. *Journal of Magnetism and Magnetic Materials*, 402:150 – 155, 2016.
- [23] Stefan Schrittwieser, Frank Ludwig, Jan Dieckhoff, Andreas Tschoepe, Annegret Guenther, Michael Richter, Andreas Huetten, Hubert Brueckl, and Joerg Schotter. Direct Protein Detection in the Sample Solution by Monitoring Rotational Dynamics of Nickel Nanorods. *Small*, 10(2):407–411, 2014.
- [24] A. Günther, P. Bender, A. Tschöpe, and R. Birringer. Rotational diffusion of magnetic nickel nanorods in colloidal dispersions. *Journal of Physics: Condensed Matter*, 23(32):325103, 2011.
- [25] Annegret Günther. *Hydrodynamische Eigenschaften von magnetischen Nickel-nanostäben in kolloidaler Suspension*. PhD thesis, Universität des Saarlandes, Postfach 151141, 66041 Saarbrücken, 2011.
- [26] Vishwas V. Hardikar and Egon Matijević. Coating of Nanosize Silver Particles with Silica. *Journal of Colloid and Interface Science*, 221(1):133 – 136, 2000.
- [27] Luis M. Liz-Marzan, Michael Giersig, and Paul Mulvaney. Synthesis of nanosized gold-silica core-shell particles. *Langmuir*, 12(18):4329–4335, 1996.
- [28] Isabel Pastoriza-Santos, Jorge Perez-Juste, and Luis M. Liz-Marzan. Silica-Coating and Hydrophobation of CTAB-Stabilized Gold Nanorods. *Chemistry of Materials*, 18(10):2465–2467, 2006.
- [29] Nynke A. M. Verhaegh and Alfons van Blaaderen. Dispersions of Rhodamine-Labeled Silica Spheres: Synthesis, Characterization, and Fluorescence Confocal Scanning Laser Microscopy. *Langmuir*, 10(5):1427–1438, 1994.

- [30] Michela Puddu, Daniela Paunescu, Wendelin J. Stark, and Robert N. Grass. Magnetically Recoverable, Thermostable, Hydrophobic DNA/Silica Encapsulates and Their Application as Invisible Oil Tags. *ACS Nano*, 8(3):2677–2685, 2014. PMID: 24568212.
- [31] Gustav Mie. Beiträge zur Optik trüber Medien, speziell kolloidaler Metallösungen. *Annalen der Physik*, 330(3):377–445, 1908.
- [32] Shoji Asano and Giichi Yamamoto. Light Scattering by a Spheroidal Particle. *Applied Optics*, 14(1):29–49, 1975.
- [33] Shoji Asano. Light scattering properties of spheroidal particles. *Appl. Opt.*, 18(5):712–723, Mar 1979.
- [34] N.V. Voshchinnikov and V.G. Farafonov. Optical properties of spheroidal particles. *Astrophysics and Space Science*, 204(1):19–86, 1993.
- [35] J. Parsons, C.P. Burrows, J.R. Sambles, and W.L. Barnes. A comparison of techniques used to simulate the scattering of electromagnetic radiation by metallic nanostructures. *Journal of Modern Optics*, 57(5):356–365, 2010.
- [36] Thomas Wriedt. Light scattering theories and computer codes. *Journal of Quantitative Spectroscopy & Radiative Transfer*, 110(11):833 – 843, 2009.
- [37] Kyeong-Seok Lee and Mostafa A. El-Sayed. Dependence of the Enhanced Optical Scattering Efficiency Relative to That of Absorption for Gold Metal Nanorods on Aspect Ratio, Size, End-Cap Shape, and Medium Refractive Index. *The Journal of Physical Chemistry B*, 109(43):20331–20338, 2005.
- [38] S. Link, M. B. Mohamed, and M. A. El-Sayed. Simulation of the optical absorption spectra of gold nanorods as a function of their aspect ratio and the effect of the medium dielectric constant. *The Journal of Physical Chemistry B*, 103(16):3073–3077, 1999.
- [39] A.V. Alekseeva, V.A. Bogatyrev, B.N. Khlebtsov, A.G. Melnikov, L.A. Dykman, and N.G. Khlebtsov. Gold nanorods: Synthesis and optical properties. *Colloid Journal*, 68(6):661–678, 2006.
- [40] E. Stefan Kooij and Bene Poelsema. Shape and size effects in the optical properties of metallic nanorods. *Phys. Chem. Chem. Phys.*, 8:3349–3357, 2006.

## BIBLIOGRAPHY

---

- [41] P. Bender, A. Günther, A. Tschöpe, and R. Birringer. Synthesis and characterization of uniaxial ferrogels with Ni nanorods as magnetic phase. *Journal of Magnetism and Magnetic Materials*, 323(15):2055 – 2063, 2011.
- [42] Philipp Bender. *Untersuchung der elastischen Eigenschaften von Gelatine-Gelen mittels Magnetisierungsmessungen unter Verwendung von Nickelnanostäben als Sonden*. PhD thesis, Universität des Saarlandes, Postfach 151141, 66041 Saarbrücken, 2012.
- [43] Florian Krämer, Micha Gratz, and Andreas Tschöpe. Analysis of the static magnetic field-dependent optical transmission of Ni nanorod colloidal suspensions. *Journal of Applied Physics*, 120(4), 2016.
- [44] Hideki Masuda and Masahiro Satoh. Fabrication of Gold Nanodot Array Using Anodic Porous Alumina as an Evaporation Mask. *Japanese Journal of Applied Physics*, 35(Part 2, No. 1B):L126–L129, 1996.
- [45] Jeong Min Baik, Martin Schierhorn, and Martin Moskovits. Fe Nanowires in Nanoporous Alumina: Geometric Effect versus Influence of Pore Walls. *The Journal of Physical Chemistry C*, 112(7):2252–2255, 2008.
- [46] Kornelius Nielsch, Frank Müller, An-Ping Li, and Ulrich Gösele. Uniform Nickel Deposition into Ordered Alumina Pores by Pulsed Electrodeposition. *Advanced Materials*, 12(8):582–586, 2000.
- [47] G. E. Thompson and G. C. Wood. Porous anodic film formation on aluminium. *Nature*, 290(5803):230–232, 1981.
- [48] Oliver P. Watt. Rapid nickel plating. *Scientific American*, 82:90–91, 1916.
- [49] Chih-Hung LO, Tsing-Tshih TSUNG, and Liang-Chia CHEN. Ni Nano-Magnetic Fluid Prepared by Submerged Arc Nano Synthesis System (SANSS). *JSME International Journal Series B Fluids and Thermal Engineering*, 48(4):750–755, 2005.
- [50] Ha-Young Lee, Sang-Hoon Lee, Chenjie Xu, Jin Xie, Jin-Hyung Lee, Bing Wu, Ai Leen Koh, Xiaoying Wang, Robert Sinclair, Shan X Wang, Dwight G Nishimura, Sandip Biswal, Shouheng Sun, Sun Hang Cho, and Xiaoyuan Chen. Synthesis and characterization of PVP-coated large core iron oxide nanoparticles as an MRI contrast agent. *Nanotechnology*, 19(16):165101, 2008.

- [51] Werner Stöber, Arthur Fink, and Ernst Bohn. Controlled Growth of Monodisperse Silica Spheres in the Micron Size Range. *Journal of colloid and interface science*, 26(1):62–69, 1968.
- [52] N. Haselmaier. Präparation magnetischer Nanostäbchen in einer SiO<sub>2</sub>-Hülle mit Hilfe des Stöber Verfahrens. 2011.
- [53] Lu Yu, Yin Yadong, Li Zhi-Yuan, and Xia Younan. Synthesis and Self-Assembly of AuSiO<sub>2</sub> Core-Shell Colloids. *Nano Letters*, 2(7):785–788, 2002.
- [54] I. Artaki, M. Bradley, T. W. Zerda, and J. Jonas. NMR and Raman study of the hydrolysis reaction in sol-gel processes. *The Journal of Physical Chemistry*, 89(20):4399–4404, 1985.
- [55] Chen Sheng-Li, Dong Peng, Yang Guang-Hua, and Yang Jiu-Jin. Kinetics of Formation of Monodisperse Colloidal Silica Particles through the Hydrolysis and Condensation of Tetraethylorthosilicate. *Industrial & Engineering Chemistry Research*, 35(12):4487–4493, 1996.
- [56] Lu Yu, Yin Yadong, T. Mayers Brian, and Xia Younan. Modifying the Surface Properties of Superparamagnetic Iron Oxide Nanoparticles through A Sol-Gel Approach. *Nano Letters*, 2(3):183–186, 2002.
- [57] Christina Graf, Dirk L. J. Vossen, Arnout Imhof, and Alfons van Blaaderen. A General Method To Coat Colloidal Particles with Silica. *Langmuir*, 19(17):6693–6700, 2003.
- [58] Yin Yadong, Lu Yu, Sun Yugang, and Xia Younan. Silver Nanowires Can Be Directly Coated with Amorphous Silica To Generate Well-Controlled Coaxial Nanocables of Silver/Silica. *Nano Letters*, 2(4):427–430, 2002.
- [59] Wuyou Fu, Haibin Yang, Lianxia Chang, Minghui Li, Hari Bala, Qingjiang Yu, and Guangtian Zou. Preparation and characteristics of core-shell structure nickel/silica nanoparticles. *Colloids and Surfaces A: Physicochemical and Engineering Aspects*, 262(1-3):71–75, 2005.
- [60] USA Wayne Rasband, National Institutes of Health. *ImageJ*. (1.47v).
- [61] Ralph Skomski and JMD Coey. *Permanent magnetism*. Institute of Physics Pub., 1999.

## BIBLIOGRAPHY

---

- [62] K Nielsch. *Hochgeordnete ferromagnetische Nano-Stabensembles*. PhD thesis, Martin-Luther-Universität Halle-Wittenberg, 2002.
- [63] J.M.D. Coey. *Magnetism and magnetic materials*. Cambridge University Press, 2010.
- [64] Stephen Blundell. *Magnetism in condensed matter*. Oxford Univ. Press, 2001.
- [65] A. Huber and R. Schäfer. *Magnetic Domains*. Springer, Berlin, 1998.
- [66] C. A. Ross, M. Hwang, M. Shima, J. Y. Cheng, M. Farhoud, T. A. Savas, Henry I. Smith, W. Schwarzacher, F. M. Ross, M. Redjfal, and F. B. Humphrey. Micro-magnetic behavior of electrodeposited cylinder arrays. *Phys. Rev. B*, 65:144417, Mar 2002.
- [67] Hans Koop. Untersuchung des Einflusses der geometrischen Form auf das Schaltverhalten magnetischer Tunnelelemente im sub- $\mu\text{m}$  Größenbereich. 2004.
- [68] E. C. Stoner and E. P. Wohlfarth. A mechanism of magnetic hysteresis in heterogeneous alloys. *IEEE Transactions on Magnetism*, 27:3475, 1991.
- [69] Louis Néel. Thermoremanent magnetization of fine powders. *Reviews of Modern Physics*, 25(1):293, 1953.
- [70] CP Bean and JD Livingston. Superparamagnetism. *Journal of Applied Physics*, 30(4):S120–S129, 1959.
- [71] P. Bender, A. Tschöpe, and R. Birringer. Determination of the shear modulus of gelatine hydrogels by magnetization measurements using dispersed nickel nanorods as mechanical probes. *Journal of Magnetism and Magnetic Materials*, 346(0):152 – 160, 2013.
- [72] P Bender, F Krämer, A Tschöpe, and R Birringer. Influence of dipolar interactions on the angular-dependent coercivity of nickel nanocylinders. *Journal of Physics D: Applied Physics*, 48(14):145003, 2015.
- [73] DC Crew, SH Farrant, PG McCormick, and R Street. Measurement of magnetic viscosity in a Stoner-Wohlfarth material. *Journal of Magnetism and Magnetic Materials*, 163(3):299–312, 1996.

- [74] William Fuller Brown. Thermal fluctuations of a single-domain particle. *Phys. Rev.*, 130:1677–1686, Jun 1963.
- [75] Nikolaj E. Kotschin, Ilja A. Kibel, and Nikolaj V. Rose. *Theoretische Hydrodromechanik*, volume 2:. Akad.-Verl., Berlin, 1955. Mit 156 Abb. im Text.
- [76] Gustav Robert Kirchhoff. Vorlesungen über mathematische Physik, 1897.
- [77] D. Edwards. Unknown title. *Quart. J. Math.*, 26:70, 1893.
- [78] Perrin, Francis. Mouvement brownien d'un ellipsoïde - i. dispersion dielectrique pour des molecules ellipsoidales. *J. Phys. Radium*, 5(10):497–511, 1934.
- [79] Richard Gans. Zur Theorie der Brownschen Molekularbewegung. *Annalen der Physik*, 391(12):628–656, 1928.
- [80] Seymour H Koenig. Brownian motion of an ellipsoid. A correction to Perrin's results. *Biopolymers*, 14(11):2421–2423, 1975.
- [81] M. Doi and S. F. Edwards. *The Theory of Polymer Dynamics*. Oxford University Press, 1986.
- [82] George Gabriel Stokes. *On the effect of the internal friction of fluids on the motion of pendulums*, volume IX. 1851.
- [83] L.D. Landau and E.M. Lifshitz. Fluid Mechanics. 1987.
- [84] Maria M. Tirado and José García de la Torre. Translational friction coefficients of rigid, symmetric top macromolecules. Application to circular cylinders. *The Journal of Chemical Physics*, 71(6):2581–2587, 1979.
- [85] María M. Tirado and José García de la Torre. Rotational dynamics of rigid, symmetric top macromolecules. Application to circular cylinders. *The Journal of Chemical Physics*, 73(4):1986–1993, 1980.
- [86] M. Mercedes Tirado, Carmen López Martínez, and José García de la Torre. Comparison of theories for the translational and rotational diffusion coefficients of rod-like macromolecules. Application to short DNA fragments. *The Journal of Chemical Physics*, 81(4):2047–2052, 1984.
- [87] Sergio Aragon. A precise boundary element method for macromolecular transport properties. *Journal of computational chemistry*, 25(9):1191–1205, 2004.

## BIBLIOGRAPHY

---

- [88] Sergio R. Aragon and Dina Flamik. High Precision Transport Properties of Cylinders by the Boundary Element Method. *Macromolecules*, 42(16):6290–6299, 2009.
- [89] Sergio R Aragon. Recent advances in macromolecular hydrodynamic modeling. *Methods*, 54(1):101–114, 2011.
- [90] Hiromi Yamakawa. Some remarks on the transport theory for wormlike cylinder models. *Macromolecules*, 16(12):1928–1931, 1983.
- [91] Karl M Krueger, Ali M Al-Somali, Michelle Mejia, and Vicki L Colvin. The hydrodynamic size of polymer stabilized nanocrystals. *Nanotechnology*, 18(47):475709, 2007.
- [92] Carlos A. R. Costa, Carlos A. P. Leite, and Fernando Galembeck. Size Dependence of Stöber Silica Nanoparticle Microchemistry. *The Journal of Physical Chemistry B*, 107(20):4747–4755, 2003.
- [93] Craig F. Bohren and Donald R. Huffman. *Absorption and Scattering of Light by Small Particles*. Wiley-VCH, Weinheim, 2004.
- [94] Richard Courant and David Hilbert. *Methods of mathematical physics, Volume I*. Interscience Publishers, New York, 1953.
- [95] Michael I. Mishchenko, Joachim W. Hovenier, and Larry D. Travis. *Light Scattering by Nonspherical Particles: Theory, Measurements, and Applications*. Academic press, 2000.
- [96] J.A. Osborn. Demagnetizing Factors of the General Ellipsoid. *Physical Review*, 67(11-12):351–357, 1945.
- [97] P.B. Johnson and R.W. Christy. Optical constants of transition metals: Ti, V, Cr, Mn, Fe, Co, Ni, and Pd. *Physical Review B*, 9:5056–5070, 1974.
- [98] George M. Hale and Marvin R. Querry. Optical Constants of Water in the 200-nm to 200- $\mu$ m Wavelength Region. *Applied Optics*, 12(3):555–563, Mar 1973.
- [99] C. P. Bean and J. D. Livingston. Superparamagnetism. *Journal of Applied Physics*, 30(4):S120–S129, 1959.
- [100] P Debye. *Polar Molecules* (New York). 1945.

- [101] Jianing Chen, Pablo Albella, Zhaleh Pirzadeh, Pablo Alonso-González, Florian Huth, Stefano Bonetti, Valentina Bonanni, Johan Åkerman, Josep Nogués, Paolo Vavassori, Alexandre Dmitriev, Javier Aizpurua, and Rainer Hillenbrand. Plasmonic Nickel Nanoantennas. *Small*, 7(16):2341–2347, 2011.
- [102] Nikolai Voshchinnikov. The software was kindly provided by Nikolai Voshchinnikov.
- [103] A. Tschöpe, F. Krämer, K. Birster, M. Gratz, and R. Birringer. Quantification of magneto-optically active nanorods and inactive aggregates in nickel nanorod colloids. *Colloids and Interface Science Communications*, 10:11–14, 2016.
- [104] Monica Tanase, Laura Ann Bauer, Anne Hultgren, Daniel M. Silevitch, Li Sun, Daniel H. Reich, Peter C. Searson, and Gerald J. Meyer. Magnetic alignment of fluorescent nanowires. *Nano Letters*, 1(3):155–158, 2001.
- [105] Prashant K. Jain, Susie Eustis, and Mostafa A. El-Sayed. Plasmon coupling in nanorod assemblies: Optical absorption, discrete dipole approximation simulation, and exciton-coupling model. *The Journal of Physical Chemistry B*, 110(37):18243–18253, 2006. PMID: 16970442.
- [106] Alison M. Funston, Carolina Novo, Tim J. Davis, and Paul Mulvaney. Plasmon Coupling of Gold Nanorods at Short Distances and in Different Geometries. *Nano Letters*, 9(4):1651–1658, 2009.
- [107] Boris N. Khlebtsov, Vitaly A. Khanadeev, and Nikolai G. Khlebtsov. Determination of the size, concentration, and refractive index of silica nanoparticles from turbidity spectra. *Langmuir*, 24(16):8964–8970, 2008. PMID: 18590302.
- [108] LF Hoyt. New table of the refractive index of pure glycerol at 20° C. *Industrial & Engineering Chemistry*, 26(3):329–332, 1934.
- [109] Nian-Sheng Cheng\*. Formula for the Viscosity of a Glycerol–Water Mixture. *Industrial & Engineering Chemistry Research*, 47(9):3285–3288, 2008.
- [110] A.-K. Schmidt, C. Gräfe, F. Krämer, A. Tschöpe, R. Birringer, A. Hochhaus, J. H. Clement. Ni nanorods interact with human cells and induce changes in intracellular signalling and gene expression. Poster, 2016. 11th International Conference on the Scientific and Clinical Applications of Magnetic Carriers, Vancouver.

## BIBLIOGRAPHY

---

- [111] Ann-Kathrin Schmidt. Effects of coated ferromagnetic nickel nanorods on cell vitality and intracellular signalling of human brain microvascular endothelial cells, 2016.
- [112] Aliasger K Salem, Peter C Searson, and Kam W Leong. Multifunctional nano-rods for gene delivery. *Nature materials*, 2(10):668–671, 2003.
- [113] Dadong Guo, Chunhui Wu, Hongli Hu, Xuemei Wang, Xiaomao Li, and Baoan Chen. Study on the enhanced cellular uptake effect of daunorubicin on leukemia cells mediated via functionalized nickel nanoparticles. *Biomedical Materials*, 4(2):025013, 2009.
- [114] Monique F Stins, Julie Badger, and Kwang Sik Kim. Bacterial invasion and transcytosis in transfected human brain microvascular endothelial cells. *Microbial pathogenesis*, 30(1):19–28, 2001.

